

1 LEVERAGING MULTI-MESSENGER ASTROPHYSICS FOR DARK MATTER SEARCHES

By

Daniel Nicholas Salazar-Gallegos

A DISSERTATION

Submitted to
Michigan State University
in partial fulfillment of the requirements
for the degree of

Physics—Doctor of Philosophy
Computational Mathematics in Science and Engineering—Dual Major

Today

ABSTRACT

3 I did Dark Matter with HAWC and IceCube. I also used Graph Neural Networks

⁴ Copyright by

⁵ DANIEL NICHOLAS SALAZAR-GALLEGOS

⁶ Today

ACKNOWLEDGMENTS

8 I love my friends. Thanks to everyone that helped me figure this out. Amazing thanks to the people
9 at LANL who supported me. Eames, etc Dinner Parties Jenny and her child Kaydince Kirsten, Pat,
10 Andrea Family. You're so far but so critical to my formation. Unconditional love. Roommate

TABLE OF CONTENTS

12	LIST OF TABLES	vii
13	LIST OF FIGURES	ix
14	LIST OF ABBREVIATIONS	xx
15	CHAPTER 1 INTRODUCTION	1
16	CHAPTER 2 DARK MATTER IN THE COSMOS	2
17	2.1 Introduction	2
18	2.2 Dark Matter Basics	3
19	2.3 Evidence for Dark Matter	4
20	2.4 Searching for Dark Matter: Particle DM	11
21	2.5 Sources for Indirect Dark Matter Searches	16
22	2.6 Multi-Messenger Dark Matter	18
23	CHAPTER 3 HIGH ALTITUDE WATER CHERENKOV (HAWC) OBSERVATORY	21
24	3.1 The Detector	21
25	3.2 Events Reconstruction	26
26	3.3 Remote Monitoring	29
27	CHAPTER 4 ICECUBE NEUTRINO OBSERVATORY	30
28	4.1 The Detector	30
29	4.2 Events Reconstruction and Data Acquisition	30
30	4.3 Northern Test Site	30
31	CHAPTER 5 GLORY DUCK: MULTI-WAVELENGTH SEARCH FOR DARK MATTER ANNIHILATION TOWARDS DWARF SPHEROIDAL GALAXIES	31
32	5.1 Introduction	31
33	5.2 Dataset and Background	33
34	5.3 Analysis	35
35	5.4 Likelihood Methods	39
36	5.5 HAWC Results	46
37	5.6 Glory Duck Combined Results	48
38	5.7 HAWC Systematics	53
39	5.8 J -factor distributions	55
40	5.9 Discussion and Conclusions	61
43	CHAPTER 6 MULTITHREADING HAWC ANALYSES FOR DARK MATTER SEARCHES	65
44	6.1 Introduction	65
45	6.2 Dataset and Background	65
46	6.3 Analysis	67

48	6.4	Likelihood Methods	71
49	6.5	Computational Methods: Multithreading	71
50	6.6	Analysis Results	77
51	6.7	Systematics	82
52	6.8	Conclusion and Discussion	82
53	CHAPTER 7	HEAVY DARK MATTER ANNIHILATION SEARCH WITH ICE-CUBE'S NORTH SKY TRACK DATA	84
55	7.1	Introduction	84
56	7.2	Dataset and Background	84
57	7.3	Analysis	86
58	7.4	Likelihood Methods	95
59	7.5	Background Simulation	95
60	7.6	Signal Recovery	113
61	7.7	Systematics	116
62	7.8	Conclusions	119
63	CHAPTER 8	NU DUCK: CONCLUSIONS AND FUTURE DIRECTIONS	121
64	8.1	Conclusions	121
65	8.2	Future Directions	122
66	APPENDIX A	MULTI-EXPERIMENT SUPPLEMENTARY FIGURES	124
67	APPENDIX B	MULTITHREADING DARK MATTER ANALYSES SUPPLEMENTARY MATERIAL	125
69	B.1	Remaining Spectral Models	125
70	B.2	<code>mpu_analysis.py</code>	126
71	B.3	Comparison with Glory Duck	135
72	APPENDIX C	ICECUBE HEAVY DARK MATTER ANALYSIS SUPPLEMENTARY MATERIAL	138
74	C.1	Docker Image for Oscillating Neutrino Spectra	138
75	C.2	Spline Fitting Statuses	141
76	C.3	Neutrino Composite Spectra	142
77	C.4	Segue 1 And Ursa Major II Signal Recovery	143
78	C.5	n_s Sensitivities	149
79	BIBLIOGRAPHY		151

LIST OF TABLES

81	Table 5.1	Summary of the relevant properties of the dSphs used in the present work. Column 1 lists the dSphs. Columns 2 and 3 present their heliocentric distance and galactic coordinates, respectively. Columns 4 and 5 report the J -factors of each source given from the \mathcal{GS} and \mathcal{B} independent studies and their estimated $\pm 1\sigma$ uncertainties. The values $\log_{10} J$ (\mathcal{GS} set) [55] correspond to the mean J -factor values for a source extension truncated at the outermost observed star. The values $\log_{10} J$ (\mathcal{B} set) [59] are provided for a source extension at the tidal radius of each dSph. Bolded sources are within HAWC's field of view and provided to the Glory Duck analysis.	40
90	Table 5.2	Summary of dSph observations by each experiment used in this work. A '-' indicates the experiment did not observe the dSph for this study. For Fermi-LAT, the exposure at 1 GeV is given. For HAWC, $ \Delta\theta $ is the absolute difference between the source declination and HAWC latitude. HAWC is more sensitive to sources with smaller $ \Delta\theta $. For IACTs, we show the zenith angle range, the total exposure, the energy range, the angular radius θ of the signal or ON region, the ratio of exposures between the background-control (OFF) and signal (ON) regions (τ), and the significance of gamma-ray excess in standard deviations, σ .	41
99	Table 6.1	Summary of the relevant properties of the dSphs used in the present work. Column 1 lists the dSphs. Columns 2 and 3 present their heliocentric distance and galactic coordinates, respectively. Column 4 reports the J -factors of each source given from the \mathcal{LS} studies and estimated $\pm 1\sigma$ uncertainties. The values $\log_{10} J$ (\mathcal{LS} set) [76] correspond to the mean J -factor values for a source extension truncated at 0.5° .	71
105	Table 6.2	Timing summaries for analyses for serial and multithreaded processes. M tasks is the number of functional-parallel tasks ran for the computation. $T_{p,c}$ is a single run time in hours:minutes:seconds for runs utilizing p nodes and c threads. Runs are run interactively on the same computer to maximize consistency. Empty entries are indicated with '-'. (\cdot) entries are estimated entries extrapolated from data earlier in the column.	75
111	Table 6.3	Speed up summaries for analyses for serial and multithreaded processes. M tasks is the number of functional-parallel tasks ran for the computation. $S_{p,c}$ is a single speedup comparison for runs utilizing p nodes and c threads. $[\cdot]$ are the estimated speedups calculated from Tab. 6.2, Eq. (6.7), and Eq. (6.4). Empty entries are indicated with '-'.	77

116	Table 7.1	Spline err tolerances used for input in particle physics component to Eq. (5.1).	
117		Column 1 is the DM annihilation channel being fit. Columns 2, 3, and 4	
118		are the tolerances for "GOOD" (pass), "OK" requires inspection, and "FAIL"	
119		(tune and refit) respectively. Column 5 has the X ranges over which the error	
120		is evaluated. MAX/MIN $[\cdot, \cdot]$ takes the maximum or minimum of the two	
121		enclosed values.	92
122	Proof I know how to include		

LIST OF FIGURES

<p>124 Figure 2.1 Rotation curve fit to NGC 6503 from [7]. Dashed line is the contribution 125 from visible matter. Dotted curves are from gas. Dash-dot curves are from 126 dark matter (DM). Solid line is the composite contribution from all matter 127 and DM sources. Data are indicated with bold dots with error bars. Data 128 agree strongly with a matter + DM composite prediction.</p> <p>129 Figure 2.2 Light from distant galaxy is bent in unique ways depending on the distribution 130 of mass between the galaxy and Earth. Yellow dashed lines indicate where 131 the light would have gone if the matter were not present [8].</p> <p>132 Figure 2.3 (left) Optical image of galactic cluster 1E0657-558. (right) X-ray image of the 133 cluster with redder meaning hotter and higher baryon density. (both) Green 134 contours are reconstruction of gravity contours from weak lensing. White 135 rings are the best fit mass maxima at 68.3%, 95.5%, and 99.7% confidence. 136 The matter maxima of the clusters are clearly separated from x-ray maxima. [9]</p> <p>137 Figure 2.4 Plank CMB sky. Sky map features small variations in temperature in primor- 138 dial light. These anisotropies are used to make inferences about the universe's 139 energy budget and developmental history. [10]</p> <p>140 Figure 2.5 Observed Cosmic Microwave Background power spectrum as a function of 141 multipole moment from Plank [10]. Blue line is best fit model from ΛCDM. 142 Red points and lines are data and error, respectively.</p> <p>143 Figure 2.6 Predicted power spectra of CMB for different $\Omega_m h^2$ values for fixed baryon 144 density from [11]. (left) Low $\Omega_m h^2$ increases the prominence of first and 145 second peaks. (middle) $\Omega_m h^2$ is most similar to the observed power spectrum. 146 The second and third peaks are similar in height. (right) $\Omega_m h^2$ is large which 147 suppresses the first peak and raises the prominence of the third peak.</p> <p>148 Figure 2.7 The Standard Model (SM) of particle physics. Figure taken from http://www.quantumdiaries.org/2014/03/14/the-standard-model-a-beautiful-but-flawed-theory/</p> <p>151 Figure 2.8 Simplified Feynman diagram demonstrating with different ways DM can 152 interact with SM particles. The 'X's refer to the DM particles whereas the 153 SM refer to fundamental particles in the SM. The large circle in the center 154 indicates the vertex of interaction and is purposely left vague. The colored 155 arrows refer to different directions of time as well as their respective labels. 156 The arrows indicate the initial and final state of the DM -SM interaction in time.</p>	<p style="margin-bottom: 20px;">5</p> <p style="margin-bottom: 20px;">7</p> <p style="margin-bottom: 20px;">8</p> <p style="margin-bottom: 20px;">9</p> <p style="margin-bottom: 20px;">10</p> <p style="margin-bottom: 20px;">10</p> <p style="margin-bottom: 20px;">12</p> <p style="margin-bottom: 20px;">13</p>
---	---

157	Figure 2.9 A single jet event in ATLAS detector from 2017 [16]. Jet momentum was 158 observed to be 1.9 TeV. Missing transverse momentum was observed to be 159 1.9 TeV compared to the initial transverse momentum of the event was 0. 160 Implied MET is traced by a red dashed line in event display.	14
161	Figure 2.10 More detailed pseudo-Feynman diagram of particle cascade from dark matter 162 annihilation into 2 quarks. The quarks hadronize and down to stable particles 163 like γ or the anti-proton (p^-). Diagram pulled from ICRC 2021 presentation 164 on DM annihilation search [17].	15
165	Figure 2.11 Dark Matter (DM) decay spectrum for $b\bar{b}$ initial state and γ final state. Redder 166 spectra are for larger DM masses. Bluer spectra are light DM masses. x is a 167 unitless factor defined as the ratio of the mass of DM, m_χ , and the final state 168 particle energy E_γ . Figure from [19].	17
169	Figure 2.12 Different dark matter density profiles compared. Some models produce ex- 170 ceptionally large densities at small r [20].	18
171	Figure 2.13 The Milky Way Galaxy in photons (γ) and neutrinos (ν) [22]. The Galactic 172 center is at $l=0^\circ$ and is the brightest region in all panels. (top) An Optical 173 color image of the Milky Way galaxy seen from Earth. Clouds of gas and dust 174 obscure some light from stars. (2nd down) Integrated flux of γ -rays observed 175 by the Fermi-LAT telescope [23]. (middle) Expected neutrino emission 176 that corresponds with Fermi-LAT observations. (2nd up) Expected neutrino 177 emission profile after considering detector systematics of IceCube. (bottom) 178 Observed neutrino emission from region of the galactic plane. Substantial 179 neutrino emission was detected.	19
180	Figure 2.14 Dark Matter annihilation spectra for different final state particle and standard 181 model annihilation channels [24]. Photons (red), e^\pm (green), \bar{p} (blue), ν (black).	20
182	Figure 3.1 Photo of the HAWC detector that I took on May 17, 2023. Main array is 183 centered in the photo and comprised of the larger tanks. Outriggers are the 184 smaller tanks around the main array.	21
185	Figure 3.2 A particle physics illustration of high energy particle showers. Left shower is 186 an electromagnetic shower from a high energy gamma-ray. Most particles in 187 the shower will be a combination of photons and charged leptons, in this case 188 electrons (e). Right figure shows a cosmic ray particle shower. The cosmic 189 ray will produce many more types of particles including pions (π), neutrinos, 190 and charged leptons. Figure pulled from [26].	22
191	Figure 3.3 The WCDs. Left image features several WCDs looking from within the main 192 array of HAWC. Right image shows a schematic of a WCD pulled from [25].	23

193	Figure 3.4	TODO: copied from nim. Top-level diagram of the HAWC electronics showing a summary of the critical subsystems and the interconnections, including HV and optical fiber cabling. NMEA refers to the National Marine Electric Association format in which GPS presents data [66,67]; CLR, TRG and RST are control signals for the TDC system. The LoToT andHiToT time over threshold signals are discussed in Section 4.1	24
199	Figure 3.5	TODO: copied from NIM. Schematic overview [68] of the HAWC data acquisition and online processing system, as described in the text of Section 4	24
202	Figure 3.6	TODO: text copied from nim. The analog PMT signals are split and passed through two paths. In each path, there is an amplifier and discriminator circuit. The ratio of the amplifier gains is 7 to 1. The higher gain circuit has an effectively lower threshold (Low Th). There is a time (T) delay in the high threshold (High Th) path. The 2-edge event is related with the Low Th, while the 4 edge event is related to the High Th.	25
208	Figure 3.7	TODO: copied from A's thesis. An illustration of the angle reconstruction of the original particle. The secondary particles of an air shower travel in a plane perpendicular to the direction of the original particle, allowing for the reconstruction of the initial angle after corrections due to the curvature of the plane. Figure from [33].	27
213	Figure 3.8	TODO: pulled for thesis. Charge deposited in each PMT for a reconstructed gamma-ray event. Each large circle represents a WCD and each of the 4 smaller circles within represent a PMT. The color scale represents the amount of charge deposited in each PMT. The red star in the center of the dashed circle shows the location of the shower core fit by the SFCF algorithm. [34] . .	28
218	Figure 5.1	Sensitivities of five gamma-ray experiments compared to percentages of the Crab nebula's emission and dark matter annihilation. Solid lines present estimated sensitivities to power law spectra [FACT CHECK THIS] for each experiment. Green lines are Fermi-LAT sensitivities where lighter green is the sensitivity to the galactic center and dark green is its sensitivity to higher declinations. Orange, red, and purple solid lines represent the MAGIC, HESS, and VERITAS 50 hour sensitivities respectively. The maroon and brown lines are the HAWC 1 year and 5 year sensitivities. Across four decades of gamma-ray energy, these experiments have similar sensitivities on the order 10^{-12} erg cm $^{-2}$ s $^{-1}$. The dotted lines are estimated dark matter fluxes assuming $m_\chi = 5$ TeV DM annihilating to bottom quarks (red), tau leptons (blue), and W bosons (green). Faded gray lines outline percentage flux of the Crab nebula. Figure is an augmented version of [36]	32

231	Figure 5.2 Effect of Electroweak (EW) corrections on expected DM annihilation spec-	
232	trum for $\chi\chi \rightarrow W^-W^+$. Solid lines are spectral models that consider EW	
233	corrections. Dash-dot lines are spectral models without EW corrections. Red	
234	lines are models for $M_\chi = 1$ TeV. Blue lines represent models for $M_\chi = 100$	
235	TeV. All models are sourced from the PPPC4DMID [54].	36
236	Figure 5.3 $\frac{dJ}{d\Omega}$ maps for Segue1 (top) and Coma Berenices (bottom). Origin is centered	
237	on the specific dwarf spheroidal galaxies (dSph). X and Y axes are the angular	
238	separation from the center of the dwarf. Profile is truncated at the scale radius.	
239	Plots of the remaining 11 dSph HAWC studied are linked in Fig. A.1.	38
240	Figure 5.4 Illustration of the combination technique showing a comparison between	
241	$-2 \ln \lambda$ provided by four instruments (colored lines) from the observation	
242	of the same dSph without any J nuisance and their sum, <i>i.e.</i> the resulting	
243	combined likelihood (thin black line). According to the test statistics of	
244	Equation (5.7), the intersection of the likelihood profiles with the line $-2 \ln \lambda$	
245	= 2.71 indicates the 95% C.L. upper limit on $\langle \sigma v \rangle$. The combined likelihood	
246	(thin black line) shows a smaller value of upper limit on $\langle \sigma v \rangle$ than those	
247	derived by individual instruments. We also show how the uncertainties on	
248	the J factor effects the combined likelihood and degrade the upper limit on	
249	$\langle \sigma v \rangle$ (thick black line). All likelihood profiles are normalized so that the global	
250	minimum $\widehat{\langle \sigma v \rangle}$ is 0. We note that each profile depends on the observational	
251	conditions in which a target object was observed. The sensitivity of a given	
252	instrument can be degraded and the upper limits less constraining if the	
253	observations are performed in non-optimal conditions such as a high zenith	
254	angle or a short exposure time.	44
255	Figure 5.5	47
256	Figure 5.6 HAWC TS values for best fit $\langle \sigma v \rangle$ versus m_χ for seven SM annihilation	
257	channels with J factors from \mathcal{GS} . The solid black line shows the combined	
258	best fit TS values. The colored, dashed lines are the TS values for each of the	
259	13 sources HAWC studied.	48
260	Figure 5.7 HAWC Brazil bands at 95% confidence level on $\langle \sigma v \rangle$ versus DM mass for	
261	seven annihilation channels with J -factors from \mathcal{GS} [65]. The solid line	
262	represents the combined limit from 13 dSphs. The dashed line is the expected	
263	limit. The green band is the 68% containment. The yellow band is the 95%	
264	containment.	49

265	Figure 5.8	Upper limits at 95% confidence level on $\langle \sigma v \rangle$ in function of the DM mass for 266 eight annihilation channels, using the set of J factors from Ref. [65] (\mathcal{GS} set 267 in Table 5.1). The black solid line represents the observed combined limit, 268 the black dashed line is the median of the null hypothesis corresponding 269 to the expected limit, while the green and yellow bands show the 68% and 270 95% containment bands. Combined upper limits for each individual detector 271 are also indicated as solid, colored lines. The value of the thermal relic 272 cross-section in function of the DM mass is given as the red dotted-dashed 273 line [66].	50
274	Figure 5.9	Same as Fig. 5.8, using the set of J factors from Ref. [59, 67] (\mathcal{B} set in Table 5.1).	51
275	Figure 5.10	Comparisons of the combined limits at 95% confidence level for each of the 276 eight annihilation channels when using the J factors from Ref. [65] (\mathcal{GS} set in 277 Table 5.1), plain lines, and the J factor from Ref. [59, 67] (\mathcal{B} set in Table 5.1), 278 dashed lines. The cross-section given by the thermal relic is also indicated [66].	53
279	Figure 5.11	Comparisons of the combined limits at 95% confidence level for a point source 280 analysis and extended source using [65] \mathcal{GS} J-factor distributions and PPPC 281 [54] annihilation spectra. Shown are the limits for Segue1 which will have 282 the most significant impact on the combined limit. 6 of the 7 DM annihilation 283 channels are shown. Solid lines are extended source studies. Dashed lines 284 are point source studies. Overall, the extended source analysis improves the 285 limit by a factor of 2.	55
286	Figure 5.12	Same as Fig. 5.11 on Coma Berenices. This dSph also contributes signifi- 287 cantly to the limit. The limits are identical in this case.	56
288	Figure 5.13	Comparison of combined limits when correcting for HAWC's pointing sys- 289 tematic. All DM annihilation channels are shown. The solid black line is the 290 ratio between published limit to the declination corrected limit. The blue solid 291 line or "Combined_og" represented the limits computed for Glory Duck. The 292 solid orange line or "Combined_ad" represented the limits computed after 293 correcting for the pointing systematic.	57
294	Figure 5.14	Differential map of dJ/Ω from model built in Section 5.8.1 and profiles 295 provided directly from authors. (Top) Differential from Segue1. (bottom) 296 Differential from Coma Berenices. Note that their scales are not the same. 297 Segue1 shows the deepest discrepancies which is congruent with its large 298 uncertainties. Both models show anuli where unique models become apparent. .	58

299	Figure 5.15 HAWC limits for Coma Berenices (top) and Segue1 (bottom) for two different 300 map sets. Blue lines are limits calculated on maps with poor model repre- 301 sentation. Orange lines are limits calculated on spatial profiles provided by 302 the authors of [55]. Black line is the ratio of the poor spatial model limits to 303 the corrected spatial models. The left y-axis measures $\langle \sigma v \rangle$ for the blue and 304 orange lines. The right y-axis measures the ratio and is unitless.	59
305	Figure 5.16 Comparisons between the J -factors versus the angular radius for the com- 306 putation of J factors from Ref. [65] (\mathcal{GS} set in Table 5.1) in blue and for 307 the computation from Ref. [59, 67] (\mathcal{B} set in Tab. 5.1) in orange. The solid 308 lines represent the central value of the J -factors while the shaded regions 309 correspond to the 1σ standard deviation.	61
310	Figure 5.17 Comparisons between the J -factors versus the angular radius for the computa- 311 tion of J factors from Ref. [65] (\mathcal{GS} set in Tab. 5.1) in blue and for the 312 computation from Ref. [59, 67] (\mathcal{B} set in Tab. 5.1) in orange. The solid 313 lines represent the central value of the J -factors while the shaded regions 314 correspond to the 1σ standard deviation.	62
315	Figure 6.1 Spectral hypotheses from PPPC [54] and HDM [75] for DM annihilation: 316 $\chi\chi \rightarrow W^-W^+$. Solid lines are spectral models with EW corrections from the 317 PPPC. Dash-dot lines are spectral models from HDM. Red lines are models 318 for $M_\chi = 1$ TeV. Blue lines represent models for $M_\chi = 100$ TeV.	67
319	Figure 6.2 Photon spectra for $\chi\chi \rightarrow \gamma\gamma$ (left) and $\chi\chi \rightarrow ZZ$ (right) after Gaussian 320 convolution of line features. Both spectra have δ -features at photon energies 321 equal to the DM mass. Bluer lines are annihilation spectra with lower DM 322 mass. Redder lines are spectra from larger DM mass. All spectral models are 323 sourced from the Heavy Dark Matter models [75]. Axes are drawn roughly 324 according to the energy sensitivity of HAWC.	68
325	Figure 6.3 $\frac{dJ}{d\Omega}$ maps for Coma Berenices, Draco, Segue1, and Sextans. Columns are 326 divided for the $\pm 1\sigma$ uncertainties in $dJ/d\Omega$ around the mean value from \mathcal{LS} 327 [76]. Origin is centered on the specific dwarf spheroidal galaxies (dSph). θ 328 and ϕ axes are the angular separation from the center of the dwarf. Profiles 329 are truncated at 1° and flattened beyond.	70
330	Figure 6.4 Infographic on how jobs and DM computation was organized in Section 5.3. 331 Jobs were built for each permutation of CHANS and SOURCES shown by the 332 left block in the figure. Each job, which took on the order 2 hrs to compute, 333 had the following work flow: 1. Import HAWC analysis software, 2 min to 334 run. 2. Load HAWC count maps, 5 min to run. 3. Load HAWC energy and 335 spatial resolutions, 4 min. 5. Load DM spatial source templates and spectral 336 models, less than 1 s. 6. Perform likelihood fit on data and model, about 8 337 min per DM mass. 7. Write results to file, less than 1s.	72

338	Figure 6.5	Graphic of Gustafson parallel coding pattern. f_s is the fraction of a program, 339 in time, spent on serial computation. f_p is the fraction of computing time 340 that is parallelizable. T_p is the total time for a parallel program to run. T_1 is 341 the total time for a parallel program to run if only 1 processor is allocated. 342 P_N is the N -th processor where it's row is the computation the processor 343 performs. The Gustafson pattern is most similar to what is implemented for 344 this analysis. Figure is pulled from [78].	73
345	Figure 6.6	Task chart for one multithreaded job developed for this project. Green blocks 346 indicate a shared resource across the threads AND computation performed 347 serially. Red blocks indicate functional parallel processing within each thread. 348 3 threads are represented here, yet many more can be employed during the 349 full analysis. Jobs are defined by the SOURCE as these require unique maps 350 to be loaded into the likelihood estimator. The m_χ , CHAN, and $\langle\sigma v\rangle$ variables 351 are entered into the thread pool and allocated as evenly as possible across the 352 threads.	75
353	Figure 6.7	HAWC upper limits at 95% confidence level on $\langle\sigma v\rangle$ versus m_χ for $\chi\chi \rightarrow b\bar{b}$, $t\bar{t}$, $u\bar{u}$, $d\bar{d}$, $s\bar{s}$, $c\bar{c}$, gg , W^+W^- , and hh . Limits are with \mathcal{LS} J-factors 354 [76]. The solid line represents the observed combined limit. Dashed lines 355 represent limits from individual dSphs.	78
357	Figure 6.8	HAWC upper limits at 95% confidence level on $\langle\sigma v\rangle$ versus m_χ for $\chi\chi \rightarrow \nu_e\bar{\nu}_e$, $\nu_\mu\bar{\nu}_\mu$, $\nu_\tau\bar{\nu}_\tau$, $e\bar{e}$, $\mu\bar{\mu}$, $\tau\bar{\tau}$, $\gamma\gamma$ and ZZ . Limits use \mathcal{LS} J-factors [76]. The 358 solid line represents the observed combined limit. Dashed lines represent 359 limits from individual dSphs.	79
361	Figure 6.9	HAWC TS values for best fit $\langle\sigma v\rangle$ versus m_χ for SM annihilation channels: 362 $\chi\chi \rightarrow b\bar{b}$, $t\bar{t}$, $u\bar{u}$, $d\bar{d}$, $s\bar{s}$, $c\bar{c}$, gg , W^+W^- , and hh . Limits use \mathcal{LS} J-factors. 363 The solid black line shows the combined best fit TS values. The colored, 364 dashed lines are the TS values from each dSph.	80
365	Figure 6.10	HAWC TS values for best fit $\langle\sigma v\rangle$ versus m_χ for SM annihilation channels: 366 $\chi\chi \rightarrow \nu_e\bar{\nu}_e$, $\nu_\mu\bar{\nu}_\mu$, $\nu_\tau\bar{\nu}_\tau$, $e\bar{e}$, $\mu\bar{\mu}$, $\tau\bar{\tau}$, $\gamma\gamma$ and ZZ . Limits use \mathcal{LS} J-factors. 367 The solid black line shows the combined best fit TS values. The colored, 368 dashed lines are the TS values from each dSph.	81
369	Figure 6.11	Comparison of HAWC limits from this analysis to Glory Duck (Fig. 5.5) 370 for 3 dSphs and 3 DM annihilation channels: $b\bar{b}$, $\tau\bar{\tau}$, and $e\bar{e}$. Each sector 371 shows the 95% confidence limit from Glory Duck (blue line) and this analysis 372 (orange line) in the top plot. The lower plot features the ratio in log scale of 373 Glory Duck to this analysis in a red solid line. Horizontal dashed lines are 374 for ratios of 1.0 (black) and $\sqrt{2}$ (blue). Ratios larger than 1.0 are for limits 375 smaller, or stricter, than Glory Duck. Ratios larger than $\sqrt{2}$ indicates limits 376 are stricter than a simple doubling of the Glory Duck data.	83

377	Figure 7.1	Neutrino spectra at production (left panels) and after oscillation at Earth 378 (right panels). Blue, orange, and green lines are the ν_e , ν_μ , and ν_τ spectra 379 respectively. Top panels show the spectra in $\frac{dN}{dE}$. Lower panels plot the flavor 380 ratio to $\nu_e + \nu_\mu + \nu_\tau$. SM annihilation channels $b\bar{b}$, $\tau\bar{\tau}$, and $\nu_\mu\bar{\nu}_\mu$ are shown 381 for $M_\chi = 1$ PeV, TeV, and EeV.	88
382	Figure 7.2	Signal recovery for 100 TeV DM annihilation into $\nu_\mu\bar{\nu}_\mu$ for a source at Dec 383 = 16.06° . n_{inj} is the number of injected signal events in simulation. n_s is the 384 number of reconstructed signal events from the simulation data. Although 385 the uncertainties are small and tight, the reconstructed n_s are systematically 386 underestimated.	89
387	Figure 7.3	Left panel shows the two kernels overlaying the original spectrum from 388 χ arony after propagation to Earth [81]. The vertical red line indicates where 389 the original neutrino line is maximized. Blue line is the output from χ aroy. 390 Green line is the spectrum after convolution with a flat kernel. Orange line 391 is the spectrum after Gaussian convolution. Right panel shows the signal 392 recovery of the spectral model using the Gaussian kernel with parameters 393 enumerated above.	90
394	Figure 7.4	Example spline that failed the fit. Failed splined are corrected on a case by 395 case basis unless the SM channel has a systematic problem fitting the splines. 396 In this case, I made a bookkeeping error and loaded the incorrect spectral model	92
397	Figure 7.5	Summary of input spectral models that were smoothed with Gaussian kernels. 398 Spectral models are for $\chi\chi \rightarrow e\bar{e}, \mu\bar{\mu}, \tau\bar{\tau}, \nu_e\bar{\nu}_e, \nu_\mu\bar{\nu}_\mu$, and $\nu_\tau\bar{\nu}_\tau$. These spectra 399 are the composite ($\nu_\mu + \nu_\tau$) of neutrino flavors. Every spectral model used 400 for this analysis is featured as a colored solid line. Bluer lines are for low 401 m_χ models. m_χ ranges from 681 GeV to 100 PeV. HDM [75], χ aroy [81], 402 and Photospline [85] are used to generate these spectra. Energy (x-axis) was 403 chosen to roughly represent the energy sensitivity of NST.	93
404	Figure 7.6	Test statistic (TS) distributions for Segue 1 and $\chi\chi \rightarrow b\bar{b}$. Each subplot, 405 except the final, is the TS distribution for a specific DM mass listed in the 406 subplot. Orange dashed lines are the traces for a χ^2 distribution with 1 degree 407 of freedom. $\epsilon[\cdot]$ is the fraction of trials smaller than the bracketed value. The 408 final subplot features the all DM spectral models, similar to Fig. 7.5, used as 409 input for the TS distributions.	96
410	Figure 7.7	Same as Fig. 7.6 for Segue 1 $\chi\chi \rightarrow \tau\bar{\tau}$	97
411	Figure 7.8	Same as Fig. 7.6 for Segue 1 $\chi\chi \rightarrow \nu_\mu\bar{\nu}_\mu$	98
412	Figure 7.9	Same as Fig. 7.6 for Ursa Major II 1 $\chi\chi \rightarrow b\bar{b}$	99
413	Figure 7.10	Same as Fig. 7.6 for Ursa Major II 1 $\chi\chi \rightarrow \tau\bar{\tau}$	100

414	Figure 7.11 Same as Fig. 7.6 for Ursa Major II 1 $\chi\chi \rightarrow \nu_\mu\bar{\nu}_\mu$	101
415	Figure 7.12 Same as Fig. 7.6 for 15, \mathcal{GS} J -factor, stacked sources and $\chi\chi \rightarrow b\bar{b}$	102
416	Figure 7.13 Same as Fig. 7.6 for 15, \mathcal{GS} J -factor, stacked sources and $\chi\chi \rightarrow t\bar{t}$	103
417	Figure 7.14 Same as Fig. 7.6 for 15, \mathcal{GS} J -factor, stacked sources and $\chi\chi \rightarrow u\bar{u}$	104
418	Figure 7.15 Same as Fig. 7.6 for 15, \mathcal{GS} J -factor, stacked sources and $\chi\chi \rightarrow d\bar{d}$	105
419	Figure 7.16 Same as Fig. 7.6 for 15, \mathcal{GS} J -factor, stacked sources and $\chi\chi \rightarrow e\bar{e}$	106
420	Figure 7.17 Same as Fig. 7.6 for 15, \mathcal{GS} J -factor, stacked sources and $\chi\chi \rightarrow \mu\bar{\mu}$	107
421	Figure 7.18 Same as Fig. 7.6 for 15, \mathcal{GS} J -factor, stacked sources and $\chi\chi \rightarrow \tau\bar{\tau}$	108
422	Figure 7.19 Same as Fig. 7.6 for 15, \mathcal{GS} J -factor, stacked sources and $\chi\chi \rightarrow W^+W^-$	109
423	Figure 7.20 Same as Fig. 7.6 for 15, \mathcal{GS} J -factor, stacked sources and $\chi\chi \rightarrow ZZ$	110
424	Figure 7.21 Same as Fig. 7.6 for 15, \mathcal{GS} J -factor, stacked sources and $\chi\chi \rightarrow \nu_e\bar{\nu}_e$	111
425	Figure 7.22 Same as Fig. 7.6 for 15, \mathcal{GS} J -factor, stacked sources and $\chi\chi \rightarrow \nu_\mu\bar{\nu}_\mu$	112
426	Figure 7.23 Signal Recovery study for an analysis with 15 stacked sources using the \mathcal{GS} J -factors [55]. Above shows 14 studies for DM mass ranging between 1 TeV and 20 PeV for $\chi\chi \rightarrow \mu_\mu\bar{\mu}_\mu$. The bottom right subplot features every spectral model used as input for the remaining subplots. The remaining subplots show n_{inj} as the number of signal events injected into background simulation. Whereas, n_s is the number of signal events recovered from analyzing the injected simulation. Blue line represents the median values of 100 simulations. Light blue bands show the 1σ statistical uncertainty around the median.	114
435	Figure 7.24 Same as Fig. 7.23 but for $\chi\chi \rightarrow t\bar{t}$ (top) and $b\bar{b}$ (bottom).	115
436	Figure 7.25 IceCube North Sky Track Sensitivities. Each panel shows sensitivity curves for various DM annihilation channels. Sensitivities are for the velocity-weighted cross-section $\langle\sigma v\rangle$ versus m_χ . Dotted, colored lines are sensitivities for individual sources. Solid white lines are for the combined sensitivity of all 15 \mathcal{GS} sources used in this study.	117
441	Figure 7.26 Same as Fig. 7.25 for three additional DM annihilation channels.	118

442	Figure 7.27 Panel A: Neutrino's from the Northern sky and incident on the IceCube 443 detector will travel through the Earth. How much of the Earth these neutrinos 444 travels is a function of zenith from the vertical axis. Panel B: SM prediction of 445 neutrino transmission probabilities for neutrinos arriving at $90^\circ - 180^\circ$ zenith 446 and with 100 GeV to 100 PeV energies. High-energy neutrinos traversing 447 the whole Earth are completely absorbed, whereas low-energy neutrinos pass 448 through unimpeded. Neutrinos coming from above the horizon will arrive 449 unimpeded for all neutrino energies. Figure pulled from [88].	119
450	Figure 7.28 $\langle\sigma v\rangle$ sensitivities for 5 imaginary sources with $\log_{10} J = 19.42 \log_{10}(\text{GeV}^2\text{cm}^{-5})$. 451 Each imaginary source shares a declination with a source in Tab. 5.1	120
452	Figure 8.1 The prompt electron neutrino and photon spectrum resulting from the decay 453 of a 2EeV DM particle to $\nu_e \bar{\nu}_e$, as currently being searched for at IceCube 454 [5]. Solid curves represent the results of this work, and predict orders of 455 magnitude more flux at certain energies than the dashed results of Pythia 8.2, 456 one of the only existing methods to generate spectra at these masses. In both 457 cases energy conservation is satisfied: there is a considerable contribution to 458 a δ -function at $x = 1$, associated with events where an initial W or Z was never 459 emitted and thus no subsequent shower developed. Large disagreements are 460 generically observed at these masses for electroweak dominated channels, 461 while the agreement is better for colored initial SM states.	122
462	Figure 8.2 TODO: neutrino and bb plot with nu Sensitivities[NEEDS A SOURCE][FACT 463 CHECK THIS]	123
464	Figure A.1 Sister figure to Figure 5.3. Sources in the first row from left to right: Bootes 465 I, Canes Venatici I, II. In second row: Draco, Hercules, Leo I. In the first row: 466 Leo II, Leo IV, Sextans. In the final row: Ursa Major I, Ursa Major II.	124
467	Figure B.1 Sister figure to Figure 6.2 for remaining SM primary annihilation channels 468 studied for this thesis. These did not require any post generation smoothing 469 and so are directly pulled from [75] with a binning scheme most helpful for a 470 HAWC analysis.	125
471	Figure B.2 Comparison of HAWC limits from this analysis to Glory Duck (Fig. 5.5) for 472 Coma Berenices and 7 DM annihilation channels.	135
473	Figure B.3 Same as Fig. B.2 but for Segue 1.	136
474	Figure B.4 Same as Fig. B.2 but for Sextans.	137

475	Figure C.1 Current status of spline tables according to constraints defined by Tab. 7.1.	
476	Green splines are splines that passed under the GOOD tolerance. Yellow	
477	are splines that are OK. Red are splines that FAIL. All yellow splines were	
478	inspected individually before running the analysis. Splines were made for the	
479	μ (PID 14; top panel) flavor and τ (PID 16; bottom panel) neutrino flavors.	141
480	Figure C.2 Sister figure to Fig. 7.5 for annihilation channels that did not require kernel	
481	smoothing. These spectra are the composite ($\nu_\mu + \nu_\tau$) of neutrino flavors.	
482	Every spectral model used for this analysis is featured as a colored solid line.	
483	Bluer lines are for lower DM mass spectral models. DM masses range from	
484	681 GeV to 100 PeV.	142
485	Figure C.3 Same as Fig. 7.23 but for Segue 1 and $\chi\chi \rightarrow b\bar{b}$	143
486	Figure C.4 Same as Fig. 7.23 but for Segue 1 and $\chi\chi \rightarrow t\bar{t}$	144
487	Figure C.5 Same as Fig. 7.23 but for Segue 1 and $\chi\chi \rightarrow \nu_\mu \bar{\nu}_\mu$	145
488	Figure C.6 Same as Fig. 7.23 but for Ursa Major II and $\chi\chi \rightarrow b\bar{b}$	146
489	Figure C.7 Same as Fig. 7.23 but for Ursa Major II and $\chi\chi \rightarrow t\bar{t}$	147
490	Figure C.8 Same as Fig. 7.23 but for Ursa Major II and $\chi\chi \rightarrow \nu_\mu \bar{\nu}_\mu$	148
491	Figure C.9 IceCube North Sky Track Sensitivities for $n_s/\langle N \rangle$. n_s values are the counts	
492	fed into Eq. (7.8) to produce Fig. 7.26 and Fig. 7.25.	149
493	Figure C.10 Same as Fig. C.9 for three additional DM annihilation channels.	150

LIST OF ABBREVIATIONS

- 495 **MSU** Michigan State University
496 **LANL** Los Alamos National Laboratory
497 **DM** Dark Matter
498 **SM** Standard Model
499 **HAWC** High Altitude Water Cherenkov Observatory
500 **dSph** Dwarf Spheroidal Galaxy

501

CHAPTER 1

INTRODUCTION

502 Is the text not rendering right? Ah ok it knows im basically drafting the doc still

CHAPTER 2

503

DARK MATTER IN THE COSMOS

504 **2.1 Introduction**

505 The dark matter problem can be summarized in part by the following thought experiment.

506 Let us say you are the teacher for an elementary school classroom. You take them on a field
507 trip to your local science museum and among the exhibits is one for mass and weight. The exhibit
508 has a gigantic scale, and you come up with a fun problem for your class.

509 You ask your class, "What is the total weight of the classroom? Give your best estimation to
510 me in 30 minutes, and then we'll check your guess on the scale. If your guess is within 10% of the
511 right answer, we will stop for ice cream on the way back."

512 The students are ecstatic to hear this, and they get to work. The solution is some variation of
513 the following strategy. The students should give each other their weight or best guess if they do
514 not know. Then, all they must do is add each student's weight and get a grand total for the class.
515 The measurement on the giant scale should show the true weight of the class. When comparing
516 the measured weight to your estimation, multiply the measurement by 1.0 ± 0.1 to get the $\pm 10\%$
517 tolerances for your estimation.

518 Two of your students, Sandra and Mario, return to you with a solution.

519 They say, "We weren't sure of everyone's weight. We used 65 lbs. for the people we didn't
520 know and added everyone who does know. There are 30 of us, and we got 2,000 lbs.! That's a ton!"

521 You estimated 1,900 lbs. assuming the average weight of a student in your class was 60 lbs.
522 So, you are pleased with Sandra's and Mario's answer. You instruct your students to all gather on
523 the giant scale and read off the weight together. To all your surprise, the scale reads *10,000 lbs.*!
524 10,000 is significantly more than a 10% error from 2,000. In fact, it is approximately 5 times more
525 massive than either your or your students' estimates. You think to yourself and conclude there
526 must be something wrong with the scale. You ask an employee to check the scale and verify it is
527 well calibrated. They confirm that the scale is in working order. You weigh a couple of students
528 individually to assess that the scale is well calibrated. Sandra weighs 59 lbs., and Mario weighs

529 62 lbs., typical weights for their age. You then weigh each student individually and see that their
530 weights individually do not deviate greatly from 60 lbs. So, where does all the extra weight come
531 from?

532 This thought experiment serves as an analogy to the Dark Matter problem. The important
533 substitution to make however is to replace the students with stars and the classroom with a galaxy,
534 say the Milky Way. Individually the mass of stars is well measured and defined with the Sun as our
535 nearest test case. However, when we set out to measure the mass of a collection of stars as large as
536 galaxies, our well-motivated estimation is wildly incorrect. There simply is no way to account for
537 this discrepancy except without some unseen, or dark, contribution to mass and matter in galaxies.
538 I set out in my thesis to narrow the possibilities of what this Dark Matter could be.

539 This chapter is organized like the following... **TODO: Text should look like ... Chapter x has**
540 **blah blah blah.**

541 2.2 Dark Matter Basics

542 Presently, a more compelling theory of cosmology that includes Dark Matter (DM) in order
543 to explain a variety of observations is Λ Cold Dark Matter, or Λ CDM. I present the evidence
544 supporting Λ CDM in Section 2.3 yet discuss the conclusions of the Λ CDM model here. According
545 to Λ CDM fit to observations on the Cosmic Microwave Background (CMB), DM is 26.8% of the
546 universe's current energy budget. Baryonic matter, stuff like atoms, gas, and stars, contributes to
547 4.9% of the universe's current energy budget [1, 2, 3].

548 DM is dark; it does not interact readily with light at any wavelength. DM also does not interact
549 noticeably with the other standard model forces (Strong and Weak) at a rate that is readily observed
550 [3]. DM is cold, which is to say that the average velocity of DM is below relativistic speeds [1].
551 'Hot' DM would not likely manifest the dense structures we observe like galaxies, and instead
552 would produce much more diffuse galaxies than what is observed [3, 1]. DM is old; it played a
553 critical role in the formation of the universe and the structures within it [1, 2].

554 Observations of DM have so far been only gravitational. The parameter space available to what
555 DM could be therefore is extremely broad. The broad DM parameter space is iteratively tested in

556 DM searches by supposing a hypothesis that has not yet been ruled out and performing observations
557 to test them. When the observations yield a null result, the parameter space is constrained further.
558 I present some approaches for DM searches in Section 2.4.

559 **2.3 Evidence for Dark Matter**

560 Dark Matter (DM) has been a looming problem in physics for almost 100 years. Anomalies
561 have been observed by astrophysicists in galactic dynamics as early as 1933 when Fritz Zwicky
562 noticed unusually large velocity dispersion in the Coma cluster. Zwicky's measurement was the
563 first recorded to use the Virial theorem to measure the mass fraction of visible and invisible matter
564 in celestial bodies [4]. From Zwicky in [5], "*If this would be confirmed, we would get the surprising*
565 *result that dark matter is present in much greater amount than luminous matter.*" Zwicky's and
566 others' observation did not instigate a crisis in astrophysics because the measurements did not
567 entirely conflict with their understanding of galaxies [4]. In 1978, Rubin, Ford, and Norbert
568 measured rotation curves for ten spiral galaxies [6]. Rubin et al.'s 1978 publication presented a
569 major challenge to the conventional understanding of galaxies that could no longer be dismissed by
570 measurement uncertainties. Evidence has been mounting ever since for this exotic form of matter.
571 The following subsections provide three compelling pieces of evidence in support of the existence
572 of DM.

573 **2.3.1 First Clues: Stellar Velocities**

574 Zwicky, and later Rubin, measured the stellar velocities of various galaxies to estimate their
575 virial mass. The Virial Theorem upon which these observations are interpreted is written as

$$2T + V = 0. \quad (2.1)$$

576 Where T is the kinetic energy and V is the potential energy in a self-gravitating system. The
577 classical Newton's law of gravity from stars and gas was used for gravitational potential modeled in
578 the observed galaxies:

$$V = -\frac{1}{2} \sum_i \sum_{j \neq i} \frac{m_i m_j}{r_{ij}}. \quad (2.2)$$

579 Zwicky et al. measured just the velocities of stars apparent in optical wavelengths [5]. Rubin et al.
 580 added by measuring the velocity of the hydrogen gas via the 21 cm emission line of Hydrogen [6].
 581 The velocities of the stars and gas are used to infer the total mass of galaxies and galaxy clusters
 582 via Equation (2.1). An inferred mass is obtained from the luminosity of the selected sources. The
 583 two inferences are compared to each other as a luminosity to mass ratio which typically yielded [1]

$$\frac{M}{L} \sim 400 \frac{M_{\odot}}{L_{\odot}} \quad (2.3)$$

584 M_{\odot} and L_{\odot} referring to stellar mass and stellar luminosity, respectively. These ratios clearly indicate
 585 a discrepancy in apparent light and mass from stars and gas and their velocities.

586 Rubin et al. [6] demonstrated that the discrepancy was unlikely to be an underestimation of
 587 the mass of the stars and gas. The inferred "dark" mass was up to 5 times more than the luminous
 588 mass. This dark mass also needed to extend well beyond the extent of the luminous matter.

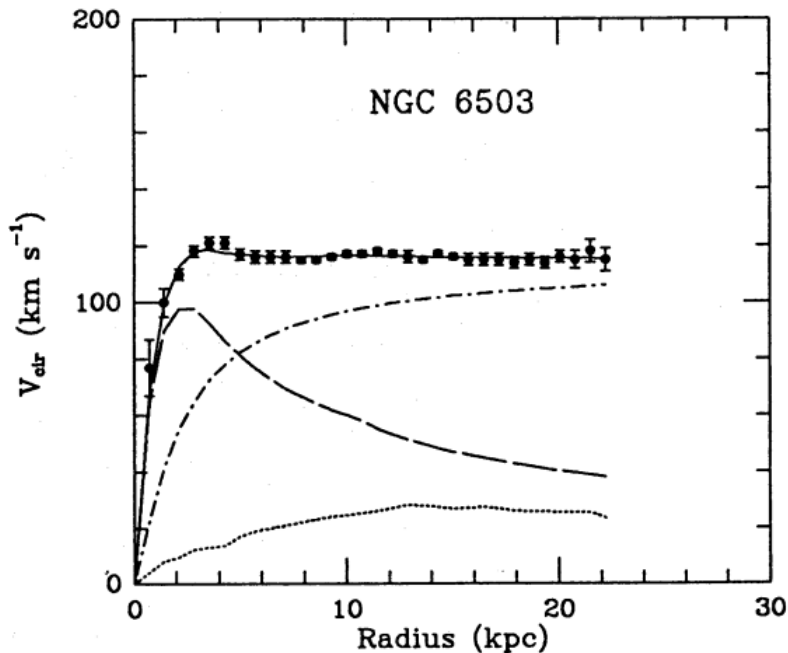


Figure 2.1 Rotation curve fit to NGC 6503 from [7]. Dashed line is the contribution from visible matter. Dotted curves are from gas. Dash-dot curves are from dark matter (DM). Solid line is the composite contribution from all matter and DM sources. Data are indicated with bold dots with error bars. Data agree strongly with a matter + DM composite prediction.

589 Figure 2.1 features one of many rotation curves plotted from the stellar velocities within galaxies.

590 The measured rotation curves mostly feature a flattening of velocities at higher radius which is not
591 expected if the gravity was only coming from gas and luminous matter. The extension of the
592 flat velocity region also indicates that the DM is distributed far from the center of the galaxy.
593 Modern velocity measurements include significantly larger objects, galactic clusters, and smaller
594 objects, dwarf galaxies. Yet, measurements along this regime are leveraging the Virial theorem
595 with Newtonian potential energies. We know Newtonian gravity is not a comprehensive description
596 of gravity. New observational techniques have been developed since 1978, and those are discussed
597 in the following sections.

598 **2.3.2 Evidence for Dark Matter: Gravitational Lensing**

599 Modern evidence for dark matter comes from new avenues beyond stellar velocities. Grav-
600 itational lensing from DM is a new channel from general relativity. General relativity predicts
601 aberrations in light caused by massive objects. In recent decades we have been able to measure the
602 lensing effects from compact objects and DM halos. Figure 2.2 shows how different massive ob-
603 jects change the final image of a faraway galaxy resulting from gravitational lensing. Gravitational
604 lensing developed our understanding of dark matter in two important ways.

605 Gravitational lensing provides additional compelling evidence for DM. The observation of two
606 merging galactic clusters in 2006, shown in Figure 2.3, provided a compelling argument for DM
607 outside the Standard Model. These clusters merged recently in astrophysical time scales. Galaxies
608 and star cluster have mostly passed by each other as the likelihood of their collision is low. Therefore,
609 these massive objects will mostly track the highest mass, dark and/or baryonic, density. Yet, the
610 intergalactic gas is responsible for the majority of the baryonic mass in the systems [4]. These gas
611 bodies will not phase through and will heat up as they collide together. The hot gas is located via
612 x-ray emission from the cluster. Two observations of the clusters were performed independently of
613 each other.

614 The first was the lensing of light around the galaxies due to their gravitational influences.
615 When celestial bodies are large enough, the gravity they exert bends space and time itself. The
616 warped space-time lenses light and will deflect in an analogous way to how glass lenses will bend

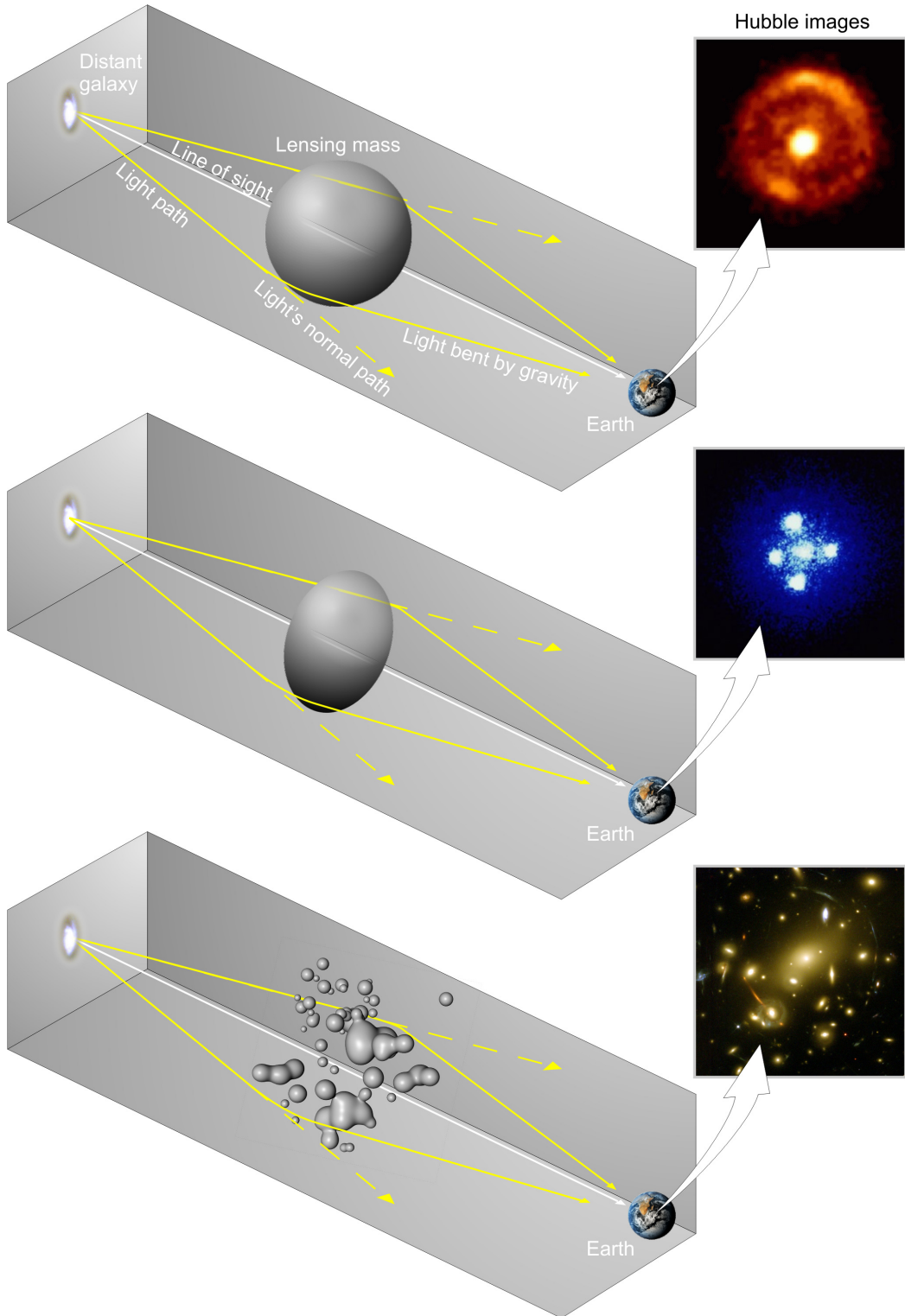


Figure 2.2 Light from distant galaxy is bent in unique ways depending on the distribution of mass between the galaxy and Earth. Yellow dashed lines indicate where the light would have gone if the matter were not present [8].

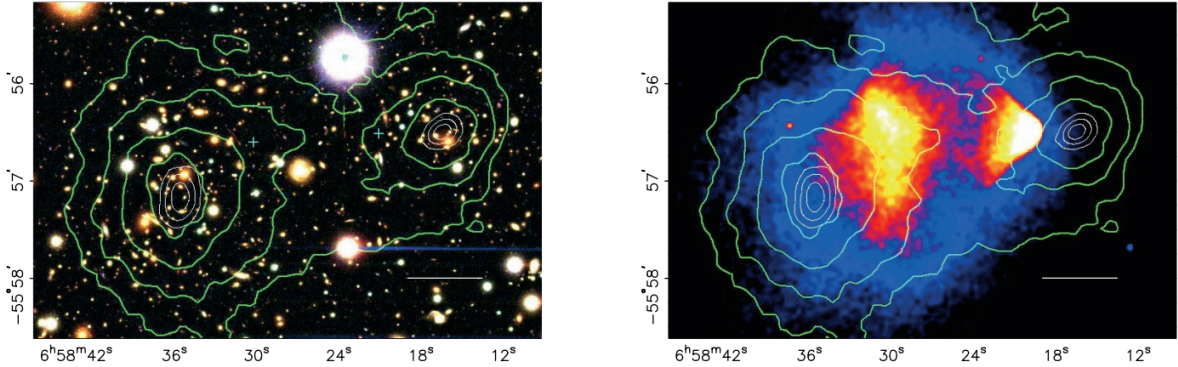


Figure 2.3 (left) Optical image of galactic cluster 1E0657-558. (right) X-ray image of the cluster with redder meaning hotter and higher baryon density. (both) Green contours are reconstruction of gravity contours from weak lensing. White rings are the best fit mass maxima at 68.3%, 95.5%, and 99.7% confidence. The matter maxima of the clusters are clearly separated from x-ray maxima. [9]

617 light, see Figure 2.2. With a sufficient understanding of light sources behind a massive object, we
 618 can reconstruct the contours of the gravitational lenses. The gradient of the contours shown in
 619 Figure 2.3 then indicates how dense the matter is and where it is.

620 The x-ray emission can then be observed from the clusters. Since these galaxies are mostly gas
 621 and are merging, then the gas should be getting hotter. If they are merging, the x-ray emissions
 622 should be the strongest where the gas is mostly moving through each other. Hence, X-ray emission
 623 maps out where the gas is in the merging galaxy cluster.

624 The lensing and x-ray observations were done on the Bullet cluster featured on Figure 2.3.
 625 The x-ray emissions do not align with the gravitational contours from lensing. The incongruence
 626 in mass density and baryon density suggests that there is a lot of matter somewhere that does
 627 not interact with light. Moreover, this dark matter cannot be baryonic [9]. The Bullet Cluster
 628 measurement did not really tell us what DM is exactly, but it did give the clue that DM also does
 629 not interact with itself very strongly. If DM did interact strongly with itself, then it would have been
 630 more aligned with the x-ray emission [9]. There have been follow-up studies of galaxy clusters with
 631 similar results. The Bullet Cluster and others like it provide a persuasive case against something
 632 possibly amiss in our gravitational theories.

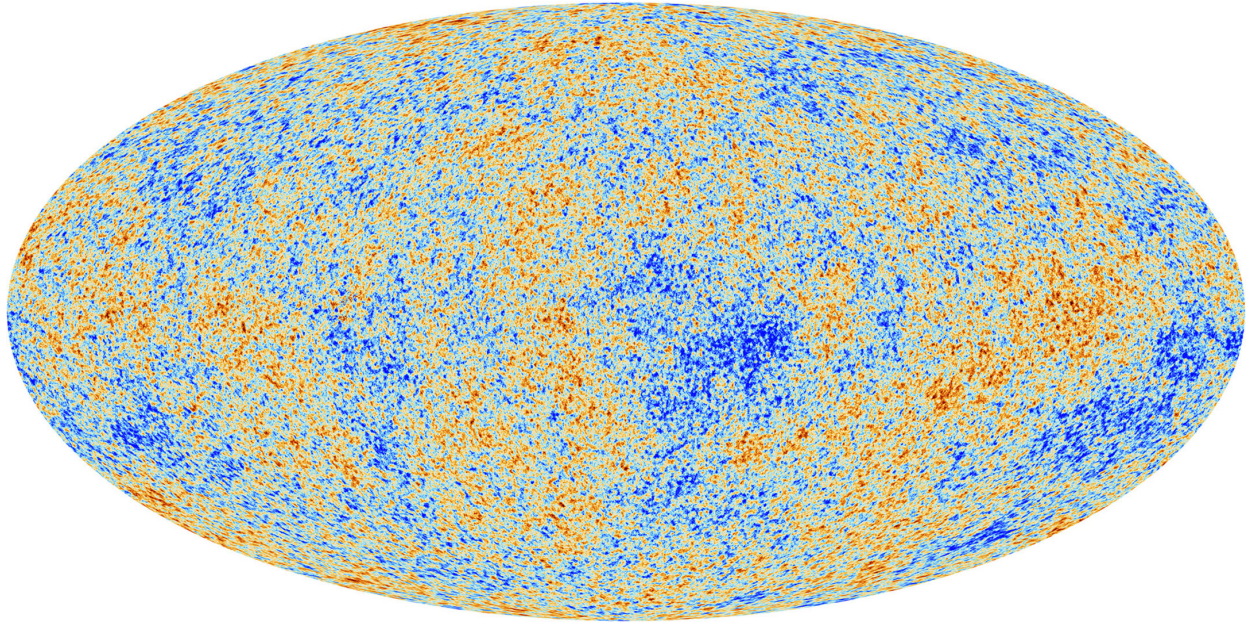


Figure 2.4 Plank CMB sky. Sky map features small variations in temperature in primordial light. These anisotropies are used to make inferences about the universe’s energy budget and developmental history. [10]

633 **2.3.3 Evidence for Dark Matter: Cosmic Microwave Background**

634 The Cosmic Microwave Background (CMB) is the primordial light from the early universe
635 when Hydrogen atoms formed from the free electron and proton soup in the early universe. The
636 CMB is the earliest light we can observe; released when the universe was about 380,000 years old.
637 Then we look at how the simulated universes look like compared to what we see. Figure 2.4 is the
638 most recent CMB image from the Plank satellite after subtracting the average value and masking the
639 galactic plane [10]. Redder regions indicate a slightly hotter region in the CMB, and blue indicates
640 colder. The intensity variations are on the order of 1 in 1000 with respect to the average value.

641 The Cosmic Microwave Background shows that the universe had DM in it from an incredibly
642 early stage. To measure the DM, Dark Energy, and matter fractions of the universe from the CMB,
643 the image is analyzed into a power spectrum, which shows the amplitude of the fluctuations as
644 a function of spherical multipole moments. Λ CDM provides the best fit to the power spectra of
645 the CMB as shown in Figure 2.5. The CMB power spectrum is quite sensitive to the fraction
646 of each energy contribution in the early universe. Low l modes are dominated by variations
647 in gravitational potential. Intermediate l emerge from oscillations in photon-baryon fluid from

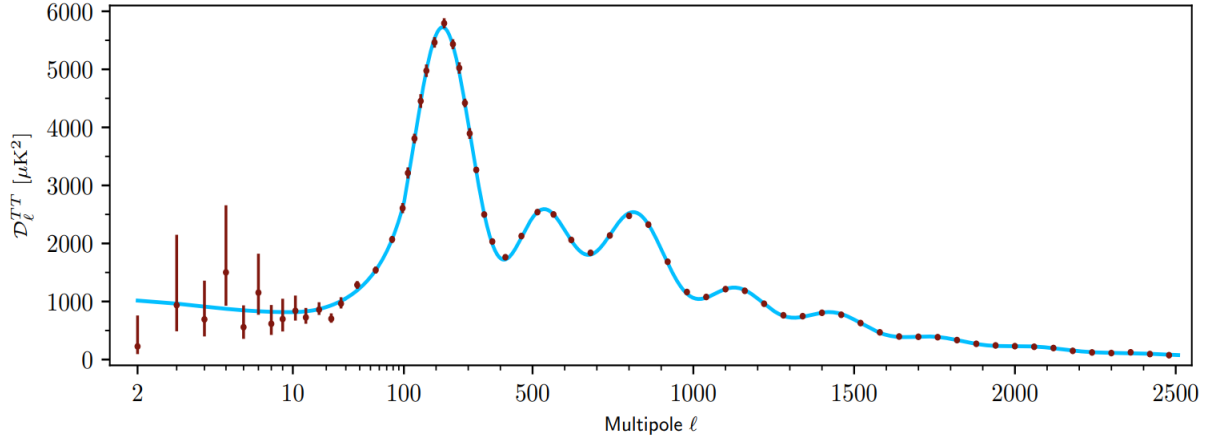


Figure 2.5 Observed Cosmic Microwave Background power spectrum as a function of multipole moment from Plank [10]. Blue line is best fit model from Λ CDM. Red points and lines are data and error, respectively.

648 competing baryon pressures and gravity. High l is a damped region from the diffusion of photons
 649 during electron-proton recombination. [1]

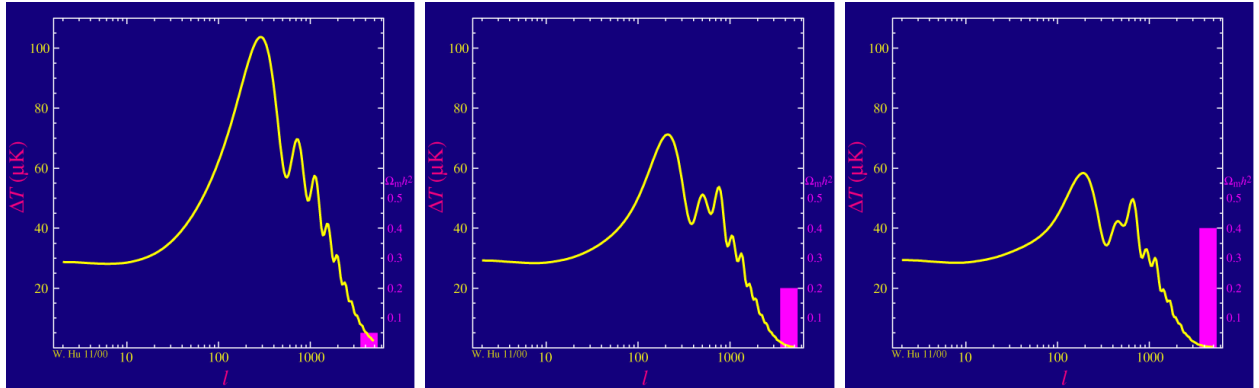


Figure 2.6 Predicted power spectra of CMB for different $\Omega_m h^2$ values for fixed baryon density from [11]. (left) Low $\Omega_m h^2$ increases the prominence of first and second peaks. (middle) $\Omega_m h^2$ is most similar to the observed power spectrum. The second and third peaks are similar in height. (right) $\Omega_m h^2$ is large which suppresses the first peak and raises the prominence of the third peak.

650 The harmonics would look quite different for a universe with less DM. Figure 2.6 demonstrates
 651 the effect $\Omega_m h^2$ has on the expected power spectrum for fixed baryon matter density. [11] Sweeping
 652 $\Omega_m h^2$ in this way clearly shows the effect dark matter has on the CMB power spectrum. The
 653 observations fit well with the Λ CDM model, and the derived fractions are as follows. The matter
 654 fraction: $\Omega_m = 0.3153$; and the baryon fraction: $\Omega_b = 0.04936$ [10]. Plank's observations also
 655 provide a measure of the Hubble constant, H_0 . H_0 especially has seen a growing tension in the

656 past decade that continues to deepened with observations from instruments like the James Webb
657 Telescope [12, 13]. As Hubble tensions deepen, we may find that perhaps Λ **CDM**, despite its
658 successes, is missing some critical physics.

659 Overall, the Newtonian motion of stars in galaxies, weak lensing from galactic clusters, and
660 power spectra from primordial light form a compelling body of research in favor of dark matter.
661 It takes another leap of theory and experimentation to make observations of DM that are non-
662 gravitational in nature. In Section 2.3, the evidence for DM implies strongly that the DM is matter
663 and not a lost parameter in the gravitational fields between massive objects. Finally, if we take one
664 axiom: that this matter has quantum behavior, such as being described by some Bohr wavelength
665 and abiding by some fermion or boson statistics; then we arrive at particle dark matter. One particle
666 DM hypothesis is the Weakly Interacting Massive Particle (WIMP). This DM candidate theory is
667 discussed further in the next section and is the focus of this thesis.

668 **2.4 Searching for Dark Matter: Particle DM**

669 Section 2.4 shows the Standard Model of particle physics and is currently the most accurate
670 model for the dynamics of fundamental particles like electrons and photons. The current status
671 of the SM does not have a viable DM candidate. When looking at the standard model, we can
672 immediately exclude any charged particle because charged particles interact strongly with light.
673 Specifically, this will rule out the following charged, fundamental particles: $e, \mu, \tau, W, u, d, s, c, t, b$
674 and their corresponding antiparticles. Recalling from Section 2.2 that DM must be long-lived and
675 stable over the age of the universe which excludes all SM particles with decay half-lives at or shorter
676 than the age of the universe. The lifetime constraint additionally eliminates the Z and H bosons.
677 Finally, the candidate DM needs to be somewhat massive. Recall from Section 2.2 that DM is cold
678 or not relativistic through the universe. This eliminates the remaining SM particles: $\nu_{e,\mu,\tau}, g, \gamma$ as
679 DM candidates. Because there are no DM candidates within the SM, the DM problem strongly
680 hints to physics beyond the SM (BSM).

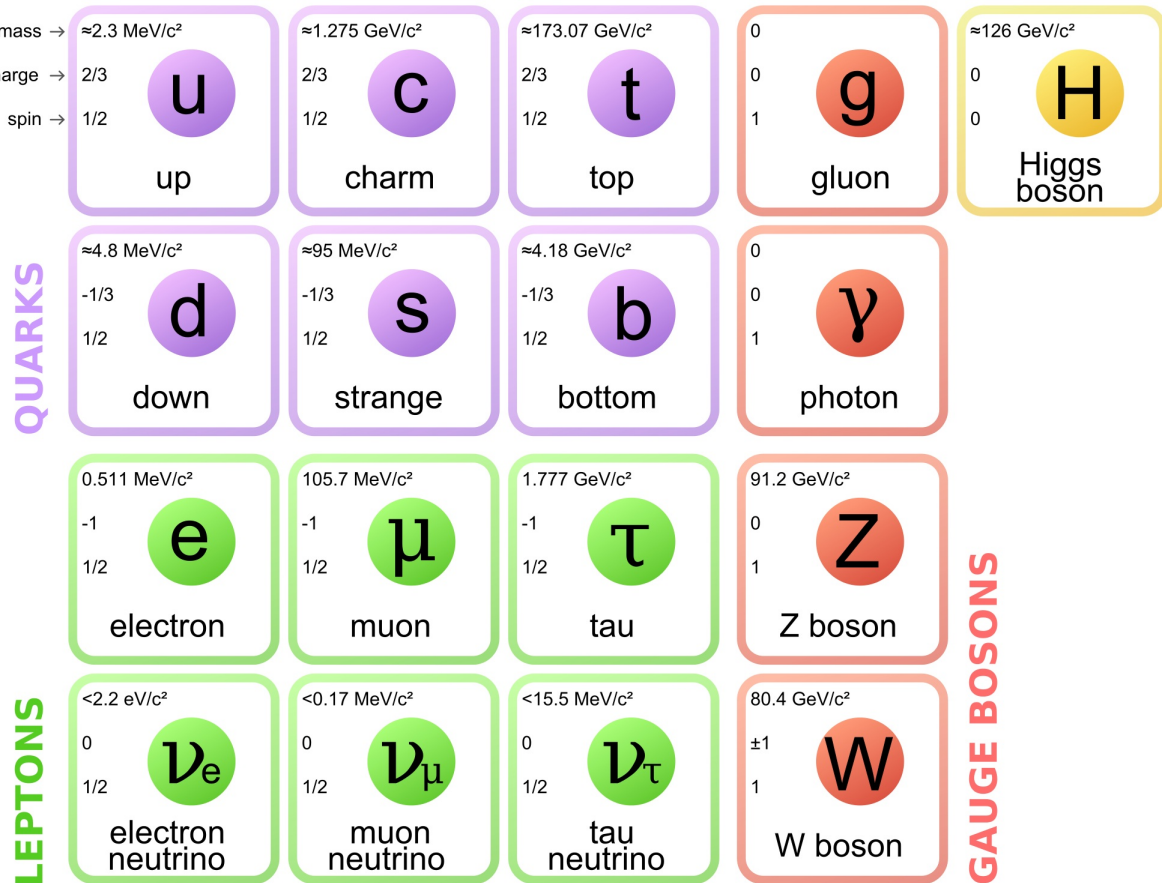


Figure 2.7 The Standard Model (SM) of particle physics. Figure taken from <http://www.quantumdiaries.org/2014/03/14/the-standard-model-a-beautiful-but-flawed-theory/>

681 2.4.1 Shake it, Break it, Make it

682 When considering DM that couples in some way with the SM, the interactions are roughly
 683 demonstrated by interaction demonstrated in Figure 2.8. The figure is a simplified Feynman
 684 diagram where the arrow of time represents the interaction modes of: **Shake it, Break it, Make it.**

685 **Shake it** refers to the direct detection of dark matter. Direct detection interactions start with
 686 a free DM particle and an SM particle. The DM and SM interact via elastic or inelastic collision
 687 and recoil away from each other. The DM remains in the dark sector and imparts some momentum
 688 onto the SM particle. The hope is that the momentum imparted onto the SM particle is sufficiently
 689 high enough to pick up with extremely sensitive instruments. Because we cannot create the DM in
 690 the lab, a direct detection experiment must wait until DM is incident on the detector. Most direct
 691 detection experiments are therefore placed in low-background environments with inert detection

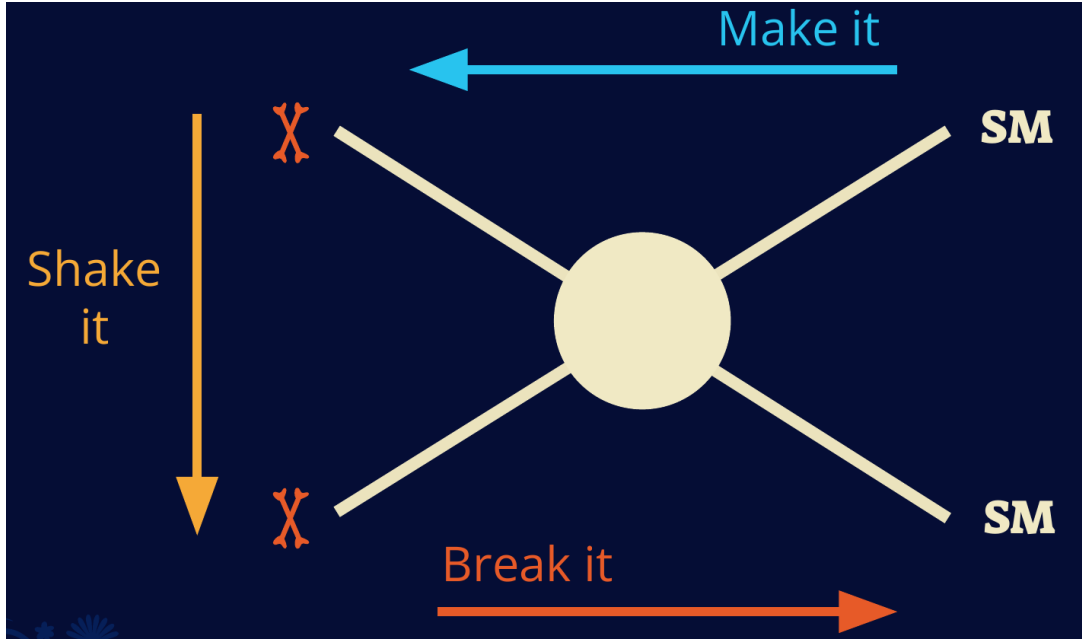


Figure 2.8 Simplified Feynman diagram demonstrating different ways DM can interact with SM particles. The 'X's refer to the DM particles whereas the SM refer to fundamental particles in the SM. The large circle in the center indicates the vertex of interaction and is purposely left vague. The colored arrows refer to different directions of time as well as their respective labels. The arrows indicate the initial and final state of the DM -SM interaction in time.

692 media like the noble gas Xenon. [14]

693 **Make it** refers to the production of DM from SM initial states. The experiment starts with
 694 particles in the SM. These SM particles are accelerated to incredibly high energies and then collide
 695 with each other. In the confluence of energy, DM hopefully emerges as a byproduct of the SM
 696 annihilation. Often it is the collider experiments that are energetic enough to hypothetically produce
 697 DM. These experiments include the world-wide collaborations ATLAS and CMS at CERN where
 698 proton collide together at extreme energies. The DM searches, however, are complex. DM likely
 699 does not interact with the detectors and lives long enough to escape the detection apparatus of
 700 CERN's colliders. This means any DM production experiment searches for an excess of events
 701 with missing momentum or energy in the events. An example event with missing transverse
 702 momentum is shown in Figure 2.9. The missing momentum with no particle tracks implies a
 703 neutral particle carried the energy out of the detector. However, there are other neutral particles
 704 in the SM, like neutrons or neutrinos, so any analysis has to account for SM signatures of missing

705 momentum. [15]

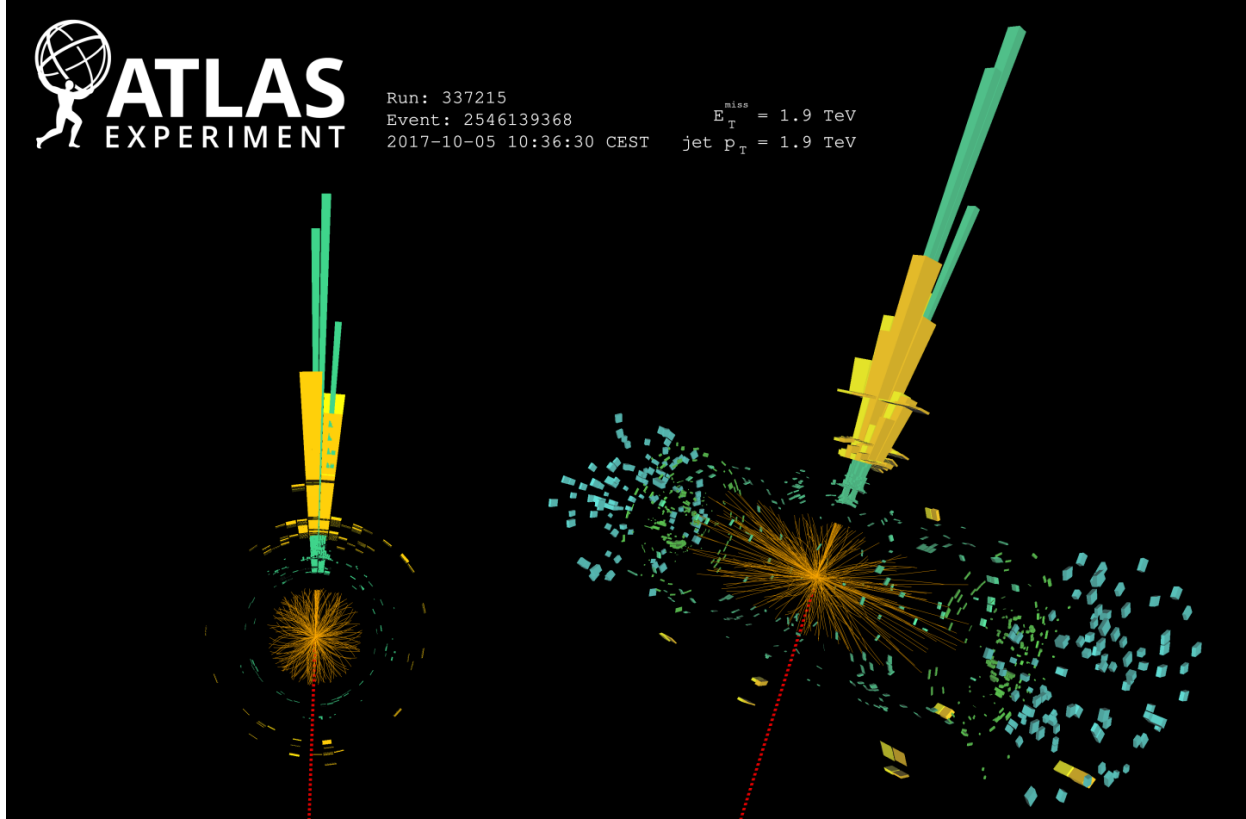


Figure 2.9 A single jet event in ATLAS detector from 2017 [16]. Jet momentum was observed to be 1.9 TeV. Missing transverse momentum was observed to be 1.9 TeV compared to the initial transverse momentum of the event was 0. Implied MET is traced by a red dashed line in event display.

706 2.4.2 Break it: Standard Model Signatures of Dark Matter through Indirect Searches

707 **Break it** refers to the creation of SM particles from the dark sector, and it is the primary focus
708 of this thesis. The interaction begins with DM or in the dark sector. The hypothesis is that this
709 DM will either annihilate with itself or decay and produce an SM byproduct. This method is
710 often referred to as the Indirect Detection of DM because we have no lab to directly control or
711 manipulate the DM. Therefore, most indirect DM searches are performed using observations of
712 known DM densities among the astrophysical sources. The strength is that we have the whole of the
713 universe and its 13.6-billion-year lifespan to use as a detector and particle accelerator. Additionally,
714 locations of dark matter are well cataloged since it was astrophysical observations that presented

715 the problem of DM in the first place.

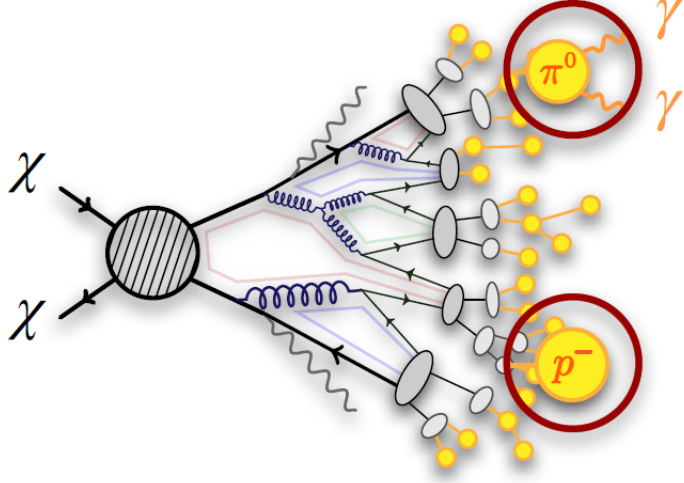


Figure 2.10 More detailed pseudo-Feynman diagram of particle cascade from dark matter annihilation into 2 quarks. The quarks hadronize and down to stable particles like γ or the anti-proton (p^-). Diagram pulled from ICRC 2021 presentation on DM annihilation search [17].

716 However, anything can happen in the universe. There are many difficult to deconvolve back-
717 grounds when searching for DM. One prominent example is the galactic center. We know the
718 galactic center has a large DM content because of stellar kinematics in our Milky Way and DM halo
719 simulations. Yet, any signal from the galactic center is challenging to parse apart from the extreme
720 environment of our supermassive black hole, unresolved sources, and diffuse emission from the
721 interstellar medium [18]. Despite the challenges, any DM model that yields evidence in the other
722 two observation methods, **Shake it or Make it** must be corroborated with indirect observations of
723 the known DM sources. Without corroborating evidence, DM observation in the lab is hard-pressed
724 to demonstrate that it is the model contributing to the DM seen at the universal scale.

725 In the case of WIMP DM, signals are described in terms of primary SM particles produced
726 from DM decay or annihilation. The SM initial state particles are then simulated down to stable
727 final states such as the γ , ν , p , or e which can traverse galactic lengths to reach Earth.

728 Figure 2.10 shows the quagmire of SM particles that emerges from SM initial states that are not
729 stable [17]. There are many SM particles with varying energies that can be produced in such an

730 interaction. For any arbitrary DM source and stable SM particle, the SM flux from DM annihilating
 731 to a neutral particle in the SM, ϕ , from a region in the sky is described by the following.

$$\frac{d\Phi_\gamma}{dE_\gamma} = \frac{\langle\sigma v\rangle}{8\pi m_\chi^2} \frac{dN_\gamma}{dE_\gamma} \times \int_{\text{source}} d\Omega \int_{l.o.s} \rho_\chi^2 dl(r, \theta') \quad (2.4)$$

732 In Equation (5.1), $\langle\sigma v\rangle$ is the velocity-weighted annihilation cross-section of DM to the SM. m_χ
 733 refers to the mass of DM, noted with Greek letter χ . $\frac{dN_\phi}{dE_\phi}$ is the N particle flux weighted by the
 734 particle energy. An example is provided in Figure 2.11 for the γ final state. The integrated terms
 735 are performed over the solid angle, $d\Omega$, and line of sight, l.o.s. ρ is the density of DM for a
 736 location (r, θ') in the sky. The terms left of the '×' are often referred to as the particle physics
 737 component. The terms on the right are referred to as the astrophysical component. For decaying
 738 DM, the equation changes to...

$$\frac{d\Phi_\phi}{dE_\phi} = \frac{1}{4\pi\tau m_\chi} \frac{dN_\phi}{dE_\phi} \times \int_{\text{source}} d\Omega \int_{l.o.s} \rho_\chi dl(r, \theta') \quad (2.5)$$

739 In Equation (2.5), τ is the decay lifetime of the DM. Just as in Equation (5.1), the left and right
 740 terms are the particle physics and the astrophysical components respectively. The integrated
 741 astrophysical component of Equation (5.1) is often called the J-Factor. Whereas the integrated
 742 astrophysical component of Equation (2.5) is often called the D-Factor.

743 Exact DM $\text{DM} \rightarrow \text{SM SM}$ branching ratios are not known, so it is usually assumed to go 100%
 744 into an SM particle/anti-particle. Additionally, when a DM annihilation or decay produces one of
 745 the neutral, long-lived SM particles (ν or γ), the particle is traced back to a DM source. For DM
 746 above GeV energies, there are very few SM processes that can produce particles with such a high
 747 energy. Seeing such a signal would almost certainly be an indication of the presence of dark matter.
 748 Fortunately, the universe provides us with the largest volume and lifetime ever for a particle physics
 749 experiment.

750 2.5 Sources for Indirect Dark Matter Searches

751 The first detection of DM relied on optical observations. Since then, we have developed new
 752 techniques to find DM dense regions. As described in Section 2.3.1, many DM dense regions were
 753 through observing galactic rotation curves. Our Milky Way galaxy is among DM dense regions

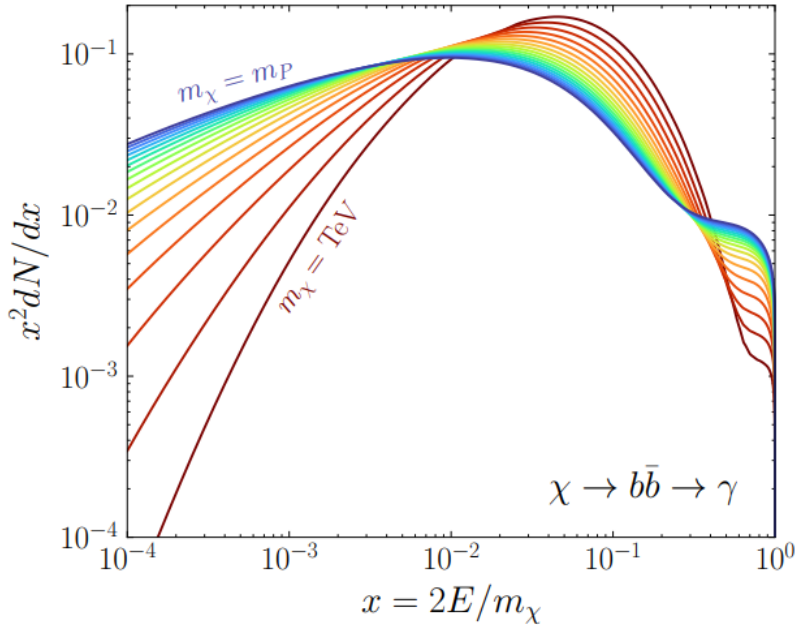


Figure 2.11 Dark Matter (DM) decay spectrum for $b\bar{b}$ initial state and γ final state. Redder spectra are for larger DM masses. Bluer spectra are light DM masses. x is a unitless factor defined as the ratio of the mass of DM, m_χ , and the final state particle energy E_γ . Figure from [19].

discovered, and it is the largest nearby DM dense region to look at. Additionally, the DM halo surrounding the Milky Way is clumpy [18]. There are regions in the DM halo of the Milky Way that have more DM than others that have captured gas over time. These sub-halos were dense enough to collapse gas and form stars. These apparent sub galaxies are known as dwarf spheroidal galaxies and are the main sources studied in this thesis. Each source type comes with different trade-offs. Galactic Center studies will be very sensitive to the assumed distribution of DM. The central DM density can vary substantially as demonstrated in Figure 2.12. At distances close to the center of the galaxy, or small r , the differences in DM densities can be 3-4 orders of magnitude. Searches toward the galactic center will therefore be quite sensitive to the assumed DM distribution.

Searches toward Dwarf Spheroidal Galaxies (dSph's) suffer from uncertainties in the DM density less than the galactic center studies. This is mostly from their diminutive size being smaller than the angular resolution of most γ -ray observatories [18]. The DM content dSph's are typically determined with the Virial theorem, Equation (2.1), and are usually majority DM [18] in mass. DSph's tend to be ideal sources to look at for DM searches. Their environments are quiet with little

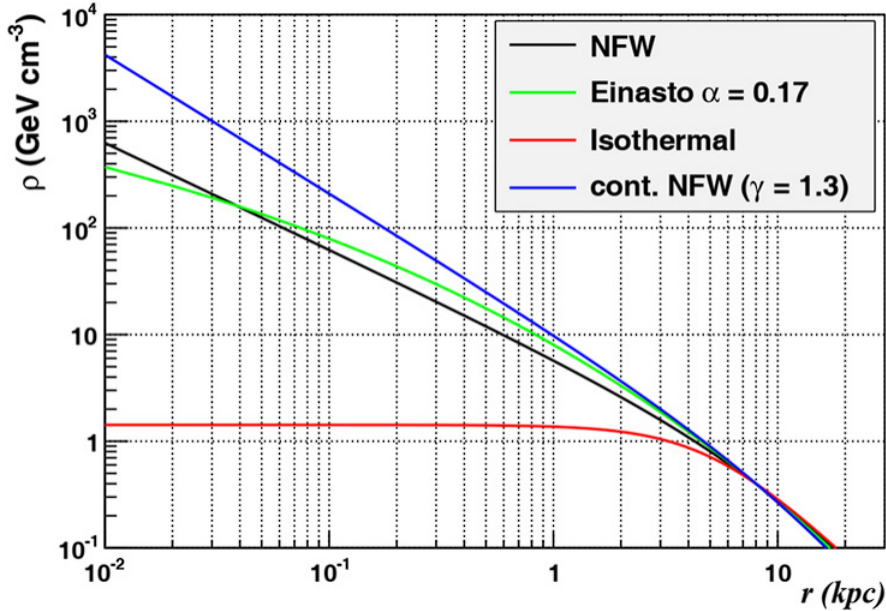


Figure 2.12 Different dark matter density profiles compared. Some models produce exceptionally large densities at small r [20].

768 astrophysical background. Unlike the galactic center, the most active components of dSph's are the
 769 stars within them versus a violent accretion disc around a black hole. All this together means that
 770 dSph's are among the best sources to look at for indirect DM searches. dSph's are the targets of
 771 focus for this thesis.

772 2.6 Multi-Messenger Dark Matter

773 Astrophysics entered a new phase in the past few decades that leverages our increasing sensitivity
 774 to SM channels and general relativity (GR). Up until the 21st century, astrophysical observations
 775 were performed with photons (γ) only. Astrophysics with this 'messenger' is fairly mature now.
 776 Novel observations of the universe have since only adjusted the sensitivity of the wavelength of
 777 light that is observed except at MeV energies. Gems like the CMB [10], and more have ultimately
 778 been observations of different wavelengths of light. Multi-messenger astrophysics proposes using
 779 other SM particles such the p^{+-} , or ν or gravitation waves predicted by general relativity.

780 The experiment LIGO had a revolutionary discovery in 2016 with the first detection of a binary
 781 black hole merger [21]. This opened the collective imagination to observing the universe through
 782 gravitational waves. There has also been a surge of interest in the neutrino (ν) sector. IceCube

783 demonstrated that we are sensitive to neutrinos in regions that correlate with significant photon
 784 emission like the galactic plane [22]. Neutrinos, like gravitational waves and light, travel mostly
 785 unimpeded from their source to our observatories. This makes pointing to the originating source
 786 of these messengers much easier than it is for cosmic rays which are deflected from their source by
 787 magnetic fields.

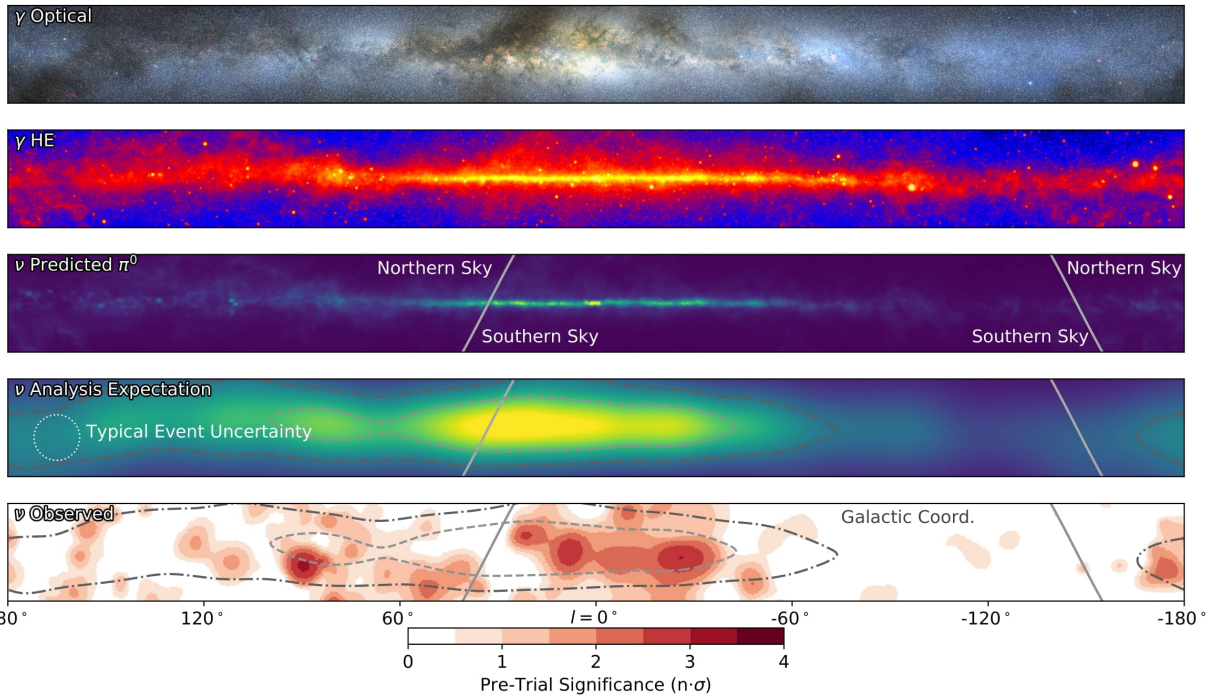


Figure 2.13 The Milky Way Galaxy in photons (γ) and neutrinos (ν) [22]. The Galactic center is at $l=0^\circ$ and is the brightest region in all panels. (top) An Optical color image of the Milky Way galaxy seen from Earth. Clouds of gas and dust obscure some light from stars. (2nd down) Integrated flux of γ -rays observed by the Fermi-LAT telescope [23]. (middle) Expected neutrino emission that corresponds with Fermi-LAT observations. (2nd up) Expected neutrino emission profile after considering detector systematics of IceCube. (bottom) Observed neutrino emission from region of the galactic plane. Substantial neutrino emission was detected.

788 The IceCube collaboration recently published a groundbreaking result of the Milky Way in
 789 neutrinos. The recent result from IceCube, shown in Figure 2.13, proves that we can make
 790 observations under different messenger regimes. The top two panels show the appearance of the
 791 galactic plane to different wavelengths of light. Some sources are more apparent in some panels,
 792 while others are not. This new channel is powerful because neutrinos are readily able to penetrate
 793 through gas and dust in the Milky Way. This new image also refines our understanding of how high

794 energy particles are produced. For example, the fit to IceCube data prefers neutrino production
 795 from the decay of π^0 [22].

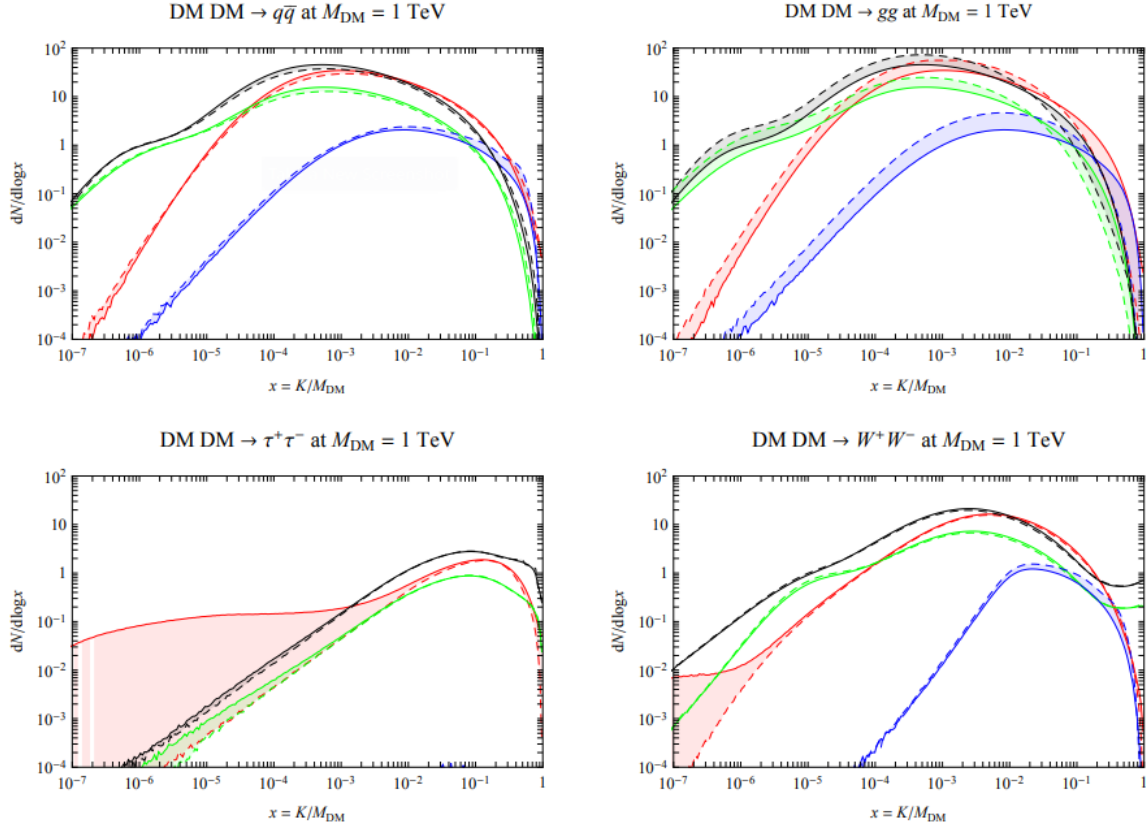


Figure 2.14 Dark Matter annihilation spectra for different final state particle and standard model annihilation channels [24]. Photons (red), e^\pm (green), \bar{p} (blue), ν (black).

796 Exposing our observations to more cosmic messengers greatly increases our sensitivity to
 797 rare processes. In the case of DM, Figure 2.14, there are many SM particles produced in DM
 798 annihilation. Among the final state fluxes are gammas and neutrinos. Charged particles are also
 799 produced however they would not likely make it to Earth since they will be deflected by magnetic
 800 fields between the source and Earth. This means observatories that can see the neutral messengers
 801 are especially good for DM searches and for combining data for a multi-messenger DM search.

CHAPTER 3

802

HIGH ALTITUDE WATER CHERENKOV (HAWC) OBSERVATORY

803



Figure 3.1 Photo of the HAWC detector that I took on May 17, 2023. Main array is centered in the photo and comprised of the larger tanks. Outriggers are the smaller tanks around the main array.

804

The High Altitude Water Cherenkov (HAWC) Observatory is a specialized instrument designed

805

for the observation of high energy gamma-rays and cosmic rays [25]. Located on the Sierra

806

Negra volcano in Mexico, HAWC observes gamma rays and cosmic rays in the energy range of

807

approximately 100 GeV to 100'ss of TeV. HAWC is strategically situated to maximize observational

808

efficiency due to its high altitude. At an elevation of 4,100 meters, it monitors about two-thirds of

809

the sky every day with an uptime above 90%. This capability is essential for studying high-energy

810

astronomical phenomena.

811

HAWC comprises of 300 water Cherenkov detectors (WCDs) spread over 22,000 square meters.

812

Each main array detector is filled with purified water and equipped with four, upward-facing

813

photomultiplier tubes (PMTs). These PMTs detect Cherenkov radiation from charged particles

814

passing through the tanks. These charged particles are generated when a high energy gamma or

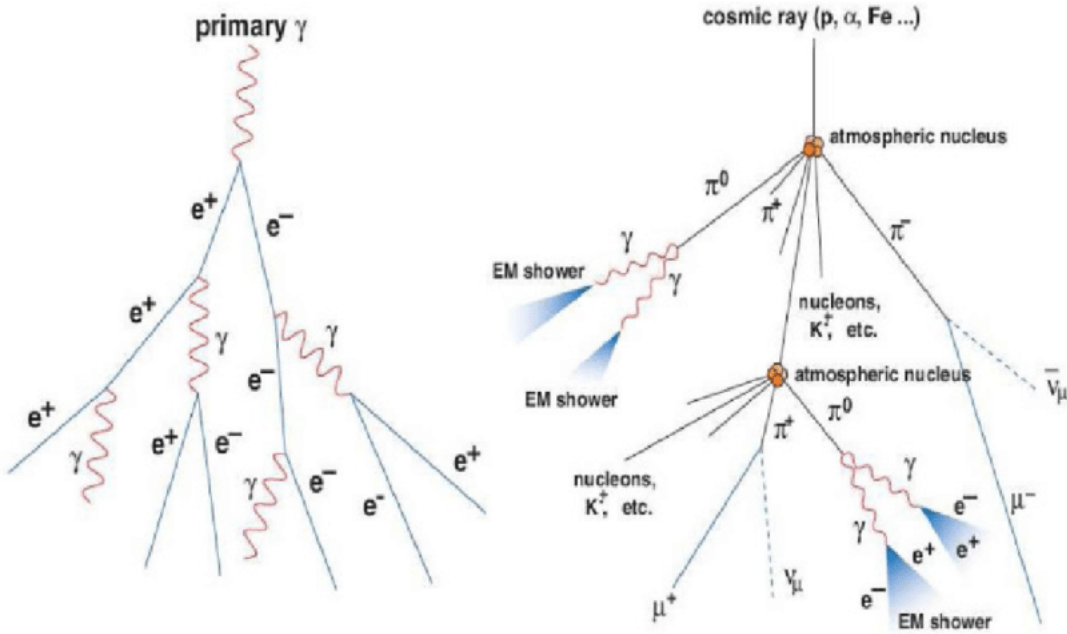


Figure 3.2 A particle physics illustration of high energy particle showers. Left shower is an electromagnetic shower from a high energy gamma-ray. Most particles in the shower will be a combination of photons and charged leptons, in this case electrons (e). Right figure shows a cosmic ray particle shower. The cosmic ray will produce many more types of particles including pions (π), neutrinos, and charged leptons. Figured pulled from [26].

815 cosmic ray collides with gas in the atmosphere to create a charged particle shower, see Fig. 3.2.
 816 The observatory includes a separate tank configuration which are referred to as the outriggers. They
 817 are a secondary array of 345 smaller WCD's. Surrounding the main array, each outrigger tank
 818 measures 1.55 meters in diameter and height and contain a single upward-facing eight-inch PMT.
 819 This expansion increases the instrumented footprint fourfold. It improves the reconstruction of
 820 showers extending beyond the main array, especially for events above 10 TeV. However, at the time
 821 of writing this thesis, the outriggers have not been fully integrated into HAWC's reconstruction
 822 software.

823 3.1.1 Construction and Hardware

824 **TODO: fact check the content below. GPT may have hallucinated** Each main array WCD is a
 825 cylindrical tank with dimensions of 7.3 m in diameter and 5.4 m in height and filled with 180,000
 826 liters of water [25]. The metal shell of these tanks is made from bolted together, corrugated,

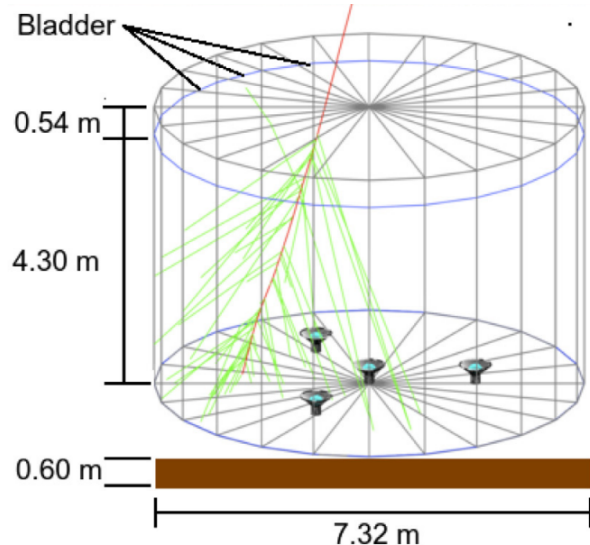


Figure 3.3 The WCDs. Left image features several WCDs looking from within the main array of HAWC. Right image shows a schematic of a WCD pulled from [25].

galvanized steel panels. The tanks are placed into 0.6 m deep trenches filled with rammed earth to secure it against seismic activity. The interior of each tank is lined with a black, low-density polyethylene bladder, designed to be impermeable to external light and to prevent reflection of Cherenkov light within the tank. This bladder is approximately 0.4 mm thick and composed of two layers of three-substrate film. To further minimize light penetration, a black agricultural foil covers the bladder. The ground and walls inside the tank are protected with felt and sand to safeguard against punctures. The tanks are filled 4.5 m deep of purified water, achieving a photon attenuation length for Cherenkov photons that exceeds the tank's dimensions. This purification level ensures the optimal detection environment for the photons generated by traversing charged particles.

At the base of each tank, four photomultiplier tubes (PMTs) are installed to detect the Cherenkov radiation emitted by charged particles. Three 8-inch diameter PMTs surround a larger 10 inch PMT from Hamamatsu [27]. The variation in PMT response is carefully accounted for in event reconstruction algorithms. Signals from the PMTs travel 610 ft cables to the counting house, where they are processed by Front-End Boards (FEBs). These FEBs, along with Time to Digital Converters (TDCs), digitize the signals and manage the high voltage supply to the PMTs.

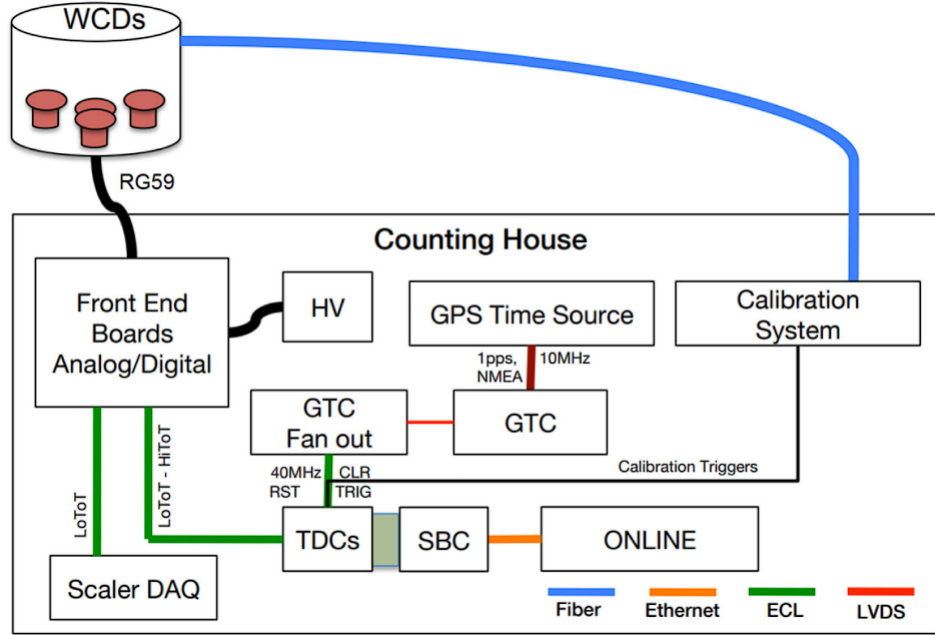


Figure 3.4 TODO: copied from nim. Top-level diagram of the HAWC electronics showing a summary of the critical subsystems and the interconnections, including HV and optical fiber cabling. NMEA refers to the National Marine Electric Association format in which GPS presents data [66,67]; CLR, TRG and RST are control signals for the TDC system. The LoToT andHiToT time over threshold signals are discussed in Section 4.1

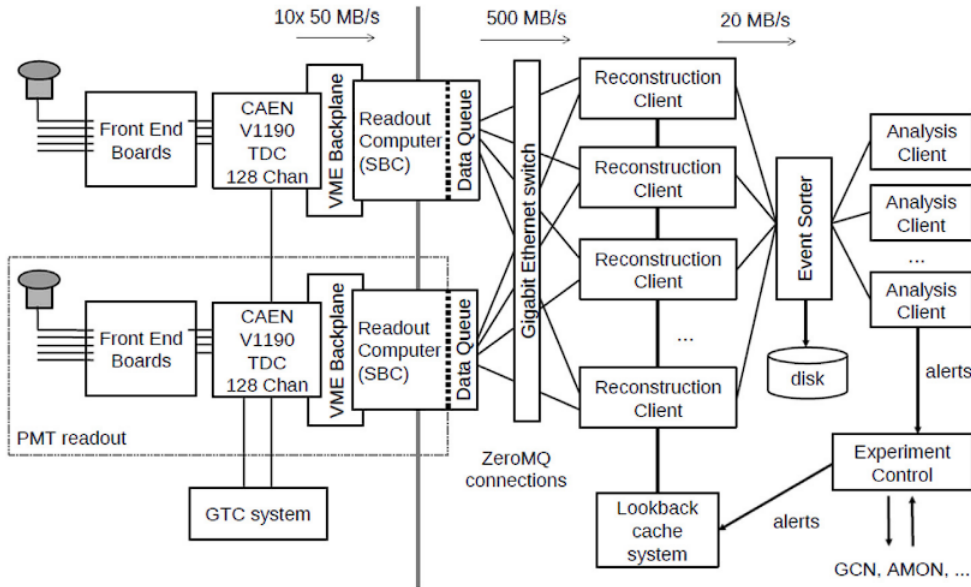


Figure 3.5 TODO: copied from NIM. Schematic overview [68] of the HAWC data acquisition and online processing system, as described in the text of Section 4

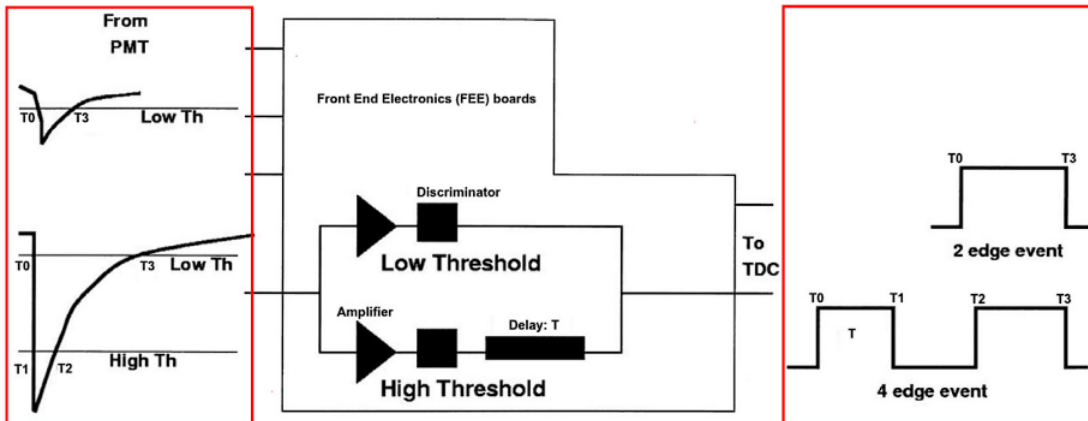


Figure 3.6 TODO: text copied from nim. The analog PMT signals are split and passed through two paths. In each path, there is an amplifier and discriminator circuit. The ratio of the amplifier gains is 7 to 1. The higher gain circuit has an effectively lower threshold (Low Th). There is a time (T) delay in the high threshold (High Th) path. The 2-edge event is related with the Low Th, while the 4 edge event is related to the High Th.

842 3.1.2 Data Acquisition and Signal Processing

843 The HAWC data acquisition (DAQ) and signal processing systems convert the physical detection
 844 of particles into analyzable data. This process involves a series of steps from initial signal detection
 845 by PMTs to digital conversion and preliminary analysis, see Fig. 3.4 and Fig. 3.5.

846 Once the signal from the PMTs arrive at the counting house, they enter the Front-End Boards
 847 (FEBs). The FEBs are responsible for the initial processing of these signals, which includes
 848 amplification and integration [28]. Each PMT signal is compared against preset LOW/HIGH
 849 voltage thresholds in the FEBs Fig. 3.6, identifying signals that correspond to about 1/4 and
 850 4 photoelectrons, respectively. This differentiation allows the system to gauge the strength of
 851 the detected Cherenkov radiation. The processed signals are then digitized by Time to Digital
 852 Converters (TDCs). These converters measure the time over threshold (ToT) for each signal, a
 853 parameter that reflects both the duration and amplitude of the signal. This digitization facilitates
 854 reconstruction of the original event for translating the physical interactions within the detectors into
 855 data [29, 30, 28].

856 Synchronization across the HAWC observatory is maintained by a central GPS Timing and
 857 Control (GTC) system, which achieves a timing resolution of 98 ps. This high-resolution timing

858 is vital for accurately reconstructing the timing and location of air showers initiated by cosmic
859 and gamma rays. The GTC system ensures that all components of the DAQ operate in unison to
860 preserve the temporal integrity of the detected events [29, 31].

861 Once digitized, the data are transferred to an online event reconstruction system. This system
862 runs the Reconstruction Client, which utilizes the raw PMT data to reconstruct the characteristics
863 of the air showers, such as their direction and energy [30]. The capacity for real-time analysis
864 allows HAWC to promptly respond to astrophysical phenomena like Gamma Ray Bursts (GRBs)
865 and to participate in multi-messenger astronomy by following up on alerts from other observatories.
866 This real-time processing system is designed to handle high data throughput, using ZeroMQ [32]
867 for efficient data transfer between software components. Analysis Clients perform specific online
868 analyses that require immediate data, including monitoring for GRBs, solar flare activity, and
869 participation in global efforts to track gravitational waves and neutrinos [29].

870 The DAQ system is overseen by an Experiment Control system and crew that manage the
871 operational aspects of data collection. This includes initiating and terminating data collection
872 runs and monitoring the experiment for errors. In the event of a system crash, often caused by
873 environmental factors such as lightning, the Experiment Control system is designed to automatically
874 restart the experiment and minimize downtime [29, 30].

875 **3.2 Events Reconstruction**

876 Event reconstruction at the HAWC Observatory is a critical procedure that converts the raw data
877 from the observatory’s WCDs into a coherent framework for understanding cosmic and gamma-
878 ray events. This process includes several distinct steps. Core Fitting determines the geometric
879 center of the air shower on the detector plane. Angle Reconstruction assesses the trajectory of the
880 incoming particle, revealing its origin in the sky. Energy Estimation is performed using both f -hit
881 and Neural Network (NN) methods to quantify the energy of the detected events. Gamma-hadron
882 (\tilde{G}) discrimination differentiates between gamma-ray and hadronic cosmic ray initiated showers,
883 a vital step for astrophysical interpretations. Each of these steps is integral to the observatory’s
884 objective of investigating the high-energy universe and enable the transformation of signals into

885 detailed insights about high energy cosmic phenomena.

886 3.2.1 Core Fitting

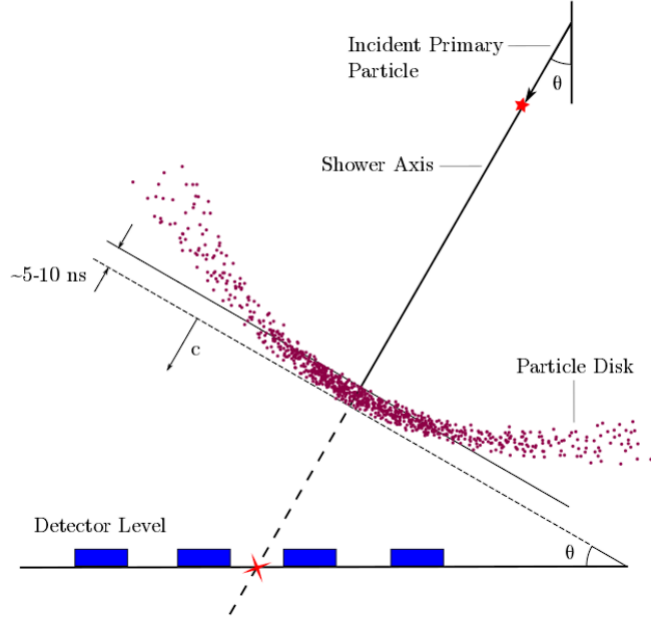


Figure 3.7 TODO: copied from A's thesis. An illustration of the angle reconstruction of the original particle. The secondary particles of an air shower travel in a plane perpendicular to the direction of the original particle, allowing for the reconstruction of the initial angle after corrections due to the curvature of the plane. Figure from [33].

887 In the study of air showers, accurately determining the location of the air shower core on the
888 ground is crucial for reconstructing the direction of the originating primary particle. An illustration
889 of this can be seen in a HAWC event plot, where the lateral charge distribution across the array is
890 displayed. The core is identified and marked with a red star, reconstructed using a predetermined
891 functional form.

892 The signal S_i from the i th PMT is given by the following equation:

$$S_i = S(A, \tilde{x}, \tilde{x}_i) = A \left(\frac{1}{2\pi\sigma^2} e^{-\frac{|\vec{x}_i - \vec{x}|^2}{2\sigma^2}} + \frac{N}{(0.5 + |\vec{x}_i - \vec{x}|/R_m)^3} \right) \quad (3.1)$$

893 In this model, \tilde{x} represents the core location and \tilde{x}_i is the position of the i th PMT. R_m stands for
894 the Molière radius, which is approximately 120 meters at the altitude of HAWC, while σ , is the
895 standard deviation of the Gaussian distribution. The equation incorporates fixed values of $\sigma = 10$

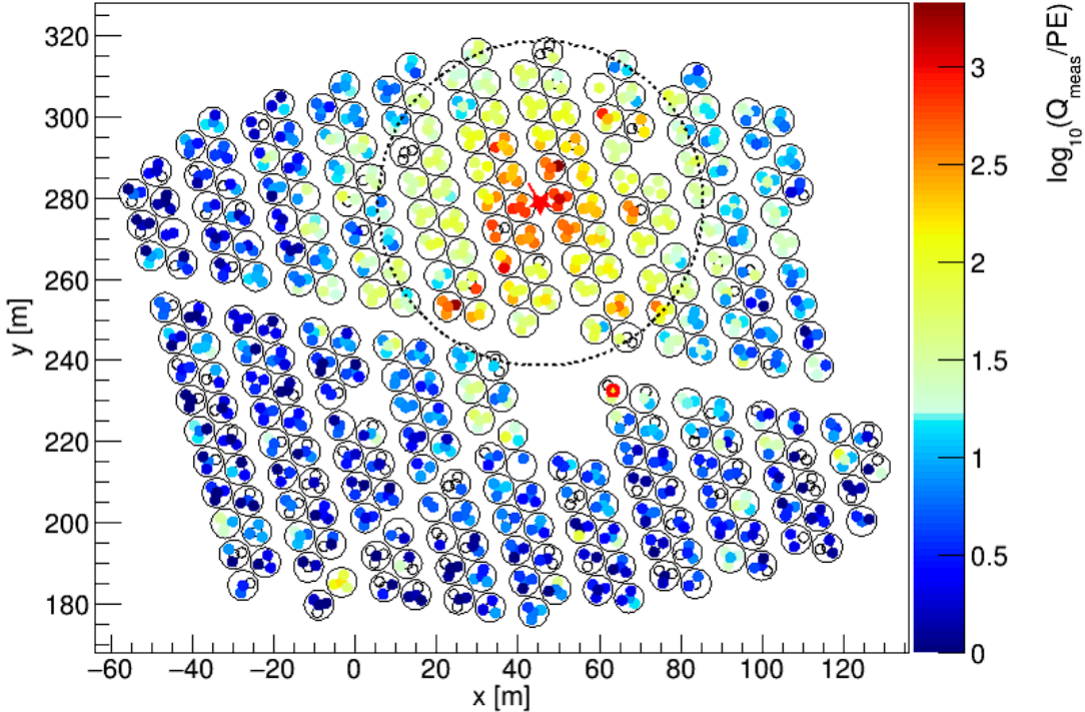


Figure 3.8 TODO: pulled for thesis. Charge deposited in each PMT for a reconstructed gamma-ray event. Each large circle represents a WCD and each of the 4 smaller circles within represent a PMT. The color scale represents the amount of charge deposited in each PMT. The red star in the center of the dashed circle shows the location of the shower core fit by the SFCF algorithm. [34]

896 m and $N = 5.10^{-5}$. N is the normalization factor for the tail of the distribution. This leaves the
 897 core location and overall amplitude A as the free parameters to be determined during fitting.

898 The chosen functional form for the Super Fast Core Fit (SFCF) algorithm is a simplified version
 899 of a modified Nishimura-Kamata-Greisen (NKG) function [35], selected for its computational
 900 efficiency which is essential for rapid fitting of air shower cores. The SFCF form allows numerical
 901 minimization to converge more quickly due to the function's simplicity, the analytical computation
 902 of its derivatives, and the absence of a pole at the core location.

903 Figure 2 provides a visualization of a recorded event, with the plot depicting the charge recorded
 904 by each PMT as a function of the distance to the reconstructed shower core. The caption explains the
 905 plot details, including the reconstructed arrival coordinates and data acquisition run information,
 906 and also mentions variables relevant for gamma/hadron separation, as discussed in Section 4.3.1.

907 Through the application of the SFCF, core locations can be identified with a median error of

908 approximately 2 meters for large events and about 4 meters for smaller ones, assuming the gamma-
909 ray event core impacts directly upon the HAWC detector array. It is noted that as the core's distance
910 from the array increases, the precision in locating the core diminishes, highlighting the importance
911 of proximity in the accuracy of core reconstruction.

912 **3.2.2 Angle Reconstruction**

913 **3.2.3 *f*-hit Energy Estimation**

914 **3.2.4 Neural Network Energy Estimation**

915 **3.2.5 G/H Discrimination**

916 **3.3 Remote Monitoring**

917 **3.3.1 ATHENA Database**

918 **3.3.2 HOMER**

919

CHAPTER 4

ICECUBE NEUTRINO OBSERVATORY

920 **4.1 The Detector**

921 **4.2 Events Reconstruction and Data Acquisition**

922 **4.2.1 Angle**

923 **4.2.2 Energy**

924 **4.3 Northern Test Site**

925 **4.3.1 PIgeon remote dark rate testing**

926 **4.3.2 Bulkhead Construction**

CHAPTER 5

927 **GLORY DUCK: MULTI-WAVELENGTH SEARCH FOR DARK MATTTER** 928 **ANNIHILATION TOWARDS DWARF SPHEROIDAL GALAXIES**

929 **5.1 Introduction**

930 The field of astrophysics now has several instruments and observatories sensitive to high energy
931 gamma-rays. The energy sensitivity for the modern gamma-ray program spans many orders of
932 magnitude. Figure 5.1 demonstrates these comparable sensitivities across energies for the five
933 experiments: Fermi-LAT, HAWC, HESS, MAGIC, and VERITAS.

934 Each of the five experiments featured in Figure 5.1 have independently searched for DM
935 annihilation from dwarf spheroidal galaxies (dSph) and set limits on annihilation cross-section of
936 WIMPs. Intriguingly, there are regions of substantial overlap in their energy sensitivities. This
937 clearly motivates an analysis that combines data from these five. Each experiment has unique
938 gamma-ray detection methods and their weaknesses and strengths can be leveraged with each other.
939 The HAWC gamma-ray observatory is extensively introduced in chapter 3, so it is not introduced
940 here. A brief description of the remaining experiments are in the following paragraphs.

941 The Large Area Telescope (LAT) is a pair conversion telescope mounted on the NASA Fermi
942 satellite in orbit \sim 550 km above the Earth [37]. LAT's field of view covers about 20% of the
943 whole sky, and it sweeps the whole sky approximately every 3 hours. LAT's gamma-ray energy
944 sensitivity ranges from 20 MeV up to 1 TeV. Previous DM searches towards dSphs using Fermi-LAT
945 are published in [38] and [39].

946 The High Energy Spectroscopic System (HESS), Major Atmospheric Gamma Imaging
947 Cherenkov (MAGIC), and Very Energetic Radiation Imaging Telescope Array System (VERI-
948 TAS) are arrays of Imaging Atmospheric Cherenkov Telescopes (IACT). These telescopes observe
949 the Cherenkov light emitted from gamma-ray showers in the Earth's atmosphere. The field of
950 view for these telescopes is no larger than 5° with energy sensitivities ranging from 30 GeV up
951 to 100 TeV [40, 41, 42]. IACTs are able to make precise observations in selected regions of the
952 sky, however can only be operated in ideal dark conditions. HESS's observations of the dwarves

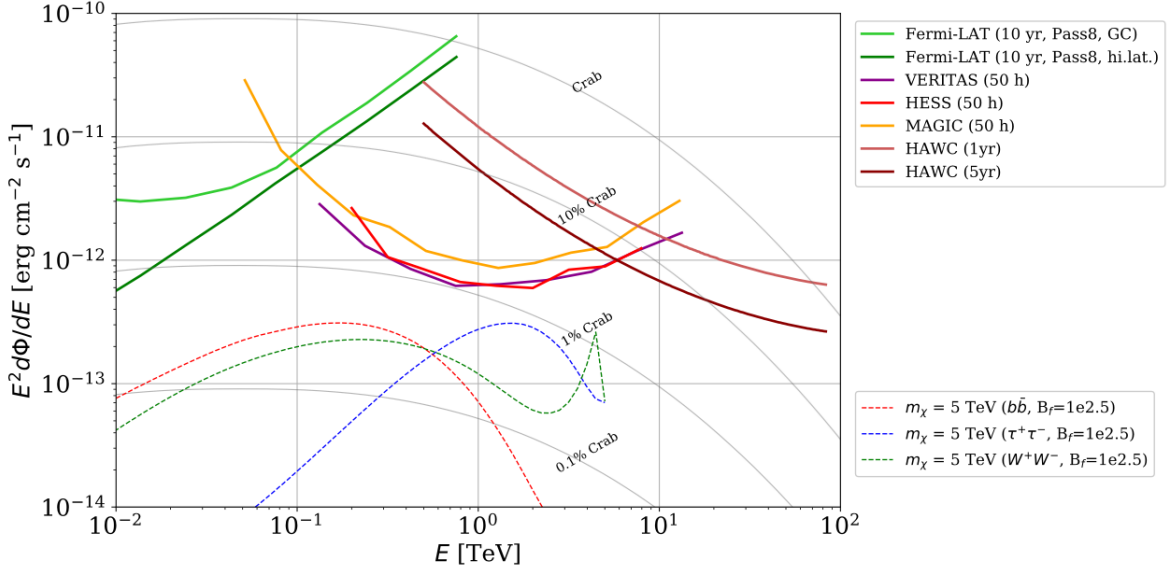


Figure 5.1 Sensitivities of five gamma-ray experiments compared to percentages of the Crab nebula's emission and dark matter annihilation. Solid lines present estimated sensitivities to power law spectra [FACT CHECK THIS] for each experiment. Green lines are Fermi-LAT sensitivities where lighter green is the sensitivity to the galactic center and dark green is its sensitivity to higher declinations. Orange, red, and purple solid lines represent the MAGIC, HESS, and VERITAS 50 hour sensitivities respectively. The maroon and brown lines are the HAWC 1 year and 5 year sensitivities. Across four decades of gamma-ray energy, these experiments have similar sensitivities on the order 10^{-12} erg cm $^{-2}$ s $^{-1}$. The dotted lines are estimated dark matter fluxes assuming $m_\chi = 5$ TeV DM annihilating to bottom quarks (red), tau leptons (blue), and W bosons (green). Faded gray lines outline percentage flux of the Crab nebula. Figure is an augmented version of [36]

953 Sculptor and Carina were between January 2008 and December 2009. HESS's observations of
 954 Coma Berenices were taken from 2010 to 2013, and Fornax was observed in 2010 [43, 44, 45].
 955 MAGIC provided deep observations of Segue1 between 2011 and 2013 [46]. MAGIC also provides
 956 data for three additional dwarves: Coma Berenices, Draco, and Ursa Major II where observations
 957 were made in: January - June 2019 [47], March - September 2018 [47], and 2014 - 2016 [48]
 958 respectively. VERITAS provided data for Boötes I, Draco, Segue 1, and Ursa Minor from 2009 to
 959 2016 [49].

960 This chapter presents the Glory Duck analysis, the name given for the search for dark matter
 961 annihilation from dSph by combining data from the five gamma-ray observatories: Fermi-LAT,
 962 HAWC, HESS, MAGIC, and VERITAS. Specifically, the methods in analysis and modeling are
 963 presented for the HAWC gamma-ray observatory. This work will be published in the Journal of

964 Cosmology and Astroparticle Physics and presented at the International Cosmic Ray Conference
965 in 2019, 2021, and 2023 [50, 51, 52] and others.

966 **5.2 Dataset and Background**

967 This section enumerates the data analysis and background estimation methods used for HAWC's
968 study of dSphs. Section 5.2.1 and Section 5.2.2 are most useful for fellow HAWC collaborators
969 looking to replicate the Glory Duck analysis.

970 **5.2.1 Itemized HAWC files**

971 These files are only available withing HAWC's internal documentation and collaborators. They
972 are not meant for public access, and are presented here so that HAWC collaborators can reproduce
973 results accurately.

- 974 • Detector Response: `response_aerie_svn_27754_systematics_best_mc_test_noBr`
975 `oadpulse\10pctlogchargesmearing_0.63qe_25kHzNoise_run5481_curvature`
976 `0_index3.root`
- 977 • Data Map: `maps-20180119/liff/maptree_1024.root`
- 978 • Spectral Dictionary: `DM_CirrelliSpectrum_dict_gammas.npy`
- 979 • Analysis wiki: https://private.hawc-observatory.org/wiki/index.php/Glory_Duck_Multi-Experiment_Dark_Matter_Search

981 **5.2.2 Software Tools and Development**

982 This analysis was performed using HAL and 3ML [34, 53] in Python version 2. I built software
983 to implement the *A Poor Particle Physicist Cookbook for Dark Matter Indirect Detection* (PPPC)
984 [54] DM spectral model and dSphs spatial model from [55] for HAWC analysis. A NumPy version
985 of this dictionary was made for both Py2 and Py3. The code base for creating this dictionary is
986 linked on my GitLab sandbox:

- 987 • Py2: [Dictionary Generator \(Deprecated\)](#)

- 988 • Py3: [PPPC2Dict](#)

989 The analysis was performed using the f_{hit} framework as used and described in the HAWC Crab
990 paper [34]. The Python2 NumPy dictionary file for gamma-ray final states is `dmCirSpecDict.npy`.
991 The corresponding Python3 file is `DM_CirrelliSpectrum_dict_gammas.npy`. These files can
992 also be used for decay channels and the PPPC describes how [54]. All other software used for data
993 analysis, DM profile generation, and job submission to SLURM are also kept in my sandbox for
994 [the Glory Duck](#) project.

995 **5.2.3 Data Set and Background Description**

996 The HAWC data maps used for this analysis contain 1017 days of data between runs 2104
997 (2014-11-26) and 7476 (2017-12-20). They were generated from pass 4.0 reconstruction. The
998 analysis is performed using the f_{hit} energy binning scheme with bins (1-9) similar to what was done
999 for the Crab and previous HAWC dSph analysis [34, 56]. Bin 0 was excluded as it has substantial
1000 hadronic contamination and poor angular resolution.

1001 This analysis was done on dSphs because of their large DM mass content relative to baryonic
1002 mass. We consider the following to estimate the background to this study.

- 1003 • The dSphs' angular extent are small relative to HAWC's spatial resolution, so the analysis is
1004 not sensitive to large or small scale anisotropies.
- 1005 • The dSphs used in this analysis are off the galactic plane and therefore not contaminated by
1006 diffuse emission from the galaxy.
- 1007 • The dSphs are baryonically faint relative to their expected dark matter content and are not
1008 expected to contain high energy gamma-ray sources.

1009 Therefor we make no additional assumptions on the background from our sources and use
1010 HAWC's standard direct integration method for background estimation [34]. The largest background
1011 under this consideration is from an isotropic flux of cosmic rays. The contamination of this hadronic
1012 flux is worse at lower energies where HAWC's gamma/hadron discrimination worse. It is possible

1013 for gamma rays from DM annihilation to scatter in transit to HAWC via Inverse Compton Scattering
1014 (ICS). This was investigated and its impact on the flux is negligible. Supporting information on
1015 this is in Section 5.7.1

1016 **5.3 Analysis**

1017 The expected differential photon flux from DM-DM annihilation to standard model particles,
1018 $d\Phi_\gamma/dE_\gamma$, over solid angle, Ω , is described by the familiar equation.

$$\frac{d\Phi_\gamma}{dE_\gamma} = \frac{\langle\sigma v\rangle}{8\pi m_\chi^2} \frac{dN_\gamma}{dE_\gamma} \times \int_{\text{source}} d\Omega \int_{l.o.s} dl \rho_\chi^2 J(r, \theta') \quad (5.1)$$

1019 Where $\langle\sigma v\rangle$ is the velocity weighted annihilation cross-section. $\frac{dN}{dE}$ is the expected differential
1020 number of photons produced at each energy per annihilation. m_χ is the rest mass of the supposed
1021 DM particle. ρ_χ is the DM density. J is the astrophysical J-factor and is defined as

$$J = \int d\Omega \int_{l.o.s} dl \rho_\chi^2(r, \theta') \quad (5.2)$$

1022 l is the distance to the source from Earth. r is the radial distance from the center of the source. θ' is
1023 the half angle defining a cone containing the DM source. How each component is synthesized and
1024 considered for HAWC's analysis is presented in the following sections. Section 5.3.1 presents the
1025 particle physics model for DM annihilation. Section 5.3.2 presents the spatial distributions built
1026 for each dSph.

1027 **5.3.1 $\frac{dN_\gamma}{dE_\gamma}$ - Particle Physics Component**

1028 For these spectra, we import the PPPC with Electroweak (EW) corrections [54]. Public versions
1029 of the imported tables are provided by the [authors online](#). The spectrum is implemented as a model
1030 script in astromodels for 3ML. The EW corrections were previously not considered for HAWC and
1031 are significant for DM annihilating to EW coupled SM particles such as all leptons, and the γ ,
1032 Z , and W bosons [56]. Figure 5.2 demonstrates the significance of EW corrections for W boson
1033 annihilation. Across EW SM channels, the gamma-ray spectra become harder than spectra without
1034 EW corrections. Tables from the PPPC were reformatted into Python NumPy dictionaries for
1035 collaboration-wide use. A class in astromodels was developed to include the EW correction from
1036 the PPPC and is aptly named `PPPCSpectra` within `DM_models.py`.

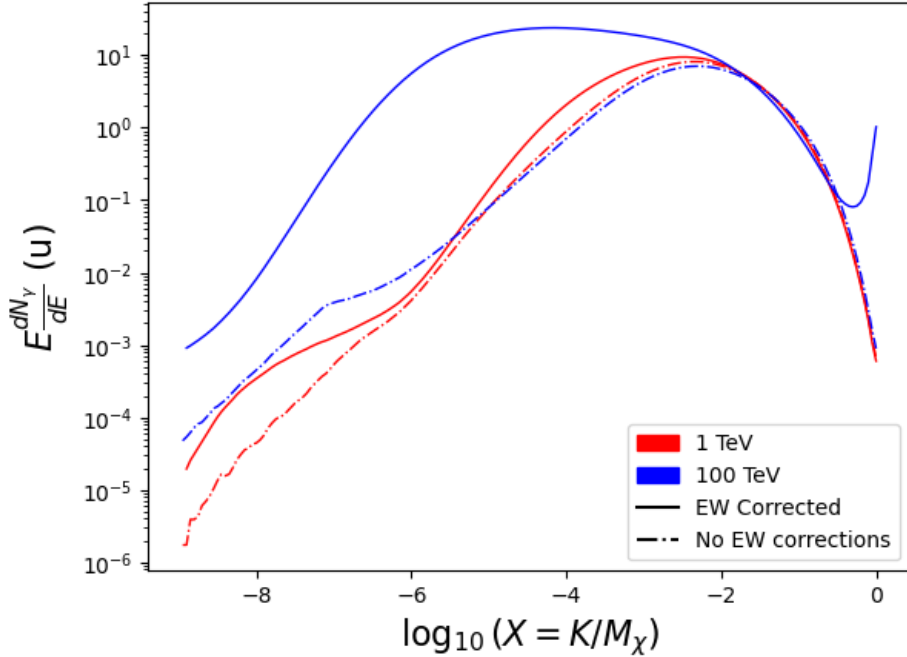


Figure 5.2 Effect of Electroweak (EW) corrections on expected DM annihilation spectrum for $\chi\chi \rightarrow W^-W^+$. Solid lines are spectral models that consider EW corrections. Dash-dot lines are spectral models without EW corrections. Red lines are models for $M_\chi = 1$ TeV. Blue lines represent models for $M_\chi = 100$ TeV. All models are sourced from the PPPC4DMID [54].

1037 5.3.2 J- Astrophysical Component

1038 The J-factor profiles for each source are imported from Geringer-Sameth (referred to with \mathcal{GS})
 1039 [55]. \mathcal{GS} fits the Zhao DM profile to the dSphs which has a DM density described as [57]

$$\rho(r) = \frac{\rho_0}{(r/R_s)^\gamma (1 + (r/R_s)^\alpha)^{(\beta-\gamma)}}. \quad (5.3)$$

1040 R_s is the scale radius and free parameter in the model. γ is the logarithmic slope in the region
 1041 $r \ll R_s$. β is the logarithmic slope in the region $r \gg R_s$. α is known as the sharpness of transition
 1042 where $r \approx R_s$. The classic Navarro-Frenk-White [58] (NFW) can be retrieved from Zhao by fixing
 1043 $(\alpha, \beta, \gamma) = (1, 3, 1)$.

1044 \mathcal{GS} best fits were pulled from the publication as $J(\theta)$, where θ is the angular separation from
 1045 the center of the source. HAWC requires maps in terms of $\frac{dJ}{d\Omega}$, so the conversion from the maps
 1046 was done in the following way...

1047 First, convert the angular distances to solid angles

$$\Omega = 2 \cdot \pi(1 - \cos(\theta)) \quad (5.4)$$

1048 which reduces with a small angle approximation to $\pi\theta^2$. Next, the central difference for both the
1049 ΔJ and $\Delta\Omega$ value were calculated from the discretized $J(\theta)$ with the central difference stencil:

$$\Delta\phi_i = \phi_{i+1} - \phi_{i-1} \quad (5.5)$$

1050 Where ϕ is either Ω or J . These were done separately in case the grid spacing in θ was not uniform.
1051 Finally, these lists are divided so that we are left with an approximation of the $dJ/d\Omega$ profile that
1052 is a function of θ . Admittedly, this is an approximation method for the map which introduces small
1053 errors compared to the true profile estimate. This was checked as a systematic against the author's
1054 profiling of the spatial distribution and is documented in Section 5.8.1.

1055 With $\frac{dJ}{d\Omega}(\theta)$, a map is generated, first by filling in the north-east quadrant of the map. This
1056 quadrant is then reflected twice, vertically then horizontally, to fill the full map. Maps are then
1057 normalized by dividing the discrete 2D integral of the map. The 2D integral was a simple height
1058 of bins, Newton's integral:

$$p^2 \cdot \sum_{i,j=0}^{N,M} \frac{dJ}{d\Omega}(\theta_{i,j}, \phi_{i,j}) \quad (5.6)$$

1059 These maps are HEALpix maps with NSIDE 16384 and saved in the .fits format. The hyper fine
1060 resolution was selected to better preserve the total expected counts after integrating Eq. (5.1) with
1061 the detector response.

1062 Another DM spatial distribution model from Bonnivard (\mathcal{B}) [59] was used for the Glory Duck
1063 study. However, to save computational time, limits from \mathcal{GS} were scaled to \mathcal{B} instead of each
1064 experiment performing a full study a second time. How these models compare is demonstrated
1065 for each dSph in Figure 5.16 and Figure 5.17 Plots of these maps are provided for each source
1066 in chapter A Examples of the two most impactful dSphs derived from \mathcal{GS} , Segue1 and Coma
1067 Berenices are featured in Figure 5.3

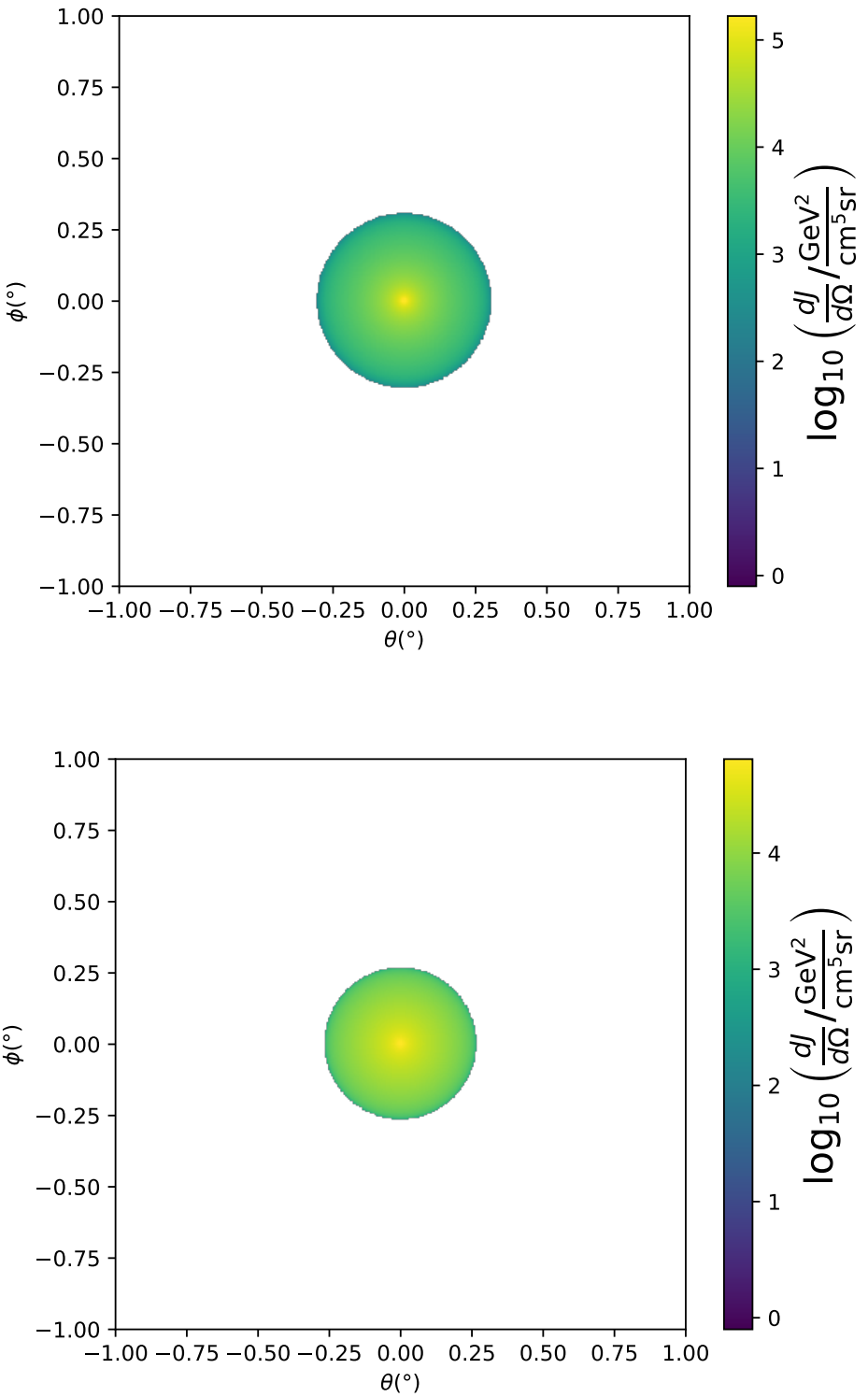


Figure 5.3 $\frac{dJ}{d\Omega}$ maps for Segue1 (top) and Coma Berenices (bottom). Origin is centered on the specific dwarf spheroidal galaxies (dSph). X and Y axes are the angular separation from the center of the dwarf. Profile is truncated at the scale radius. Plots of the remaining 11 dSph HAWC studied are linked in Fig. A.1.

1068 **5.3.3 Source Selection and Annihilation Channels**

1069 We use many of the dSphs presented in HAWC’s previous dSph DM search [56]. HAWC’s
1070 sources for Glory Duck include Boötes I, Coma Berenices, Canes Venatici I + II, Draco, Hercules,
1071 Leo I, II, + IV, Segue 1, Sextans, and Ursa Major I + II. A full description of all sources used
1072 in Glory Duck is found in Table 5.1. Triangulum II was excluded from the Glory Duck analysis
1073 because of large uncertainties in its J factor. Ursa Minor was excluded from HAWC’s contribution
1074 to the combination because the source extension model extended Ursa Minor beyond HAWC’s field
1075 of view. Ursa Minor was not expected to contribute significantly to the combined limit, so work
1076 was not invested in a solution to include Ursa Minor.

1077 This analysis improves on the previous HAWC dSph paper [56] in the following ways. Pre-
1078 viously, the dSphs were treated and implemented as point sources. For this analysis, dSphs are
1079 modeled and treated as extended source. The impact of this change with respect to the upper limit
1080 is source dependent and is explored in Section 5.7.2. Previously, the particle physics model used for
1081 gamma-ray spectra from DM annihilation did not have EW corrections where the PPPC includes
1082 them. Finally, the gamma-ray ray dataset is much larger. The study performed here analyzes over
1083 1000 days of data compared to 507.

1084 The SM annihilation channels probed for the Glory Duck combination include $b\bar{b}$, $e\bar{e}$, $\mu\bar{\mu}$, $\tau\bar{\tau}$,
1085 $t\bar{t}$, W^+W^- , and ZZ . A summary of all sources, with a description of each experiments’ sensitivity
1086 to the source, is provided in Table 5.2.

1087 **5.4 Likelihood Methods**

1088 **5.4.1 HAWC Likelihood**

1089 For every analysis bin in energy, f_{hit} bins (1-9), and location, we can expect N signal events and
1090 B background events. The expected number of excess signal events from dark matter annihilation,
1091 S , is estimated by convolving Equation (5.1) with HAWC’s energy response and pixel point spread
1092 functions. I then compute the test statistic (TS) with the log-likelihood ratio test,

$$TS_{\max} = -2 \ln \left(\frac{\mathcal{L}_0}{\mathcal{L}_{\max}} \right) \quad (5.7)$$

Table 5.1 Summary of the relevant properties of the dSphs used in the present work. Column 1 lists the dSphs. Columns 2 and 3 present their heliocentric distance and galactic coordinates, respectively. Columns 4 and 5 report the J -factors of each source given from the \mathcal{GS} and \mathcal{B} independent studies and their estimated $\pm 1\sigma$ uncertainties. The values $\log_{10} J$ (\mathcal{GS} set) [55] correspond to the mean J -factor values for a source extension truncated at the outermost observed star. The values $\log_{10} J$ (\mathcal{B} set) [59] are provided for a source extension at the tidal radius of each dSph. **Bolded sources are within HAWC's field of view and provided to the Glory Duck analysis.**

Name	Distance (kpc)	l, b ($^{\circ}$)	$\log_{10} J$ (\mathcal{GS} set) $\log_{10}(\text{GeV}^2\text{cm}^{-5}\text{sr})$	$\log_{10} J$ (\mathcal{B} set) $\log_{10}(\text{GeV}^2\text{cm}^{-5}\text{sr})$
Boötes I	66	358.08, 69.62	$18.24^{+0.40}_{-0.37}$	$18.85^{+1.10}_{-0.61}$
Canes Venatici I	218	74.31, 79.82	$17.44^{+0.37}_{-0.28}$	$17.63^{+0.50}_{-0.20}$
Canes Venatici II	160	113.58, 82.70	$17.65^{+0.45}_{-0.43}$	$18.67^{+1.54}_{-0.97}$
Carina	105	260.11, -22.22	$17.92^{+0.19}_{-0.11}$	$18.02^{+0.36}_{-0.15}$
Coma Berenices	44	241.89, 83.61	$19.02^{+0.37}_{-0.41}$	$20.13^{+1.56}_{-1.08}$
Draco	76	86.37, 34.72	$19.05^{+0.22}_{-0.21}$	$19.42^{+0.92}_{-0.47}$
Fornax	147	237.10, -65.65	$17.84^{+0.11}_{-0.06}$	$17.85^{+0.11}_{-0.08}$
Hercules	132	28.73, 36.87	$16.86^{+0.74}_{-0.68}$	$17.70^{+1.08}_{-0.73}$
Leo I	254	225.99, 49.11	$17.84^{+0.20}_{-0.16}$	$17.93^{+0.65}_{-0.25}$
Leo II	233	220.17, 67.23	$17.97^{+0.20}_{-0.18}$	$18.11^{+0.71}_{-0.25}$
Leo IV	154	265.44, 56.51	$16.32^{+1.06}_{-1.70}$	$16.36^{+1.44}_{-1.65}$
Leo V	178	261.86, 58.54	$16.37^{+0.94}_{-0.87}$	$16.30^{+1.33}_{-1.16}$
Leo T	417	214.85, 43.66	$17.11^{+0.44}_{-0.39}$	$17.67^{+1.01}_{-0.56}$
Sculptor	86	287.53, -83.16	$18.57^{+0.07}_{-0.05}$	$18.63^{+0.14}_{-0.08}$
Segue I	23	220.48, 50.43	$19.36^{+0.32}_{-0.35}$	$17.52^{+2.54}_{-2.65}$
Segue II	35	149.43, -38.14	$16.21^{+1.06}_{-0.98}$	$19.50^{+1.82}_{-1.48}$
Sextans	86	243.50, 42.27	$17.92^{+0.35}_{-0.29}$	$18.04^{+0.50}_{-0.28}$
Ursa Major I	97	159.43, 54.41	$17.87^{+0.56}_{-0.33}$	$18.84^{+0.97}_{-0.43}$
Ursa Major II	32	152.46, 37.44	$19.42^{+0.44}_{-0.42}$	$20.60^{+1.46}_{-0.95}$
Ursa Minor	76	104.97, 44.80	$18.95^{+0.26}_{-0.18}$	$19.08^{+0.21}_{-0.13}$

Table 5.2 Summary of dSph observations by each experiment used in this work. A ‘-’ indicates the experiment did not observe the dSph for this study. For Fermi-LAT, the exposure at 1 GeV is given. For HAWC, $|\Delta\theta|$ is the absolute difference between the source declination and HAWC latitude. HAWC is more sensitive to sources with smaller $|\Delta\theta|$. For IACTs, we show the zenith angle range, the total exposure, the energy range, the angular radius θ of the signal or ON region, the ratio of exposures between the background-control (OFF) and signal (ON) regions (τ), and the significance of gamma-ray excess in standard deviations, σ .

Source name	Fermi-LAT	HAWC	H.E.S.S, MAGIC, VERITAS						
	Exposure (10^{11} s m 2)	$ \Delta\theta $ ($^\circ$)	IACT	Zenith ($^\circ$)	Exposure (h)	Energy range (GeV)	θ ($^\circ$)	τ	S (σ)
Boötes I	2.6	4.5	VERITAS	15 – 30	14.0	100–41000	0.10	8.6	-1.0
Canes Venatici I	2.9	14.6	–	–	–	–	–	–	–
Canes Venatici II	2.9	15.3	–	–	–	–	–	–	–
Carina	3.1	–	H.E.S.S.	27 – 46	23.7	310 – 70000	0.10	18.0	-0.3
Coma Berenices	2.7	4.9	H.E.S.S.	47 – 49	11.4	550 – 70000	0.10	14.4	-0.4
Draco	3.8	38.1	MAGIC	5 – 37	49.5	60 – 10000	0.17	1.0	–
			MAGIC	29 – 45	52.1	70 – 10000	0.22	1.0	–
			VERITAS	25 – 40	49.8	120 – 70000	0.10	9.0	-1.0
Fornax	2.7	–	H.E.S.S.	11 – 25	6.8	230 – 70000	0.10	45.5	-1.5
Hercules	2.8	6.3	–	–	–	–	–	–	–
Leo I	2.5	6.7	–	–	–	–	–	–	–
Leo II	2.6	3.1	–	–	–	–	–	–	–
Leo IV	2.4	19.5	–	–	–	–	–	–	–
Leo V	2.4	–	–	–	–	–	–	–	–
Leo T	2.6	–	–	–	–	–	–	–	–
Sculptor	2.7	–	H.E.S.S.	10 – 46	11.8	200 – 70000	0.10	19.8	-2.2
Segue I	2.5	2.9	MAGIC	13 – 37	158.0	60 – 10000	0.12	1.0	-0.5
			VERITAS	15 – 35	92.0	80 – 50000	0.10	7.6	0.7
Segue II	2.7	–	–	–	–	–	–	–	–
Sextans	2.4	20.6	–	–	–	–	–	–	–
Ursa Major I	3.4	32.9	–	–	–	–	–	–	–
Ursa Major II	4.0	44.1	MAGIC	35 – 45	94.8	120 – 10000	0.30	1.0	-2.1
Ursa Minor	4.1	–	VERITAS	35 – 45	60.4	160 – 93000	0.10	8.4	-0.1

1093 where \mathcal{L}_0 is the null hypothesis, or no DM emission, likelihood. \mathcal{L}^{\max} is the best fit signal
 1094 hypothesis where $\langle\sigma v\rangle$ maximizes the likelihood. We calculate the likelihood of each source and
 1095 model, assuming events are Poisson distributed, with

$$\mathcal{L} = \prod_i \frac{(B_i + S_i)^{N_i} e^{-(B_i + S_i)}}{N_i!} \quad (5.8)$$

1097 where S_i is the sum of expected number of signal counts. B_i is the number of background counts
 1098 observed. N_i is the total number of counts.

1099 I also calculate an upper limit on $\langle\sigma v\rangle$ by calculating the 95% confidence level (CL). For the
 1100 CL, we define a parameter, TS_{95} , as

$$TS_{95} \equiv \sum_{\text{bins}} \left[2N \ln \left(1 + \frac{\epsilon S_{\text{ref}}}{B} \right) - 2\epsilon S_{\text{ref}} \right] \quad (5.9)$$

1101 where the expected signal counts from a dSph is scaled by ϵ . S_{ref} is the expected number of excess
 1102 counts in a bin from DM emission from a dSph with a corresponding annihilation cross-section,
 1103 $\langle\sigma v\rangle$. We scan ϵ such that

$$2.71 = TS_{\max} - TS_{95} \quad (5.10)$$

1104 HAWC's exclusive results are provided in Section 5.5.

1105 5.4.2 Glory Duck Joint Likelihood

1106 The joint likelihood for the 5-experiment combination was done similarly as Section 5.4.1. We
 1107 calculate upper limits on $\langle\sigma v\rangle$ from the TS, Eq. (5.7), and define the likelihood ratio more generally

$$\lambda(\langle\sigma v\rangle | \mathcal{D}_{\text{dSphs}}) = \frac{\mathcal{L}(\langle\sigma v\rangle; \hat{\nu} | \mathcal{D}_{\text{dSphs}})}{\mathcal{L}(\widehat{\langle\sigma v\rangle}; \hat{\nu} | \mathcal{D}_{\text{dSphs}})} \quad (5.11)$$

1108 $\mathcal{D}_{\text{dSphs}}$ is the totality of observations across experiments and dSphs. ν are the nuisance parameters
 1109 which are the J factors in this study. $\widehat{\langle\sigma v\rangle}$ and $\hat{\nu}$ are the respective estimate that maximize \mathcal{L}
 1110 globally. Finally, $\hat{\nu}$ is the set of nuisance parameters that maximize \mathcal{L} for a fixed value of $\langle\sigma v\rangle$.

1111 The *complete* joint likelihood, \mathcal{L} that encompasses all observations from all instruments and
 1112 dSphs can be factorized into *partial* functions for each dSph l (with $\mathcal{L}_{\text{dSph},l}$) and its J factor (\mathcal{J}_l):

$$\mathcal{L}(\langle\sigma v\rangle; \nu | \mathcal{D}_{\text{dSphs}}) = \prod_{l=1}^{N_{\text{dSphs}}} \mathcal{L}_{\text{dSph},l}(\langle\sigma v\rangle; J_l, \nu_l | \mathcal{D}_l) \times \mathcal{J}_l(J_l | J_{l,\text{obs}}, \sigma_{\log J_l}). \quad (5.12)$$

1113 For this study, $N_{\text{dSphs}} = 20$ is the number of dSphs studied. \mathcal{D}_l are the gamma-ray observations
 1114 of dSph, l . ν_l are the nuisance parameters modifying the gamma-ray observations of dSph, l ,
 1115 but excludes \mathcal{J}_l . \mathcal{J}_l is the J factor for dSph, l , as defined in Equation (5.2), and it is a nuisance
 1116 parameter whose value is unknown. $\log_{10} J_{l,\text{obs}}$ and $\sigma_{\log J_l}$ are obtained by fitting a log-normal
 1117 function of $J_{l,\text{obs}}$ to the posterior distribution of J_l [60]. $\log_{10} J_{l,\text{obs}}$ and $\sigma_{\log J_l}$ values are provided
 1118 in Table 5.1. The term \mathcal{J}_l constraining J_l is written as:

$$\mathcal{J}_l(J_l | J_{l,\text{obs}}, \sigma_{\log J_l}) = \frac{1}{\ln(10)J_{l,\text{obs}}\sqrt{2\pi}\sigma_{\log J_l}} \exp\left(-\frac{(\log_{10} J_l - \log_{10} J_{l,\text{obs}})^2}{2\sigma_{\log J_l}^2}\right). \quad (5.13)$$

1119 Both the \mathcal{GS} and \mathcal{B} , displayed in Table 5.1, sets of J factors are used in this analysis. Equation (5.13)
 1120 is also normalized, so it can also be interpreted as a probability density function (PDF) for $J_{l,\text{obs}}$.
 1121 From Equation (5.1), we can also see that $\langle\sigma v\rangle$ and J_l are degenerate when computing $\mathcal{L}_{\text{dSph},l}$.
 1122 Therefore, as noted in [61], it is sufficient to compute $\mathcal{L}_{\text{dSph},l}$ versus $\langle\sigma v\rangle$ for a fixed value of J_l .
 1123 We used $J_{l,\text{obs}}(\mathcal{GS})$ reported in Tab. 5.1, in order to perform the profile of \mathcal{L} with respect to J_l .
 1124 The degeneracy implies that for any $J'_l \neq J_{l,\text{obs}}$ (in practice in our case we used $J'_l = J_{l,\text{obs}}(\mathcal{B})$ to
 1125 compute results from a different set of J factors):

$$\mathcal{L}_{\text{dSph},l}(\langle\sigma v\rangle; J'_l, \nu_l | \mathcal{D}_l) = \mathcal{L}_{\text{dSph},l}\left(\frac{J'_l}{J_{l,\text{obs}}} \langle\sigma v\rangle; J_{l,\text{obs}}, \nu_l | \mathcal{D}_l\right), \quad (5.14)$$

1126 which is a straightforward rescaling operation that reduces the computational needs of the profiling
 1127 operation since:

$$\mathcal{L}(\langle\sigma v\rangle; \hat{\nu} | \mathcal{D}_{\text{dSphs}}) = \prod_{l=1}^{N_{\text{dSphs}}} \max_{J_l} \left[\mathcal{L}_{\text{dSph},l}(\langle\sigma v\rangle; J_l, \hat{\nu}_l | \mathcal{D}_l) \times \mathcal{J}_l(J_l | J_{l,\text{obs}}, \sigma_{\log J_l}) \right]. \quad (5.15)$$

1128 In addition, Eq. (5.14) enables the combination of data from different gamma-ray instruments and
 1129 observed dSphs via tabulated values of $\mathcal{L}_{\text{dSph},l}$, or equivalently of λ from Eq. (5.11) as was done in
 1130 this work, versus $\langle\sigma v\rangle$. $\mathcal{L}_{\text{dSph},l}$ is computed for a fixed value of J_l and profiled with respect to all
 1131 instrumental nuisance parameters ν_l , these nuisance parameters are discussed in more detail below.
 1132 These values are produced by each detector independently and therefore there is no need to share
 1133 sensitive low-level information used to produce them, such as event lists. Figure 5.4 illustrates the
 1134 multi-instrument combination technique used in this study with a comparison of the upper limit

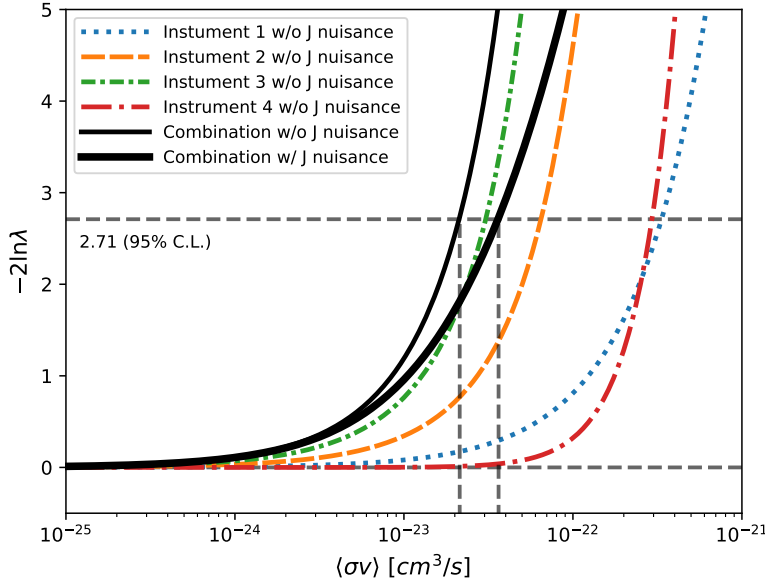


Figure 5.4 Illustration of the combination technique showing a comparison between $-2 \ln \lambda$ provided by four instruments (colored lines) from the observation of the same dSph without any J nuisance and their sum, *i.e.* the resulting combined likelihood (thin black line). According to the test statistics of Equation (5.7), the intersection of the likelihood profiles with the line $-2 \ln \lambda = 2.71$ indicates the 95% C.L. upper limit on $\langle\sigma v\rangle$. The combined likelihood (thin black line) shows a smaller value of upper limit on $\langle\sigma v\rangle$ than those derived by individual instruments. We also show how the uncertainties on the J factor effects the combined likelihood and degrade the upper limit on $\langle\sigma v\rangle$ (thick black line). All likelihood profiles are normalized so that the global minimum $\widehat{\langle\sigma v\rangle}$ is 0. We note that each profile depends on the observational conditions in which a target object was observed. The sensitivity of a given instrument can be degraded and the upper limits less constraining if the observations are performed in non-optimal conditions such as a high zenith angle or a short exposure time.

1135 on $\langle\sigma v\rangle$ obtained from the combination of the observations of four experiments towards one dSph
 1136 versus the upper limit from individual instruments. It also shows graphically the effect of the
 1137 J -factor uncertainty on the combined observations.

1138 The *partial* joint likelihood function for gamma-ray observations of each dSph ($\mathcal{L}_{\text{dSph},l}$) is
 1139 written as the product of the likelihood terms describing the $N_{\text{exp},l}$ observations performed with
 1140 any of our observatories:

$$\mathcal{L}_{\text{dSph},l} (\langle\sigma v\rangle; J_l, \nu_l | \mathcal{D}_l) = \prod_{k=1}^{N_{\text{exp},l}} \mathcal{L}_{lk} (\langle\sigma v\rangle; J_l, \nu_{lk} | \mathcal{D}_{lk}), \quad (5.16)$$

1141 where each \mathcal{L}_{lk} term refers to an observation of the l -th dSph with associated k -th instrument

1142 responses. $N_{\text{exp},l}$ varies from dSph to dSph and can be inferred from Table 5.2.

1143 Each collaboration separately analyzes their data for \mathcal{D}_{lk} corresponding to dSph l and gamma-
1144 ray detector k , using as many common assumptions as possible in the analysis. HAWC's treatment
1145 was described earlier in Section 5.4.1 whereas the specifics of the remaining experiments is left to
1146 the publication. We compute the values for the likelihood functions \mathcal{L}_{lk} (see Eq. (5.16)) for a fixed
1147 value of J_l and profile over the rest of the nuisance parameters ν_{lk} . Then, values of λ from Eq. (5.11)
1148 are computed as a function of $\langle\sigma v\rangle$, and shared using a common format. Results are computed for
1149 seven annihilation channels, W^+W^- , ZZ , $b\bar{b}$, $t\bar{t}$, e^+e^- , $\mu^+\mu^-$, and $\tau^+\tau^-$ over 62 m_χ values between
1150 5 GeV and 100 TeV provided in [54]. The $\langle\sigma v\rangle$ range is defined between 10^{-28} and $10^{-18}\text{cm}^3 \cdot \text{s}^{-1}$,
1151 with 1001 logarithmically spaced values. The likelihood combination, i.e. Equation (5.12), and
1152 profile over the J -factor to compute the profile likelihood ratio λ , Equation (5.11), are carried out
1153 with two different public analysis software packages, namely `gLike` [62] and `LklCom` [63], that
1154 provide the same results [64].

1155 As mentioned previously, each experiment computes the \mathcal{L}_{lk} from Equation (5.11) differently.
1156 The remainder of this section highlights the differences in this calculation across the experiments.
1157 Four experiments, namely *Fermi*-LAT, H.E.S.S., HAWC and MAGIC, use a binned likelihood to
1158 compute the \mathcal{L}_{lk} . For these experiments, for each observation \mathcal{D}_{lk} of a given dSph l carried out
1159 using a given gamma-ray detector k , the binned likelihood function is:

$$\mathcal{L}_{lk} (\langle\sigma v\rangle; J_l, \nu_{lk} | \mathcal{D}_{lk}) = \prod_{i=1}^{N_E} \prod_{j=1}^{N_P} \left[\mathcal{P}(s_{lk,ij}(\langle\sigma v\rangle, J_l, \nu_{lk}) + b_{lk,ij}(\nu_{lk}) | N_{lk,ij}) \right] \times \mathcal{L}_{lk,\nu} (\nu_{lk} | \mathcal{D}_{\nu_{lk}}) \quad (5.17)$$

1160 where N_E and N_P are the number of considered bins in reconstructed energy and arrival direction,
1161 respectively; \mathcal{P} represents a Poisson PDF for the number of gamma-ray candidate events $N_{lk,ij}$
1162 observed in the i -th bin in energy and j -th bin in arrival direction, when the expected number is
1163 the sum of the expected mean number of signal events s_{ij} (produced by DM annihilation) and of
1164 background events b_{ij} ; $\mathcal{L}_{lk,\nu}$ is the likelihood term for the extra ν_{lk} nuisance parameters that vary
1165 from one instrument k to another. The expected counts for signal events s_{ij} for a given dSph l and

1166 detector k is given by:

$$s_{ij}(\langle\sigma\nu\rangle, J) = \int_{E'_{\min,i}}^{E'_{\max,i}} dE' \int_{P'_{\min,j}}^{P'_{\max,j}} d\Omega' \int_0^\infty dE \int_{\Delta\Omega_{tot}} d\Omega \int_0^{T_{\text{obs}}} dt \frac{d^2\Phi(\langle\sigma\nu\rangle, J)}{dEd\Omega} \text{IRF}(E', P' | E, P, t) \quad (5.18)$$

1167 where E' and E are the reconstructed and true energies, P' and P the reconstructed and true
1168 arrival directions; $E'_{\min,i}$, $P'_{\min,j}$, $E'_{\max,i}$, and $P'_{\max,j}$ are their lower and upper limits of the i -th
1169 energy bin and the j -th arrival direction bin; T_{obs} is the (dead-time corrected) total observation
1170 time; t is the time along the observations; $d^2\Phi/dEd\Omega$ is the DM flux in the source region (see
1171 Equation (5.1)); and $\text{IRF}(E', P' | E, P, t)$ is the IRF, which can be factorized as the product of the
1172 effective collection area of the detector $A_{\text{eff}}(E, P, t)$, the PDFs for the energy estimator $f_E(E' | E, t)$,
1173 and arrival direction $f_P(P' | E, P, t)$ estimators. Note that for Fermi-LAT, HAWC, MAGIC, and
1174 VERITAS the effect of the finite angular resolution is taken into account through the convolution
1175 of $d\Phi/dEd\Omega$ with f_P in Equation (5.18), whereas in the cases of H.E.S.S. f_P is approximated by a
1176 delta function. This approximation has been made in order to maintain compatibility of the result
1177 with what has been previously published. The difference introduced by this approximation is $< 5\%$
1178 for all considered dSphs. A more comprehensive review of the differences between the analyses of
1179 different instruments can be found in [36].

1180 5.5 HAWC Results

1181 13 of the 20 dSphs considered for the Glory Duck analysis are within HAWC's field of view.
1182 These dSph are analyzed for emission from DM annihilation according to the likelihood method
1183 described in Section 5.4. The 13 likelihood profiles are then stacked to synthesize a combined
1184 limit on the dark matter cross-section, $\langle\sigma\nu\rangle$. This combination is done for the 7 SM annihilation
1185 channels used in the Glory Duck analysis. Figure 5.5 shows the combined limit for all annihilation
1186 channels with HAWC only observations. We also perform 300 studies of Poisson trials on the
1187 background. These trials are used to produce HAWC sensitivities with $\pm 1\sigma$ and $\pm 2\sigma$ uncertainty
1188 bands which were shared with the other collaborators for combination. The results on fitting to
1189 HAWC's Poisson trials of the DM hypothesis is shown in Figure 5.7 for all the DM annihilation
1190 channels studied for Glory Duck.

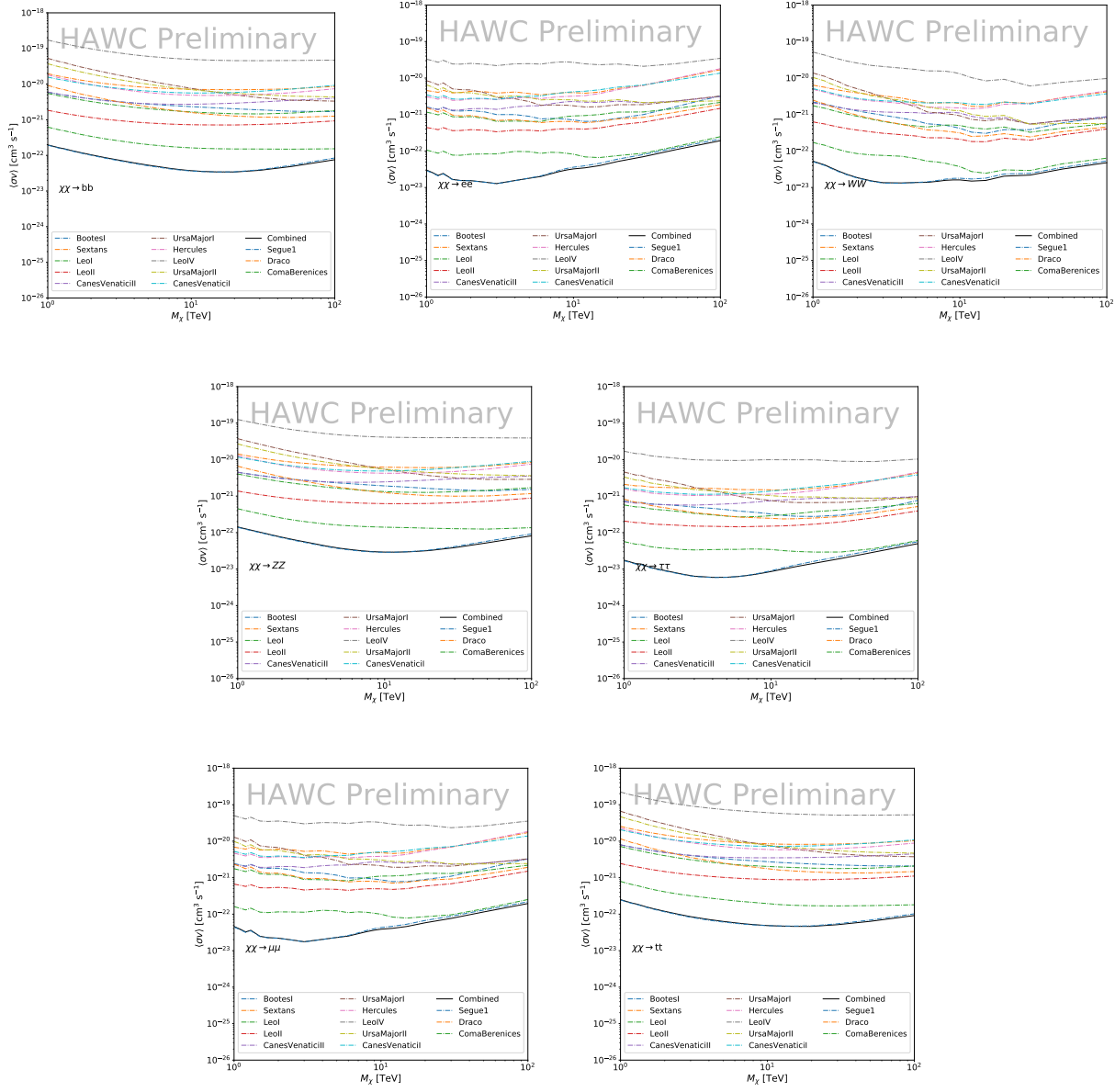


Figure 5.5

1191 No DM was found in HAWC observations. HAWC's limits are dominated by the dSphs Segue1
 1192 and Coma Berenices. The remaining 11 dSphs do not contribute significantly to the limit because
 1193 they are at high zenith and/or have much smaller J factors. Even though some remaining dSphs
 1194 have large J factors, they are towards the edge of HAWC's field of view where HAWC analysis is
 1195 less sensitive.

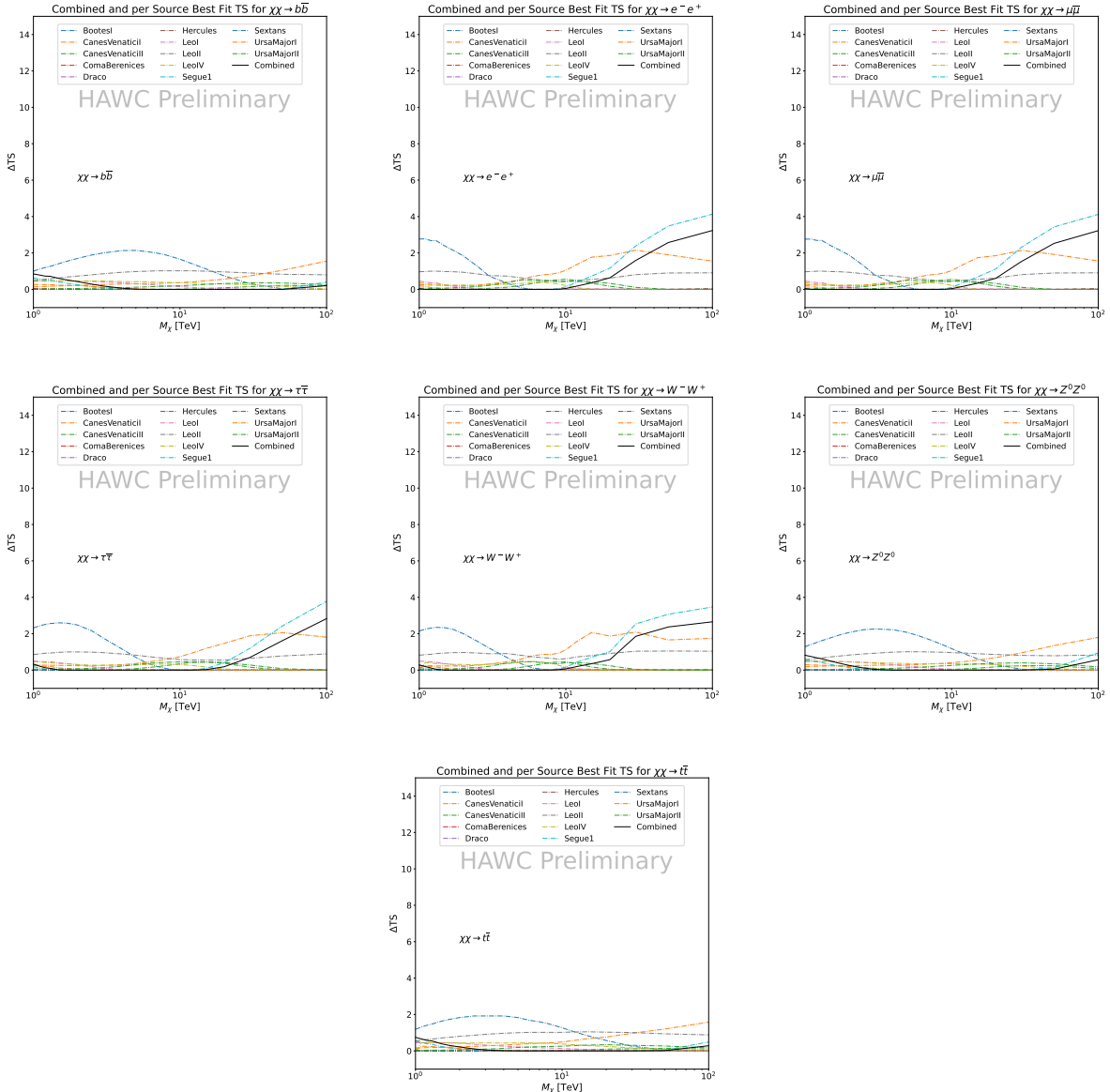


Figure 5.6 HAWC TS values for best fit $\langle\sigma v\rangle$ versus m_χ for seven SM annihilation channels with J factors from \mathcal{GS} . The solid black line shows the combined best fit TS values. The colored, dashed lines are the TS values for each of the 13 sources HAWC studied.

1196 5.6 Glory Duck Combined Results

1197 The crux of this analysis is that HAWC's results are combined with 4 other gamma-ray observa-
 1198 tories: Fermi-LAT, H.E.S.S., MAGIC, and VERITAS. No significant DM emission was observed
 1199 by any of the five instruments. We present the upper limits on $\langle\sigma v\rangle$ assuming seven independent
 1200 DM self annihilation channels, namely W^+W^- , Z^+Z^- , $b\bar{b}$, $t\bar{t}$, e^+e^- , $\mu^+\mu^-$, and $\tau^+\tau^-$. The 68%

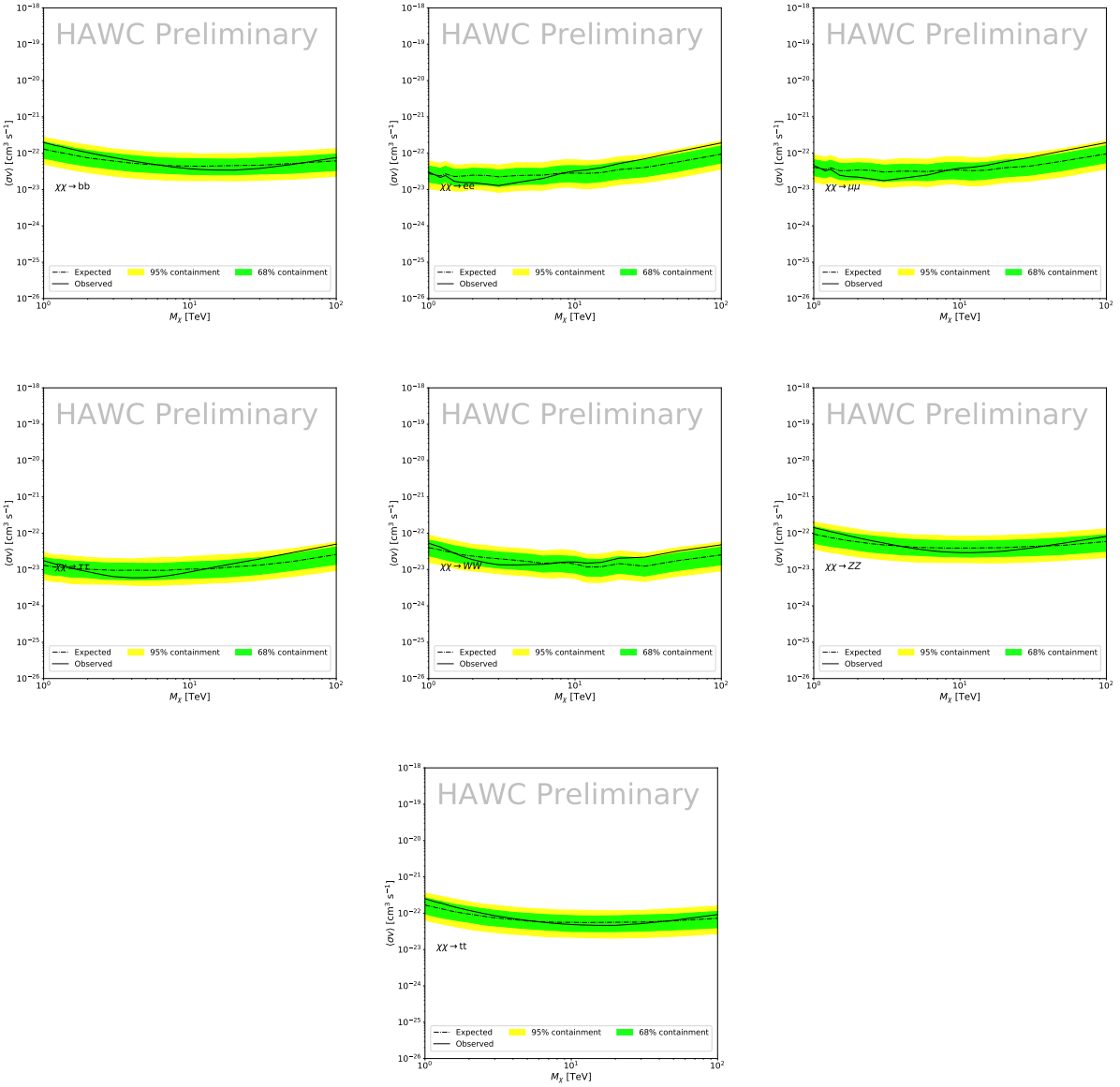


Figure 5.7 HAWC Brazil bands at 95% confidence level on $\langle\sigma v\rangle$ versus DM mass for seven annihilation channels with J -factors from GS [65]. The solid line represents the combined limit from 13 dSphs. The dashed line is the expected limit. The green band is the 68% containment. The yellow band is the 95% containment.

and 95% containment bands are produced from 300 Poisson realizations of the null hypothesis corresponding to each of the combined datasets. These 300 realizations are combined identically to dSph observations. The containment bands and the median are extracted from the distribution of resulting limits on the null hypothesis. These 300 realizations are obtained either by fast simulations of the OFF observations, for H.E.S.S., MAGIC, VERITAS, and HAWC, or taken from real

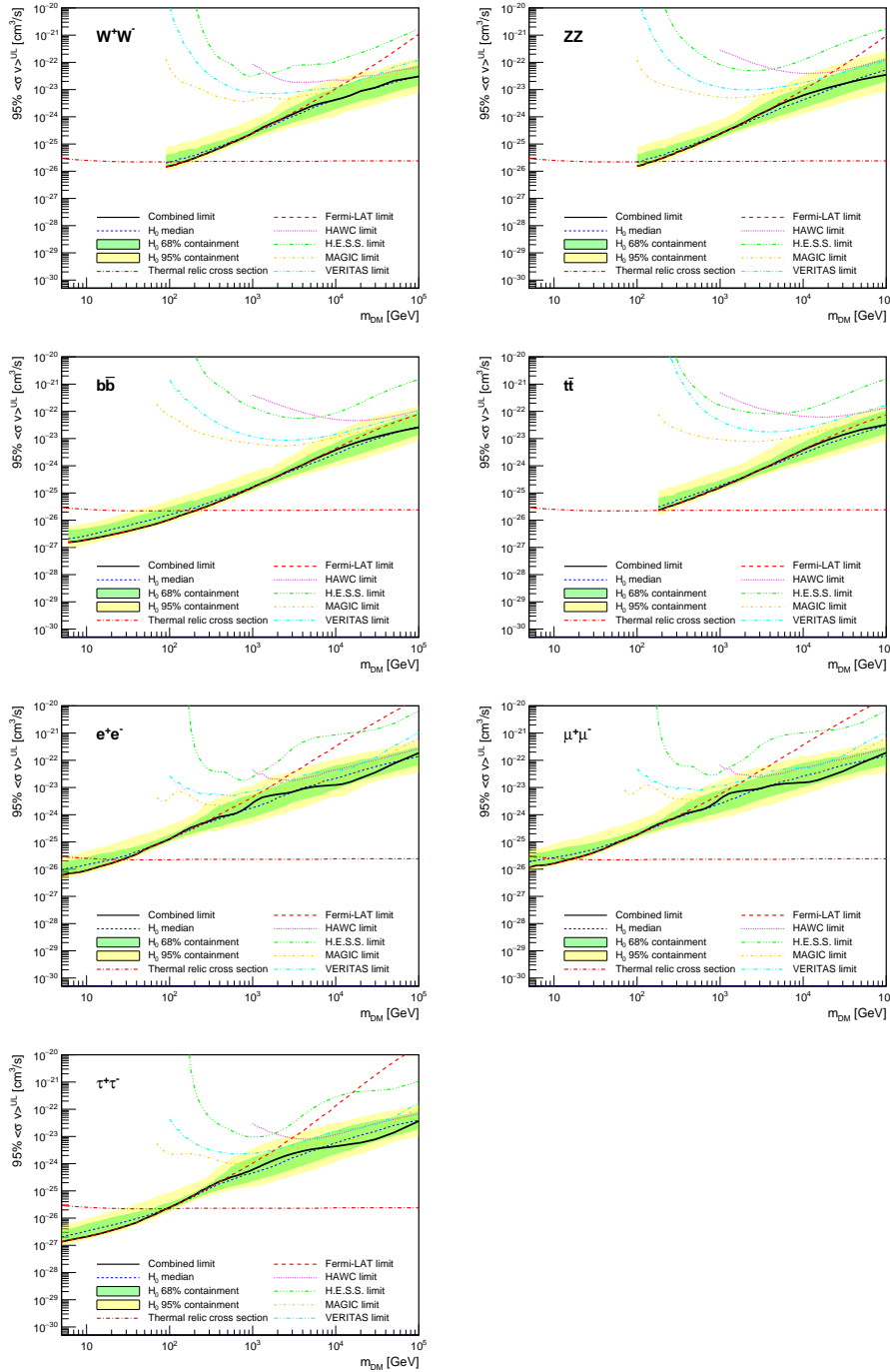


Figure 5.8 Upper limits at 95% confidence level on $\langle\sigma v\rangle$ in function of the DM mass for eight annihilation channels, using the set of J factors from Ref. [65] (\mathcal{GS} set in Table 5.1). The black solid line represents the observed combined limit, the black dashed line is the median of the null hypothesis corresponding to the expected limit, while the green and yellow bands show the 68% and 95% containment bands. Combined upper limits for each individual detector are also indicated as solid, colored lines. The value of the thermal relic cross-section in function of the DM mass is given as the red dotted-dashed line [66].

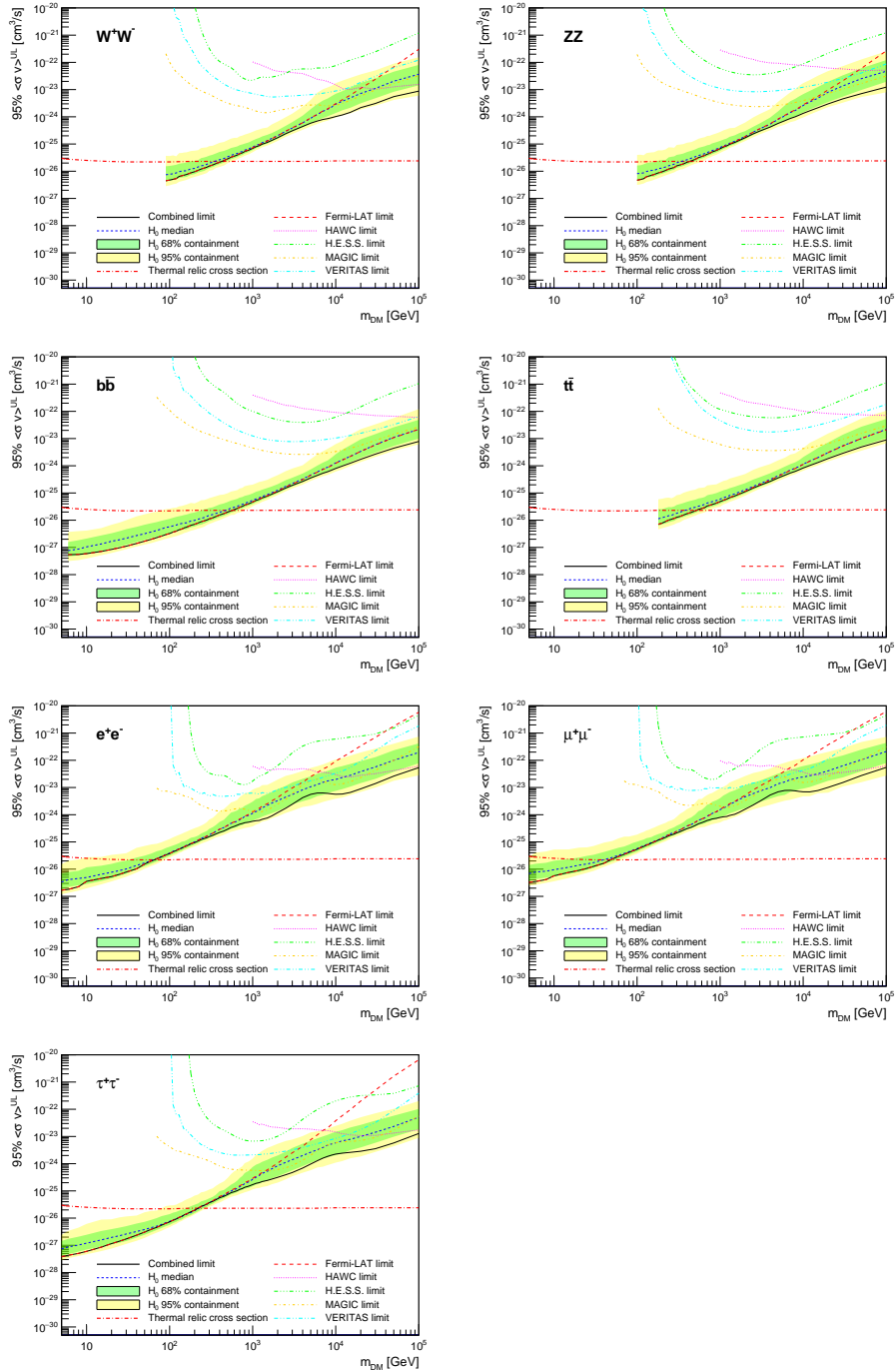


Figure 5.9 Same as Fig. 5.8, using the set of J factors from Ref. [59, 67] (\mathcal{B} set in Table 5.1).

1206 observations of empty fields of view in the case of Fermi-LAT [60, 68, 69].

1207 The obtained limits are shown in Figure 5.8 for the \mathcal{GS} set of J -factors [65] and in Figure 5.9
1208 for the \mathcal{B} set of J -factors [59, 67]. The combined limits are presented with their 68% and 95%
1209 containment bands, and are expected to be close to the median limit when no signal is present.

1210 We observe agreement with the null hypothesis for all channels, within 2σ standard deviations,
1211 between the observed limits and the expectations given by the median limits. Limits obtained from
1212 each detector are also indicated in the figures, where limits for all dSphs observed by the specific
1213 instrument have been combined.

1214 Below ~ 300 GeV, the *Fermi*-LAT dominates the DM limits for all annihilation channels. From
1215 ~ 300 GeV to ~ 2 TeV, *Fermi*-LAT continues to dominate for the hadronic and bosonic DM channels,
1216 yet the IACTs (H.E.S.S., MAGIC, and VERITAS) and *Fermi*-LAT all contribute to the limit for
1217 leptonic DM channels. For DM masses between ~ 2 TeV to ~ 10 TeV, the IACTs dominate leptonic
1218 DM annihilation channels, whereas both the *Fermi*-LAT and the IACTs dominate bosonic and
1219 hadronic DM annihilation channels. From ~ 10 TeV to ~ 100 TeV, both the IACTs and HAWC
1220 contribute significantly to the leptonic DM limit. For hadronic and bosonic DM, the IACTs and
1221 *Fermi*-LAT both contribute strongly.

1222 We notice that the limits computed using the \mathcal{B} set of J -factor are always better compared to the
1223 ones calculated with the \mathcal{GS} set. For the W^+W^- , Z^+Z^- , $b\bar{b}$, and $t\bar{t}$ channels, the ratio between the
1224 limits computed with the two sets of J -factor is varying between a factor of ~ 3 and ~ 5 depending
1225 on the energy, with the largest ratio around 10 TeV. For the channels e^+e^- , $\mu^+\mu^-$, and $\tau^+\tau^-$, the
1226 ratio lies between ~ 2 to ~ 6 , being maximum around 1 TeV. Examining Figure 5.16 and Figure 5.17
1227 in Section 5.8, these differences are explained by the fact that the \mathcal{B} set provides higher J -factors
1228 for the majority of the studied dSphs, with the notable exception of Segue I. The variation on the
1229 ratio of the limits for the two sets is due to different dSph dominating the limits depending on the
1230 energy. One set, \mathcal{B} , pushes the range of which thermal cross-section which can be excluded to
1231 higher mass. This comparison demonstrates the magnitude of systematic uncertainties associated
1232 with the choice of the J -factor calculation. The \mathcal{GS} and \mathcal{B} sets present a difference in the limits for
1233 all channels of about This difference is explained, see Figure 5.16 and Figure 5.17, by the fact that
1234 the \mathcal{B} set provides higher J -factors for all dSph except for Segue I.

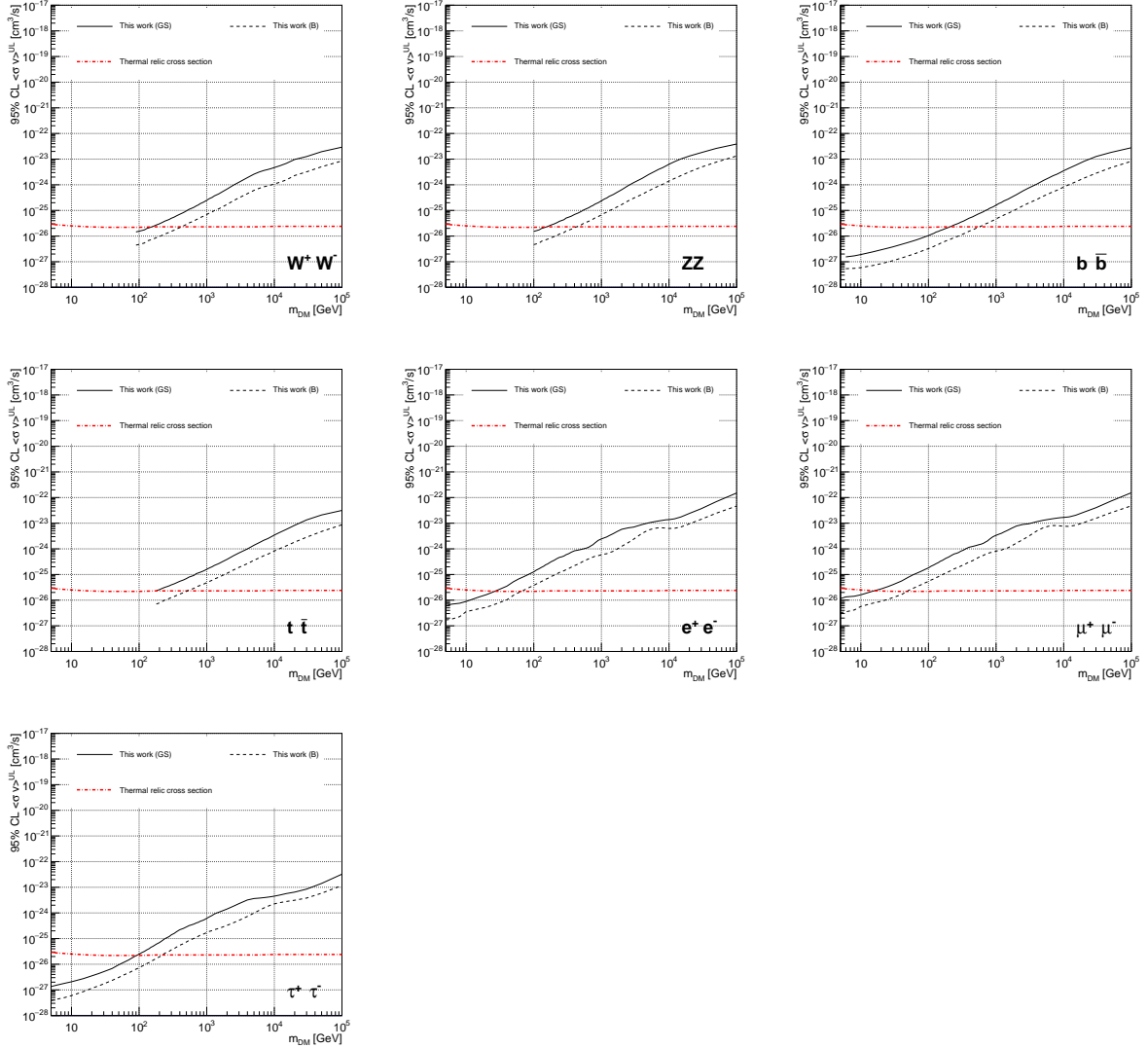


Figure 5.10 Comparisons of the combined limits at 95% confidence level for each of the eight annihilation channels when using the J factors from Ref. [65] (\mathcal{GS} set in Table 5.1), plain lines, and the J factor from Ref. [59, 67] (\mathcal{B} set in Table 5.1), dashed lines. The cross-section given by the thermal relic is also indicated [66].

1235 5.7 HAWC Systematics

1236 5.7.1 Inverse Compton Scattering

1237 The DM-DM annihilation channels produce many high energy electrons regardless of the
 1238 primary annihilation channel. These high energy electrons can produce high energy gamma-rays
 1239 through Inverse Compton Scattering (ICS). If this effect is strong, it would change the morphology
 1240 of the source and increase the total expected gamma-ray counts from any source. The PPPC [54]

1241 provides tools in Mathematica for calculating the impact of ICS for an arbitrary location in the
1242 sky for a specified annihilation channel. We calculated the change in gamma-ray counts for DM
1243 annihilation to primary $e\bar{e}$ for RA and Dec corresponding to Segue1 and Coma Berenices. These
1244 dSphs were chosen because they are the strongest contributors to the limit. $e\bar{e}$ was selected because
1245 it would have the largest number of high energy electrons. The effect was found to be on the order
1246 of 10^{-7} on the gamma-ray spectrum. As a result, this systematic is not considered in our analysis.

1247 **5.7.2 Point Source Versus Extended Source Limits**

1248 The previous DM search toward dSph approximated the dSphs as point sources [56]. In
1249 this analysis, the dSphs are implemented as extended with J-factor distributions following those
1250 produced by [65]. The resolution of the cited map is much finer than HAWC's angular resolution.
1251 The vast majority of the J-factor distribution is represented on the central HAWC pixel of the dSph
1252 spatial map. However, the neighboring 8 pixels are not negligible and contribute to our limit.

1253 Figure 5.11 shows a substantial improvement to the limit for Segue1. Fig. 5.12 however showed
1254 identical limits. These disparities are best explained by the relative difference in their J-Factors.
1255 Both dSphs pass almost overhead the HAWC detector, however Segue1 has the larger J-Factor
1256 between the two. Adjacent pixels to the central pixel will therefore contribute to the limits. This is
1257 the case for other dSph that are closer to the zenith of the HAWC detector.

1258 Comparison plots for all sources and the combined limit can be found in the sandbox for the
1259 Glory Duck project.

1260 **5.7.3 Impact of Pointing Systematic**

1261 During the analysis it was discovered that directional reconstruction of gamma-rays had a
1262 systematic bias at large zenith angles. Slides describing this systematic can be found [here](#). Shown
1263 on the presentation is dependence on the pointing systematic on declination. New spatial profiles
1264 were generated for every dSph and limits were computed for the adjusted declination.

1265 Section 5.7.3 demonstrates the impact of this systematic for all DM annihilation channels
1266 studied by HAWC. The impact is a tiny improvement, yet mostly identical, to the combined limits.

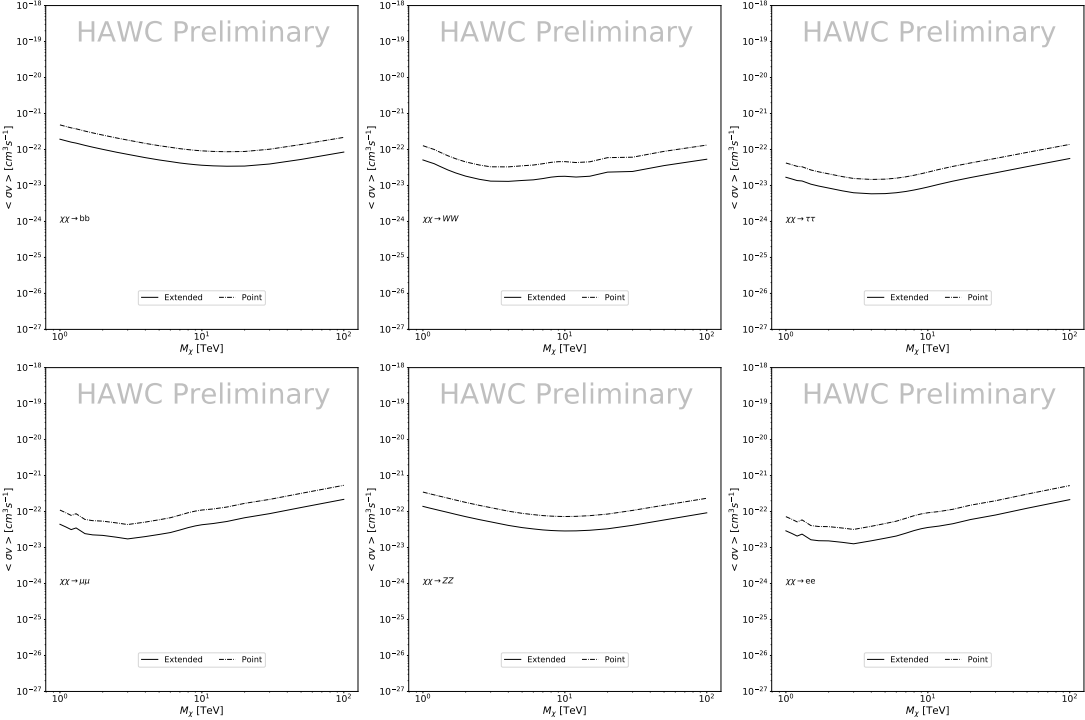


Figure 5.11 Comparisons of the combined limits at 95% confidence level for a point source analysis and extended source using [65] *GS* J-factor distributions and PPPC [54] annihilation spectra. Shown are the limits for Segue1 which will have the most significant impact on the combined limit. 6 of the 7 DM annihilation channels are shown. Solid lines are extended source studies. Dashed lines are point source studies. Overall, the extended source analysis improves the limit by a factor of 2.

1267 5.8 J-factor distributions

1268 5.8.1 Numerical integration of *GS* maps

1269 It was discovered well after the HAWC analysis was completed that the published tables from
 1270 *GS* [55] quoted median *J*-factors were computed in a non-trivial manner. The assumption myself
 1271 and collaborators had been that the published tables represented the *J*-factor as a function of θ for
 1272 the best global fit model on a per-source basis. However, this is not the case. Instead, what is
 1273 published are the best fit model for each dwarf that only considers stars up to the angular separation
 1274 θ . Therefore, the model is changing for each value of θ for each dwarf. Yet, the introduced features
 1275 from unique models at each θ are much smaller than the angular resolution of HAWC. It is not
 1276 expected for these effects to impact the limits and TS greatly as a result.

1277 Median *J*-factor model profiles were provided by the authors. New maps were generated

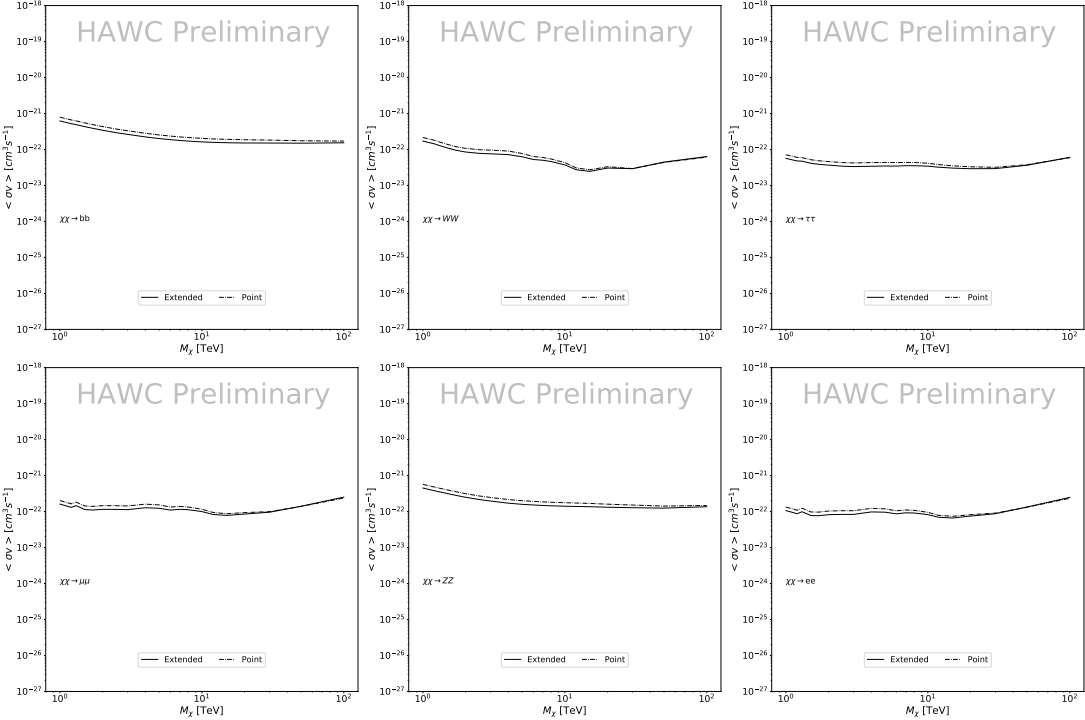


Figure 5.12 Same as Fig. 5.11 on Coma Berenices. This dSph also contributes significantly to the limit. The limits are identical in this case.

1278 and analyzed for Segue1 and Coma Berenices. Figure 5.14 shows the differential between maps
 1279 generated with the method from Section 5.8.1 and from the authors of [55]. These maps were
 1280 reanalyzed for all SM DM annihilation channels. Upper limits for these channels are shown in
 1281 Figure 5.15

1282 From Figure 5.15, we can see that the impact of these model difference was no substantial.
 1283 The observed impact was a fractional effect which is much smaller than the impact from selecting
 1284 another DM spatial distribution model as was shown in Figure 5.10.

1285 **5.8.2 \mathcal{GS} Versus \mathcal{B} spatial models**

1286 We show in this appendix a comparison between the J -factors computed by Geringer-Sameth
 1287 *et al.* [65] (the \mathcal{GS} set) and the ones computed by Bonnivard *et al.* [59, 67] (the \mathcal{B} set). The
 1288 \mathcal{GS} J -factors are computed through a Jeans analysis of the kinematic stellar data of the selected
 1289 dSphs, assuming a dynamic equilibrium and a spherical symmetry for the dSphs. They adopted
 1290 the generalized DM density distribution, known as Zhao-Hernquist, introduced by [57], carrying

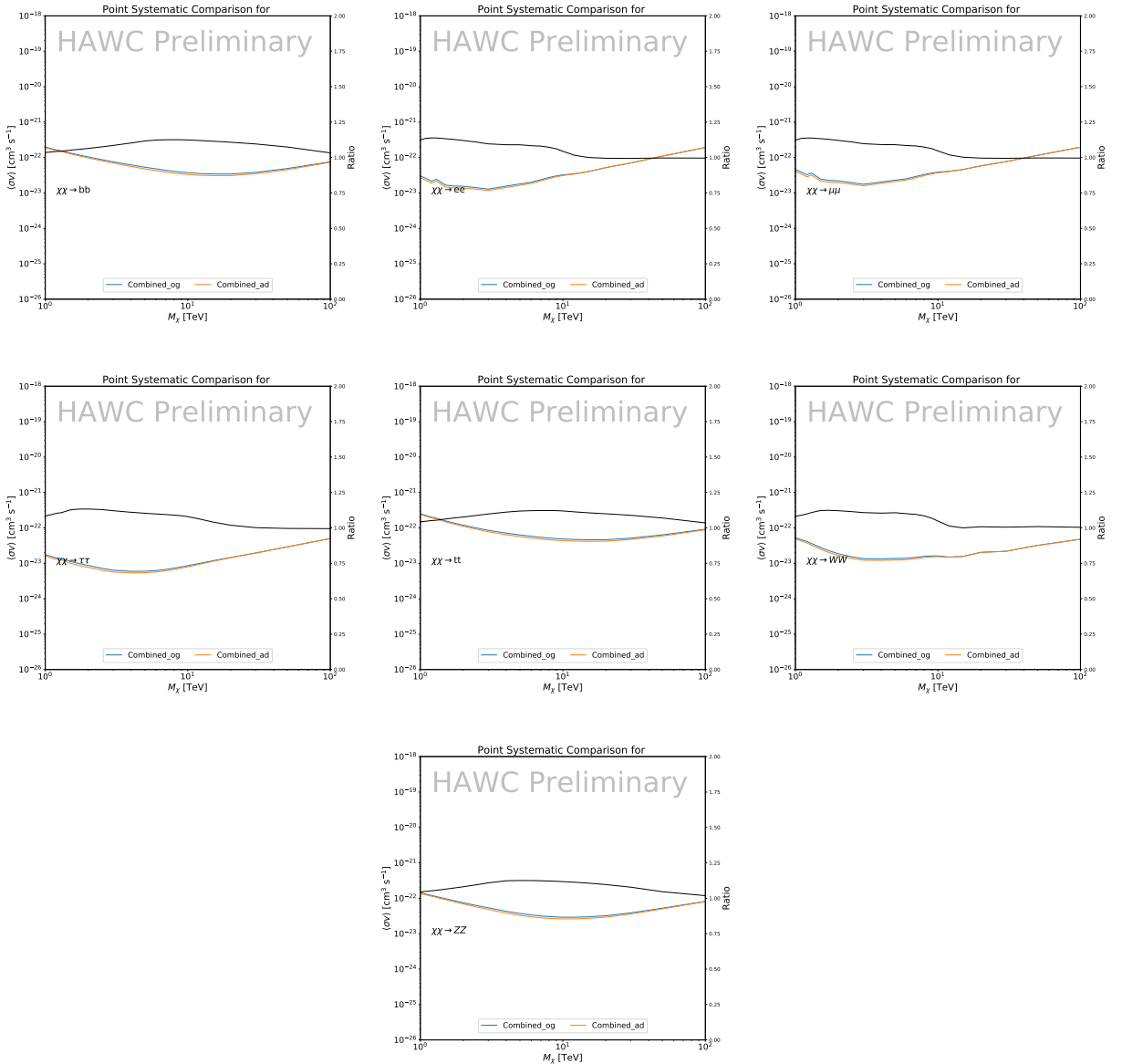


Figure 5.13 Comparison of combined limits when correcting for HAWC's pointing systematic. All DM annihilation channels are shown. The solid black line is the ratio between published limit to the declination corrected limit. The blue solid line or "Combined_og" represented the limits computed for Glory Duck. The solid orange line or "Combined_ad" represented the limits computed after correcting for the pointing systematic.

1291 three additional index parameters to describe the inner and outer slopes, and the break of the
 1292 density profile. Such a profile parametrization allows the reduction of the theoretical bias from
 1293 the choice of a specific radial dependency on the kinematic data. In other words, the increase of
 1294 free parameters with the use of the Zhao-Hernquist profile allows a better description of the mass

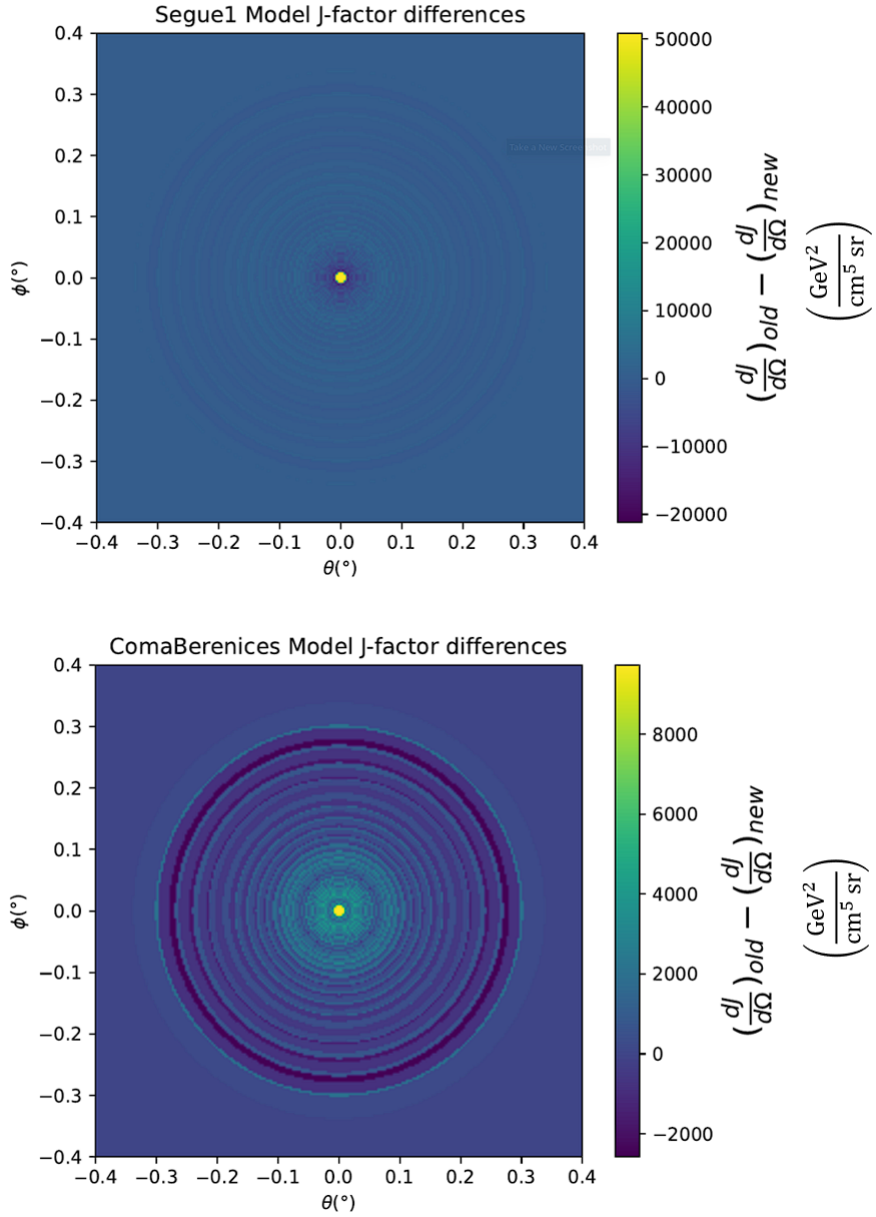


Figure 5.14 Differential map of dJ/Ω from model built in Section 5.8.1 and profiles provided directly from authors. (Top) Differential from Segue1. (bottom) Differential from Coma Berenices. Note that their scales are not the same. Segue1 shows the deepest discrepancies which is congruent with its large uncertainties. Both models show anuli where unique models become apparent.

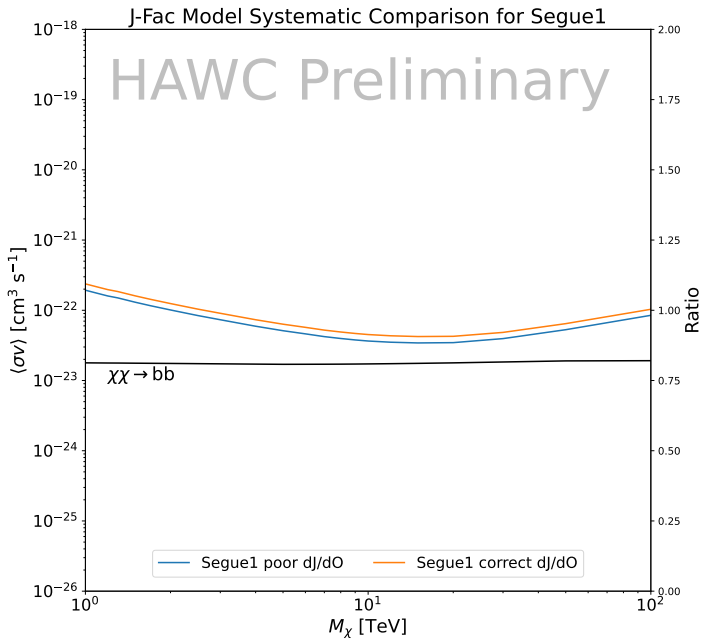
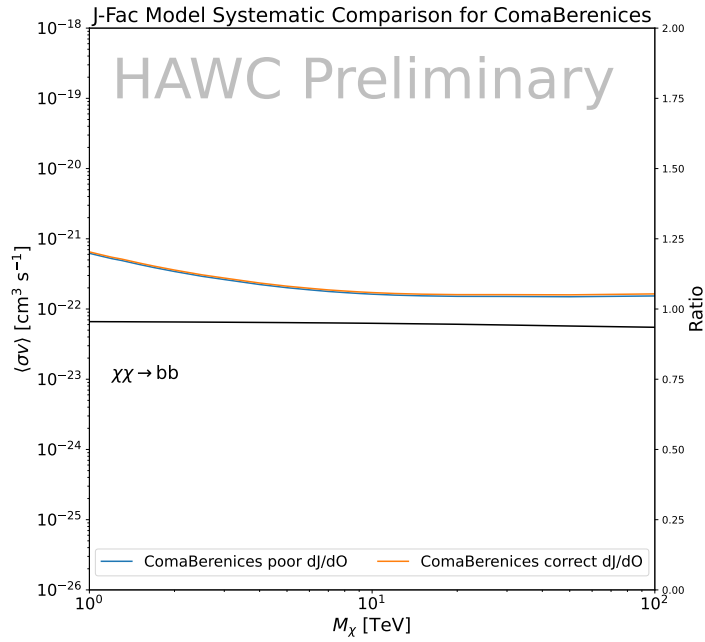


Figure 5.15 HAWC limits for Coma Berenices (top) and Segue1 (bottom) for two different map sets. Blue lines are limits calculated on maps with poor model representation. Orange lines are limits calculated on spatial profiles provided by the authors of [55]. Black line is the ratio of the poor spatial model limits to the corrected spatial models. The left y-axis measures $\langle \sigma v \rangle$ for the blue and orange lines. The right y-axis measures the ratio and is unitless.

1295 density distribution of dark matter.

1296 In addition, a constant velocity anisotropy profile and a Plummer light profile [70] for the stellar
1297 distribution were assumed. The velocity anisotropy profile depends on the radial and tangential
1298 velocity dispersion. However, its determination remains challenging since only the line-of-sight
1299 velocity dispersion can be derived from velocity measurements. Therefore, the parametrization of
1300 the anisotropy profile is obtained from simulated halos (see [71] for more details). They provide the
1301 values of the J -factors of regions extending to various angular radius up to the outermost member
1302 star.

1303 The \mathcal{B} J -factors were computed through a Jeans analysis taking into account the systematic
1304 uncertainties induced by the DM profile parametrization, the radial velocity anisotropy profile, and
1305 the triaxiality of the halo of the dwarf galaxies. They performed a more complete study of the dSph
1306 kinematics and dynamics than \mathcal{GS} for the determination of the J -factor. Conservative values of the
1307 J -factors where obtained using an Einasto DM density profile [72], a realistic anisotropy profile
1308 known as the Baes & Van Hese profile [73] which takes into account that the inner regions can be
1309 significantly non-isotropic, and a Zhao-Hernquist light profile [57].

1310 For both sets, J -factor values are provided for all dSphs as a function of the radius of the
1311 integration region [65, 59, 67]. Table 5.1 shows the heliocentric distance and Galactic coordinates
1312 of the twenty dSphs, together with the two sets of J -factor values integrated up to the outermost
1313 observed star for \mathcal{GS} and the tidal radius for \mathcal{B} . Both J -factor sets were derived through a Jeans
1314 analysis based on the same kinematic data, except for Draco where the measurements of [74] have
1315 been adopted in the computation of the \mathcal{B} value. The computations for producing the \mathcal{GS} and \mathcal{B}
1316 samples differ in the choice of the DM density, velocity anisotropy, and light profiles, for which the
1317 set \mathcal{B} takes into account some sources of systematic uncertainties.

1318 Figure 5.16 and Figure 5.17 show the comparisons for the J -factor versus the angular radius
1319 for each of the 20 dSphs used in this study. The uncertainties provided by the authors are also
1320 indicated in the figures. For the \mathcal{GS} set, the computation stops at the angular radius corresponding
1321 to the outermost observed star, while for the \mathcal{B} set, the computation stops at the angular radius

1322 corresponding to the tidal radius.

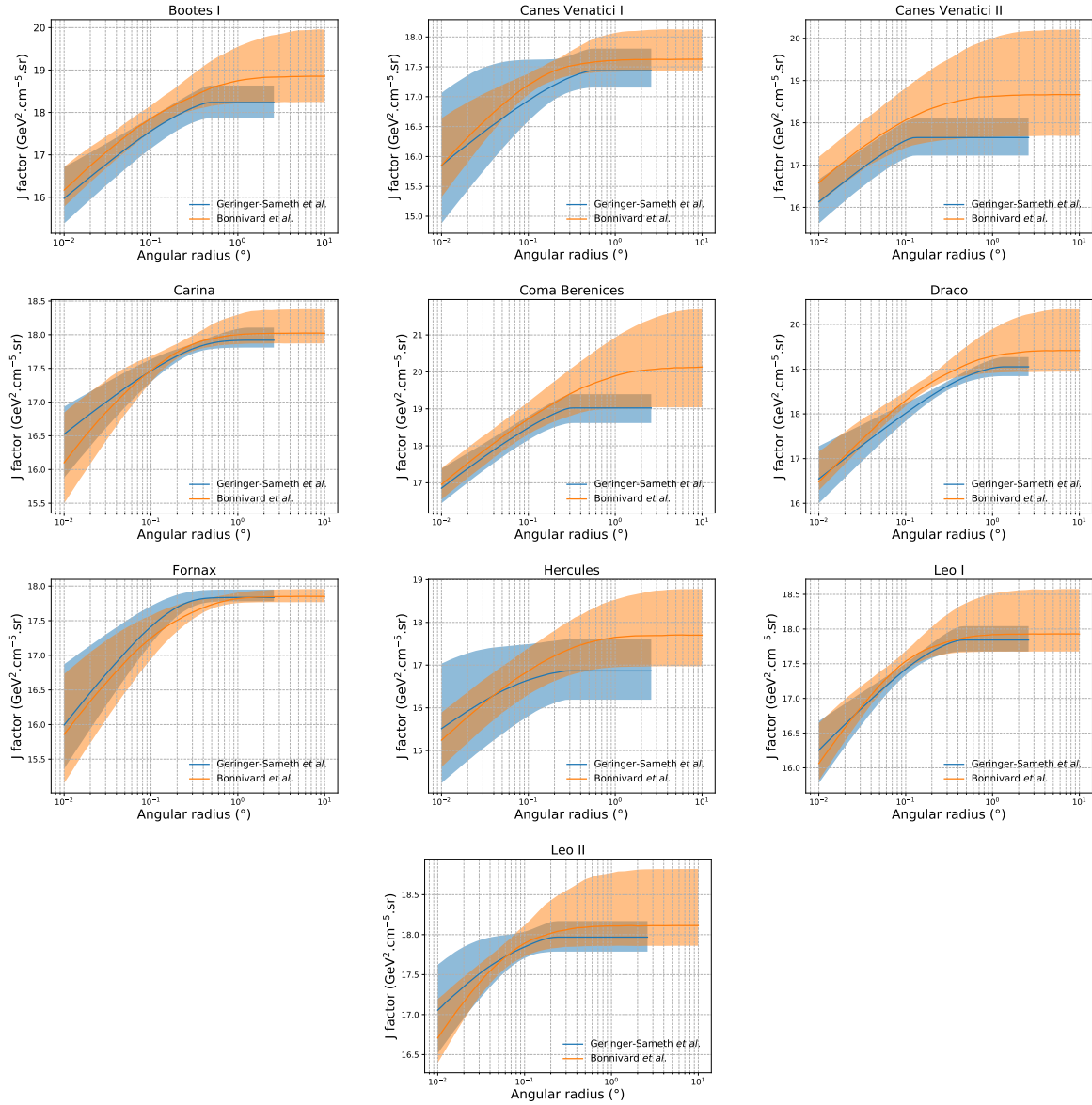


Figure 5.16 Comparisons between the J -factors versus the angular radius for the computation of J factors from Ref. [65] (\mathcal{GS} set in Table 5.1) in blue and for the computation from Ref. [59, 67] (\mathcal{B} set in Tab. 5.1) in orange. The solid lines represent the central value of the J -factors while the shaded regions correspond to the 1σ standard deviation.

1323 5.9 Discussion and Conclusions

1324 In this multi-instrument analysis, we have used observations of 20 dSphs from the gamma-ray
 1325 telescopes Fermi-LAT, H.E.S.S., MAGIC, VERITAS, and HAWC to perform a collective DM
 1326 search annihilation signals. The data were combined across sources and detectors to significantly

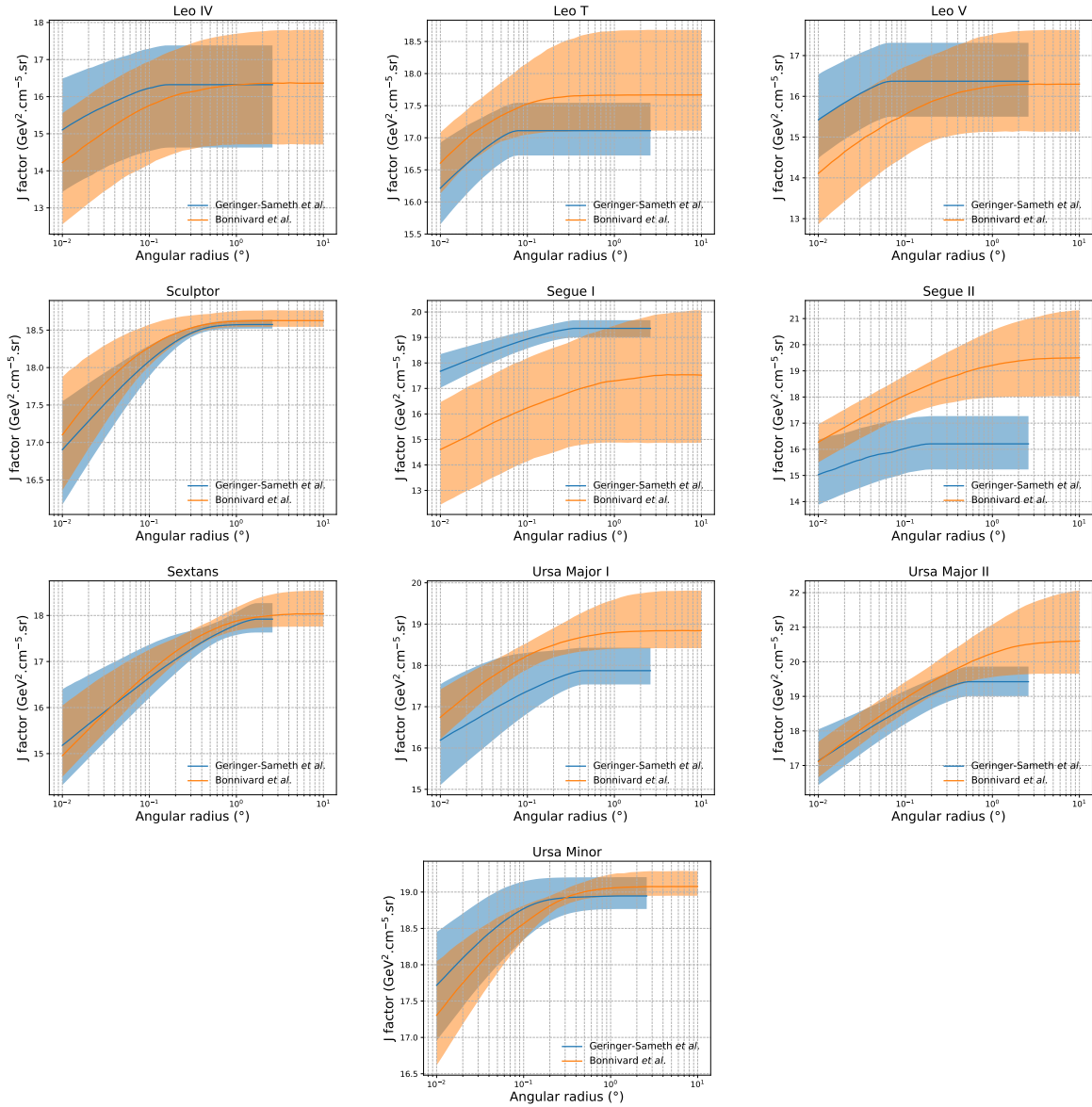


Figure 5.17 Comparisons between the J -factors versus the angular radius for the computation of J factors from Ref. [65] (\mathcal{GS} set in Tab. 5.1) in blue and for the computation from Ref. [59, 67] (\mathcal{B} set in Tab. 5.1) in orange. The solid lines represent the central value of the J -factors while the shaded regions correspond to the 1σ standard deviation.

increase the sensitivity of the search. We have observed no significant deviation from the null, no DM hypothesis, and so present our results in terms of upper limits on the annihilation cross-section for seven potential DM annihilation channels.

Fermi-LAT brings the most stringent constraints for continuum channels below approximately 1 TeV. The remaining detectors dominate at higher energies. Overall, for multi-TeV DM mass,

1332 the combined DM constraints from all five telescopes are 2-3 times stronger than any individual
1333 telescope for multi-TeV DM.

1334 Derived from observations of many dSphs, our results produce robust limits given the DM
1335 content of the dSphs is relatively well constrained. The obtained limits span the largest mass
1336 range of any WIMP DM search. Our combined analysis improves the sensitivity over previously
1337 published results from each detector which produces the most stringent limits on DM annihilation
1338 from dSphs. These results are based on deep exposures of the most promising known dSphs with
1339 the currently most sensitive gamma-ray instruments. Therefore, our results constitute a legacy of
1340 a generation of gamma-ray instruments on WIMP DM searches towards dSphs. Our results will
1341 remain the reference in the field until a new generation of more sensitive gamma-ray instruments
1342 begin operations, or until new dSphs with higher J -factors are discovered.

1343 This analysis serves as a proof of concept for future multi-instrument and multi-messenger
1344 combination analyses. With this collaborative effort, we have managed to sample over four orders
1345 in magnitude in gamma-ray energies with distinct observational techniques. Determining the nature
1346 of DM continues to be an elusive and difficult problem. Larger datasets with diverse measurement
1347 techniques could be essential to tackling the DM problem. A future collaboration using similar
1348 techniques as the ones described in this paper could grow even beyond gamma rays. The models we
1349 used for this study include annihilation channels with neutrinos in the final state. Advanced studies
1350 could aim to merge our results with those from neutrino observatories with large data sets. Efforts
1351 are already underway to add data from the IceCube, ANTARES, and KM3NeT observatories to
1352 these gamma-ray results.

1353 From this work, a selection of the best candidates for observations, according to the latest
1354 knowledge on stellar dynamics and modelling techniques for the derivation of the J -factors on
1355 the potential dSphs targets, is highly desirable at the time that new experiments are starting their
1356 dark matter programs using dSphs. Given the systematic uncertainty inherent to the derivation of
1357 the J -factors, an informed observational strategy would be to select both objects with the highest
1358 J -factors that could lead to DM signal detection, and objects with robust J -factor predictions, i.e.

1359 with kinematic measurements on many bright stars, which would strengthen the DM interpretation
1360 reliability of the observation outcome.

1361 This analysis combines data from multiple telescopes to produce strong constraints on astro-
1362 physical objects. From this perspective, these methods can be applied beyond just DM searches.
1363 Almost every astrophysical study can benefit from multi-telescope, multi-wavelength gamma-ray
1364 studies. We have enabled these telescopes to study the cosmos with greater precision and detail.
1365 Many astrophysical searches can benefit from multi-instrument gamma-ray studies, for which our
1366 analysis lays the foundation.

CHAPTER 6

1367 MULTITHREADING HAWC ANALYSES FOR DARK MATTER SEARCHES

1368 **6.1 Introduction**

1369 HAWC’s current software suite, plugins to 3ML and HAL [64, 34], do not fully utilize compu-
1370 tational advancements of recent decades. Said advancements include the proliferation of Graphical
1371 Processing Units (GPUs), and multithreading on multicore processors. The analysis described in
1372 chapter 5 took up to 3 months of wall time waiting for the full gambit of data analysis and simulation
1373 of background to compute. Additionally, with the updated 2D energy binning scheme, f_{hit} and
1374 Neural Network (NN), the time needed to compute expected to grow. Although excessive comput-
1375 ing time was, in part, from an intense use of a shared computing cluster, it was evident that there
1376 was room for improvement. In HAWC’s next generation dSph DM search, I decided to develop
1377 codes that would utilize the multicore processors on modern high performance computing clusters.
1378 The results of this work are featured in this chapter and brought a human timing improvement to
1379 computation that scales approximately as $1/N$ where N is the number of threads.

1380 **6.2 Dataset and Background**

1381 This section enumerates the data and background methods used for HAWC’s multithreaded
1382 study of dSphs. Section 6.2.1 and Section 6.2.2 are most useful for fellow HAWC collaborators
1383 looking to replicate a multithreaded dSph DM search.

1384 **6.2.1 Itemized HAWC files**

1385 These files are only available withing HAWC’s internal documentation and collaborators. They
1386 are not meant for public access, and are presented here so that HAWC collaborators can reproduce
1387 results accurately.

- 1388 • Detector Resolution: `refit-Pass5-Final-NN-detRes-zenith-dependent.root`
- 1389 • Data Map: `Pass5-Final-NN-maptree-ch103-ch1349-zenith-dependent.root`
- 1390 • Spectral Dictionary: `HDMspectra_dict_gamma.npy`

1391 **6.2.2 Software Tools and Development**

1392 This analysis was performed using HAL and 3ML [34, 53] in Python3. I built software
1393 in collaboration with Michael Martin and Letrell Harris to implement the *Dark Matter Spectra*
1394 *from the Electroweak to the Planck Scale* (HDM) [75] and dSphs spatial model from [76] for
1395 HAWC analysis. A NumPy dictionary of HDM, `HDMspectra_dict_gamma.npy`, was made for
1396 portability within the collaboration. These dictionaries were generated from the [git repository](#) [75].
1397 The analysis was performed using the Neural Network energy estimator for Pass 5.F. A description
1398 of this estimator was provided in chapter 3. [TODO: Define a subsection when it's written](#), and its
1399 key, relevant improvements are an improved energy estimation and improved sensitivities at higher
1400 zenith angles. All other software used for data analysis, DM profile generation, and job submission
1401 to SLURM are also kept in my sandbox in the [Dark Matter HAWC](#) project. The above repository
1402 also incorporates the model inputs used previously in Glory Duck, described in chapter 5, so Glory
1403 Duck remains compatible with modern software.

1404 **6.2.3 Data Set and Background Description**

1405 The HAWC data maps used for this analysis contain 2565 days of data between runs 2104 and
1406 7476. They were generated from pass 5.f reconstruction. The analysis is performed using the NN
1407 energy estimator with bin list:

1408 B1C0Ea, B1C0Eb, B1C0Ec, B1C0Ed, B1C0Ee, B2C0Ea, B2C0Eb, B2C0Ec, B2C0Ed, B2C0Ee,
1409 B3C0Ea, B3C0Eb, B3C0Ec, B3C0Ed, B3C0Ee, B3C0Ef, B4C0Eb, B4C0Ec, B4C0Ed, B4C0Ee,
1410 B4C0Ef, B5C0Ec, B5C0Ed, B5C0Ee, B5C0Ef, B5C0Eg, B6C0Ed, B6C0Ee, B6C0Ef, B6C0Eg,
1411 B6C0Eh, B7C0Ee, B7C0Ef, B7C0Eg, B7C0Eh, B7C0Ei, B8C0Ee, B8C0Ef, B8C0Eg, B8C0Eh,
1412 B8C0Ei, B8C0Ej, B9C0Ef, B9C0Eg, B9C0Eh, B9C0Ei, B9C0Ej, B10C0Eg, B10C0Eh,
1413 B10C0Ei, B10C0Ej, B10C0Ek, B10C0El

1414 Bin 0 was excluded as it has substantial hadronic contamination and poor angular resolution.

1415 Background considerations and source selection was identical to Section 5.2.3, and no additional
1416 arguments are provided here. Many of the HAWC systematics explored in Section 5.7 also apply

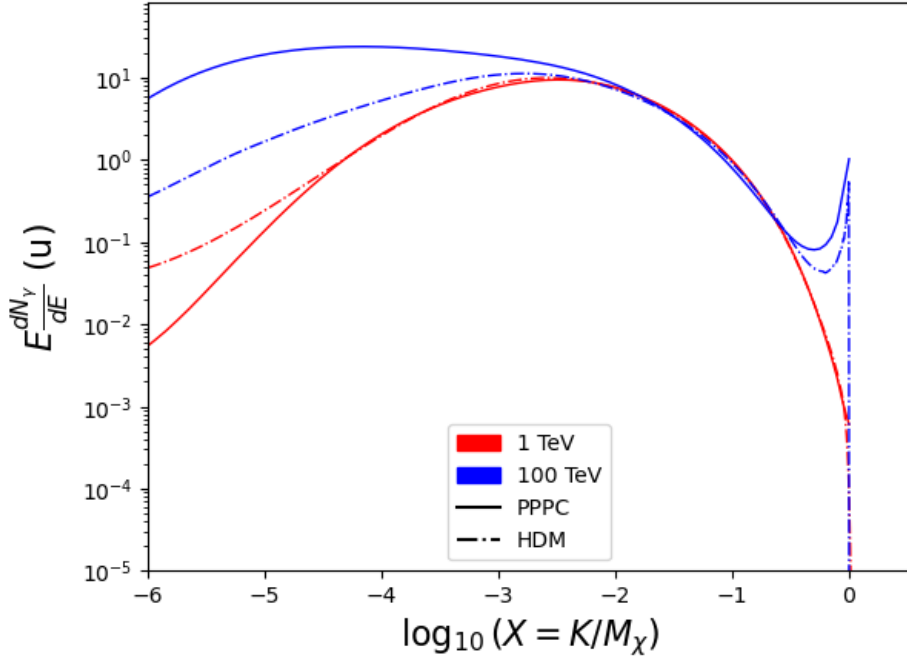


Figure 6.1 Spectral hypotheses from PPPC [54] and HDM [75] for DM annihilation: $\chi\chi \rightarrow W^-W^+$. Solid lines are spectral models with EW corrections from the PPPC. Dash-dot lines are spectral models from HDM. Red lines are models for $M_\chi = 1$ TeV. Blue lines represent models for $M_\chi = 100$ TeV.

1417 for this DM search and are not added upon here.

1418 6.3 Analysis

1419 The analysis and its systematics are almost identical to Section 5.3. Importantly, we use the
 1420 same **TODO: fix this ref** Equation (5.1) and Equation (5.2) for estimating the gamma-ray flux at
 1421 HAWC from our sources.

1422 6.3.1 $\frac{dN_\gamma}{dE_\gamma}$ - Particle Physics Component

1423 For these spectra, we import HDM with Electroweak (EW) corrections and additional correc-
 1424 tions for neutrinos above the EW scale [75]. The spectra are implemented as a model script in
 1425 astromodels for 3ML. A comprehensive description of EW corrections and neutrino considerations
 1426 are provided later in Sec. 8.

1427 Figure 6.1 demonstrates the impact of changes implemented in HDM on DM annihilation to W
 1428 bosons. A class in astromodels was developed to include HDM and is aptly named **HDMspectra**
 1429 within `DM_models.py`. The SM DM annihilation channels studied here are $\chi\chi \rightarrow$:

1430 e^+e^- , $\mu^+\mu^-$, $\tau^+\tau^-$, $b\bar{b}$, $t\bar{t}$, gg , W^+W^- , ZZ , $c\bar{c}$, $u\bar{u}$, $d\bar{d}$, $s\bar{s}$, $\nu_e\bar{\nu}_e$, $\nu_\mu\bar{\nu}_\mu$, $\nu_\tau\bar{\nu}_\tau$, $\gamma\gamma$, hh .

1431 For $\gamma\gamma$ and ZZ , a substantial fraction of the signal photons are expected to have $E_\gamma = m_\chi$ [75].
 1432 This introduces δ -function that is much narrower than the energy resolution of the HAWC detector.
 1433 To ensure that this feature is not lost in the likelihood fits, the 'line' feature is convolved with a
 1434 Gaussian kernel with a 1σ width of $0.05 \cdot m_\chi$ and total kernel window of $\pm 4\sigma$. This differs from
 1435 HAWC's previous line study where 30% of HAWC's energy resolution was used for the kernel [77].
 1436 The NN energy estimator's strength compared to f_{hit} at low gamma-ray energy enables narrower
 1437 kernels [75]. $\chi\chi \rightarrow \gamma\gamma$ and ZZ spectral hypotheses are shown in Figure 6.2. We did not explore
 1438 how well we reconstruct injected signal events for various kernels widths. This is a systematic
 1439 that should be tested before publication to journal. Spectral models for the remaining annihilation
 1440 channels are plotted for each m_χ in Figure B.1.

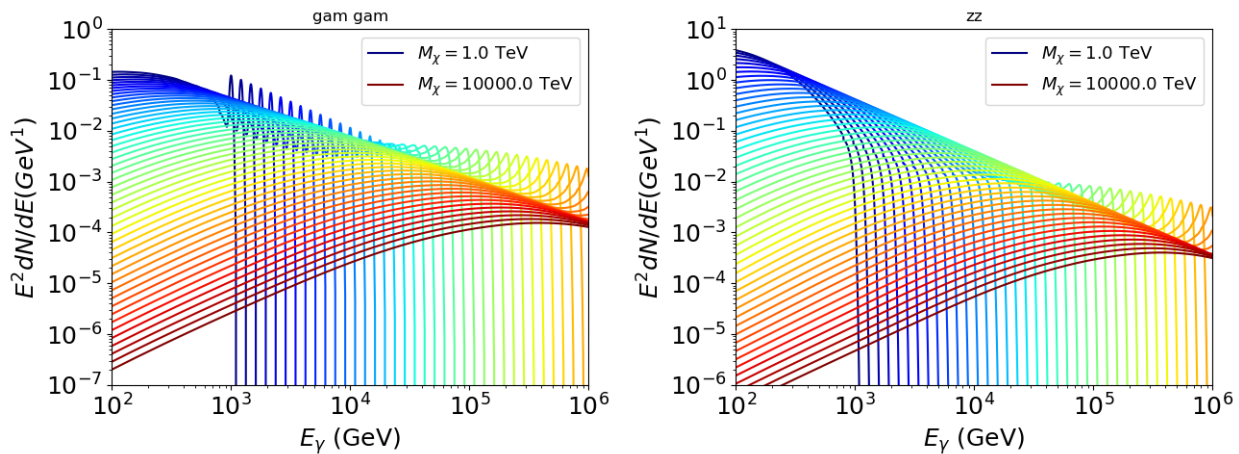


Figure 6.2 Photon spectra for $\chi\chi \rightarrow \gamma\gamma$ (left) and $\chi\chi \rightarrow ZZ$ (right) after Gaussian convolution of line features. Both spectra have δ -features at photon energies equal to the DM mass. Bluer lines are annihilation spectra with lower DM mass. Redder lines are spectra from larger DM mass. All spectral models are sourced from the Heavy Dark Matter models [75]. Axes are drawn roughly according to the energy sensitivity of HAWC.

1441 **6.3.2 J Astrophysical Components**

1442 The J-factor profiles for each source are imported from Louis Strigari et al. (referred to with
 1443 \mathcal{LS}) [76]. The \mathcal{LS} catalog fits a Navarro–Frenk–White (NFW) [58] spatial DM distributions to

1444 the dSphs which has a DM density of

$$\rho(r) = \frac{\rho_0}{\frac{r}{R_s} \left(1 + \frac{r}{R_s}\right)^2}. \quad (6.1)$$

1445 ρ_0 and the scale radius, R_s are free parameters fit for each dSph. r is the distance from the center

1446 of the dSph.

1447 Profiles in $\frac{dJ}{d\Omega}(\theta)$ up to an angular separation $\theta = 0.5^\circ$ were provided directly from the authors.

1448 Map generation from these profiles were almost identical to Section 5.3.2 except that a higher order

1449 trapezoidal integral was used for the normalization of the square, uniformly-spaced map:

$$p^2 \cdot \sum_{i=0}^N \sum_{j=0}^M w_{i,j} \frac{dJ}{d\Omega}(\theta_{i,j}, \phi_{i,j}) \quad (6.2)$$

1450 p is the angular side of one pixel in the map. $w_{i,j}$ is a weight assigned the following ways:

1451 $w_{i,j} = 1$ if $(\theta_{i,j}, \phi_{i,j})$ is fully within the region of integration

1452 $w_{i,j} = 1/2$ if $(\theta_{i,j}, \phi_{i,j})$ is on an edge of the region of integration

1453 $w_{i,j} = 1/4$ if $(\theta_{i,j}, \phi_{i,j})$ is on a corner of the region of integration

1454 Figure 6.3 shows the median and $\pm 1\sigma$ maps used as input for this DM annihilation study.

1455 6.3.3 Source Selection and Annihilation Channels

1456 HAWC's sources for this multithreaded analysis include Coma Berenices, Draco, Segue 1, and

1457 Sextans. \mathcal{LS} observed up to 43 sources in its publication, however only 4 of the best fit profiles

1458 were provided at the time this thesis was written. A full description of each source used in this

1459 analysis is found in Table 6.1.

1460 This analysis improves on chapter 5 in the following ways. Previously, the particle physics

1461 model used for gamma-ray spectra from DM annihilation was from the PPPC [54] which missed

1462 important considerations relevant for the neutrino sector. HDM is used to account for this shortfall

1463 [75]. HDM also models DM to the Planck scale which permits HAWC to probe PeV scale DM. For

1464 this study, we sample DM masses: 1 TeV - 10 PeV with 6 mass bins per decade in DM mass. In

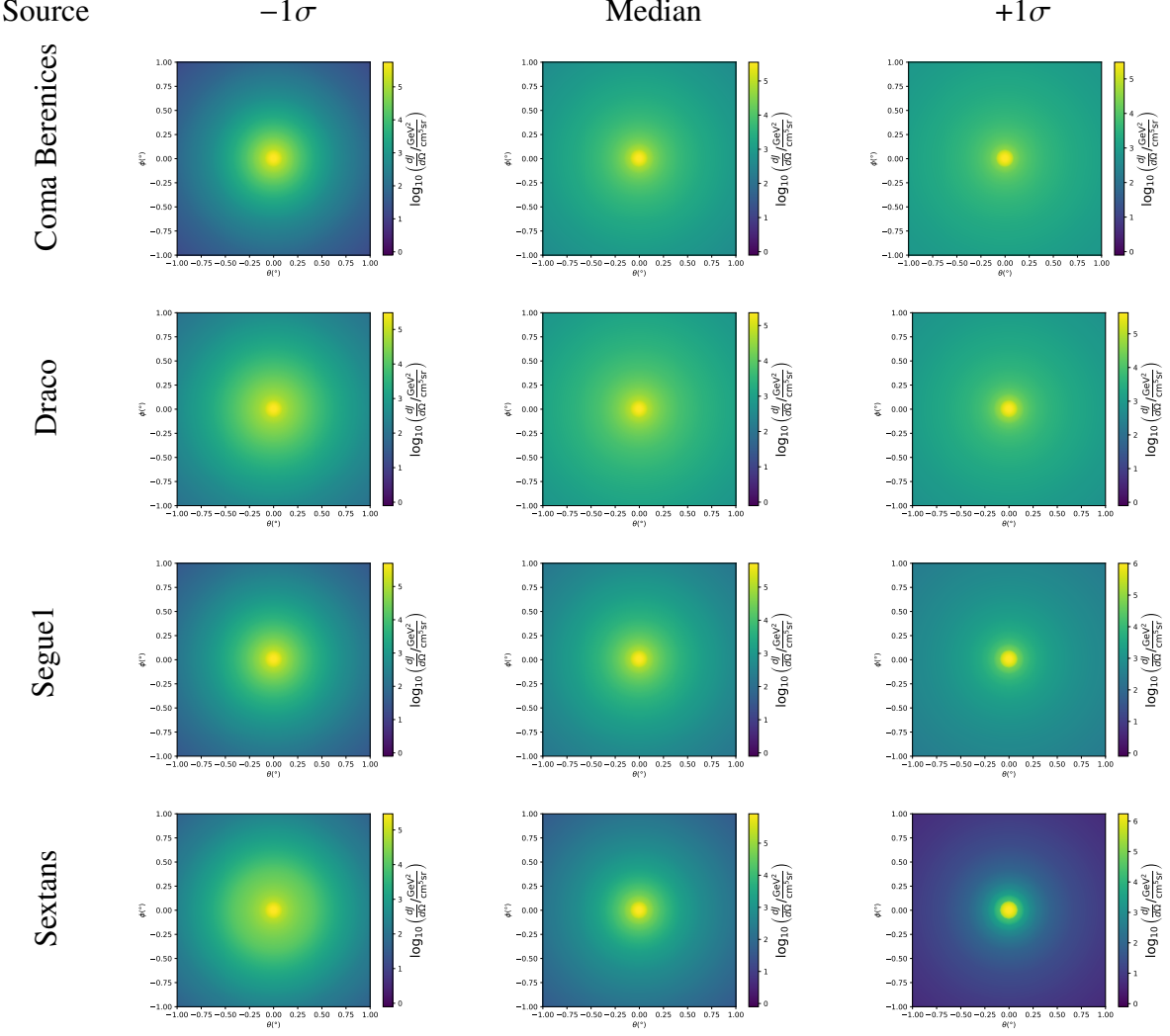


Figure 6.3 $\frac{dJ}{d\Omega}$ maps for Coma Berenices, Draco, Segue1, and Sextans. Columns are divided for the $\pm 1\sigma$ uncertainties in $dJ/d\Omega$ around the mean value from \mathcal{LS} [76]. Origin is centered on the specific dwarf spheroidal galaxies (dSph). θ and ϕ axes are the angular separation from the center of the dwarf. Profiles are truncated at 1° and flattened beyond.

1465 the case of line spectra ($\chi\chi \rightarrow \gamma\gamma$, or ZZ), we double the mass binning to 12 DM mass bins per
 1466 decade in DM mass.

1467 \mathcal{LS} provides 25 sources within HAWC's field of view. Additionally, NFW [58] DM distributions
 1468 have fewer parameters than Zhao [57], so \mathcal{LS} fits ultra-faint dwarves which expands the number of
 1469 sources. However, all sources were not provided by the authors in time for the completion of this
 1470 dissertation. Finally, the gamma-ray ray dataset is much larger. The study performed here analyzes
 1471 2565 days of data compared to 1017 days analyzed in chapter 5.

1472 **6.4 Likelihood Methods**

1473 These are identical to Section 5.4.1 and no additional changes are made to the likelihood. Bins
 1474 in this analysis are expanded to include HAWC’s NN energy estimator.

1475 **6.5 Computational Methods: Multithreading**

1476 Previously, as in Section 5.3, the likelihood was minimized for one model at a time. One model
 1477 in this case representing a DM annihilation channel (CHAN), DM mass (m_χ), and dSph ((SOURCE)).
 1478 In an effort to conserve human and CPU time, jobs submitted for high performance computing
 1479 contained a list of m_χ to iterate over for likelihood fitting. Jobs were then trivially parallelized
 1480 for each permutation of the two lists: CHANS and SOURCES. The lists for CHANS and SOURCES are
 1481 found in Section 6.3.1 and Table 6.1, respectively. Initially, 11 m_χ were serially sampled for one
 1482 job defined by a [CHAN, SOURCE] tuple. Computing the likelihoods would take between 1.5 to 2 hrs,
 1483 stochastically, for a job. We expect to compute likelihoods for data and 300 Poisson background
 1484 trials. The estimated CPU time based on the above for all CHAN (N = 17) and SOURCE (M = 25)
 1485 was estimated to 127,925 jobs. In total, 1,407,175 likelihood fits and profiles would be computed
 1486 for the 11 mass bins we wished to study. The estimated CPU time ranged between 8k CPU days
 1487 to 10k CPU days. Human time is more challenging to estimate as job allocation is stochastic and
 1488 highly dependent on what other users are submitting. Yet, it is unlikely that all jobs would run
 1489 simultaneously. Therefore, we can expect human time to be about as long as was seen in chapter 5

Name	Distance (kpc)	l, b ($^\circ$)	$\log_{10} J$ (\mathcal{LS} set) $\log_{10}(\text{GeV}^2 \text{cm}^{-5} \text{sr})$
Coma Berenices	44	241.89, 83.61	$19.00^{+0.36}_{-0.35}$
Draco	76	86.37, 34.72	$18.83^{+0.12}_{-0.12}$
Segue I	23	220.48, 50.43	$19.12^{+0.49}_{-0.58}$
Sextans	86	243.50, 42.27	$17.73^{+0.13}_{-0.12}$

Table 6.1 Summary of the relevant properties of the dSphs used in the present work. Column 1 lists the dSphs. Columns 2 and 3 present their heliocentric distance and galactic coordinates, respectively. Column 4 reports the J -factors of each source given from the \mathcal{LS} studies and estimated $\pm 1\sigma$ uncertainties. The values $\log_{10} J$ (\mathcal{LS} set) [76] correspond to the mean J -factor values for a source extension truncated at 0.5° .

1490 which was on the order of months to fully compute on a smaller analysis. A visual aid to describe
1491 how jobs were organized is provided in Figure 6.4.

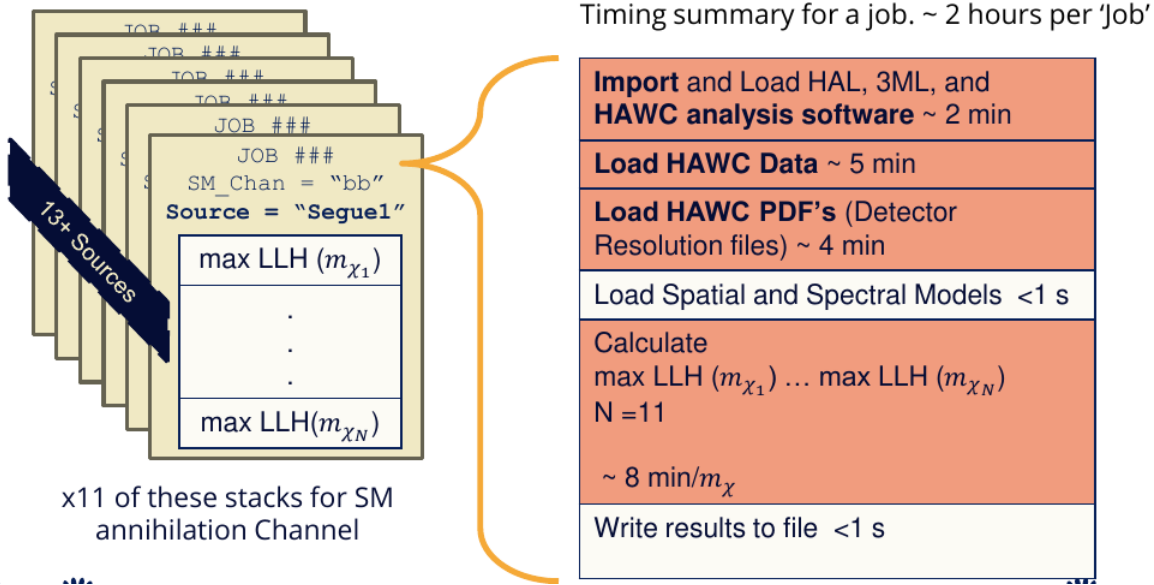


Figure 6.4 Infographic on how jobs and DM computation was organized in Section 5.3. Jobs were built for each permutation of CHANS and SOURCES shown by the left block in the figure. Each job, which took on the order 2 hrs to compute, had the following work flow: 1. Import HAWC analysis software, 2 min to run. 2. Load HAWC count maps, 5 min to run. 3. Load HAWC energy and spatial resolutions, 4 min. 5. Load DM spatial source templates and spectral models, less than 1 s. 6. Perform likelihood fit on data and model, about 8 min per DM mass. 7. Write results to file, less than 1s.

1492 The computational needs for this next generation DM analysis are extreme and is unlike other
1493 analyses performed on HAWC. It became clear that there was a lot to gain from optimizing how
1494 the likelihoods are computed. This section discusses how multi-threading was applied to solve and
1495 reduce HAWC's computing of likelihoods for large parameter spaces like in DM searches.

1496 6.5.1 Relevant Foundational Information

1497 The profiling of the likelihood for HAWC is done via gradient descent where the normalization
1498 of Equation (5.1) (linearly correlated with $\langle \sigma v \rangle$) is rescaled in the descent. Additionally, we sample
1499 the likelihood space for a defined list of $\langle \sigma v \rangle$'s described in Section 5.4.2. The time to compute
1500 these values is not predictable or consistent because many variables can change across the full
1501 model-space. Comprehensively, these variables are:

1502 • m_χ : DM rest mass
 1503 • CHAN : DM annihilation channel in SM.
 1504 • SOURCE : dSph. Involves a spatial template AND coordinate in HAWC data.
 1505 • $\langle\sigma v\rangle$: Effectively the flux normalization and free parameter in the likelihood fit.
 1506 Therefore, we develop an asynchronous, functional-parallel coding pattern. Asynchronous meaning
 1507 the instructions within a function are independent and permitted to be out of sync with sibling
 1508 computations. Functional-parallel meaning that instructions are the subject of parallelization
 1509 rather than threading the likelihood computation. This is close to trivial parallelization seen in
 1510 Figure 6.4 except that we seek to consolidate the loading stages (software, data, and detector
 1511 resolution loading). Multiple asynchronous threads are expected to reduce total serial processing
 1512 time and total overhead across the entire project in addition to saving human time.

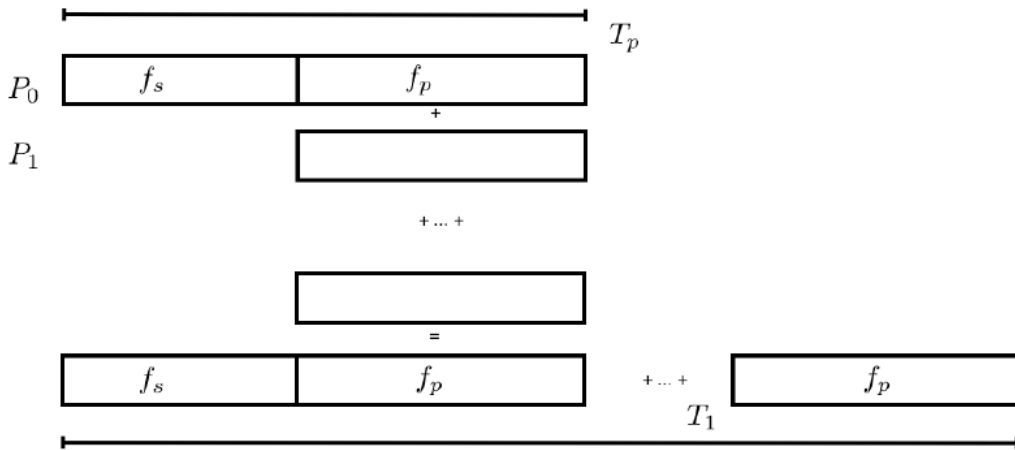


Figure 6.5 Graphic of Gustafson parallel coding pattern. f_s is the fraction of a program, in time, spent on serial computation. f_p is the fraction of computing time that is parallelizable. T_p is the total time for a parallel program to run. T_1 is the total time for a parallel program to run if only 1 processor is allocated. P_N is the N -th processor where its row is the computation the processor performs. The Gustafson pattern is most similar to what is implemented for this analysis. Figure is pulled from [78].

1513 We need a way to measure and compare the expected speedup and efficiency gain for this
 1514 asynchronous coding pattern. I pull inspiration for timing measurement from [78] and use *Amdahl's*

1515 law with hybrid programming. Hybrid programming meaning that the computation is a mix of
 1516 distributed and shared memory programming. If we assume the code is fully parallelizable over p
 1517 processors and c threads, the ideal speedup is simply pc , and ideal run-time is $T_1/(pc)$. T_1 is the
 1518 total time for a parallel program to run if only 1 processor is allocated. However, the coding pattern
 1519 contains some amount of unavoidable serial computation, as shown in Figure 6.5. In our case, the
 1520 run time, $T_{p,c}$, is estimated to be

$$T_{p,c} = \frac{T_1}{pc} (1 + F_s(c - 1)). \quad (6.3)$$

1521 F_s is the fraction of CPU time dedicated to serial computation. The expected speedup, $S_{p,c}$, is

$$S_{p,c} \equiv \frac{T_1}{T_{p,c}} = \frac{pc}{1 + F_s(c - 1)}. \quad (6.4)$$

1522 From Equation (6.4), we can see that the speed-up scales with p/F_s . We are free to minimize F_s
 1523 asymptotically by enlarging the total models that are submitted to the thread pool, thereby shrinking
 1524 the CPU fraction dedicated to serial operation. We are also free to define exactly how many threads
 1525 and processors we utilize, yet eventually hit a hard cap at the hardware available on our computing
 1526 cluster. HAWC uses Intel Xeon™processors with 48 cores and 96 threads. We see that a successful
 1527 code will scale well as the expected speedup is inversely correlated with F_s . As the total number
 1528 of models sampled grows, the speedup will also.

1529 6.5.2 Implementation

1530 The multithreaded code was written in Python3 and is documented in the `dark_matter_hawc`
 1531 [repository](#) within the script named `mpu_analysis.py`. A version of the script as of April 25
 1532 **TODO: make sure to update on this date** is also provided in Section B.2. It has many dependencies
 1533 including the HAWC analysis software. Figure 6.6 displays the workflow of a job with 3 threads.
 1534 Within a job, SOURCE is kept fixed and CHANS remains 17 elements long. More m_χ are sampled
 1535 from 11 bins up to 49 (for $\gamma\gamma$ and ZZ) and 25 (for remaining CHANS) which amounts to 12 or 6
 1536 mass bins per decade. m_χ and CHANS are permuted into a 473 element list which is split evenly
 1537 across N threads where N is [2, 8, 16]. For each m_χ -CHAN tuple, 1001 $\langle\sigma v\rangle$ values are sampled in

Timing summary for a multi-threaded job.

Import and Load HAL, 3ML, and HAWC analysis software ~ 2 min		
Load HAWC Data ~ 5 min		
Load HAWC PDF's (Detector Resolution files) ~ 4 min		
Load Spatial Model < 1s		
Load Spectra Models <1 s	Load Spectra Models <1 s	Load Spectra Models <1 s
Calculate max LLH (Chan_0, m_{χ_1}) ... max LLH (Chan_?, m_{χ_N}) N = TOTAL/N_THREADS ~ 8 min/Spec_model	Calculate max LLH (Chan_?, m_{χ_1}) ... max LLH (Chan_?, m_{χ_N}) N = TOTAL/N_THREADS ~ 8 min/Spec_model	Calculate max LLH (Chan_?, m_{χ_1}) ... max LLH (Chan_?, m_{χ_N}) N = TOTAL/N_THREADS ~ 8 min/Spec_model
Write results to file <1 s	Write results to file <1 s	Write results to file <1 s
Join Threads and terminate < 1s		

Figure 6.6 Task chart for one multithreaded job developed for this project. Green blocks indicate a shared resource across the threads AND computation performed serially. Red blocks indicate functional parallel processing within each thread. 3 threads are represented here, yet many more can be employed during the full analysis. Jobs are defined by the SOURCE as these require unique maps to be loaded into the likelihood estimator. The m_{χ} , CHAN, and $\langle \sigma v \rangle$ variables are entered into the thread pool and allocated as evenly as possible across the threads.

- 1538 the likelihood, and the value of $\langle \sigma v \rangle$ that maximizes the likelihood is found. Although rare, fits
 1539 that failed are handled on a case by case basis.

1540 6.5.3 Performance

M Tasks	$T_{p,c}$ (hr:min:s)			
	$T_{1,1}$	$T_{1,2}$	$T_{1,8}$	$T_{1,16}$
50	1:40:37.5	0:52:43.7	0:19:13.8	0:13:44.0
74	2:22:30.0	1:15:00.6	0:25:21.3	0:15:49.8
100	(3:07:51.9)	1:40:10.5	0:30:44.4	0:20:01.4
200	(6:02:20.6)	-	1:00:32.0	0:30:35.0
473	(13:58:40.3)	-	2:01:41.4	1:07:53.2

Table 6.2 Timing summaries for analyses for serial and multithreaded processes. M tasks is the number of functional-parallel tasks ran for the computation. $T_{p,c}$ is a single run time in hours:minutes:seconds for runs utilizing p nodes and c threads. Runs are run interactively on the same computer to maximize consistency. Empty entries are indicated with '-'. (·) entries are estimated entries extrapolated from data earlier in the column.

- 1541 We see a significant reduction to wall time needed for our dSph analyses to run. Table 6.2

1542 shows the timing summaries for analyses of different sizes and thread counts. Additionally, the
 1543 efficiency gained when consolidating the serial loading of data is also apparent in our ability to
 1544 study many more tasks in about the same amount of wall time as a smaller serial computation. Trials
 1545 represented in the table were run on an AMD Opteron® processor 6344 with 48 cores, 2 threads per
 1546 core; 2.6 GHz clock. This is not the same architecture used for analysis on the HAWC computing
 1547 cluster however they are similar enough that results shown here are reasonably representative of
 1548 computing on the HAWC computing cluster. I use Tab. 6.2 for the inferences and conclusions in
 1549 the following paragraphs.

1550 First, we want to find T_s , the time of serial computation. From Fig. 6.5, the timing for our
 1551 coding pattern can be written as

$$T_s + Mt_p = T_{1,1}^M. \quad (6.5)$$

1552 M is the number of functional-parallel tasks (represented as column 1 of Tab. 6.2), and t_p is the
 1553 average time to complete a single parallel task. $T_{1,1}^M$ is the total time for a parallel program to run if
 1554 only 1 processor is allocated for M parallel task. With two runs of different M (M_1 and M_2), we
 1555 can use a system of equations to compute

$$T_s = 803.1\text{s} \text{ and } t_p = 104.6\text{s} \quad (6.6)$$

1556 Now, we have specific estimation for the fraction of serial computing time, F_s :

$$F_s = \frac{803.1}{803.1 + 104.6 \cdot M}. \quad (6.7)$$

1557 The maximum M for this study is 473 which evaluates to: $F_s = 0.016$ or 1.6% of computing time.
 1558 Table 6.3 shows the resulting speedups.

1559 We see a speedup that generally exceeds expectations from Eq. (6.4) for real trail runs. We also
 1560 see that there are diminishing returns as the number of threads increases. For small jobs with large c ,
 1561 both the expected and observed speedup are significantly smaller than c . One thing not considered
 1562 in Eq. (6.4) is the time incurred via communication latency. Communication latency increases
 1563 with the number of threads and contributes to diminishing returns. Additionally, these values are

M Tasks	F_s	$S_{1,2}$	$S_{1,8}$	$S_{1,16}$
50	1.33 E-1	1.90 [1.76]	5.23 [4.14]	6.35 [5.34]
74	9.40 E-2	1.90 [1.83]	5.62 [4.82]	9.00 [6.64]
100	7.13 E-2	1.88 [1.87]	6.11 [5.34]	9.38 [7.73]
200	3.70 E-2	- [1.93]	5.98 [6.36]	11.85 [10.29]
473	1.60 E-2	- [1.97]	6.89 [7.20]	12.35 [12.91]

Table 6.3 Speed up summaries for analyses for serial and multithreaded processes. M tasks is the number of functional-parallel tasks ran for the computation. $S_{p,c}$ is a single speedup comparison for runs utilizing p nodes and c threads. [·] are the estimated speedups calculated from Tab. 6.2, Eq. (6.7), and Eq. (6.4). Empty entries are indicated with '-'.

1564 for single runs and do not consider the stochastic variation expected in a shared high performance
 1565 computing resource. Therefor, these results are not strictly conclusive, yet demonstrate the merits
 1566 of multi-threading. We see very clearly that there is a lot to gain, and this new coding pattern will
 1567 expand HAWC's analysis capabilities.

1568 **6.6 Analysis Results**

1569 3 of the 43 $\mathcal{L}\mathcal{S}$ dSphs considered for the multithreaded analysis. These dSph are analyzed
 1570 for emission from DM annihilation according to the likelihood method described in Section 5.4.
 1571 The three likelihood profiles are then stacked to synthesize a combined limit on the dark matter
 1572 annihilation cross-section, $\langle\sigma v\rangle$. This combination is done each of the 17 SM annihilation channels.
 1573 Figure 6.7 and Fig. 6.8 show the combined limits for all annihilation channels with HAWC's
 1574 observations. Test statistics of the best fit $\langle\sigma v\rangle$ values for each m_χ and CHAN are shown in Fig. 6.9
 1575 and Fig. 6.10. We also compare these limits to HAWC's Glory Duck limits shown in Section 5.5.
 1576 The comparison to Glory Duck are featured in Fig. 6.11 for all the DM annihilation channels studied
 1577 for Glory Duck. A full comparison is provided in the appendix in Fig. B.2, Fig. B.3, and Fig. B.4.
 1578 Here, we show updated limits for $\chi\chi \rightarrow b\bar{b}, e\bar{e}, \mu\bar{\mu}, \tau\bar{\tau}, t\bar{t}, W^+W^-$, $\gamma\gamma$ and ZZ . For the first time
 1579 ever, we show limits for $\chi\chi \rightarrow c\bar{c}, s\bar{s}, u\bar{u}, d\bar{d}, \nu_e\bar{\nu}_e, \nu_\mu\bar{\nu}_\mu, \nu_\tau\bar{\nu}_\tau, gg$, and hh .

1580 No DM was found in HAWC observations. The largest excess found in HAWC data was for DM
 1581 annihilating to W -bosons or $\nu_e\bar{\nu}_e$ for $m_\chi = 10$ TeV at significance 2.11σ and 2.14σ respectively.
 1582 HAWC's limits and excesses are dominated by Segue1. Coma Berenices shows excesses at higher
 1583 DM mass, yet no similar excesses were observed in Segue1 or Sextans. Sextans did not contribute

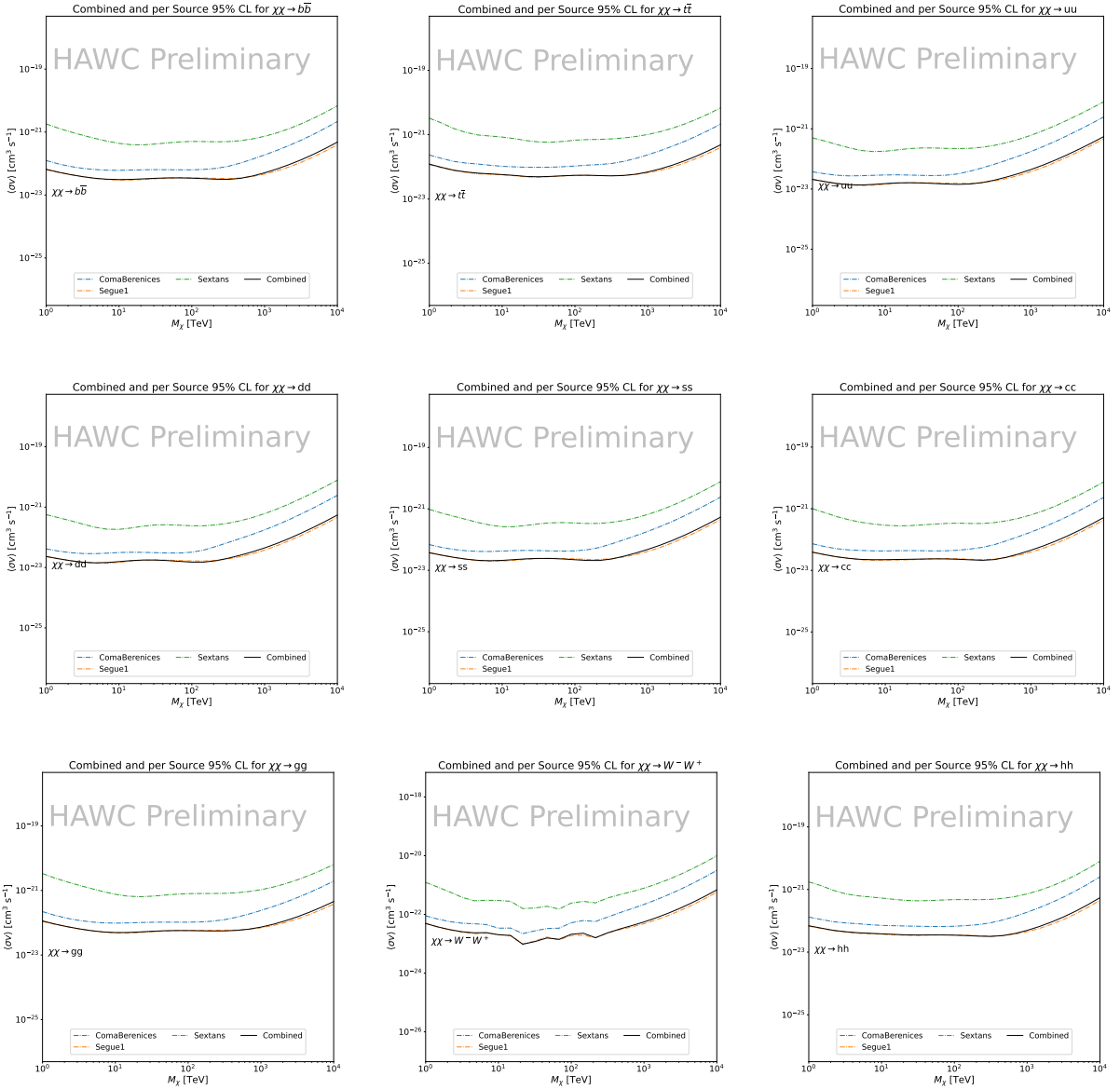


Figure 6.7 HAWC upper limits at 95% confidence level on $\langle\sigma v\rangle$ versus m_χ for $\chi\chi \rightarrow b\bar{b}$, $t\bar{t}$, $u\bar{u}$, $d\bar{d}$, $s\bar{s}$, $c\bar{c}$, gg , W^+W^- , and hh . Limits are with $\mathcal{L}\mathcal{S}$ J -factors [76]. The solid line represents the observed combined limit. Dashed lines represent limits from individual dSphs.

1584 significantly to signal excesses or the combined limit as it is at high zenith. Draco was not included
 1585 as the PDF of some of our analysis bins were wider than what is reasonable for a point source
 1586 analysis. Draco is at a high zenith for HAWC, so the effort required to include it was not justified
 1587 by the benefits.

1588 We did not generate background trials in time of writing this thesis. These are not shown and

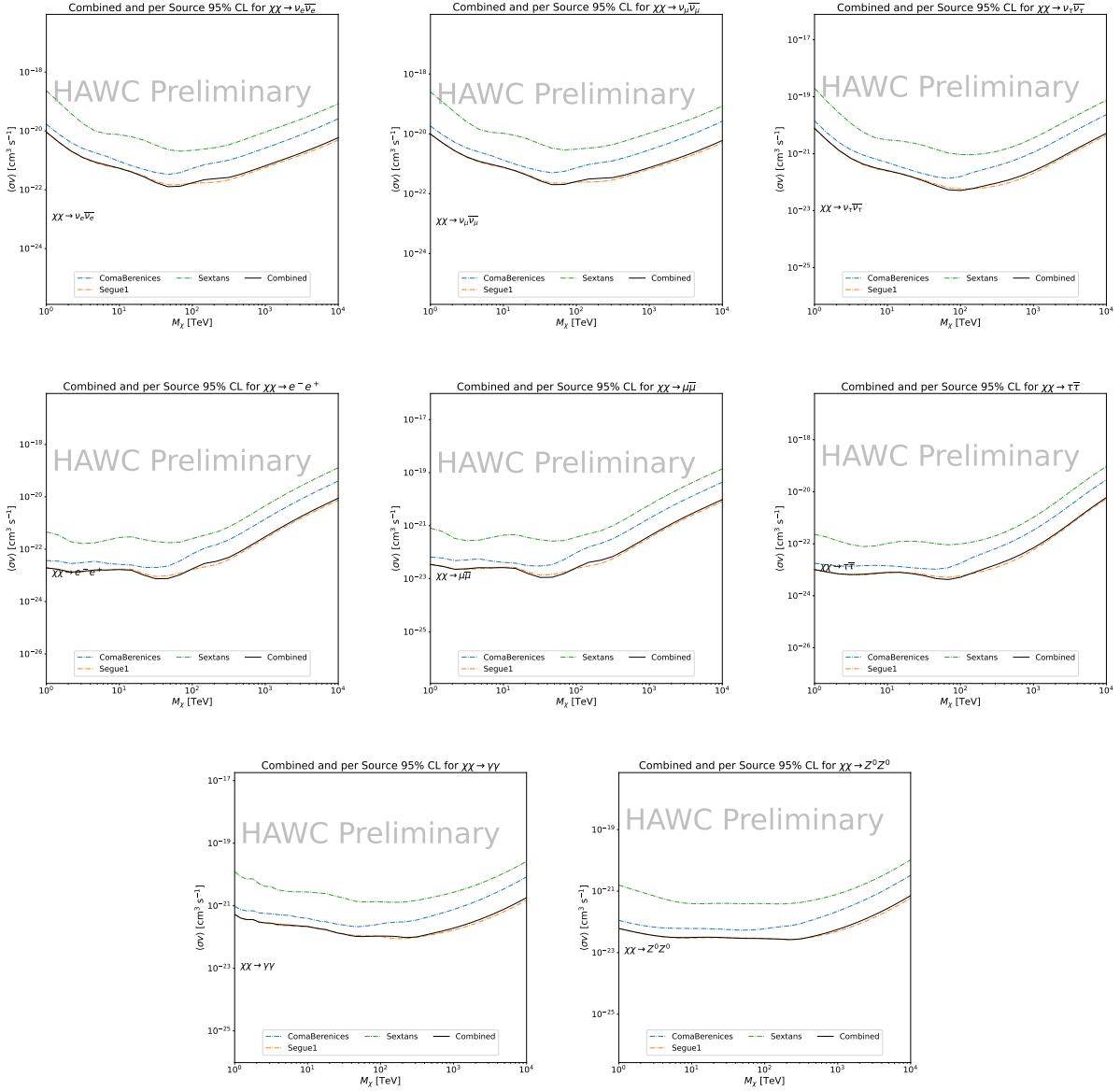


Figure 6.8 HAWC upper limits at 95% confidence level on $\langle\sigma v\rangle$ versus m_χ for $\chi\chi \rightarrow \nu_e \bar{\nu}_e$, $\nu_\mu \bar{\nu}_\mu$, $\nu_\tau \bar{\nu}_\tau$, $e \bar{e}$, $\mu \bar{\mu}$, $\tau \bar{\tau}$, $\gamma\gamma$ and ZZ . Limits use $\mathcal{L}S$ J -factors [76]. The solid line represents the observed combined limit. Dashed lines represent limits from individual dSphs.

1589 are an immediate next step for this analysis before publication.

1590 When comparing these results to Section 5.5, we see an overall decrease to the confidence limit
 1591 therefore improvement to HAWC's expected sensitivity. This improvement is generally stronger
 1592 than a doubling of data, or a factor $\sqrt{2}$ decrease. The comparison is somewhat complex and
 1593 dependent on the dSph and SM annihilation channel. Figure 6.11 shows the comparisons of limits

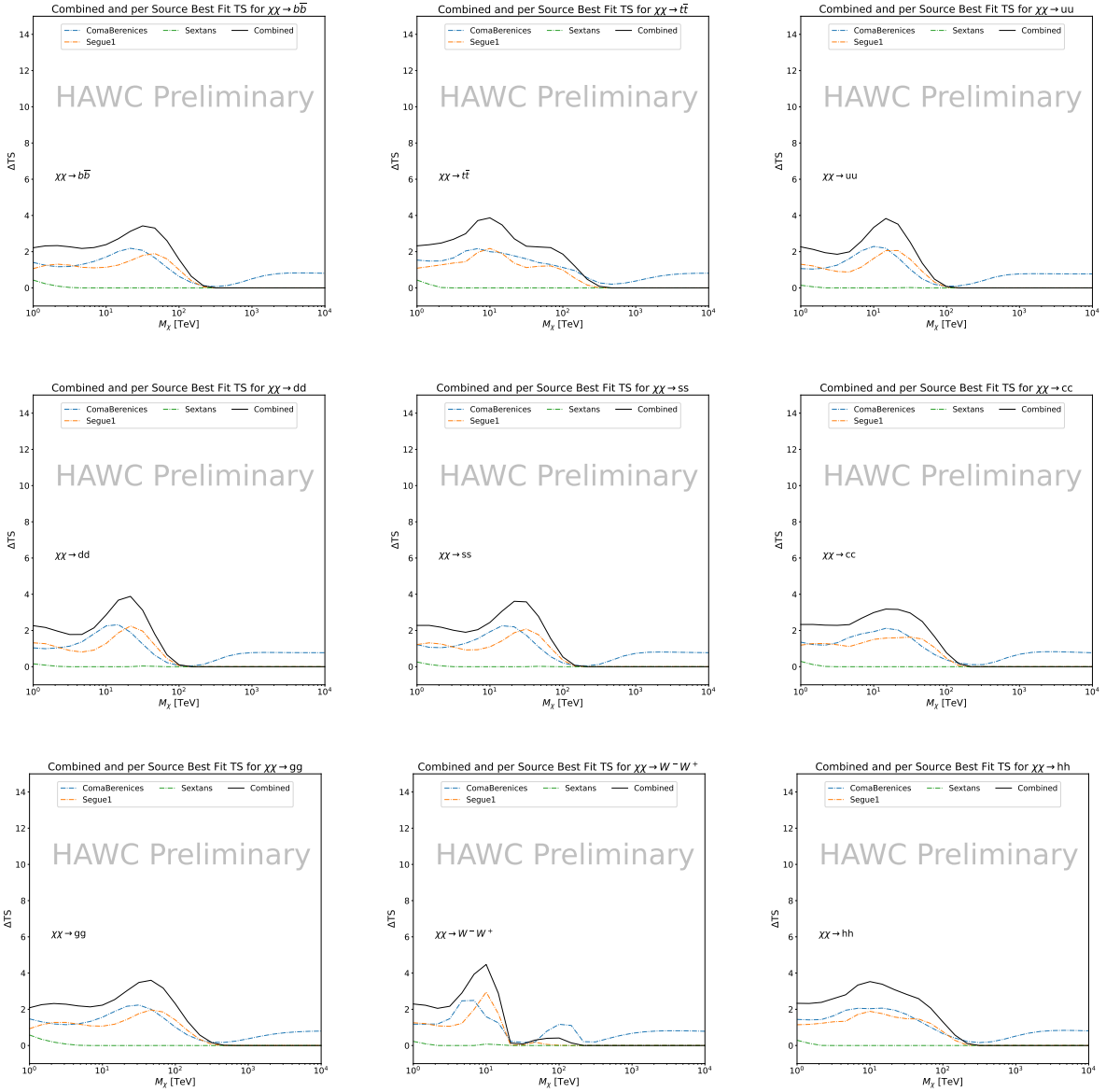


Figure 6.9 HAWC TS values for best fit $\langle\sigma v\rangle$ versus m_χ for SM annihilation channels: $\chi\chi \rightarrow b\bar{b}$, $t\bar{t}$, $u\bar{u}$, $d\bar{d}$, $s\bar{s}$, $c\bar{c}$, gg , W^-W^+ , and hh . Limits use \mathcal{LS} J -factors. The solid black line shows the combined best fit TS values. The colored, dashed lines are the TS values from each dSph.

1594 calculated for this analysis and Glory Duck (Section 5.5). Segue 1 and Coma Berenices are low
 1595 zenith where improvements to HAWC's analysis come only from energy estimation. Differences
 1596 between these two are dominantly from their differences in J -factor, half-light radii of the dSphs,
 1597 and the particle physics inputs. Substantial gains in HAWC's analysis methods (pass 5.F) were
 1598 made at high zenith which is important for sources like Sextans. The HDM particle physics model

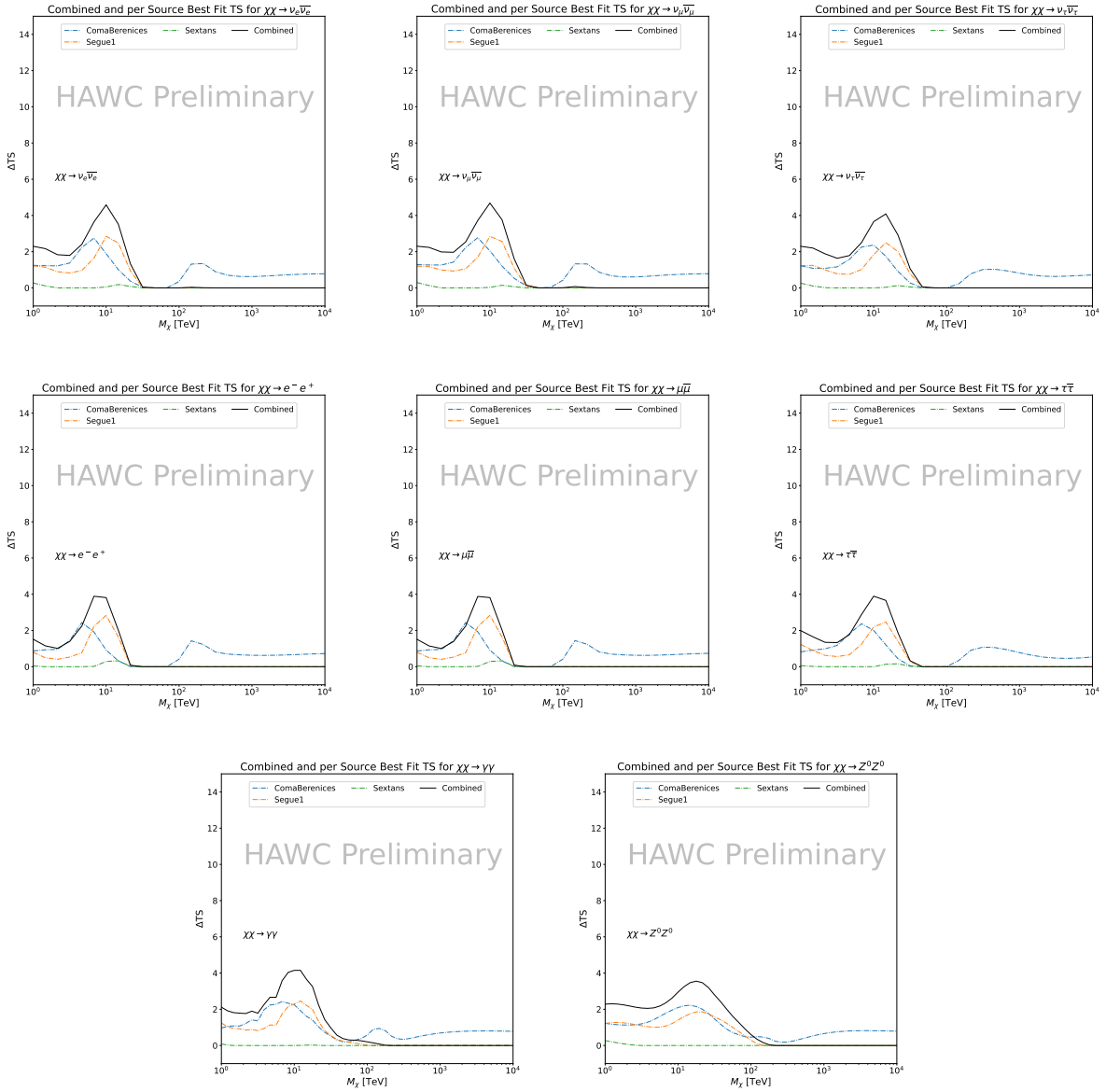


Figure 6.10 HAWC TS values for best fit $\langle\sigma v\rangle$ versus m_χ for SM annihilation channels: $\chi\chi \rightarrow \nu_e \bar{\nu}_e$, $\nu_\mu \bar{\nu}_\mu$, $\nu_\tau \bar{\nu}_\tau$, $e^- e^+$, $\mu \bar{\mu}$, $\tau \bar{\tau}$, $\gamma\gamma$ and ZZ . Limits use \mathcal{LS} J -factors. The solid black line shows the combined best fit TS values. The colored, dashed lines are the TS values from each dSph.

1599 produces almost identical spectra to the PPPC for $\chi\chi \rightarrow e^- e^+$. This channel can be used to
 1600 compare limits between dSph spatial models. Overhead sources see minimal improvement to the
 1601 limits, while high zenith sources see an order of magnitude improvement for all DM masses. Softer
 1602 SM annihilation channels see broad improvements to the limit compared to harder channels.

1603 **6.7 Systematics**

1604 Systematics to this analysis are identical to what was performed earlier in Glory Duck, Sec-
1605 tion 5.7. We are also sensitive to the choice in spatial template, and this was explored in Section 5.7.2
1606 and Section 5.8.2.

1607 **6.8 Conclusion and Discussion**

1608 In this multithreaded analysis, we have used observations of 3 dSphs from HAWC to perform
1609 a collective DM annihilation search towards dSphs. The data were combined across sources
1610 to significantly increase the sensitivity of the search. Advanced computational techniques were
1611 deployed to accelerate wall-time spent analyzing by an order of magnitude. We have observed
1612 no significant deviation from the null, no DM hypothesis, and so present our results in terms of
1613 upper limits on the velocity-weighted cross-section, $\langle\sigma v\rangle$, for seventeen potential DM annihilation
1614 channels across four decades of DM mass.

1615 This analysis serves as a proof of concept for multithreaded HAWC analyses with large parameter
1616 spaces. Larger datasets with fast techniques will be essential to tackling the DM problem. The
1617 models we used for this study include annihilation channels with neutrinos in the final state.
1618 Advanced studies could aim to merge our results with those from neutrino observatories with large
1619 data sets.

1620 A full HAWC analysis will include systematic studies of the J -factor distributions. Additionally,
1621 because of the timing reduction, the study can be doubled in size to include DM decay. We have not
1622 yet received the remaining spatial profiles to the \mathcal{LS} catalog, and limits can be quickly computed
1623 once these are received. Finally, statistical studies with Poisson variation of HAWC’s background
1624 are essential to a comprehensive understanding of our observed excesses.

Segue1

Coma Berenices

Sextans

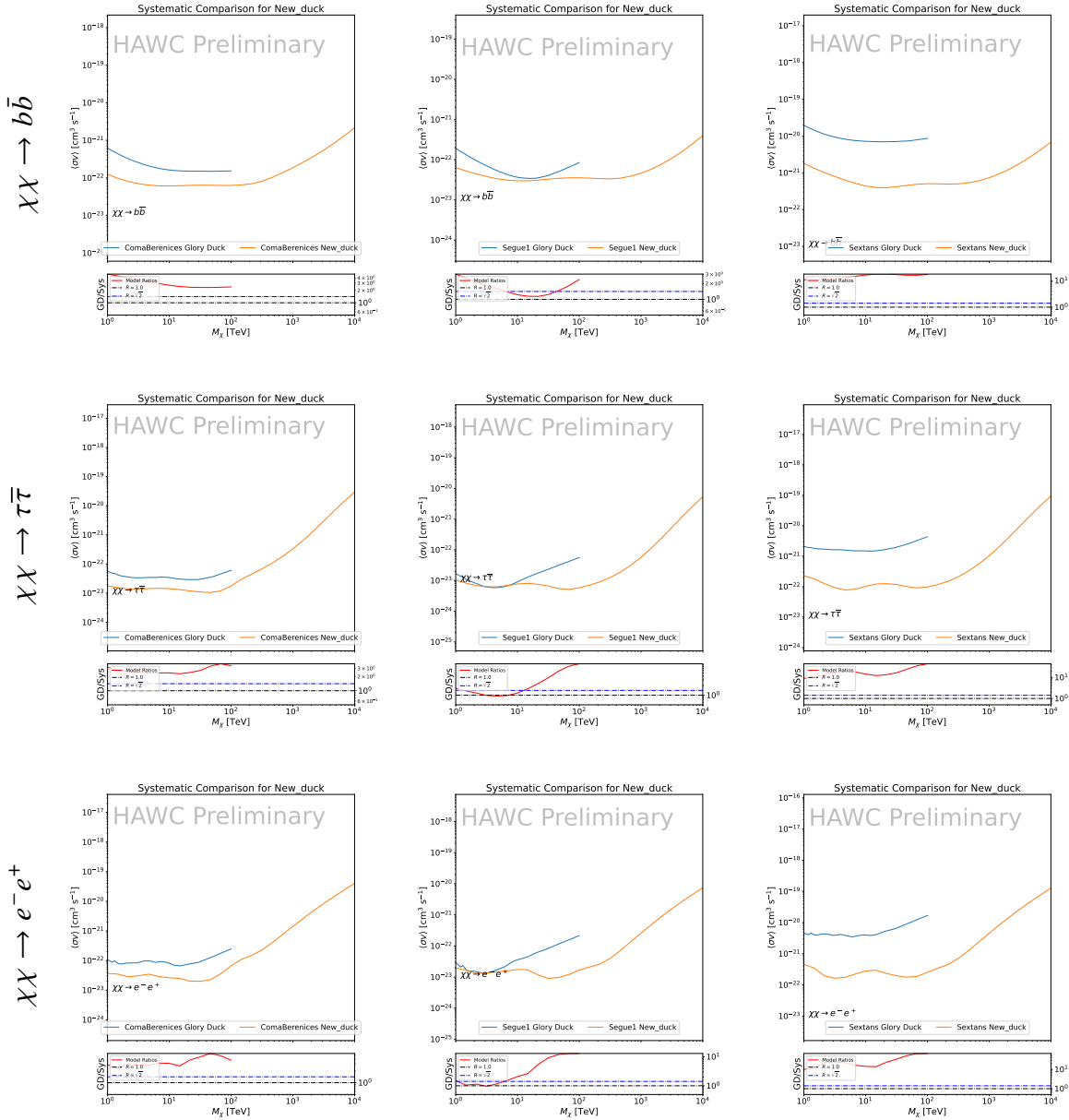


Figure 6.11 Comparison of HAWC limits from this analysis to Glory Duck (Fig. 5.5) for 3 dSphs and 3 DM annihilation channels: $b\bar{b}$, $\tau\bar{\tau}$, and e^-e^+ . Each sector shows the 95% confidence limit from Glory Duck (blue line) and this analysis (orange line) in the top plot. The lower plot features the ratio in log scale of Glory Duck to this analysis in a red solid line. Horizontal dashed lines are for ratios of 1.0 (black) and $\sqrt{2}$ (blue). Ratios larger than 1.0 are for limits smaller, or stricter, than Glory Duck. Ratios larger than $\sqrt{2}$ indicates limits are stricter than a simple doubling of the Glory Duck data.

CHAPTER 7

HEAVY DARK MATTER ANNIHILATION SEARCH WITH ICECUBE'S NORTH SKY TRACK DATA

7.1 Introduction

Neutrinos are another astrophysical messenger than can travel long distances without significant attenuation or deflection. Additionally, Neutrinos come in three flavors which triples the multiplicity of the particles we are searching for. Uniquely, they interact less readily than photons especially above PeV energies. Neutrinos therefore provide another window through which we can perform dark matter searches.

The previous IceCube DM annihilation analysis towards dwarf galaxies was performed in 2013 [79] which, in technical terms, is more than a minute ago. This is in spite of IceCube's crucial sensitivity afforded from neutrino spectral lines [80]. A lot has changed in IceCube since its previous DM annihilation search such as, additional strings, more sophisticated analysis methods, and more accurate theory modeling. It has come time for IceCube to make a DM dSph contribution.

IceCube is sensitive to annihilating DM for DM masses above 1 TeV. Additionally, IceCube's sensitivity is comparable gamma-ray observatories in spectral models that produce hard neutrino features. The goal of this analysis is to perform a DM annihilation search using the Northern Sky Tracks datasets. The search will only be towards dwarf spheroidal galaxies (dSph) for the strengths mentioned in Section 5.3.3. These sources are treated as point sources for IceCube with little loss to sensitivity or model dependence on how the DM is distributed. DM masses from 500 GeV to 100 PeV are considered for this analysis. Several DM annihilation channels available from the HDMspectra [75] are studied in this analysis. This chapter presents the analysis work for IceCube to update our DM searches toward dSphs.

7.2 Dataset and Background

This section enumerates the data and background methods used for IceCube's study of dSphs. Section 7.2.1 and Section 7.2.2 are most useful for fellow IceCube collaborators looking to replicate this analysis.

1651 **7.2.1 Itemized IceCube files**

1652 These files are only available within IceCube’s internal documentation and wikis. They are not
1653 meant for public access, and are presented here so that IceCube collaborators can reproduce results
1654 accurately.

1655 • Software Environment: CVMFS Py3-v4.1.1

1656 • Data Sample: Northern Tracks NY86v5p1

1657 • Analysis Software: csky ([nu_dark_matter](#))

1658 • Analysis wiki: https://wiki.icecube.wisc.edu/index.php/Dark_Matter_Annihilation_Search_towards_dwarf_spheroidals_with_NST_and_DNN_Cascades

1660 • Project repository

1661 **7.2.2 Software Tools and Development**

1662 This analysis was performed inside IceCube’s CVMFS (3.4.1.1) software environment using
1663 csky for likelihood calculations. Csky at first did not come with dark matter spectral models nor
1664 could accommodate custom flux models. We developed these capacities for single source and
1665 stacked source studies for this analysis. The analysis code is held in a separate repository from
1666 csky. The [nu_dark_matter branch of csky](#) manages the input of custom dark matter spectra and
1667 accompanied DM astrophysical source. Csky also enables the use of multithreading which was
1668 shown to be crucial for DM searches (see Sec. 6). Csky then calculates likelihoods with a selected
1669 data sample. The [IceCube Dark Matter dSph repository](#) manages the generation of spectral models
1670 for neutrinos, physics parameter extraction from n_{sig} , J -factor per source inputs, and bookkeeping
1671 for the large parameter space. The project repository required a secondary software environment
1672 for neutrino oscillations. How to launch and run those calculations are documented in the project
1673 repository and the Docker image is additionally saved in Section C.1.

1674 **7.2.3 Data Set and Background Description**

1675 For this analysis, I use the Northern Sky Tracks (NST) Sample (Version V005-P01). The sample
1676 contains up-going track-like events, usually from ν_μ and ν_τ , with a superior angular resolution
1677 compared to the cascade dataset. This sample covers 10.4 years of data (IC86_2011-2021). The
1678 accepted neutrino energy range used for the analysis is unique from most other IceCube searches
1679 because DM spectra are hard with large contributions close to $E_\nu = m_\chi$. Therefore, the sampled
1680 energy range is $1 < \log(E_\nu/\text{GeV}) < 9.51$ with step size 0.125.

1681 The strengths of a dwarf analysis is that there are no additional background considerations
1682 beyond nominal, baseline background estimations (see Section 5.2.3). For NST, the nominal
1683 contributions come from atmospheric neutrinos and isotropic astrophysical neutrinos. We estimate
1684 the background by scrambling NST data along Right Ascension.

1685 **7.3 Analysis**

1686 The expected differential neutrino flux from DM-DM annihilation to standard model particles,
1687 $d\Phi_\nu/dE_\nu$, over solid angle, Ω is described by the familiar equation.

$$\frac{d\Phi_\nu}{dE_\nu} = \frac{\langle\sigma\nu\rangle}{8\pi m_\chi^2} \frac{dN_\nu}{dE_\nu} \times \int_{\text{source}} d\Omega \int_{l.o.s} \rho_\chi^2 dl(r, \theta') \quad (7.1)$$

1688 This is identical to Eq. (5.1) except that there are 3 neutrino flavors, so there are a corresponding
1689 3 flux equations. Section 5.3 has a complete description of each term in Eq. (7.1). Additionally,
1690 neutrinos oscillate between flavors which needs to be considered for the expected neutrino flux
1691 at Earth. Section 7.3.1 presents the particle physics model and processing for DM annihilation.
1692 Section 7.3.2 presents the spatial distributions built for each dSph.

1693 **7.3.1 $\frac{dN_\nu}{dE_\nu}$ - Particle Physics Component**

1694 Neutrino spectra from heavy DM annihilation were generated using HDMspectra [75] and
1695 χ arov [81]. HDMspectra has tables for the decay and annihilation of heavy DM for different
1696 dark DM and SM primary annihilation channels. The simulation includes electroweak or gluon
1697 radiative corrections and higher order loop corrections from the W and Z bosons (WWZ and $WW\gamma$).
1698 These corrections are especially important for accurately estimating the prompt neutrino flux. This

1699 publication also pushes the simulated DM mass to the Plank scale (1 EeV), however this study will
1700 not explore that high.

1701 An important feature in the spectra is that neutrino line channels will be accompanied by a low
1702 energy tail [75], see Fig. 7.1. Thus, the Earth will not fully attenuate a heavy neutrino line-like
1703 signal from high declination sources where the neutrino flux must first traverse through the Earth.
1704 The DM annihilation channels that feature lines include all leptonic channels: $\nu_{e,\mu,\tau}$, e , μ , and τ . We
1705 use the `xarov` software to propagate and oscillate the neutrinos from the source to Earth. Because
1706 these sources are quite large in absolute terms, and also far (order 10 kpc or more), the resulting
1707 flavor spectra are the averages of the transition probabilities [81]:

$$P(\nu_\alpha \rightarrow \nu_\beta) \approx \begin{bmatrix} 0.55 & 0.18 & 0.27 \\ 0.18 & 0.44 & 0.38 \\ 0.27 & 0.38 & 0.35 \end{bmatrix} \quad (7.2)$$

1708 Examples of the spectra before and after propagation are shown in Fig. 7.1.

1709 When calculating the expected contribution to n_s , only ν_μ and ν_τ are considered as NST's
1710 effective area to ν_e is negligible [82]. Therefore, the expected composite neutrino spectrum is the
1711 sum of the two flavors: $\frac{dN\nu_\mu}{dE\nu_\mu} + \frac{dN\nu_\tau}{dE\nu_\tau}$. The spectral tables are then converted to splines to condense
1712 information, enable random sampling of the spectra, and reduce computing times. The spectral
1713 splines are finally implemented as a DM class in csky.

1714 7.3.1.1 Treatment of Neutrino Line Features

1715 All DM annihilation channels into leptons $\chi\chi \rightarrow [\nu_{e,\mu,\tau}, e, \mu, \tau]$ develop a prominent and
1716 narrow spectral line feature. For all neutrino flavors, this line is visible and prominent in all m_χ
1717 studied in this analysis. For charged leptons, the feature typically manifests at $m_{ch}hi > 10$ TeV, yet
1718 its prominence varies slightly between the flavors. Examples for lines in the annihilation spectra
1719 with neutrinos or charged leptons are provided in Fig. 7.1.

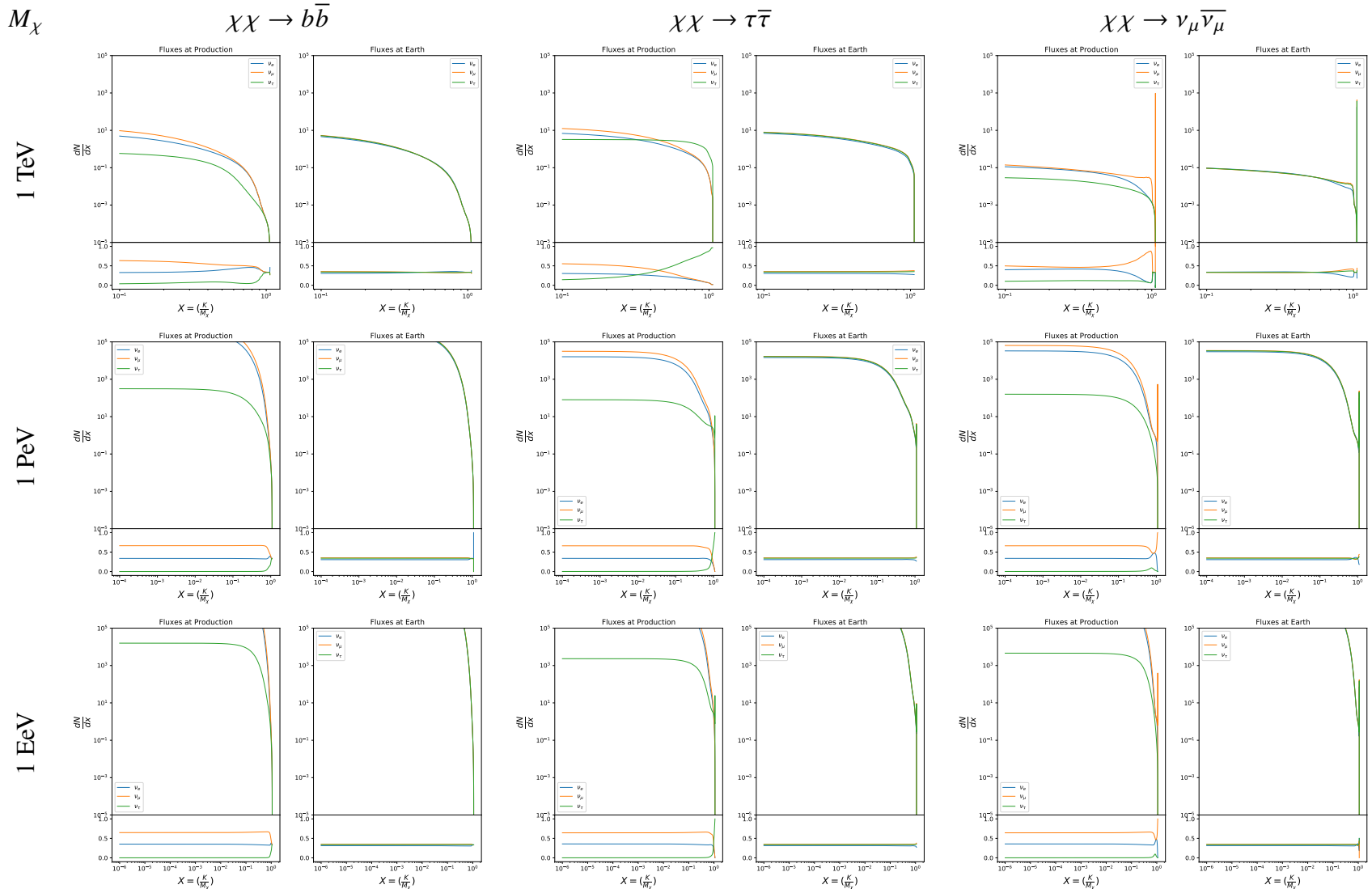


Figure 7.1 Neutrino spectra at production (left panels) and after oscillation at Earth (right panels). Blue, orange, and green lines are the ν_e , ν_μ , and ν_τ spectra respectively. Top panels show the spectra in $\frac{dN}{dE}$. Lower panels plot the flavor ratio to $\nu_e + \nu_\mu + \nu_\tau$. SM annihilation channels $b\bar{b}$, $\tau\bar{\tau}$, and $\nu_\mu\bar{\nu}_\mu$ are shown for $M_\chi = 1 \text{ PeV}$, TeV , and EeV .

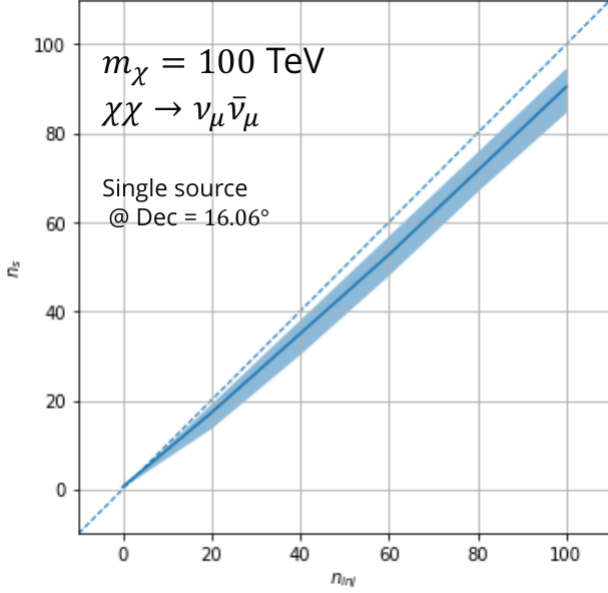


Figure 7.2 Signal recovery for 100 TeV DM annihilation into $\nu_\mu \bar{\nu}_\mu$ for a source at Dec = 16.06°. n_{inj} is the number of injected signal events in simulation. n_s is the number of reconstructed signal events from the simulation data. Although the uncertainties are small and tight, the reconstructed n_s are systematically underestimated.

1720 The neutrino line feature is so narrow relative the sampled energy range that the random
 1721 sampling of the spectra and likelihood fitting rarely capture the line in computation. As a result,
 1722 often the best fit to simulation of background will always floor to TS = 0 and the signal recovery
 1723 systematically underestimates the signal (see Fig. 7.2).

1724 To remedy this, we take a similar approach to the IceCube’s decay analysis [83] and the previous
 1725 gamma-ray study in Section 6.3.1. Two smoothing kernels were tested (Gaussian and uniform)
 1726 to widen the line feature. The widths were tuned such that the signal recovery approached unity
 1727 for DM mass 100 TeV to 1 PeV for a source at Segue 1’s declination, 16.06°. Near horizon
 1728 was chosen in order to isolate loss in signal recovery away from Earth’s attenuation of very high
 1729 energy neutrinos and atmospheric backgrounds. The kernel convolution needed closely preserve
 1730 the integrated counts of neutrinos. The optimized kernel parameters for all lines are summarized
 1731 as:

- 1732 • Gaussian kernel with 1σ width = $1.75\text{E-}3 \cdot m_\chi$
- 1733 • Minimum energy included in convolution = $\text{MIN}[0.995 \cdot m_\chi, E(\nu_{\text{line}}) - 4\sigma]$

- 1734 • Maximum energy included in convolution = $\text{MAX}[1.005 \cdot m_\chi, E(\nu_{\text{line}}) + 4\sigma]$

1735 where $E(\nu_{\text{line}})$ is the neutrino energy where the neutrino line is at the maximum.

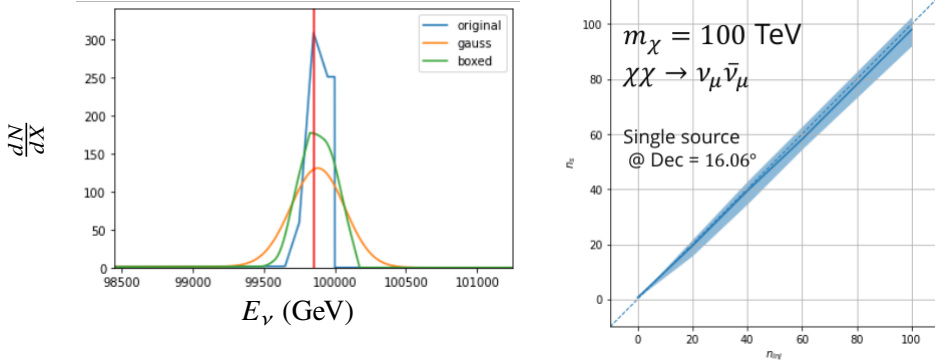


Figure 7.3 Left panel shows the two kernels overlaying the original spectrum from $\chi\text{aron}\nu$ after propagation to Earth [81]. The vertical red line indicates where the original neutrino line is maximized. Blue line is the output from $\chi\text{aron}\nu$. Green line is the spectrum after convolution with a flat kernel. Orange line is the spectrum after Gaussian convolution. Right panel shows the signal recovery of the spectral model using the Gaussian kernel with parameters enumerated above.

1736 These parameters broadly improved the signal recovery of the line spectra. An example is in
1737 Fig. 7.3. Analysis level signal recovery studies are expanded upon in Section 7.6.

1738 7.3.1.2 Spline Fitting

1739 In an effort to reduce computational work, memory burden, and align with point source methods
1740 used for NGC1068 [84], spectral splines were created and adopted for estimating the neutrino flux
1741 for the different spectral models. Software was written to generate, book keep, and calculate values
1742 on the splines.

1743 When using splines, one has to be careful of the goodness to fit. The spline software used
1744 here, Photospline [85], uses the penalized spline technique [86]. Through the penalized technique,
1745 poor fits are penalized according to the accuracy of the nominal value, and the smoothness of the
1746 first and second derivatives. However, this construction does not penalize on the integral of the
1747 fit distribution which is critical in low signal studies, such as DM searches. There are additional
1748 caveats when testing the goodness to fit to the MC generated above for all DM annihilation channels.

1749 • The splines must be Log10(*) in Energy and dN/dX to account for the exponential nature of
1750 the flux.

1751 • The fidelity of the fit matters more at $E_\nu \approx m_\chi$ where the model uncertainties are minimal
1752 and physical considerations (like the cut-off) are most important.

1753 • The fidelity of the fit matters less at low E_ν as the model uncertainties are large AND
1754 IceCube's sensitivity diminishes significantly below 500 GeV.

1755 • Total integrated counts should be well-preserved.

1756 The resulting cost function was built to evaluate the goodness of spline fits to account for the above
1757 considerations.

$$e_i = x_i \cdot \left(\frac{dN_i}{dX_i} - 10^{\hat{e}_i} \right) \quad (7.3)$$

1758 Where \hat{e}_i is the spline estimator's value for x_i . $x_i = E_{\nu_i}/m_\chi$. $\frac{dN_i}{dX_i}$ is the flux value from MC. I then
1759 take the RMS of the error distribution and the resulting value, err, is used to evaluate the fidelity of
1760 the spectral spline.

$$\text{err} = \sqrt{\frac{1}{x_{\max} - x_{\min}} \int_{x_{\min}}^{x_{\max}} e^2 dx} \quad (7.4)$$

1761 x_{\min} and x_{\max} are the scope of the error evaluation and are provided in Tab. 7.1.

1762 Each SM channel had unique tolerances for 'err'. Channels with very hard cut-offs had looser
1763 tolerance for err because a significant error would be generated from single counts over/underes-
1764 timated at the cut-off. Soft channels do not share this issue, so the tolerance is much stricter. All
1765 annihilation channels from HDM are modeled well below IceCube's NST sensitivity which falls
1766 off substantially below 100 GeV [82]. We do not think it is necessary to evaluate the spline fits
1767 below 100 GeV and use this value as the default lower cut-off. Yet, HDM's model uncertainties
1768 at $E_\nu < 10^{-6} \cdot m_\chi$ span an order of magnitude [75]. We also choose not to evaluate the splines
1769 below this critical value if it is within IceCube's sensitivity. Finally, the smoothing of the spectral
1770 lines in leptonic annihilation channels are ignored for evaluating the fit. We used the lower limit of

$\chi\chi \rightarrow$	GOOD	OK	FAIL	Limits of err calc [X_{min}, X_{max}]
$Z^0 Z^0, W^+ W^-$	1.0E-3	1.0E-3, 1.0E-2	1.0E-2	MAX[100GeV/ m_χ , 10^{-6}], 1.0
$t\bar{t}, hh$	1.0E-5	1.0E-5, 1.0E-4	1.0E-4	MAX[100GeV/ m_χ , 10^{-6}], 1.0
$b\bar{b}, d\bar{d}, u\bar{u}$	9.0E-7	9.0E-7, 9.0E-6	9.0E-6	MAX[100GeV/ m_χ , 10^{-6}], 1.0
$\nu\bar{\nu}_{e,\mu,\tau}$	1.0E-3	1.0E-3, 1.0E-2	1.0E-2	MAX[100GeV/ m_χ , 10^{-6}], MIN[0.995, ($E_n(\nu_{line}) - 4\sigma$)/ M_χ]
$e\bar{e}, \mu\bar{\mu}, \tau\bar{\tau}$	1.0E-3	1.0E-3, 1.0E-2	1.0E-2	MAX[100GeV/ m_χ , 10^{-6}], MIN[0.995, ($E_n(\nu_{line}) - 4\sigma$)/ M_χ]

Table 7.1 Spline err tolerances used for input in particle physics component to Eq. (5.1). Column 1 is the DM annihilation channel being fit. Columns 2, 3, and 4 are the tolerances for "GOOD" (pass), "OK" requires inspection, and "FAIL" (tune and refit) respectively. Column 5 has the X ranges over which the error is evaluated. MAX/MIN [·, ·] takes the maximum or minimum of the two enclosed values.

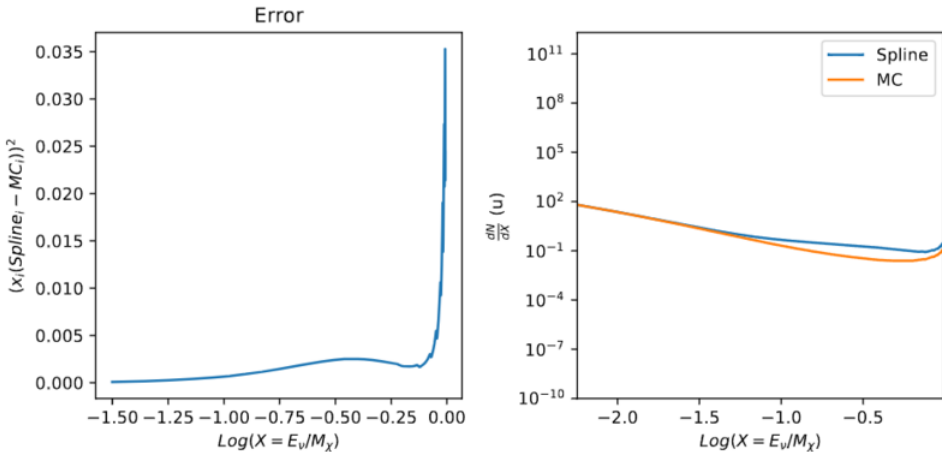


Figure 7.4 Example spline that failed the fit. Failed splined are corrected on a case by case basis unless the SM channel has a systematic problem fitting the splines. In this case, I made a bookkeeping error and loaded the incorrect spectral model

1771 the kernel mask as the upper limit of evaluation. Table 7.1 summarizes the tolerances for the DM
 1772 annihilation channels used for this analysis.

1773 The errors are then assesed in two ways. First, FAIL and OK are directly plotted with e_i as a
 1774 function of x with the full spline and MC. An example of a single failure is provided in Fig. 7.4.
 1775 Second, a summary plot of all the splines is plotted and colors coded. Figure C.1 are the spline
 1776 summaries as of writing this thesis. The goal broadly is to eliminate all red and inspect yellow
 1777 statuses.

1778 The ν_e spectra at Earth are not considered in this analysis, so no work was done to refine the

1779 spline fits for this flavor. Finally, I perform a visual inspection of the splines to verify that the spline
 1780 fitting did not introduce spurious features that would corrupt the likelihood fitting.

1781 7.3.1.3 Composite Neutrino Spectra

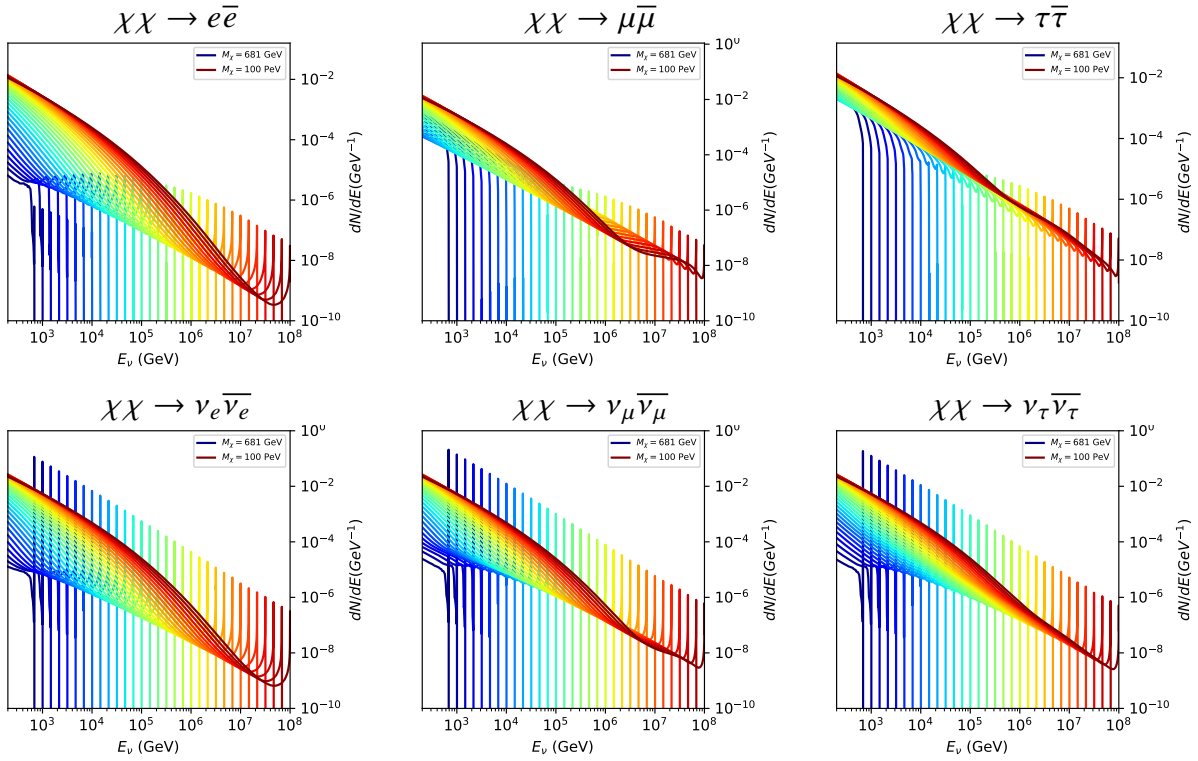


Figure 7.5 Summary of input spectral models that were smoothed with Gaussian kernels. Spectral models are for $\chi\chi \rightarrow e\bar{e}$, $\mu\bar{\mu}$, $\tau\bar{\tau}$, $\nu_e\bar{\nu}_e$, $\nu_\mu\bar{\nu}_\mu$, and $\nu_\tau\bar{\nu}_\tau$. These spectra are the composite ($\nu_\mu + \nu_\tau$) of neutrino flavors. Every spectral model used for this analysis is featured as a colored solid line. Bluer lines are for low m_χ models. m_χ ranges from 681 GeV to 100 PeV. HDM [75], χ arov [81], and Photospline [85] are used to generate these spectra. Energy (x-axis) was chosen to roughly represent the energy sensitivity of NST.

1782 With all the previously mentioned pieces, we are ready to fully assemble a comprehensive
 1783 description of the particle physics term dN/dE in Eq. (7.1).

$$\frac{dN_\nu}{dE_\nu \oplus} = \left(\frac{dN_{\nu_e}}{dE_{\nu_e}} + \frac{dN_{\nu_\mu}}{dE_{\nu_\mu}} + \frac{dN_{\nu_\tau}}{dE_{\nu_\tau}} \right)_{\text{src}} \cdot \mathbf{P}(\nu_\alpha \rightarrow \nu_\beta) \quad (7.5)$$

1784 Figure 7.5 shows the spectral models that required Gaussian smoothing, the leptonic annihilation
 1785 channels. The remaining models where the only processing were spline fitting and neutrino
 1786 oscillation are documented in Section C.3. Notice that the different neutrino flavors are unique,

1787 especially in their low energy tails. Therefore, this analysis will be sensitive to DM annihilating to
1788 the distinct neutrino flavors.

1789 **7.3.2 J- Astrophysical Component**

1790 For this analysis, we re-adopt the \mathcal{GS} model [55] used in Sec. 5 for dSphs. These models
1791 are based on a modified Navarro-Frenk-White (NFW) profile where the indices of the NFW
1792 (traditionally 1,3,1) are allowed to float. The angular width of these sources is much smaller than
1793 the angular resolution of IceCube NST [84]. We therefore treat these sources as point sources
1794 in this analysis, and forgo generating maps. These sources and the \mathcal{GS} model have already been
1795 discussed at length in Section 5.3.2 and is not repeated here. IceCube uses identical sources to
1796 Tab. 5.1 except we analyze source with declinations above 0.0° .

1797 **7.3.3 Source Selection and Annihilation Channels**

1798 We use all the dSphs presented in IceCube’s previous dSph DM search [79] and expand beyond
1799 it. IceCube’s sources for this analysis studies include Boötes I, Canes Venatici I, Canes Venatici II,
1800 Coma Berenices, Draco, Hercules, Leo I, Leo II, Leo V, Leo T, Segue 1, Segue 2, Ursa Major I,
1801 Ursa Major II, and Ursa Minor. A full description of all sources used is in Table 5.1. Sources with
1802 declinations less than 0.0 are excluded from this analysis.

1803 This analysis improves on the previous IceCube dSph paper [79] in the following ways. Previ-
1804 ously, the IceCube detector was not yet completed to the 86 string configuration. Many more dSphs
1805 will be observed, from 4 to 15. Previously, the particle physics model used for neutrino spectra
1806 from DM annihilation did not have EW corrections where they are now included [75]. The spectral
1807 models also predict substantial differences between the neutrino flavors, so this analysis will be the
1808 first DM dwarf analysis to discriminate between primary neutrino flavors. The study performed
1809 here studies 10.4 years of data.

1810 The SM annihilation channels probed for this study include $\chi\chi \rightarrow$

1811 $b\bar{b}, t\bar{t}, u\bar{u}, d\bar{d}, e\bar{e}, \mu\bar{\mu}, \tau\bar{\tau}, ZZ, W^+W^-, \nu_e\bar{\nu}_e, \nu_\mu\bar{\nu}_\mu$, and $\nu_\tau\bar{\nu}_\tau$

1812 **7.4 Likelihood Methods**

1813 I use the Point-Source search likelihood which is widely used in IceCube analyses. The
1814 likelihood function is defined as the following:

$$L(n_s) = \prod_{i=1}^N \left[\frac{n_s}{N} S_i + \left(1 - \frac{n_s}{N}\right) B_i \right] \quad (7.6)$$

1815 where i is an event index, S and B are the signal PDF and background PDF respectively. For a joint
1816 analysis where the sources are stacked the likelihood is expanded in the simplified way:

$$L(n_s) = \prod_{i=1}^{N_{\text{sources}}} L_i(n_s) \quad (7.7)$$

1817 Where L_i is the likelihood from the i -th source in the stacked analysis. The Test Statistic (TS)
1818 definition remains the same as Eq. (5.7)

1819 **7.5 Background Simulation**

1820 Before we look at data, we must first analyze background and signal injection to validate our
1821 analysis. We set out to characterize the TS distributions for each source, annihilation channel, and
1822 m_χ . Previous IceCube DM searches [83, 87] showed TS distributions that did not behave according
1823 to a χ^2 distribution with 1 degree of freedom. TS distributions can also vary significantly between
1824 DM mass and annihilation models. Therefore, Wilk's theorem may not be applicable to the analysis.
1825 Instead, a critical value is defined from many background trials. We study the TS distributions
1826 first for each source, then for the stacked analysis. The following sections show the results of the
1827 likelihood fitting for a suite of background trials.

1828 I assume that TS values are physical: $TS \geq 0$. $\epsilon[x]$ indicate the fraction of events where $TS < x$.
1829 For TS plots shown here, the decimal values of x are 1.0e-2 and 1.0e-3. Each subplot represents
1830 a simulation of 100,000 data-scrambled background trials. Section 7.5.1 show the background TS
1831 distributions obtained from Segue 1, a source with little Earth attenuation and large J -factor, and
1832 Ursa Major II, which has similarly large J -factor but significantly more Earth attenuation, assuming
1833 DM annihilation into $b\bar{b}$, $\tau\bar{\tau}$, and $\nu_\mu\bar{\nu}_\mu$. I show the TS distributions of a stacked study of 15 sources
1834 for all DM annihilation channels.

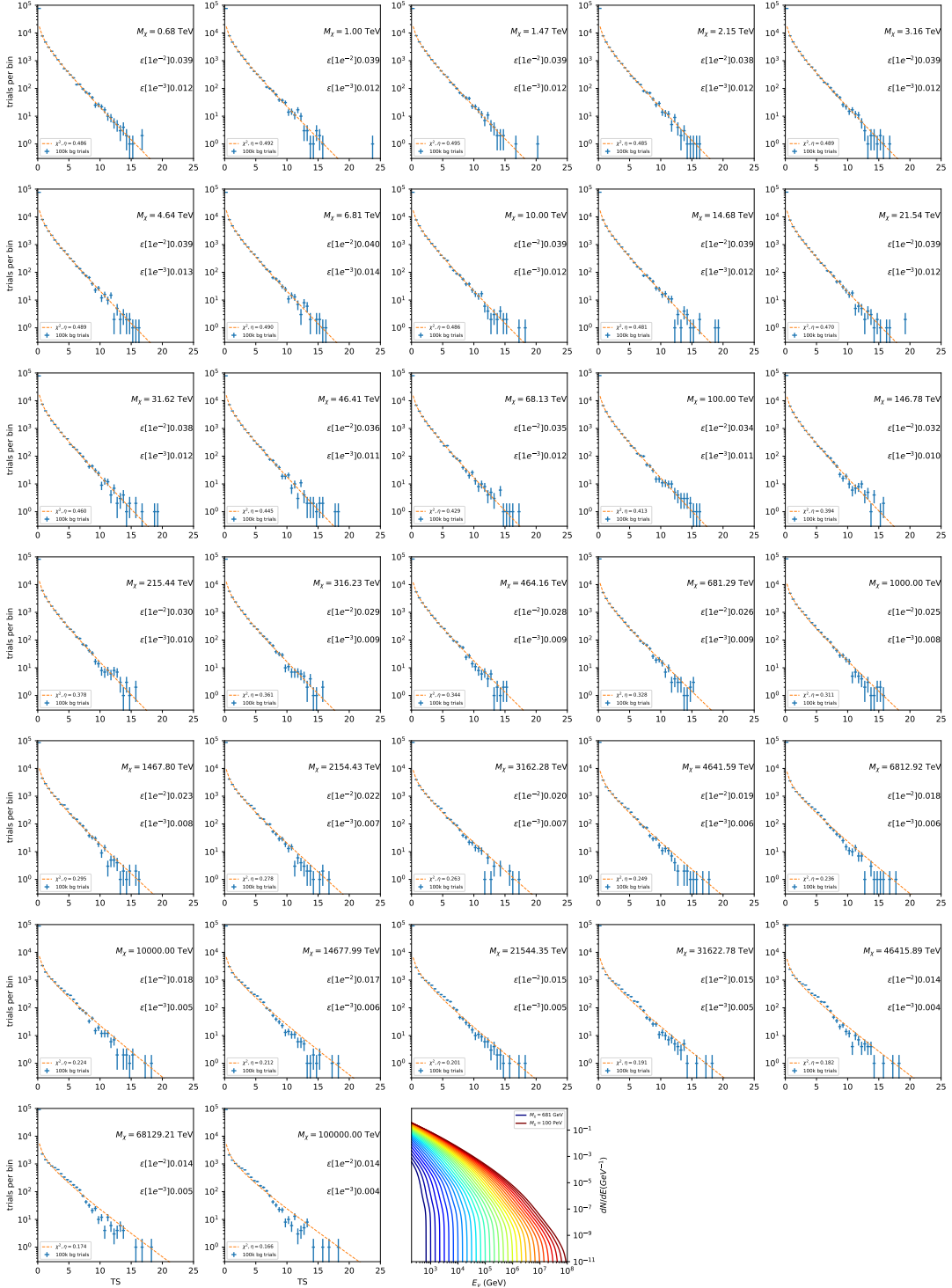


Figure 7.6 Test statistic (TS) distributions for Segue 1 and $\chi\chi \rightarrow b\bar{b}$. Each subplot, except the final, is the TS distribution for a specific DM mass listed in the subplot. Orange dashed lines are the traces for a χ^2 distribution with 1 degree of freedom. $\epsilon[\cdot]$ is the fraction of trials smaller than the bracketed value. The final subplot features the all DM spectral models, similar to Fig. 7.5, used as input for the TS distributions.

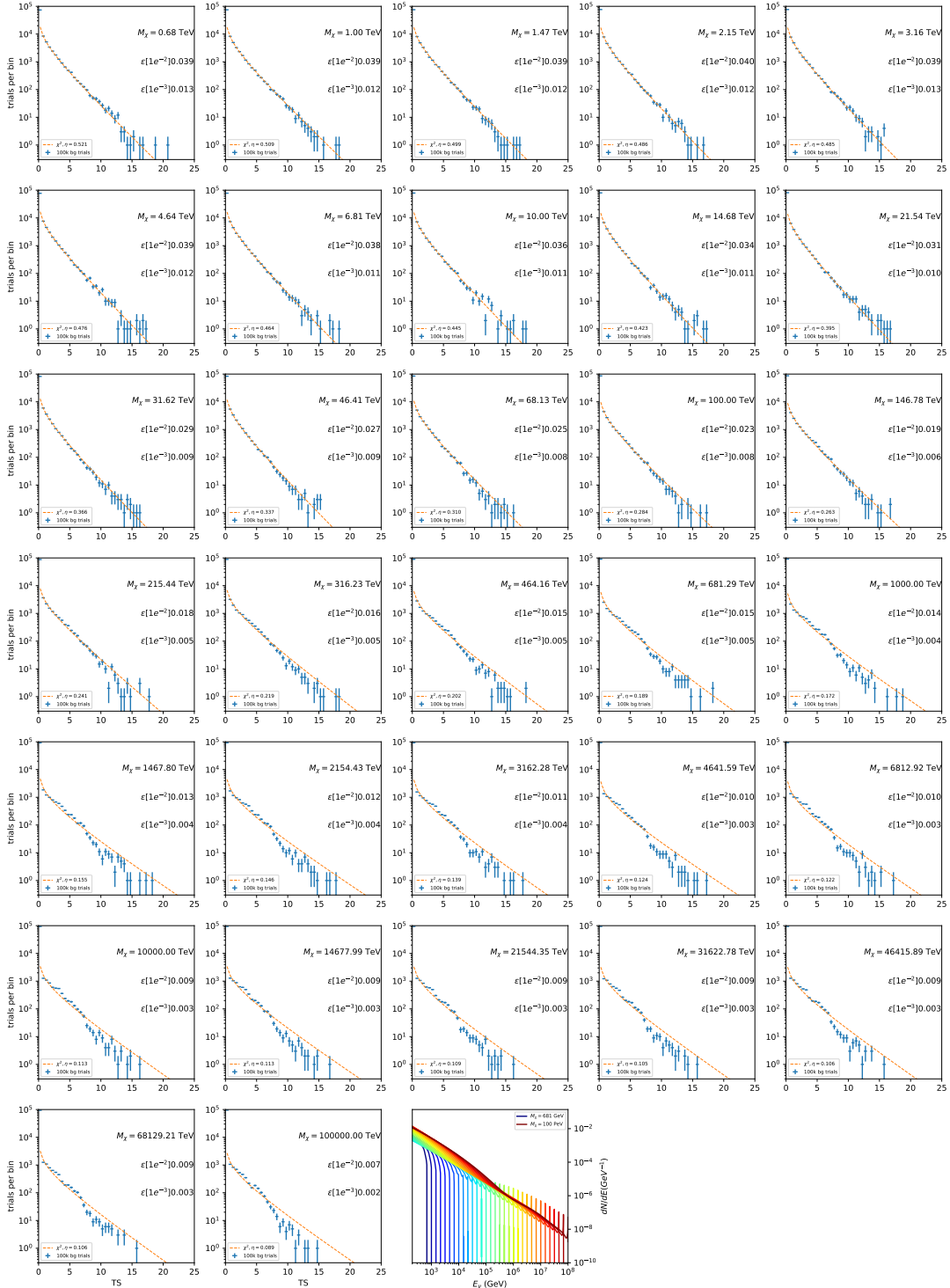


Figure 7.7 Same as Fig. 7.6 for Segue 1 $\chi\chi \rightarrow \tau\bar{\tau}$.

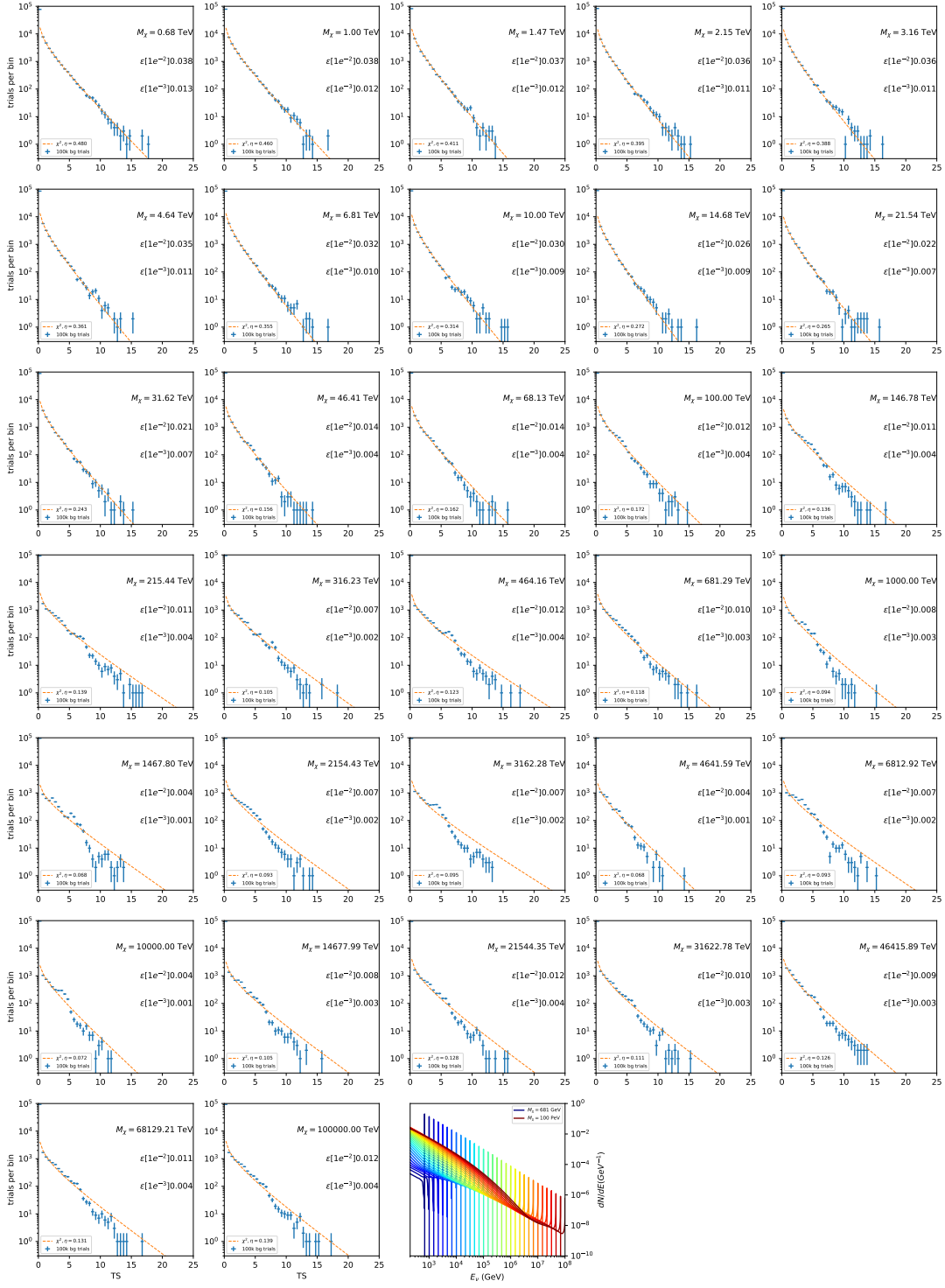


Figure 7.8 Same as Fig. 7.6 for Segue 1 $\chi\chi \rightarrow \nu_\mu\bar{\nu}_\mu$.

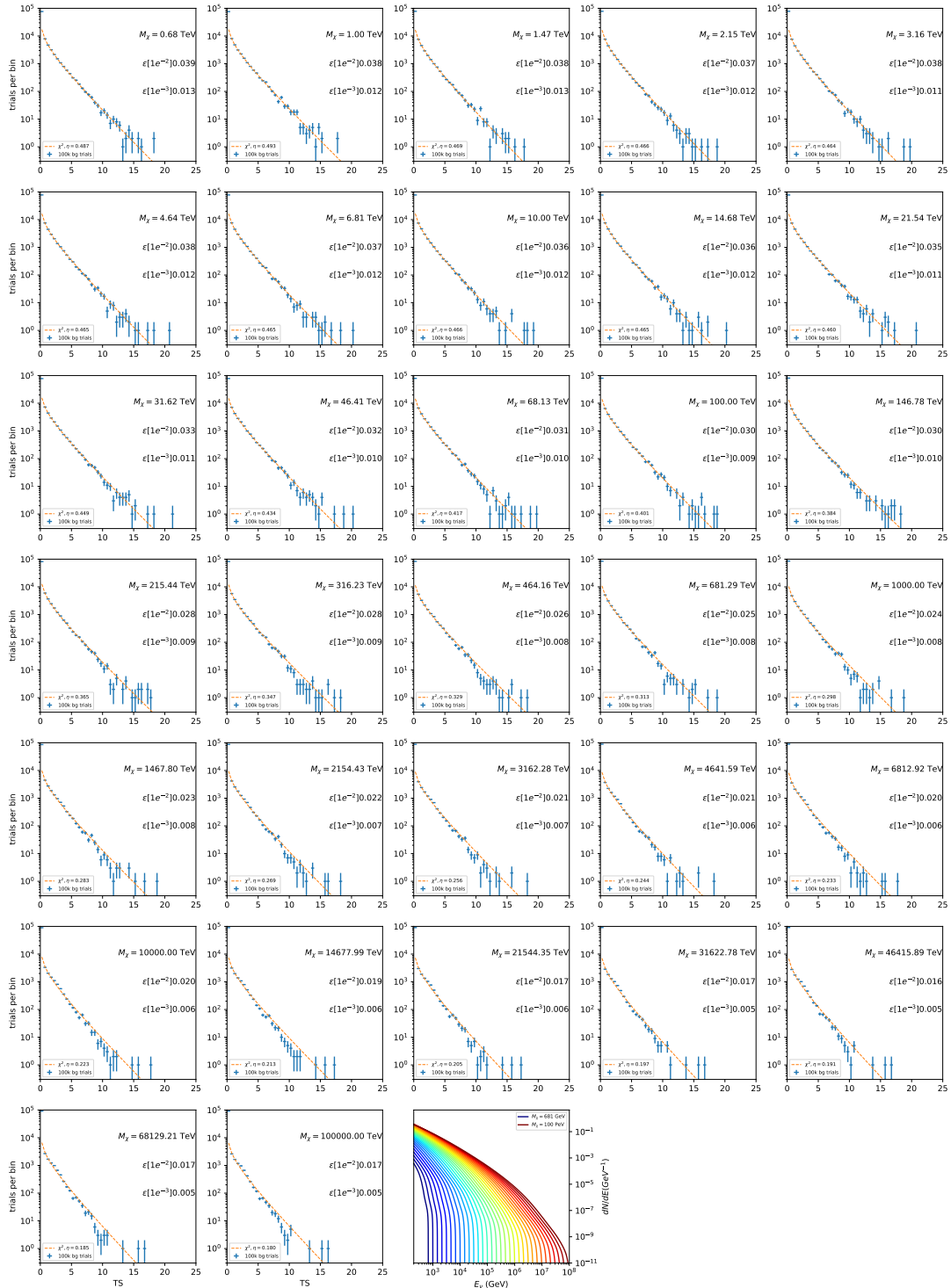


Figure 7.9 Same as Fig. 7.6 for Ursa Major II 1 $\chi\chi \rightarrow b\bar{b}$.

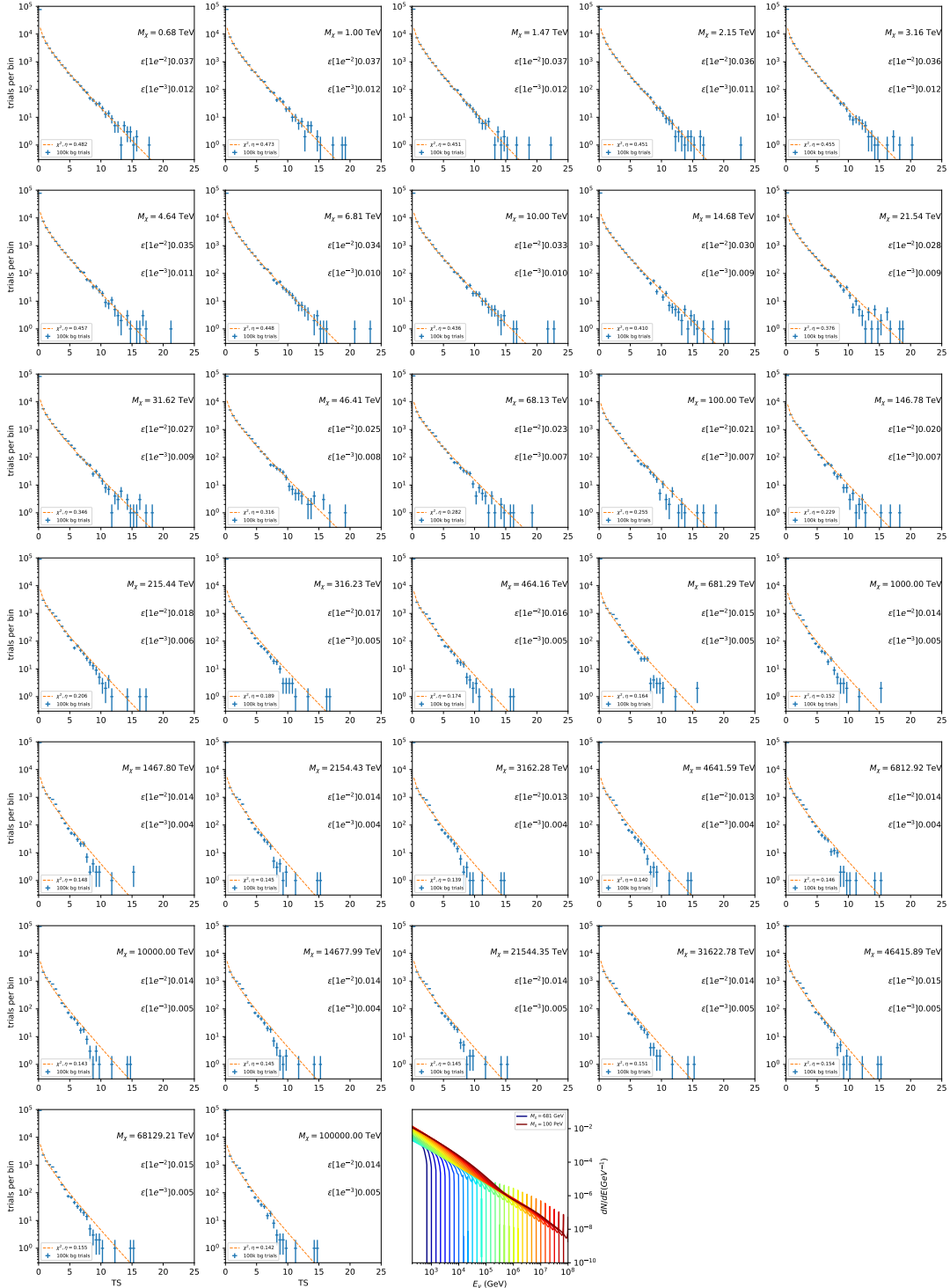


Figure 7.10 Same as Fig. 7.6 for Ursa Major II 1 $\chi\chi \rightarrow \tau\bar{\tau}$.

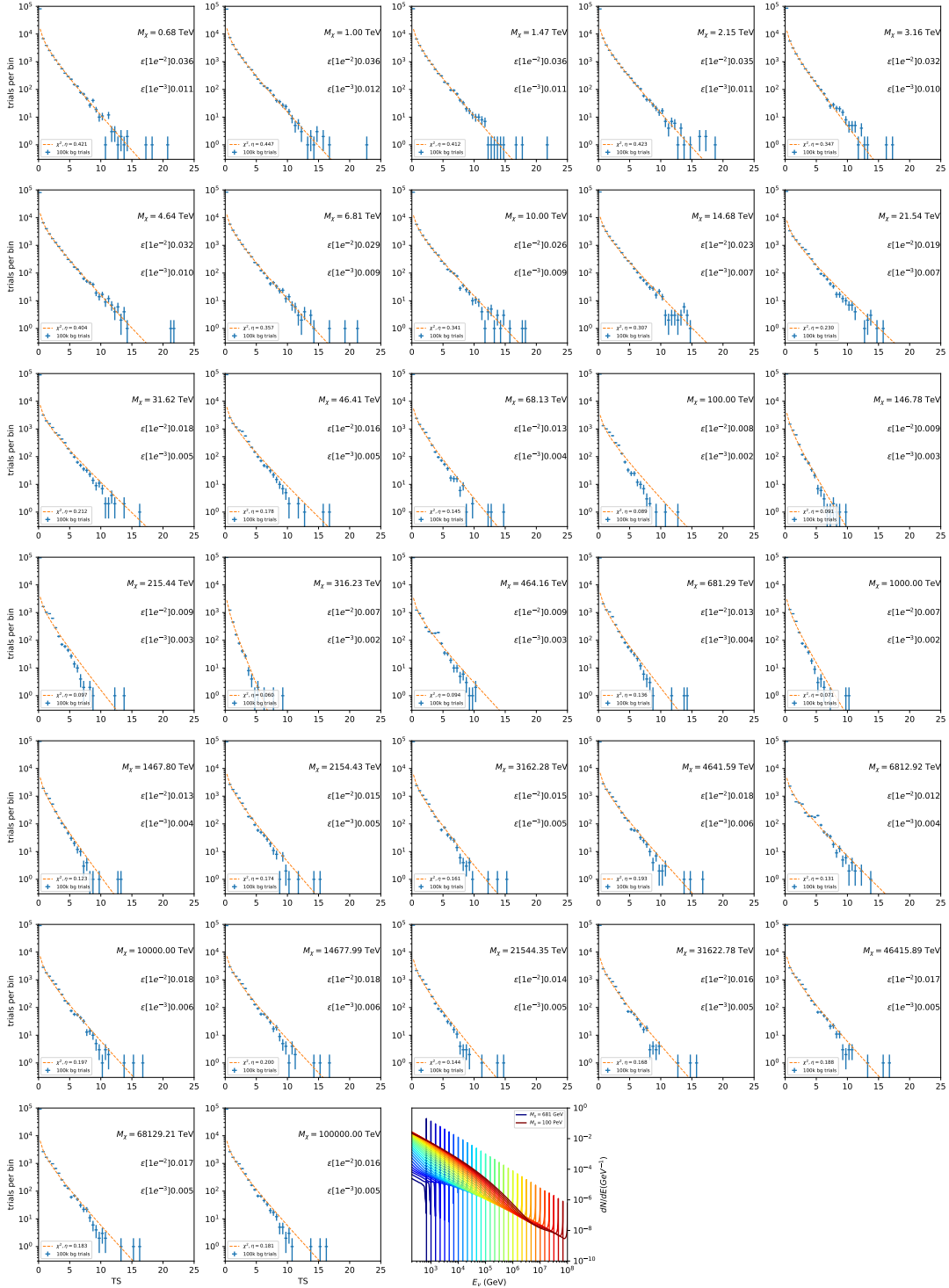


Figure 7.11 Same as Fig. 7.6 for Ursa Major II 1 $\chi\chi \rightarrow \nu_\mu\bar{\nu}_\mu$.

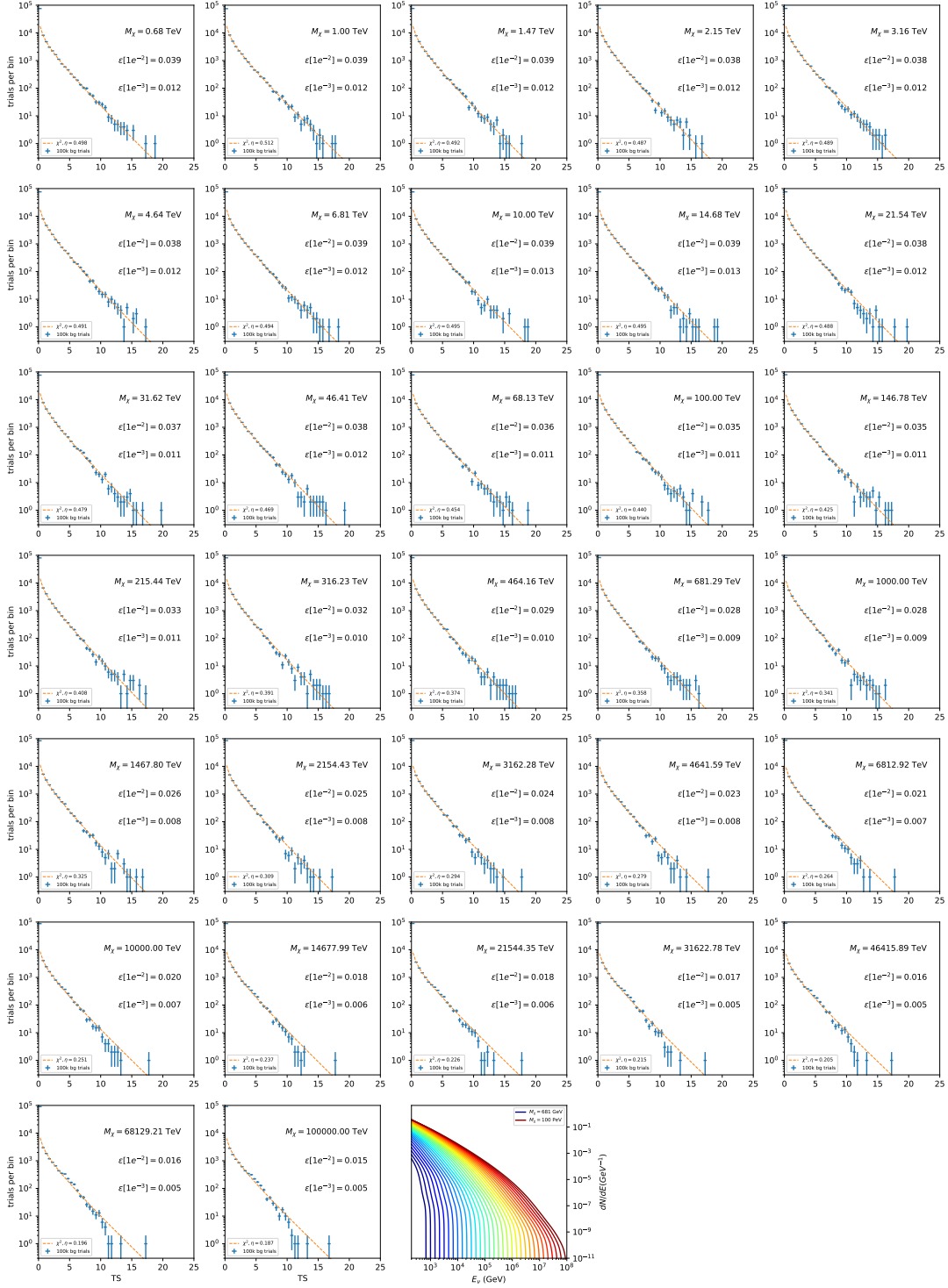


Figure 7.12 Same as Fig. 7.6 for 15, \mathcal{GS} J -factor, stacked sources and $\chi\chi \rightarrow b\bar{b}$.

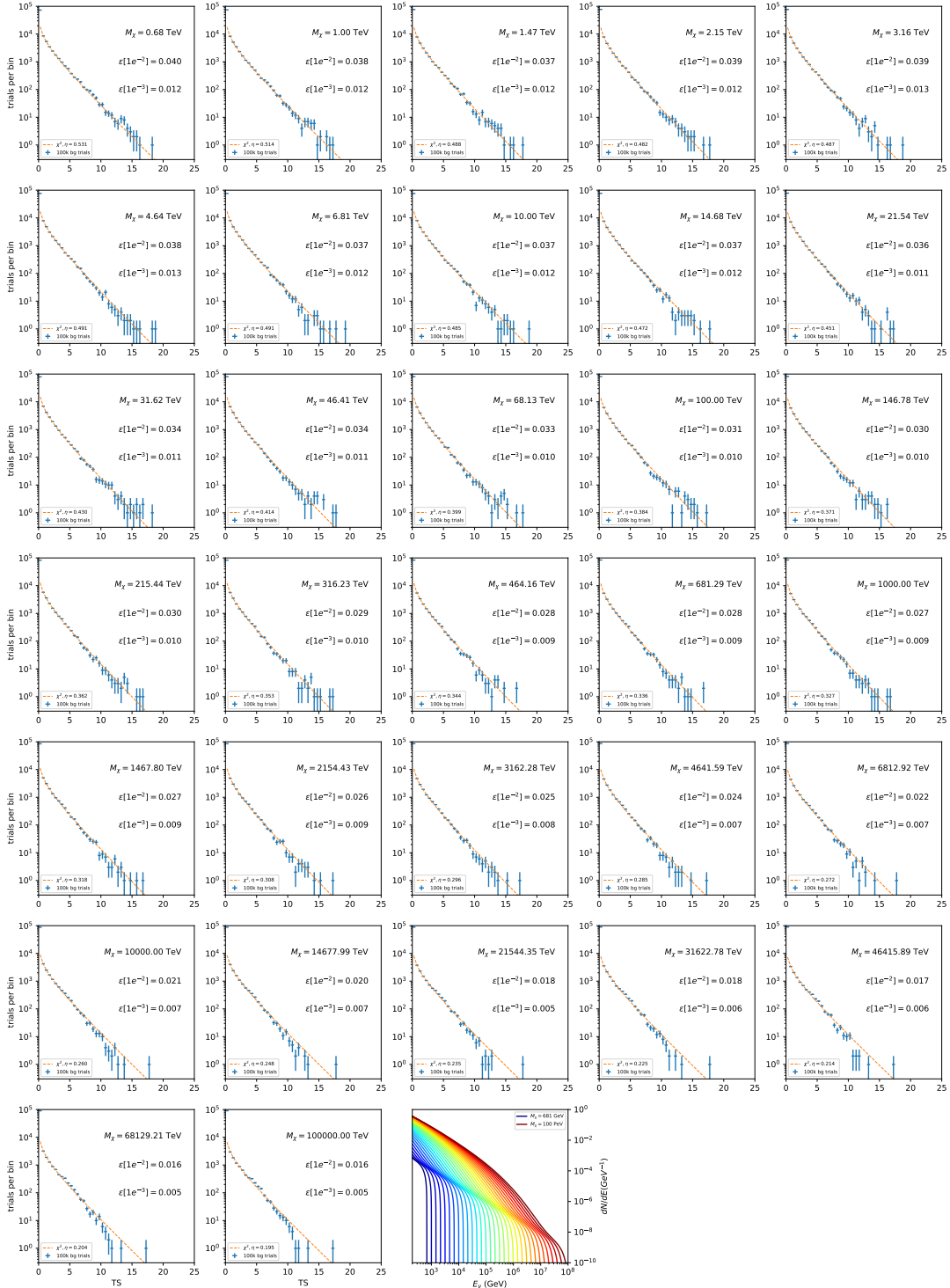


Figure 7.13 Same as Fig. 7.6 for 15, GS J-factor, stacked sources and $\chi\chi \rightarrow t\bar{t}$.

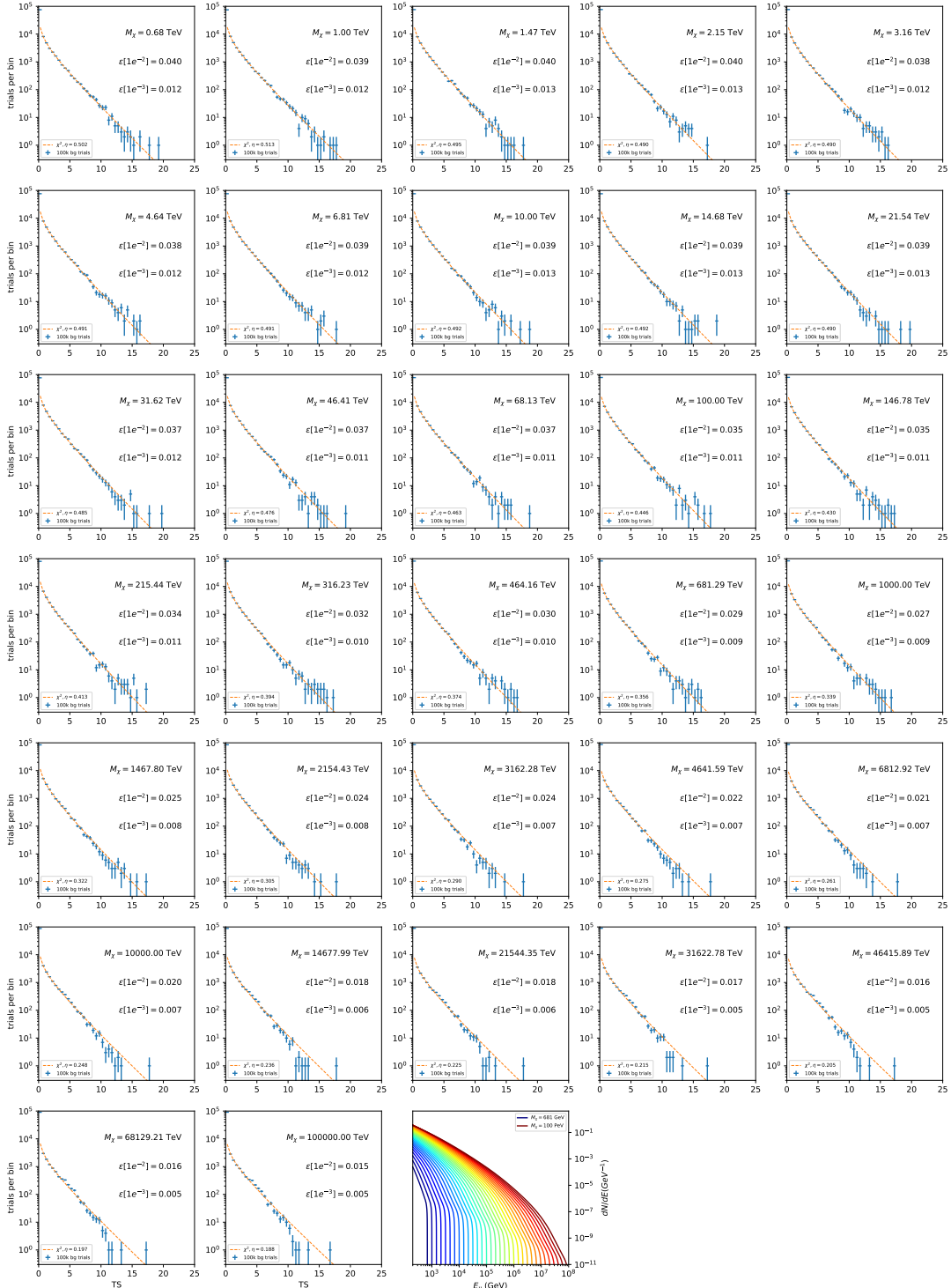


Figure 7.14 Same as Fig. 7.6 for 15, $\mathcal{G}\mathcal{S}$ J -factor, stacked sources and $\chi\chi \rightarrow u\bar{u}$.

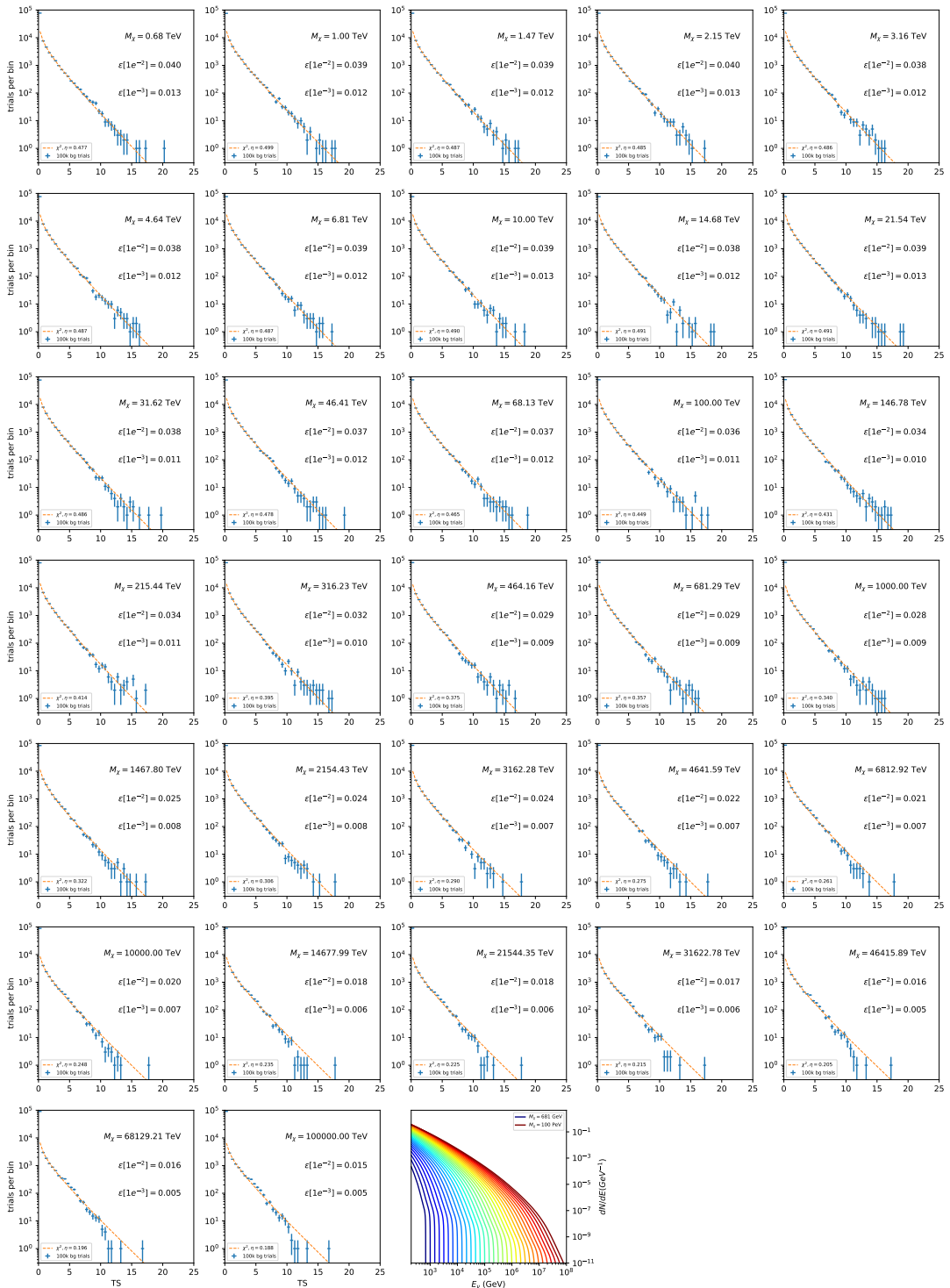


Figure 7.15 Same as Fig. 7.6 for 15, $\mathcal{G}\mathcal{S}$ J-factor, stacked sources and $\chi\chi \rightarrow d\bar{d}$.

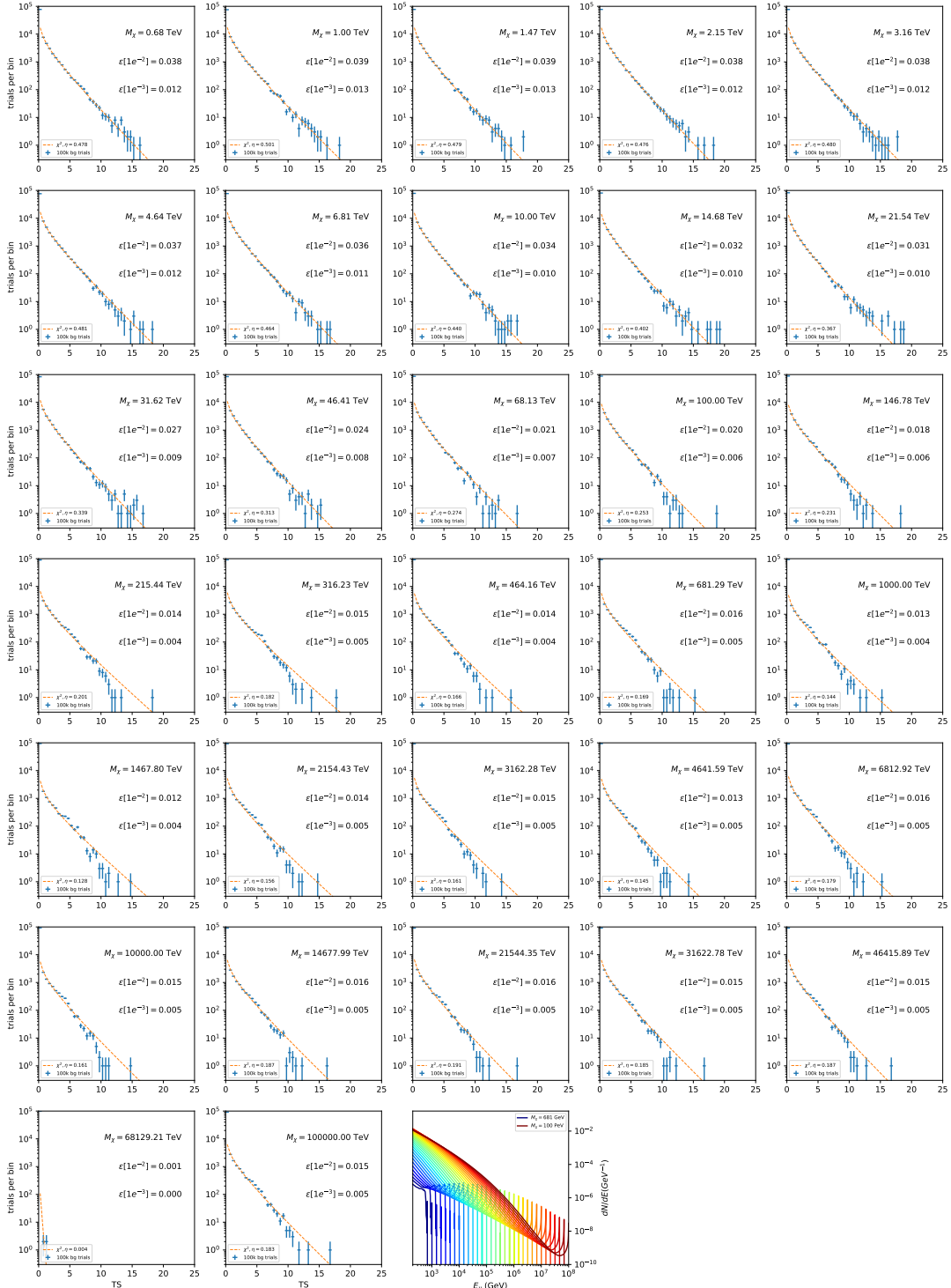


Figure 7.16 Same as Fig. 7.6 for 15, \mathcal{GS} J-factor, stacked sources and $\chi\chi \rightarrow e\bar{e}$.

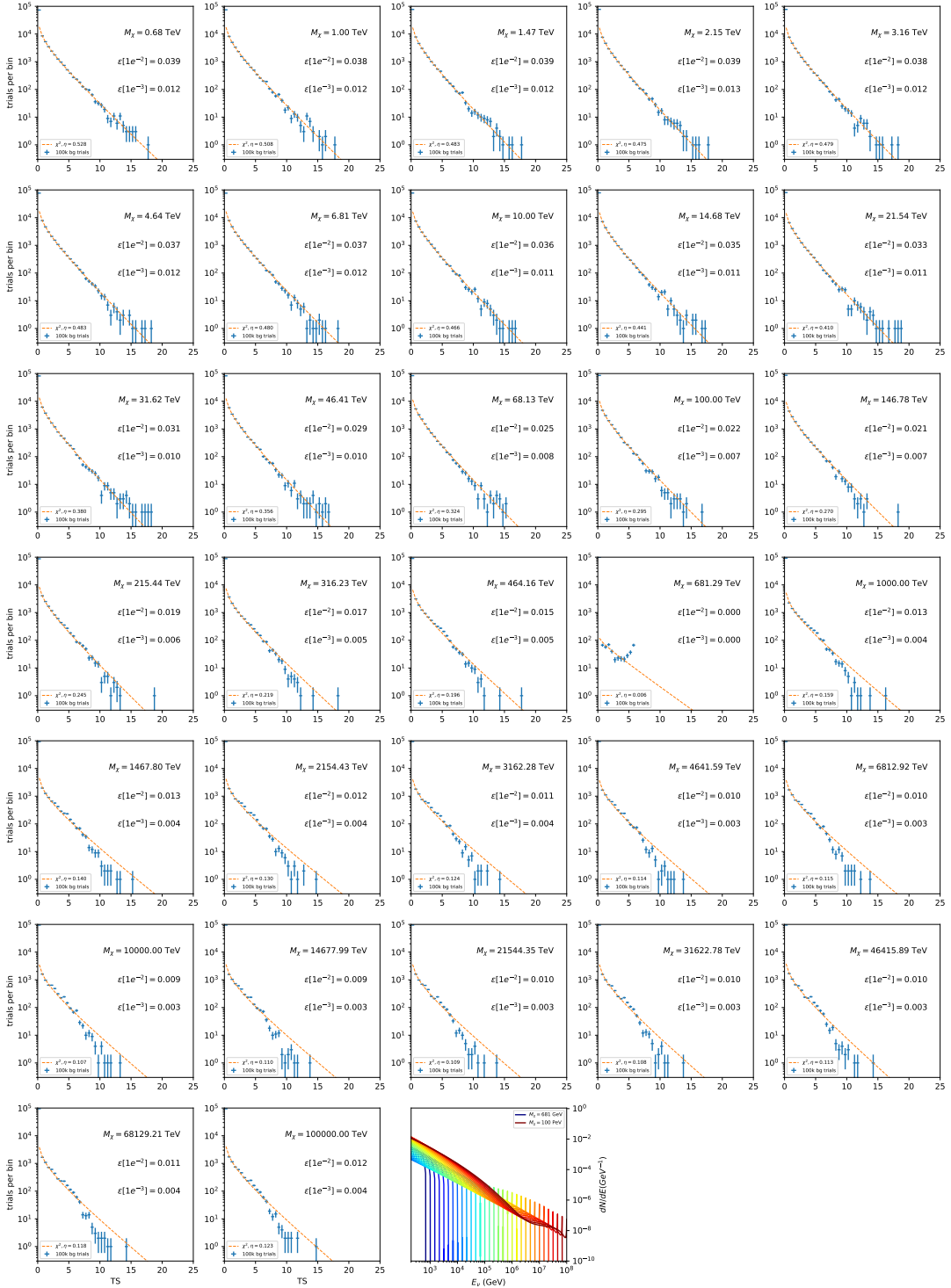


Figure 7.17 Same as Fig. 7.6 for 15, $\mathcal{G}\mathcal{S}$ J -factor, stacked sources and $\chi\chi \rightarrow \mu\bar{\mu}$.

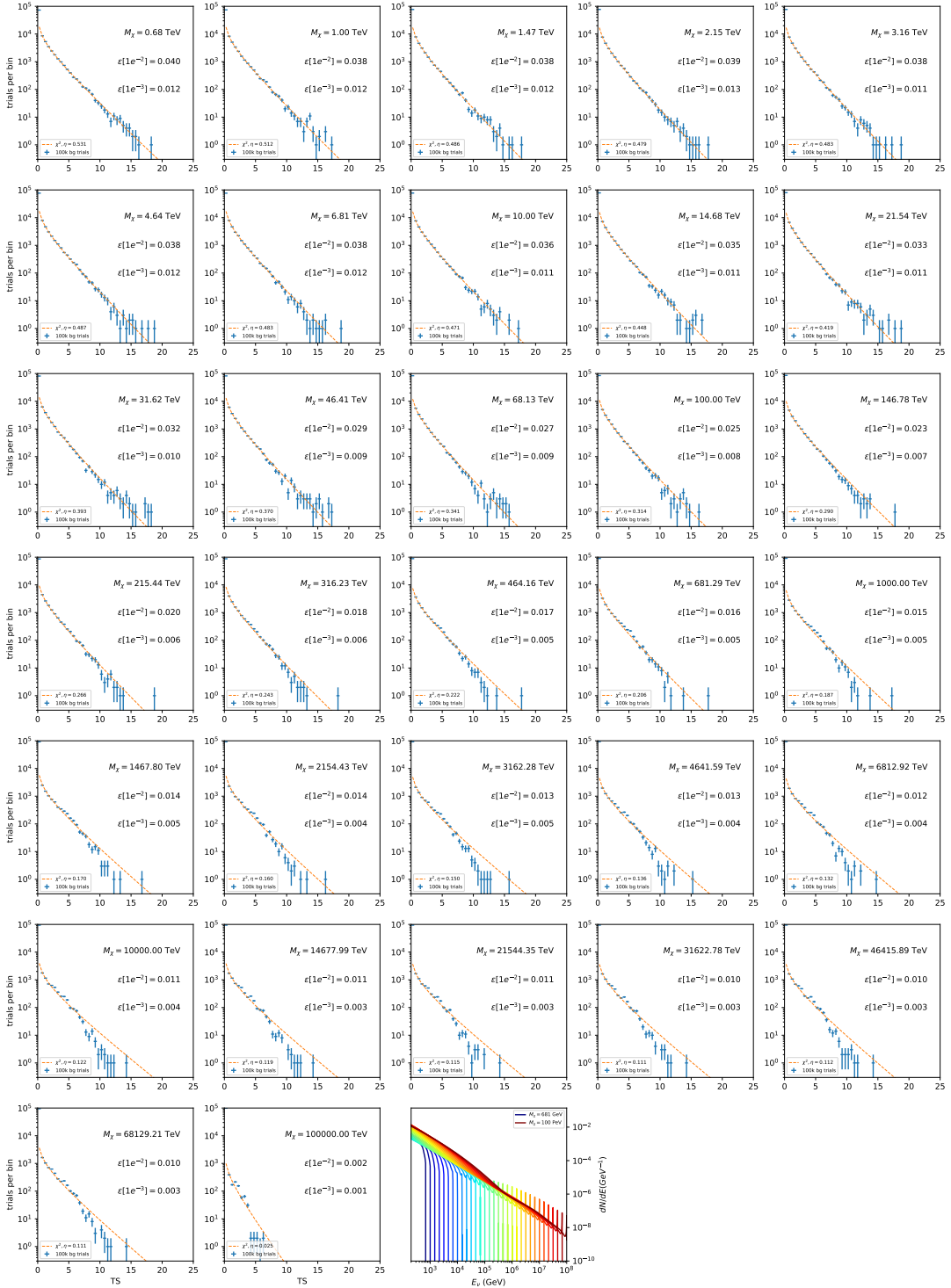


Figure 7.18 Same as Fig. 7.6 for 15, \mathcal{GS} J -factor, stacked sources and $\chi\chi \rightarrow \tau\bar{\tau}$.

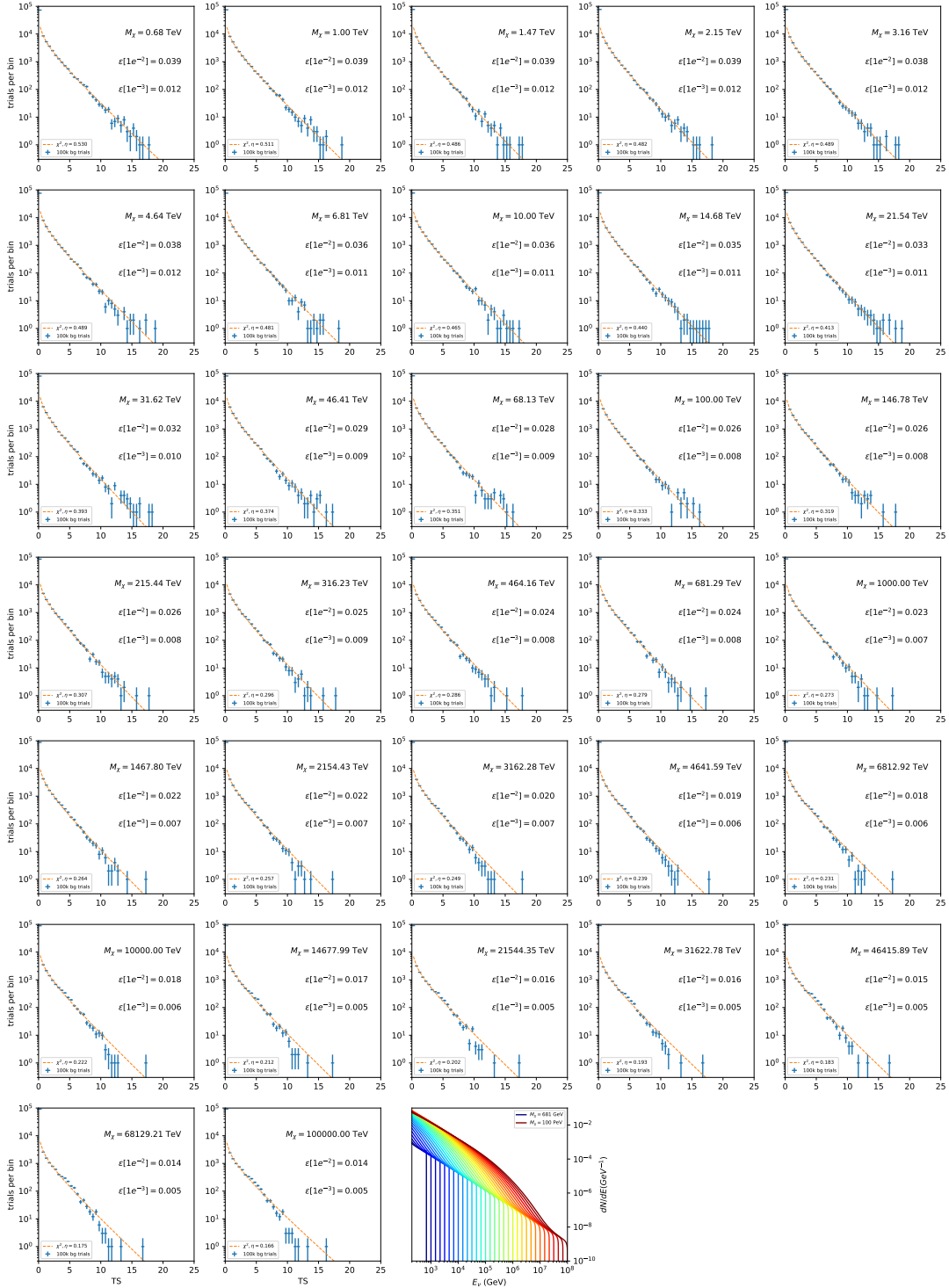


Figure 7.19 Same as Fig. 7.6 for 15, \mathcal{GS} J-factor, stacked sources and $\chi\chi \rightarrow W^+W^-$.

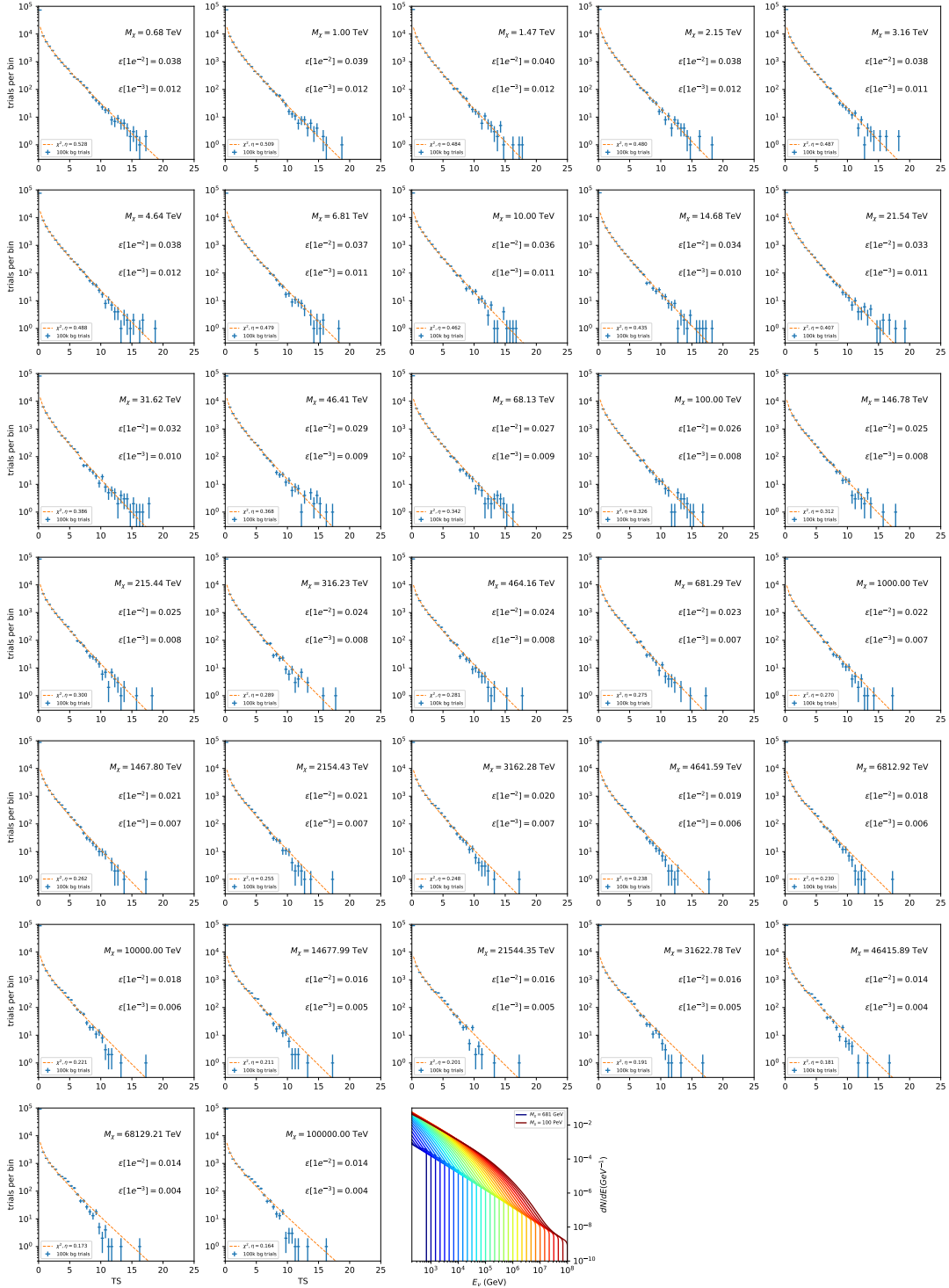


Figure 7.20 Same as Fig. 7.6 for 15, \mathcal{GS} J -factor, stacked sources and $\chi\chi \rightarrow ZZ$.

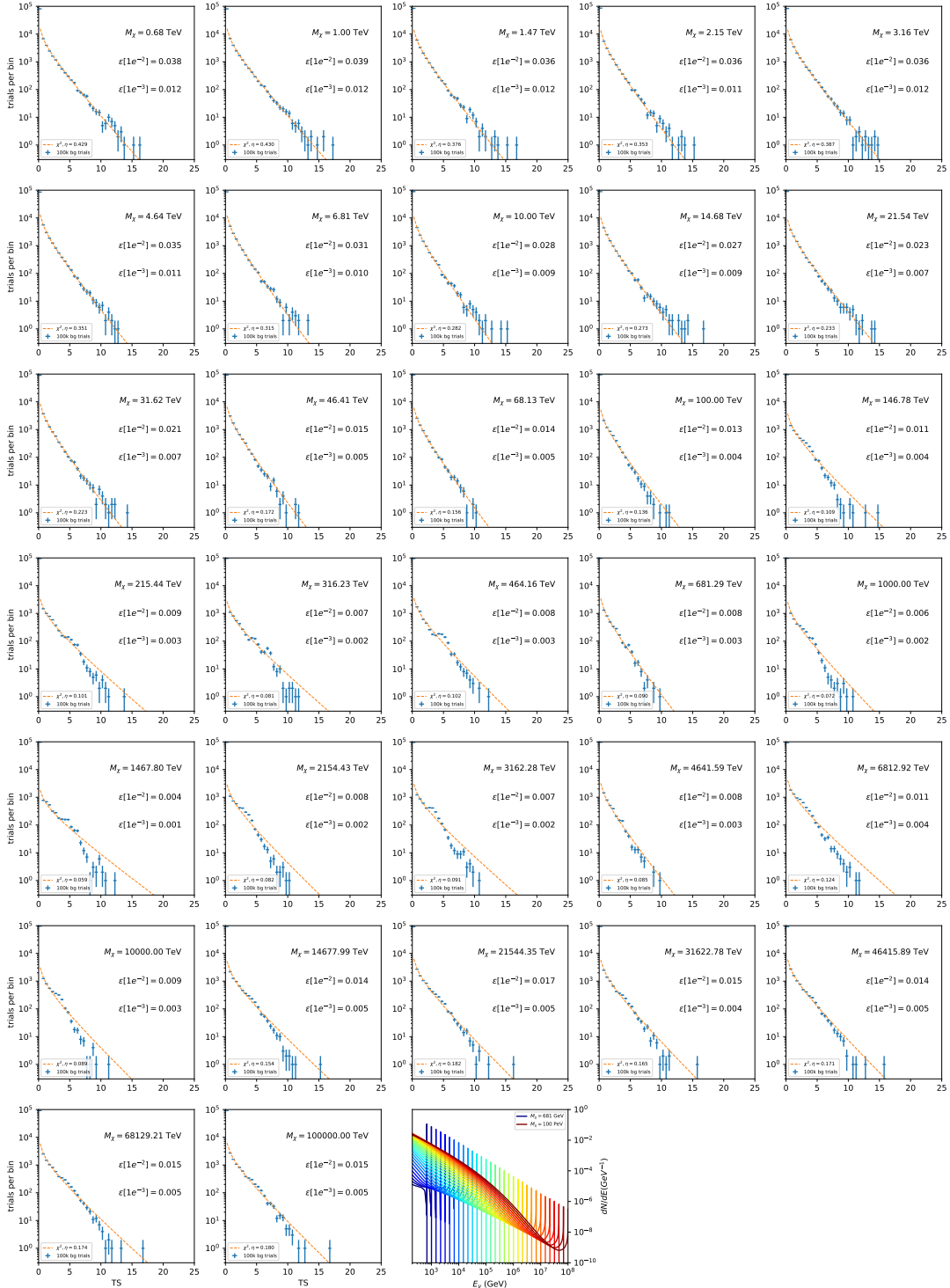


Figure 7.21 Same as Fig. 7.6 for 15, GS J-factor, stacked sources and $\chi\chi \rightarrow \nu_e \bar{\nu}_e$.

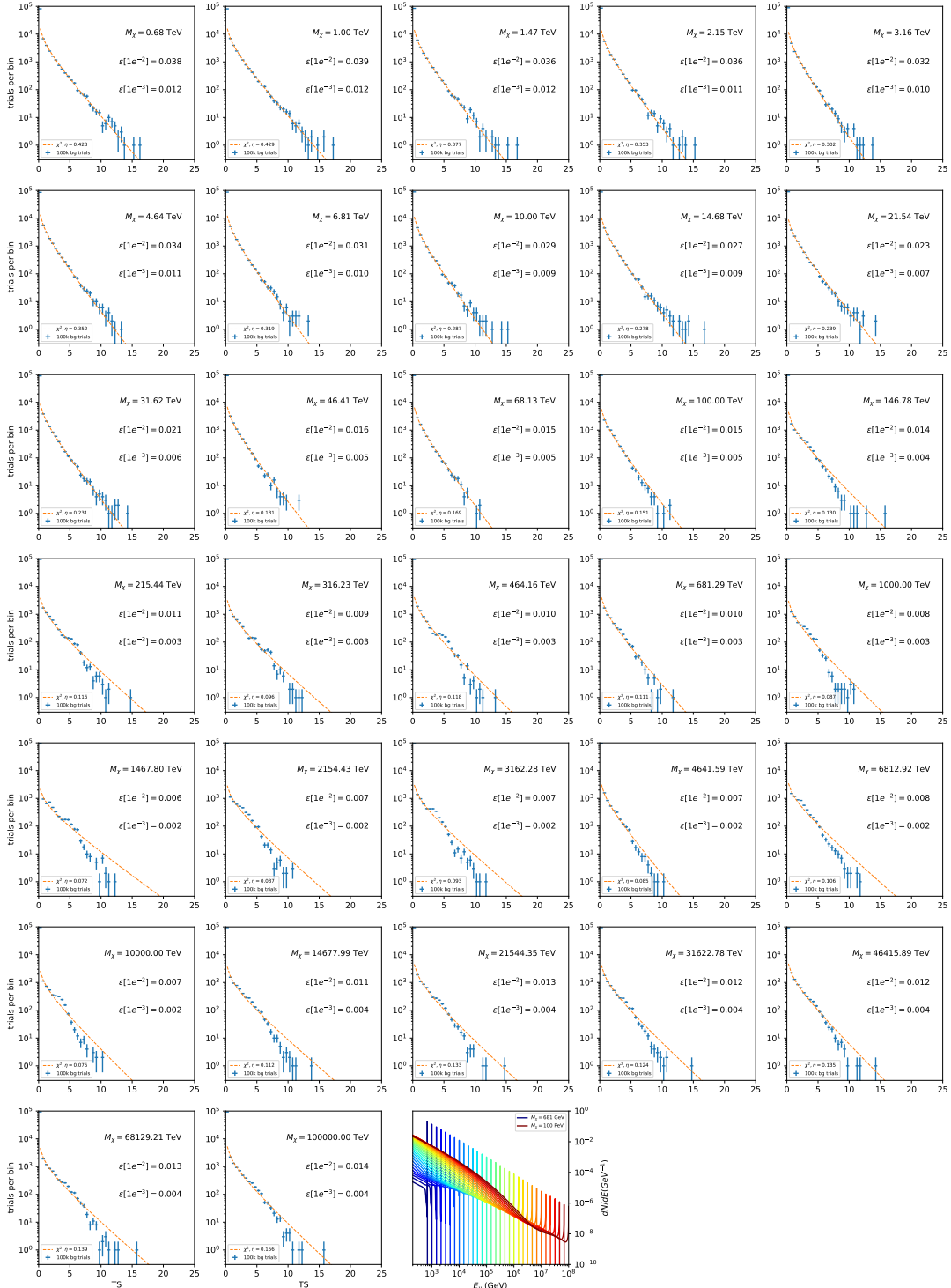


Figure 7.22 Same as Fig. 7.6 for 15, \mathcal{GS} J -factor, stacked sources and $\chi\chi \rightarrow \nu_\mu \bar{\nu}_\mu$.

1835 **7.5.1 TS per Source**

1836 Figure 7.6 to Figure 7.11 present the TS distributions for Segue 1 and Ursa Major II for 100,000
1837 trials. More studies for all annihilation channels and remaining 13 sources were also performed
1838 and are documented in IceCube’s internal wiki.

1839 Almost every distribution produced follows a χ^2 distribution with 1 degree of freedom. This is
1840 more true for low m_χ than high m_χ models. These observations are important for future assumptions
1841 made in Sec. 8 and may justify statistical calculations assuming our test statistics follow a χ^2 with
1842 1 degree of freedom.

1843 **7.5.2 Stacked TS**

1844 Figure 7.12 to Figure 7.22 present the TS distributions for a stacked study of 15 sources with
1845 \mathcal{GS} J -factors on 100,000 trials. The presentation of these plots are identical to the single source
1846 distributions in Section 7.5.1. We see similar behaviour in the stacked TS distributions compared
1847 to the single source studies.

1848 **7.6 Signal Recovery**

1849 We also wish to understand how well the analysis is able to reconstruct signal neutrinos. In
1850 order to test this, we inject neutrinos from our spectral models randomly then attempt to discern
1851 the number of signal neutrinos in the simulated data. Figure 7.23 and Figure 7.24 show this study
1852 for $\chi\chi \rightarrow b\bar{b}$, $t\bar{t}$, and $\nu_\mu\bar{\nu}_\mu$ for a stacked analysis of 15 sources. Figure C.3 to Figure C.8 show
1853 identical studies for Segue 1 and Ursa Major II. We see that the analysis is conservative at smaller
1854 m_χ , yet improves at larger m_χ . We also see that the uncertainty is small for the neutrino annihilation
1855 spectra, and the uncertainty is larger for softer channels like $b\bar{b}$.

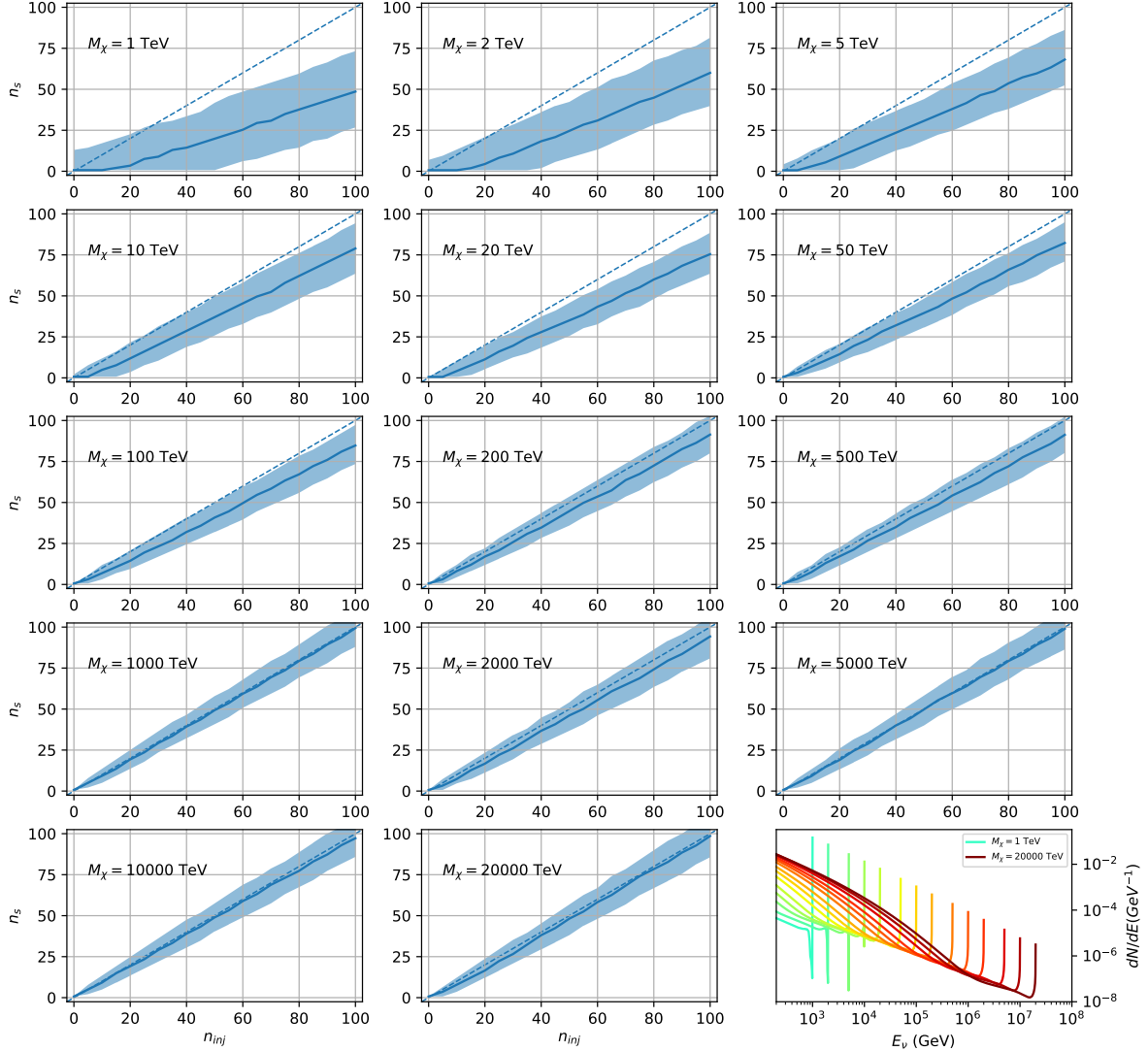


Figure 7.23 Signal Recovery study for an analysis with 15 stacked sources using the \mathcal{GS} J -factors [55]. Above shows 14 studies for DM mass ranging between 1 TeV and 20 PeV for $\chi\chi \rightarrow \mu_\mu\bar{\mu}_\mu$. The bottom right subplot features every spectral model used as input for the remaining subplots. The remaining subplots show n_{inj} as the number of signal events injected into background simulation. Whereas, n_s is the number of signal events recovered from analyzing the injected simulation. Blue line represents the median values of 100 simulations. Light blue bands show the 1σ statistical uncertainty around the median.

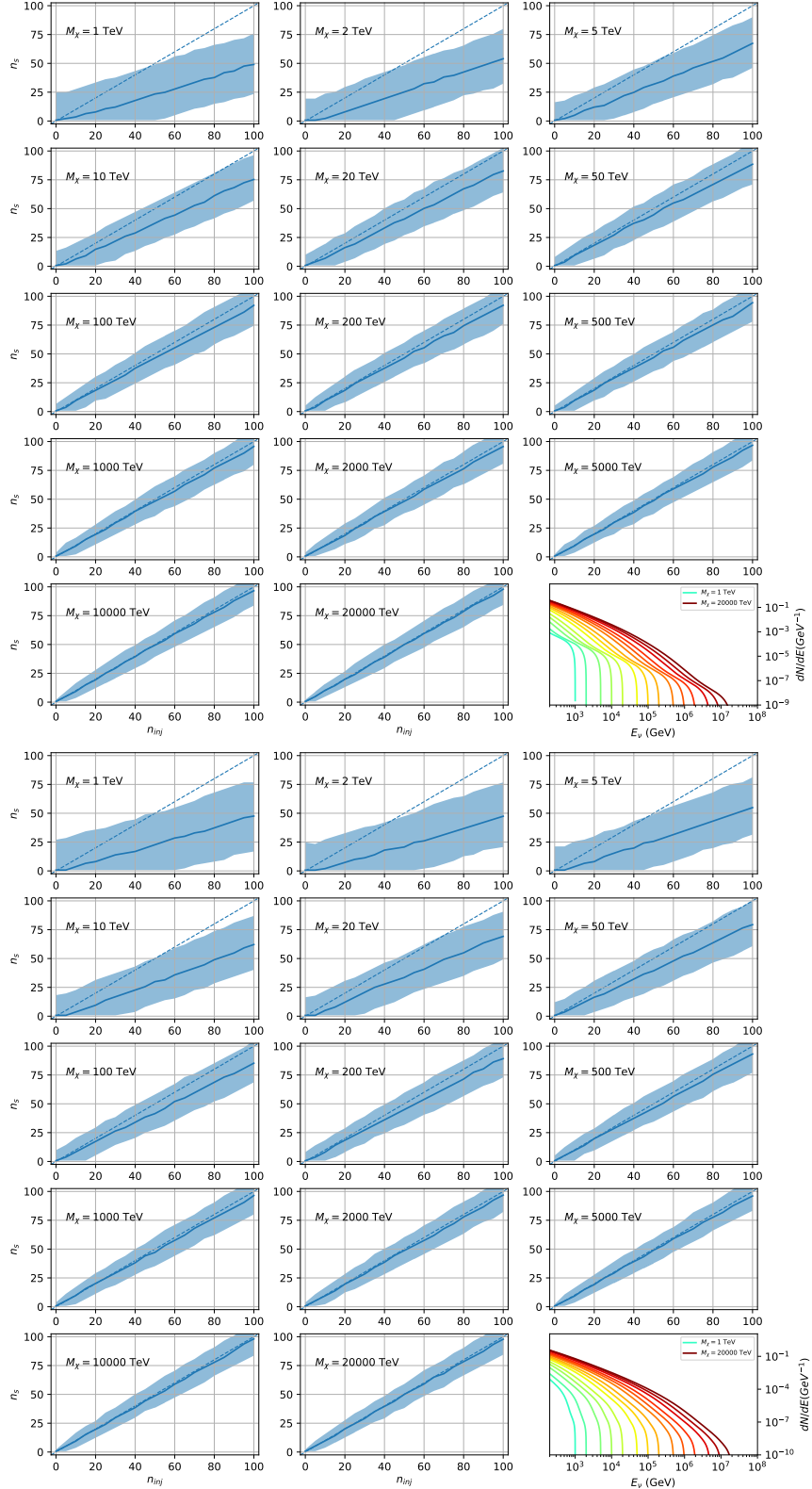


Figure 7.24 Same as Fig. 7.23 but for $\chi\chi \rightarrow t\bar{t}$ (top) and $b\bar{b}$ (bottom).

1856 **7.6.1 Sensitivities**

1857 In IceCube, we usually define the 90% confidence level (CL), as the minimum number of signal
1858 events (n_s) required to have a Type I error rate smaller than 0.5 and Type II error rate of 0.1. We
1859 compute n_s from the following equation

$$n_s = T_{\text{live}} \int_0^{\Delta\Omega} d\Omega \int_{E_{\min}}^{E_{\max}} dE_\nu A_{\text{eff}}(\hat{n}, E_\nu) \frac{d\Phi_\nu}{d\Omega dE_\nu}(\hat{n}, E_\nu), \quad (7.8)$$

1860 to extract the sensitivity on the dark matter velocity-weighted annihilation cross-section, $\langle\sigma v\rangle$. T_{live}
1861 is the detector live time, A_{eff} is the effective area of the detector, and E_{\min} , E_{\max} are the minimum,
1862 maximum energies of the expected neutrinos, respectively.

1863 Sensitivities are calculated for each source individually as if they were the only source and as a
1864 stack over 1000 trials. From Eq. (7.8) and Eq. (7.1) we can compute the $\langle\sigma v\rangle$ at a 90% confidence
1865 level. Figure 7.26 and Fig. 7.25 show the sensitivities for some DM annihilation channels. Not
1866 all channels computed successfully in time for the writing of this dissertation. Among channels
1867 missing include the charged leptons: e and τ .

1868 **7.7 Systematics**

1869 The current analysis plan is to compare these sensitivities to another J -factor catalog such as
1870 \mathcal{LS} [76] although this was not completed in time for this dissertation. Additionally, we set out to
1871 perform a standard suite of IceCube systematic studies which include: DOM efficiency, Hole ice,
1872 ice absorption, and photon scattering. We do study Earth attenuation, and Section 7.7.1 enumerates
1873 the impact of the Earth on our hardest neutrino spectra.

1874 **7.7.1 Earth Effects**

1875 We look to quantify the impact of the Earth on our sensitivity to $\chi\chi \rightarrow \nu_\mu \bar{\nu}_\mu$. This channel is
1876 expected to be among the significantly impacted annihilation channels because it has a significant
1877 contribution at PeV energies for $m_\chi \geq 1\text{PeV}$. The Earth is expected to attenuate these higher energy
1878 neutrinos. However, these neutrino spectra have significant low energy contributions, so we do not
1879 expect to entirely lose our sensitivity. This motivated a study examining our $\langle\sigma v\rangle$ sensitivity over
1880 all DM masses sampled for a selection of declinations.

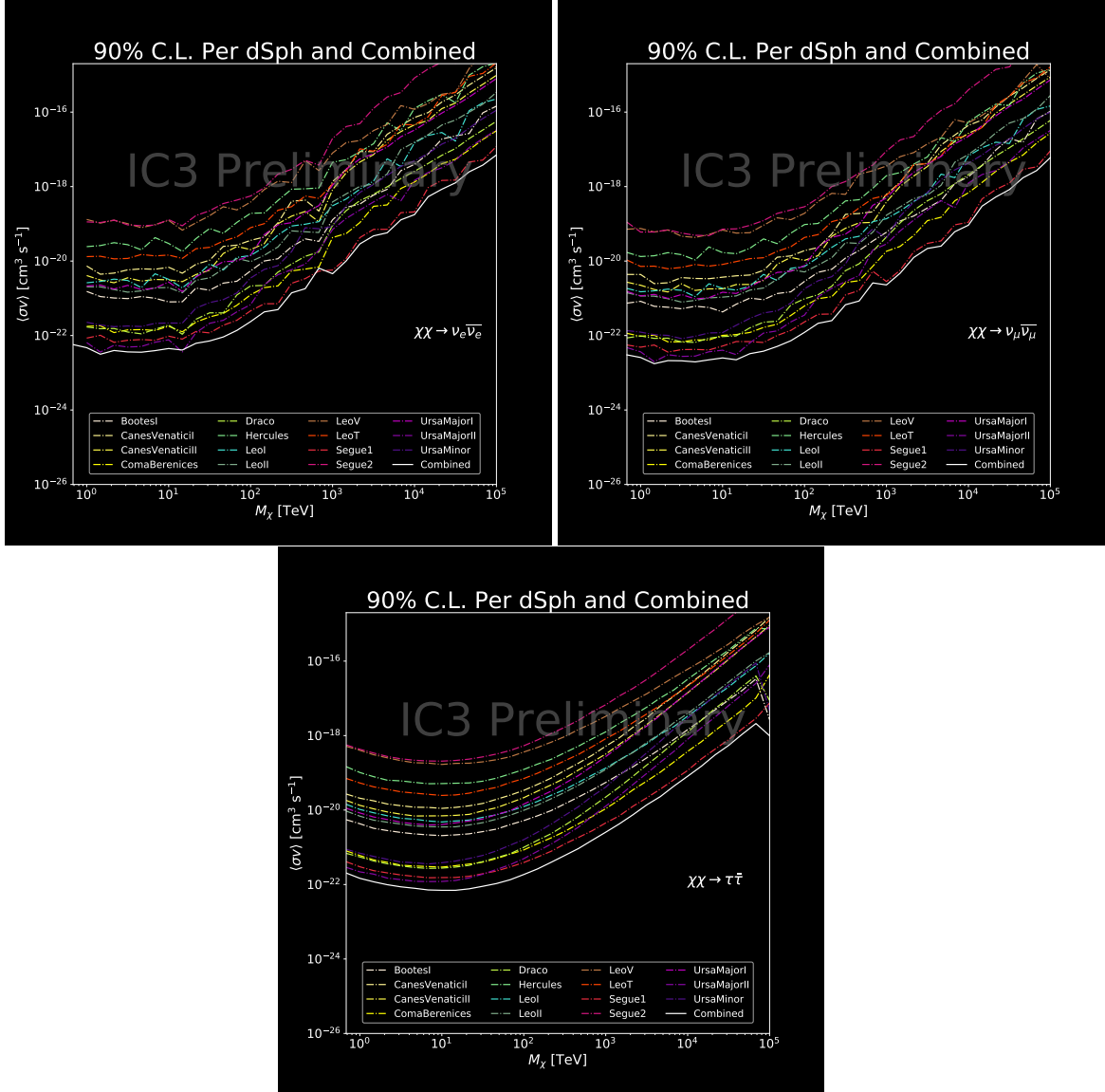


Figure 7.25 IceCube North Sky Track Sensitivities. Each panel shows sensitivity curves for various DM annihilation channels. Sensitivities are for the velocity-weighted cross-section $\langle\sigma v\rangle$ versus m_χ . Dotted, colored lines are sensitivities for individual sources. Solid white lines are for the combined sensitivity of all 15 \mathcal{GS} sources used in this study.

For this systematic study, I sample 6 DM masses per decade from 681 GeV to 100 PeV. I select

declinations that are shared with sources in the \mathcal{GS} catalog: Boötes I, Canes Venatici II, Leo V,

Ursa Major I, and Ursa Minor. I study a fake source who's J -factor is shared with Ursa Major II,

but who's coordinates belong to the aforementioned list. The sensitivity studies performed for each

source (Fig. 7.25 and Section C.5) provided n_s for 1000 trials which we extracted from Eq. (7.8).

We derive $\langle\sigma v\rangle$ using $\log_{10} J = 19.42 \log_{10}(\text{GeV}^2 \text{cm}^{-5})$. Figure 7.28 shows the results.

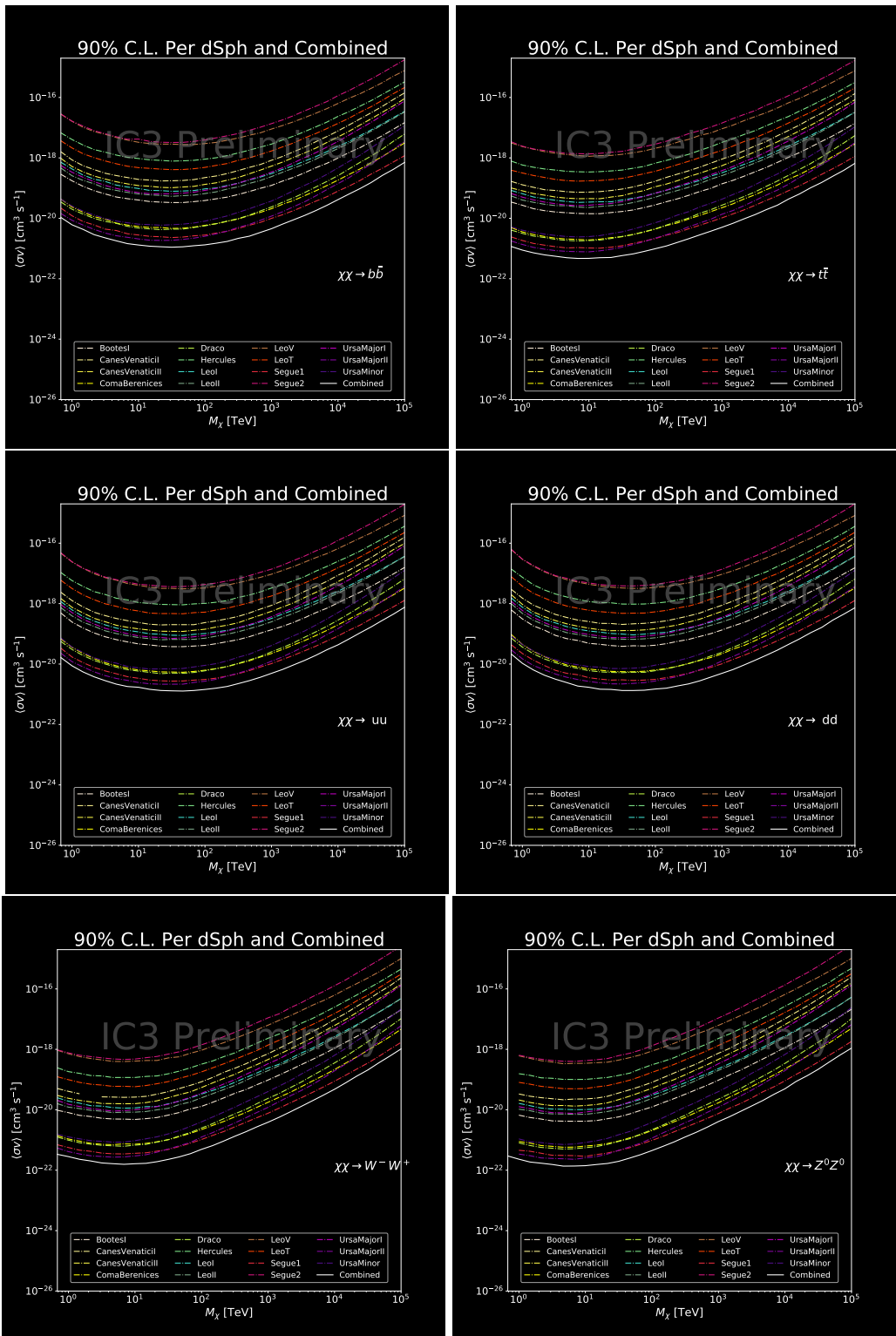


Figure 7.26 Same as Fig. 7.25 for three additional DM annihilation channels.

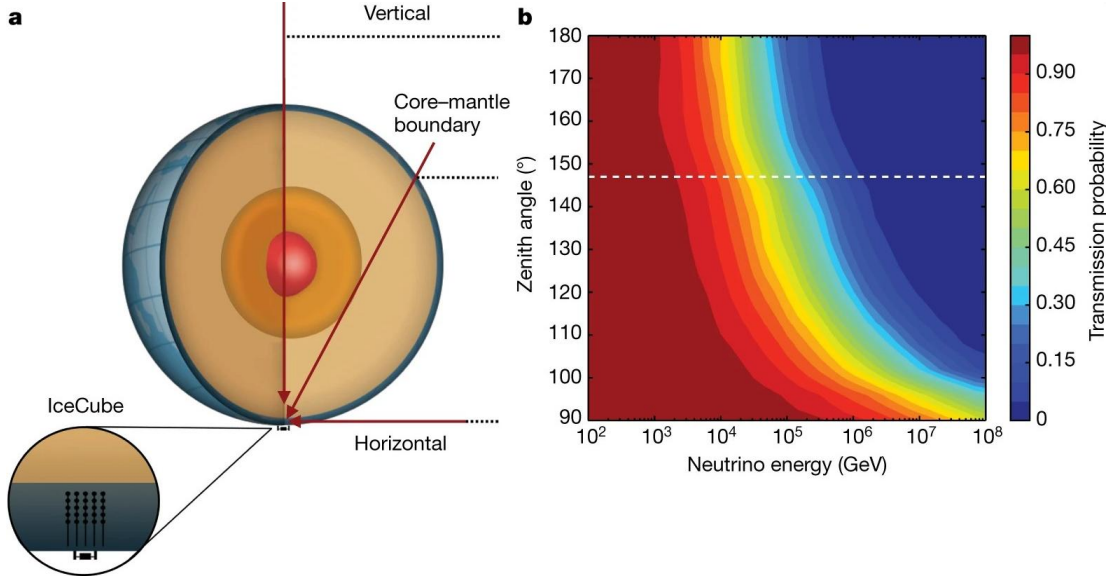


Figure 7.27 Panel A: Neutrino's from the Northern sky and incident on the IceCube detector will travel through the Earth. How much of the Earth these neutrinos travels is a function of zenith from the vertical axis. Panel B: SM prediction of neutrino transmission probabilities for neutrinos arriving at $90^\circ - 180^\circ$ zenith and with 100 GeV to 100 PeV energies. High-energy neutrinos traversing the whole Earth are completely absorbed, whereas low-energy neutrinos pass through unimpeded. Neutrinos coming from above the horizon will arrive unimpeded for all neutrino energies. Figure pulled from [88].

1887 Figure 7.28 shows that we have significant but diminishing sensitivity to sources at high
 1888 declination. We see in the worse case, the sensitivity at high declination is up to an order of
 1889 magnitude worse than at low declination. However, for $m_\chi < 1$ PeV, the sensitivities are very
 1890 similar. The comparable sensitivities imply that a stacking analysis with IceCube is most powerful
 1891 in the 500 GeV to 1 PeV region. Above 1 PeV, our limits and sensitivities are dominated by sources
 1892 near the horizon. When we additionally consider the J -factors, we expect Segue 1 to dominate
 1893 contributions to sensitivity and limits where $m_\chi > 1$ PeV.

1894 7.8 Conclusions

1895 We utilized advanced computing techniques like parallel programming and spline fitting of
 1896 particle physics Monte Carlo to greatly expand and refine IceCube's sensitivity to DM annihilation
 1897 from dSphs. Furthermore, we imported updated astrophysical and particle physics models that
 1898 better represent what we believe neutrino signals from DM annihilation should look like. We, for
 1899 the first time, build an analysis that is sensitive to PeV DM annihilation.

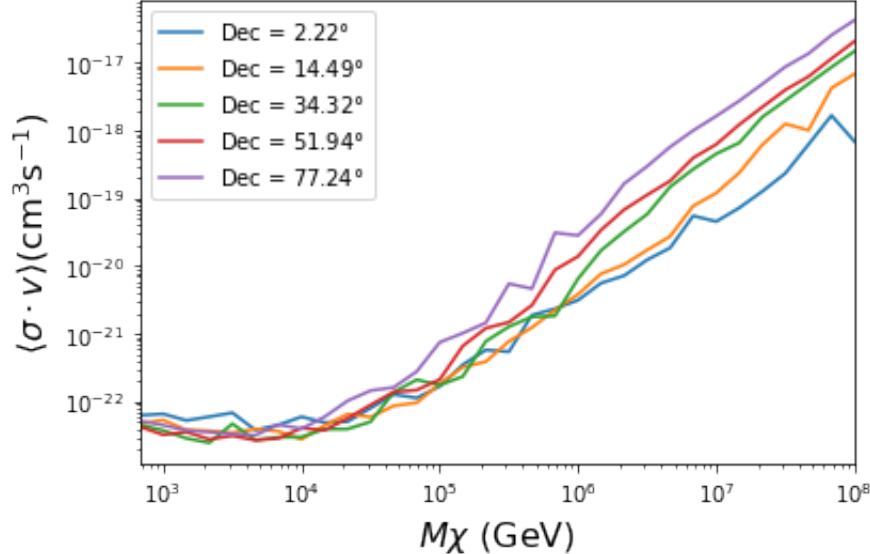


Figure 7.28 $\langle\sigma v\rangle$ sensitivities for 5 imaginary sources with $\log_{10} J = 19.42$ $\log_{10}(\text{GeV}^2 \text{cm}^{-5})$. Each imaginary source shares a declination with a source in Tab. 5.1

1900 When we compare to previous IceCube publications of dSphs [79], we see an order of magnitude
 1901 improvement to our sensitivity. This analysis has been working group approved within IceCube
 1902 and is currently under collaboration review before unblinding. These processes did not complete
 1903 in time for this dissertation. Therefore we do not show data for this thesis and is the clear next step.

1904 The test statistic distributions in this analysis also demonstrate more characteristic behavior
 1905 compared to previous DM analyses [83, 87]. With a 10-year dataset, we finally have enough
 1906 statistics to almost trivially combine with other photon observatories, such as HAWC. The first
 1907 groundwork for a multi-messenger DM search is provided with concluding remarks in chapter 8.

CHAPTER 8

1908 NU DUCK: CONCLUSIONS AND FUTURE DIRECTIONS

1909 8.1 Conclusions

1910 **TODO: Chat GPT the shit of everything below** In this work, three analyses were performed
1911 with data from the HAWC and IceCube observatories in order to explore some of the fundamental
1912 questions in particle astrophysics. The goal was to contribute to the understanding of the sources of
1913 cosmic rays, their acceleration mechanisms, and the nature of dark matter. The detection techniques
1914 and reconstruction methods for both observatories were described, along with the properties that
1915 make them ideal instruments to perform such searches.

1916 This dissertation used data from the HAWC detector to probe cutting-edge physics beyond
1917 the Standard Model. The techniques by which HAWC is able to detect cosmic gamma rays were
1918 demonstrated and the many advantages of HAWC in probing ultra-high energy gamma-ray physics
1919 were detailed. It was shown how HAWC data can be used to explore unanswered questions such as
1920 the nature of dark matter and the limits of Lorentz invariance. In particular, a search for evidence of
1921 WIMP dark matter in the Milky Way Galactic Halo was performed. To accomplish this, simulations
1922 of the dark matter density profile were combined with estimates of the HAWC sensitivity to dark
1923 matter-like energy spectra. This allowed strong constraints on dark matter annihilation and decay
1924 from the Galactic Halo to be derived that are insensitive to the large uncertainties arising from
1925 systematics in the dark matter spatial distribution. Multi-hundred TeV photon spectra were also
1926 significantly detected from HAWC sources within the Galactic Plane. These results lead to the
1927 strongest constraints on Lorentz invariance violation to be published at the time of writing.

1928 The work of this dissertation was made possible by the ongoing development of new algorithms
1929 and reconstruction techniques within the HAWC collaboration. Probing the Galactic Halo required
1930 the creation of a novel background estimation technique that relied on HAWC's wide field of view
1931 and strong ability to discriminate between gamma rays and cosmic rays. Meanwhile, the constraints
1932 on Lorentz invariance violation were enabled by the improved energy resolution from a machine
1933 learning technique. HAWC has recently completed a reprocessing of all archival data using an

1934 updated set of algorithms that can lead to compelling follow-up work on these results. Combining
 1935 the new background technique with the re-optimized energy estimators will allow for Galactic
 1936 dark matter to be probed at even higher masses, as well as for analyses that require precise energy
 1937 resolution such as gamma-ray line searches.

1938 **8.2 Future Directions**

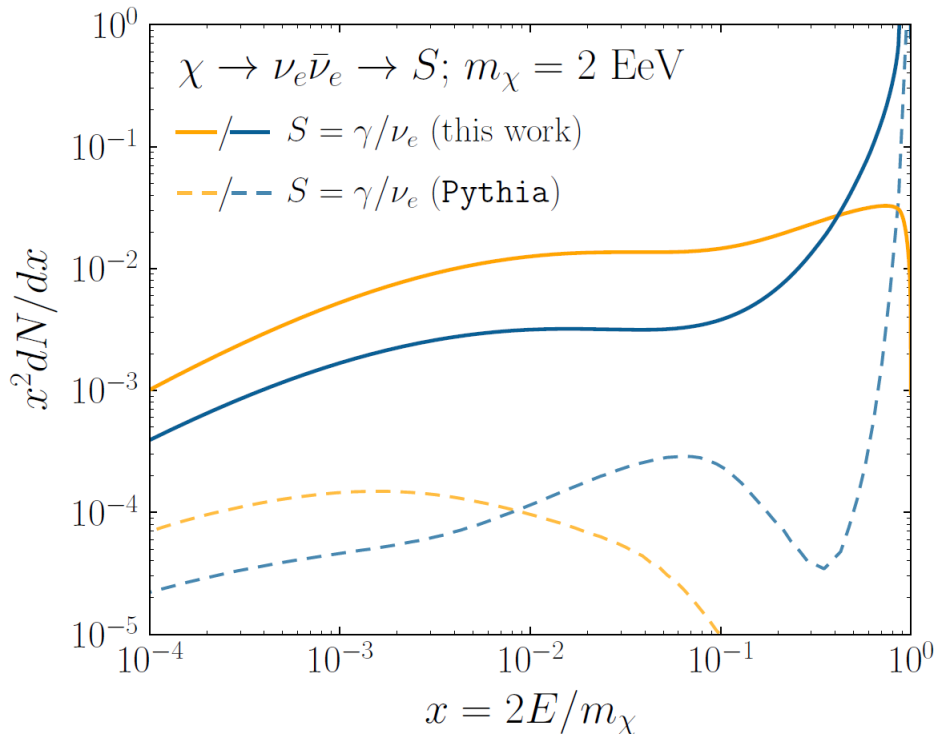


Figure 8.1 The prompt electron neutrino and photon spectrum resulting from the decay of a 2EeV DM particle to $\nu_e\bar{\nu}_e$, as currently being searched for at IceCube [5]. Solid curves represent the results of this work, and predict orders of magnitude more flux at certain energies than the dashed results of Pythia 8.2, one of the only existing methods to generate spectra at these masses. In both cases energy conservation is satisfied: there is a considerable contribution to a δ -function at $x = 1$, associated with events where an initial W or Z was never emitted and thus no subsequent shower developed. Large disagreements are generically observed at these masses for electroweak dominated channels, while the agreement is better for colored initial SM states.

1939 As I have shown previously in Sec. 5 and Sec. 6, we can build a fast and robust analysis
 1940 that shares tools with the field. The hope being that IceCube can eventually combine data with
 1941 gamma-ray observatories.



Figure 8.2 TODO: neutrino and bb plot with nu Sensitivities[NEEDS A SOURCE][FACT CHECK THIS]

MULTI-EXPERIMENT SUPPLEMENTARY FIGURES

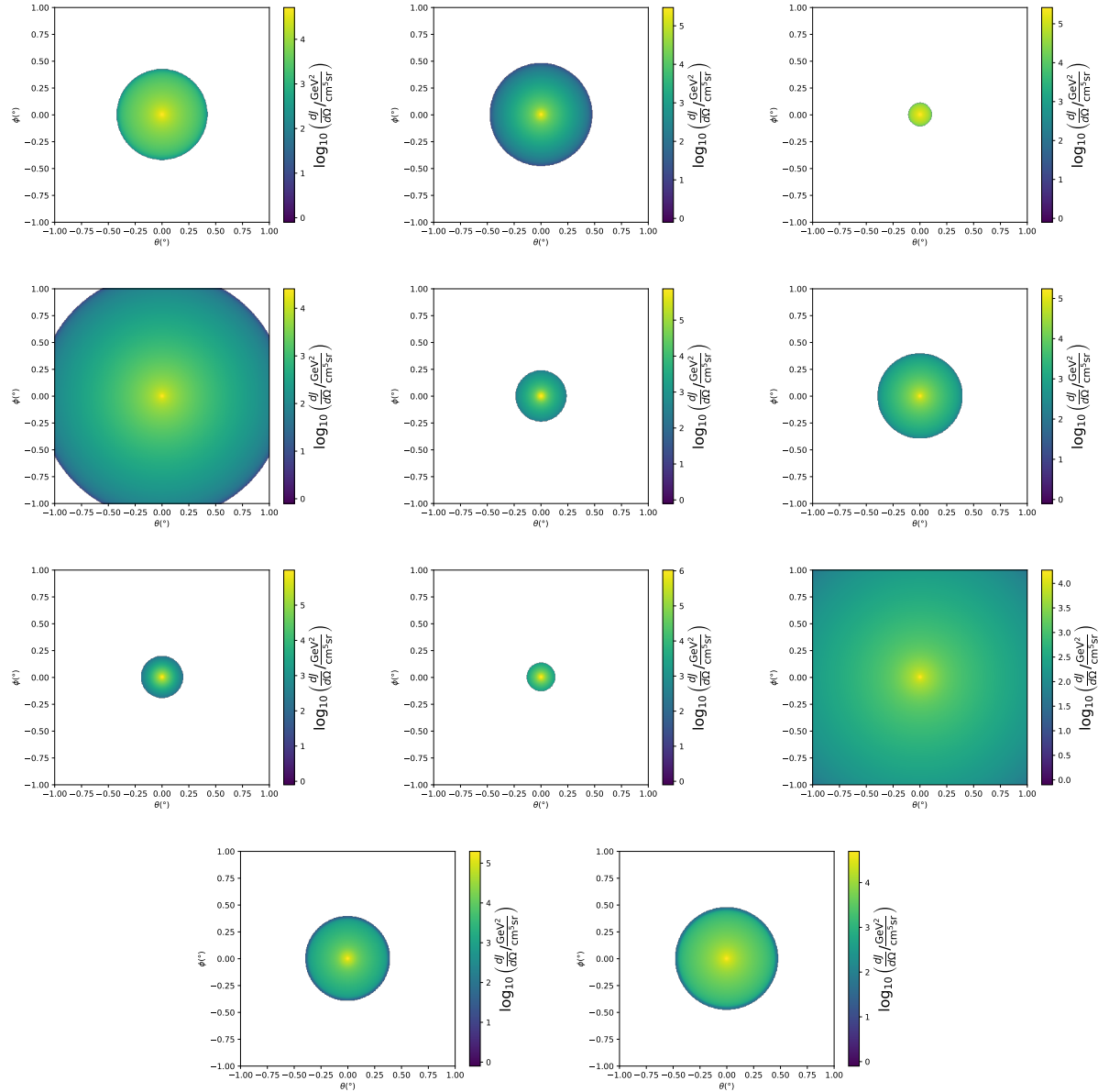


Figure A.1 Sister figure to Figure 5.3. Sources in the first row from left to right: Bootes I, Canes Venatici I, II. In second row: Draco, Hercules, Leo I. In the first row: Leo II, Leo IV, Sextans. In the final row: Ursa Major I, Ursa Major II.

1944 B.1 Remaining Spectral Models

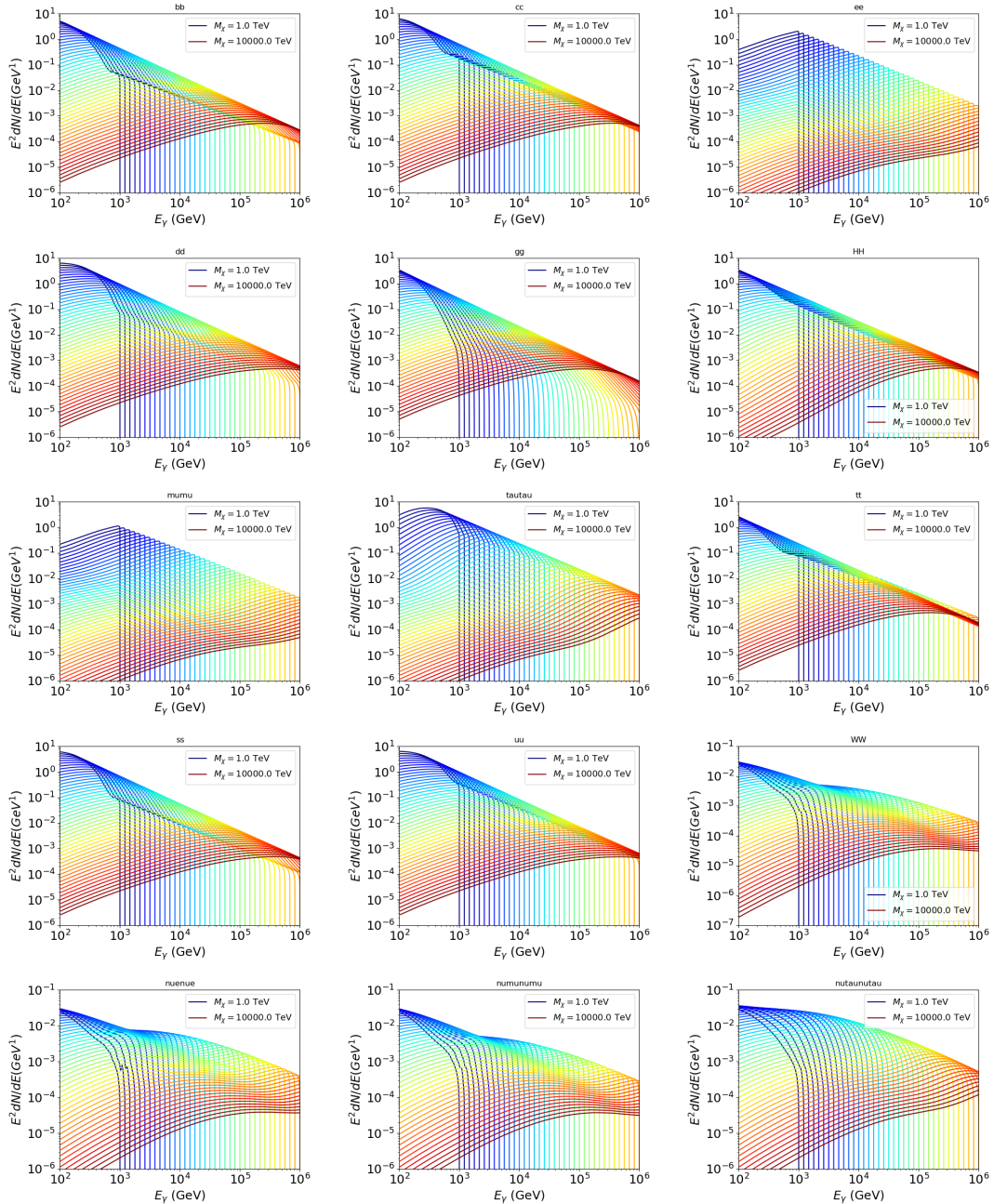


Figure B.1 Sister figure to Figure 6.2 for remaining SM primary annihilation channels studied for this thesis. These did not require any post generation smoothing and so are directly pulled from [75] with a binning scheme most helpful for a HAWC analysis.

1945 **B.2 mpu_analysis.py**

```
19461 import warnings
19472 with warnings.catch_warnings():
19483     warnings.simplefilter("ignore")
19494 # Python base libraries
19505 import os
19516 import sys
19527 import time
19538 # Import general libraries with namespace
19549 import matplotlib
19550 # Necessary for computing on cluster
19561 matplotlib.use("agg")
19572 import numpy as np
19583 import multiprocessing as mp
19594 # Import HAWC software
19605 sys.path.insert(1, os.path.join(os.environ['HOME'], 'hawc_software', 'threeML-
1961     analysis-scripts', 'fitModel'))
19626 from analysis_modules import *
19637 from threeML import *
19648 from hawc_hal import HAL, HealpixConeROI
19659 from threeML.minimizer.minimization import FitFailed
19660 # Import Dark Matter HAWC Libraries
19671 import analysis_utils as au
19682 import spectra as spec
19693 import sources as srcs
19704
19715 #* READ ONLY PATHS This block will change eventually
19726 MASS_LIST = './plotting/studies/nd/masses.txt'
19737 CHAN_LIST = './plotting/studies/nd/chans.txt'
19748
19759 #* WRITE PATHS, default location is to scratch
19760 OUT_PATH = os.path.join(os.environ["SCRATCH"], os.environ["USER"], 'New_duck')
```

```

19771 print('Our out path is going to be {}'.format(OUT_PATH))
19782
19793 # Define parallel Function. Can also be run serially
19804 def some_mass_fit(sigVs, datalist, shape, dSph, jfactor, mass_chan,
19815                         progress=None, log_file='', queue=None, i_job=0):
19826
19837     if progress is None:
19848         progress = [0]
19859     else: # Create log files for each thread
19860         log_file = log_file.replace('.log', '_ThreadNo_')
19871         log_file = log_file + str(i_job) + ".log"
19882         sys.stdout = open(log_file, "w")
19893
19904     fits = []
19915
19926     try:
19937         for m_c in mass_chan:
19948             print(f'Mass chan tuple: {m_c}')
19959             mass = int(m_c[0])
19960             ch = m_c[1]
19971             # Build path to output files
19982             outPath = os.path.join(OUT_PATH, ch, dSph)
19993             au.ut.ensure_dir(outPath)
20004
20015             if progress[i_job] < 0:
20026                 # If the master gets a Keyboard interrupt, commit suicide.
20037                 break
20048
20059                 ### Start Model Building for DM mass and SM channel #####
20060                 spectrum = spec.DM_models.HDMSpectra()
20071                 spectrum.set_channel(ch)
20082
20093                 myDwarf = ExtendedSource(dSph, spatial_shape=shape,

```

```

20104                     spectral_shape=spectrum)

20115

20126     spectrum.J = jfactor * u.GeV**2 / u.cm**5
20137     spectrum.sigmav = 1e-24 * u.cm**3 / u.s
20148     spectrum.set_dm_mass(mass * u.GeV)

20159

20160     spectrum.sigmav.bounds = (1e-30, 1e-12)
20171     model = Model(myDwarf)
20182     ##### End model Building #####
20193
20204     jl = JointLikelihood(model, datalist, verbose=False)
20215
20226     try:
20237         result, lhdf = jl.fit(compute_covariance=False)
20248         ts = -2.* (jl.minus_log_like_profile(1e-30) - jl.
2025         _current_minimum)
20269         # Also profile the LLH vs sv
20270         ll = jl.get_contours(spectrum.sigmav, sigVs[0],
20281                               sigVs[-1], len(sigVs),
20292                               progress=False, log=['False'])
20303
20314         sigv_ll = au.ut.calc_95_from_profile(ll[0], ll[2])
20325         # Write results to file
20336         outFileLL = outPath+f"/LL_{dSph}_{ch}_mass{int(mass)}_GD.txt"
20347         np.savetxt(outFileLL, (sigVs, ll[2]),
20358                               delimiter='\t', header='sigV\tLL\n')
20369
20370         with open(outPath+f"/results_{dSph}_{ch}_mass{int(mass)}_GD.
2038         txt", "w") as results_file:
20391             results_file.write("mDM [GeV]\tsigV_95\tsigV_B.F.\n")
20402
20413             results_file.write("%i\t%.5E\t%.5E\t%.5E"%(mass, sigv_ll,
20424                                         ts, result.value[0]))

```

```

20435         # End write to file
20446     except FitFailed: # Don't kill all threads if a fit fails
20457         print("Fit failed. Go back and calculate this spectral model
2046 later")
20478         fits.append((ch, mass, -1, -1))
20489         with open(log_file+'.fail', 'w') as f_file:
20490             f_file.write(f'{ch}, {mass}\n')
20501
20512         progress[i_job] += 1
20523         matplotlib.pyplot.close() # Prevent leaky memory
20534
20545         fits.append((ch, mass, result.value[0], ts))
20556         progress[i_job] += 1
20567         matplotlib.pyplot.close()
20578     except KeyboardInterrupt:
20589         progress[i_job] = -1
20590
20601     fits = np.array(fits)
20612     if queue is None:
20623         return fits
20634     else:
20645         queue.put((i_job, fits))
20656
20667 def main(args):
20678     masses = np.loadtxt(MASS_LIST, dtype=int)
20689     chans = np.loadtxt(CHAN_LIST, delimiter=',', dtype=str)
20690     mass_chan = au.ut.permute_lists(chans, masses)
20701
20712     print(f"DM masses for this study are: {masses}")
20723     print(f"SM Channels for this study are XX -> {chans}")
20734     print(mass_chan)
20745
20756 # extract information from input argument

```

```

20767 dSph = args.dSph
20778 data_mngr = au.ut.Data_Selector('P5_NN_2D')
20789 dm_profile = srcts.Spatial_DM(args.catalog, dSph, args.sigma, args.decay)
20790
20801 ##### Extract Source Information #####
20812 if dm_profile.get_dec() < -22.0 or dm_profile.get_dec() > 62.0:
20823     raise ValueError("HAWC can't see this source D: Exitting now...")
20834
20845 print(f'{dSph} information')
20856 print(f'jfac: {dm_profile.get_factor()}\tRA: {dm_profile.get_ra()}\tDec: {dm_profile.get_dec()}\n')
20867
20888 shape = SpatialTemplate_2D(fits_file=dm_profile.get_src_fits())
20899 ##### Finish Extract Source Information #####
20900
20911 ##### LOAD HAWC DATA #####
20922 roi = HealpixConeROI(data_radius=2.0, model_radius=8.0,
20933                         ra=dm_profile.get_ra(), dec=dm_profile.get_dec())
20944 bins = choose_bins.analysis_bins(args, dec=dm_profile.get_dec())
20955
20966 hawc = HAL(dSph, data_mngr.get_datmap(), data_mngr.get_detres(), roi)
20977 hawc.set_active_measurements(bin_list=bins)
20988 datalist = DataList(hawc)
20999 ##### FINISH LOAD HAWC DATA #####
21000
21011 # set up SigV sampling. This sample is somewhat standardized
21022 sigVs = np.logspace(-28,-18, 1001, endpoint=True) # NOTE This will change
2103 with HDM
21043
21054 if args.n_threads == 1:
21065     # No need to start || programming just iterate over the masses
21076     kw_arg = dict(sigVs=sigVs, datalist=datalist, shape=shape, dSph=dSph,
21087                     jfactor=dm_profile.get_factor(), mass_chan=mass_chan,

```

```

21098                 log_file=args.log)
21099             some_mass_fit(**kw_arg)
21100         else:
21101             # I Really want to suppress TQMD output
21102             from tqdm import tqdm
21103             from functools import partialmethod
21104             tqdm.__init__ = partialmethod(tqdm.__init__, disable=True)
21105
21106             x = np.array_split(mass_chan, args.n_threads)
21107             n_jobs = len(x)
21108
21109             print("Thread jobs summary by mass and SM channel")
21110             for xi in x:
21111                 print(f'{xi}')
21112
21113             queue = mp.Queue()
21114             progress = mp.Array('i', np.zeros(n_jobs, dtype=int))
21115
21116             # Define task pool that will be split amongsts threads
21117             kw_args = [dict(sigVs=sigVs, datalist=datalist, shape=shape,
21118                           dSph=dSph, jfactor=dm_profile.get_factor(),
21119                           mass_chan=mass_chan, progress=progress,
21120                           queue=queue, i_job=i, log_file=args.log)
21121                 for i, mass_chan in enumerate(x)]
21122
21123             # Define each process
21124             procs = [mp.Process(target=some_mass_fit, kwargs=kw_args[i]) \
21125                   for i in range(n_jobs)]
21126
21127             ### Start MASTER Thread only code block ###
21128             # Begin running all child threads
21129             for proc in procs: proc.start()
21130
21131

```

```

21421     try:
21422
21423         # In this case, the master does nothing except monitor progress of
21424         # the threads
21425
21426         # In an ideal world, the master thread also does some computation.
21427
21428         n_complete = np.sum(progress)
21429
21430         while_count = 0
21431
21432
21433         while n_complete < len(mass_chan):
21434
21435             if np.any(np.asarray(progress) < 0):
21436
21437                 # This was no threads are stranded when killing the script
21438
21439                 raise KeyboardInterrupt()
21440
21441             if while_count%1000 == 0:
21442
21443                 print(f'{np.sum(progress)} of {len(mass_chan)} finished')
21444
21445
21446             n_complete = np.sum(progress)
21447
21448             time.sleep(.25)
21449
21450             while_count += 1
21451
21452
21453         except KeyboardInterrupt:
21454
21455             # signal to jobs that it's time to stop
21456
21457             for i in range(n_jobs):
21458
21459                 progress[i] = -2
21460
21461             print('\nKeyboardInterrupt: terminating early.')
21462
21463             ### End MASTER Thread only code block ###
21464
21465
21466             fitss = [queue.get() for proc in procs]
21467
21468             print(fitss)
21469
21470             print(f'Thread statuses: {progress[:]}')
21471
21472
21473             # putting results in a file
21474
21475
21476             print("QUACK! All Done!")

```

```

21753
21764
21775 if __name__ == '__main__':
21786     import argparse
21797
21808     p = argparse.ArgumentParser(description="Run a DM annihilation analysis on
2181         a dwarf spheroidal for a specific SM channel for DM masses [1 TeV to 10
2182         PeV]")
21839
21840     # Dwarf spatial modeling arguements
21851     p.add_argument("-ds", "--dSph", type=str,
21862             help="dwarf spheroidal galaxy to be studied", required=
2187             True)
21883     p.add_argument("-cat", "--catalog", type=str, choices=['GS15', 'LS20'],
21894             default='LS20', help="source catalog used")
21905     p.add_argument("-sig", "--sigma", type=int, choices=[-1, 0, 1], default=0,
21916             help="Spatial model uncertainty. 0 corresponds to the
2192 median. +/-1 correspond to the +/-1sigma uncertainty respectively.")
21937
21948     # Arguements for the energy estimators
21959     p.add_argument("-e", "--estimator", type=str,
21960             choices=['P5_NHIT', 'P5_NN_2D'],
21971             default="P5_NN_2D", required=False,
21982             help="The energy estimator choice. Options are: P5_NHIT,
2199 P5_NN_2D. GP not supported (yet).")
22003     p.add_argument("--use-bins", default=None, nargs="*",
22014             help="Bins to use for the analysis", dest="use_bins")
22025     p.add_argument('--select_bins_by_energy', default=None, nargs="*",
22036             help="Does nothing. May fill in later once better
2204 understood")
22057     p.add_argument('--select_bins_by_fhit', default=None, nargs="*",
22068             help="Also does nothing see above")
22079     p.add_argument( '-ex', '--exclude', default=None, nargs="*",

```

```

22080         help="Exclude Bins", dest="exclude")
22091
22102     # Computing and logging arguements.
22113     p.add_argument('-nt', '--n_threads', type=int, default=1,
22124                         help='Maximum number of threads spawned by script. Default
2213      is 4')
22145     p.add_argument('-log', '--log', type=str, required=True,
22156                         help='Name for log files. Especially needed for threads')
22167
22178     p.add_argument('--decay', action="store_true",
22189                         help='Set spectral DM hypothesis to decay')
22190
22201     args = p.parse_args()
22212     print(args.decay)
22223     if args.exclude is None: # default exclude bins 0 and 1
22234         args.exclude = ['B0C0Ea', 'B0C0Eb', 'B0C0Ec', 'B0C0Ed', 'B0C0Ee']
22245
22256     if args.decay: OUT_PATH += '_dec'
22267     else: OUT_PATH += '_ann'
22278
22289     OUT_PATH = OUT_PATH + '_' + args.catalog
22290     if args.sigma != 0: OUT_PATH += f'_{args.sigma}sig'
22301
22312     main(args)

```

2232 B.3 Comparison with Glory Duck

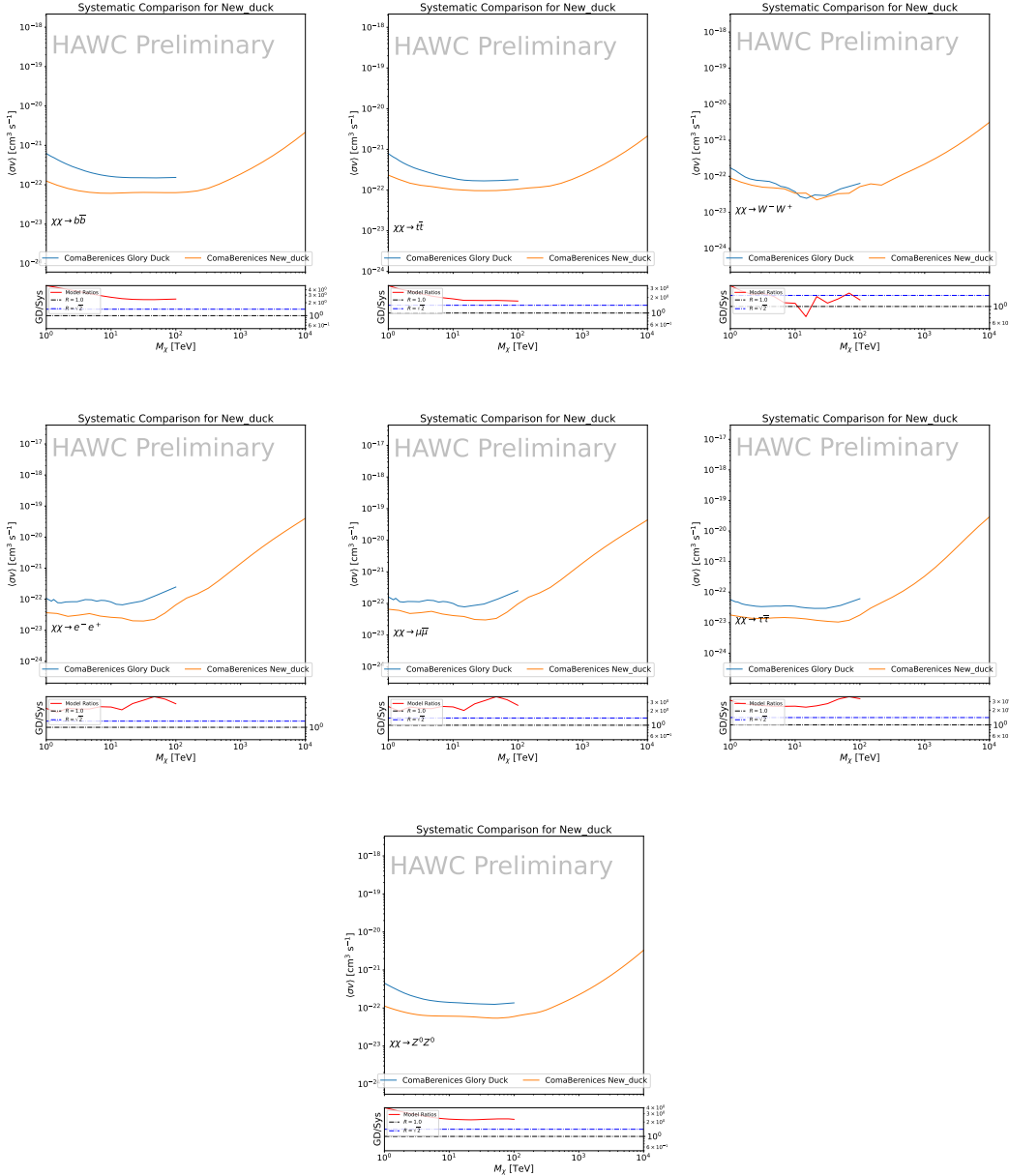


Figure B.2 Comparison of HAWC limits from this analysis to Glory Duck (Fig. 5.5) for Coma Berenices and 7 DM annihilation channels.

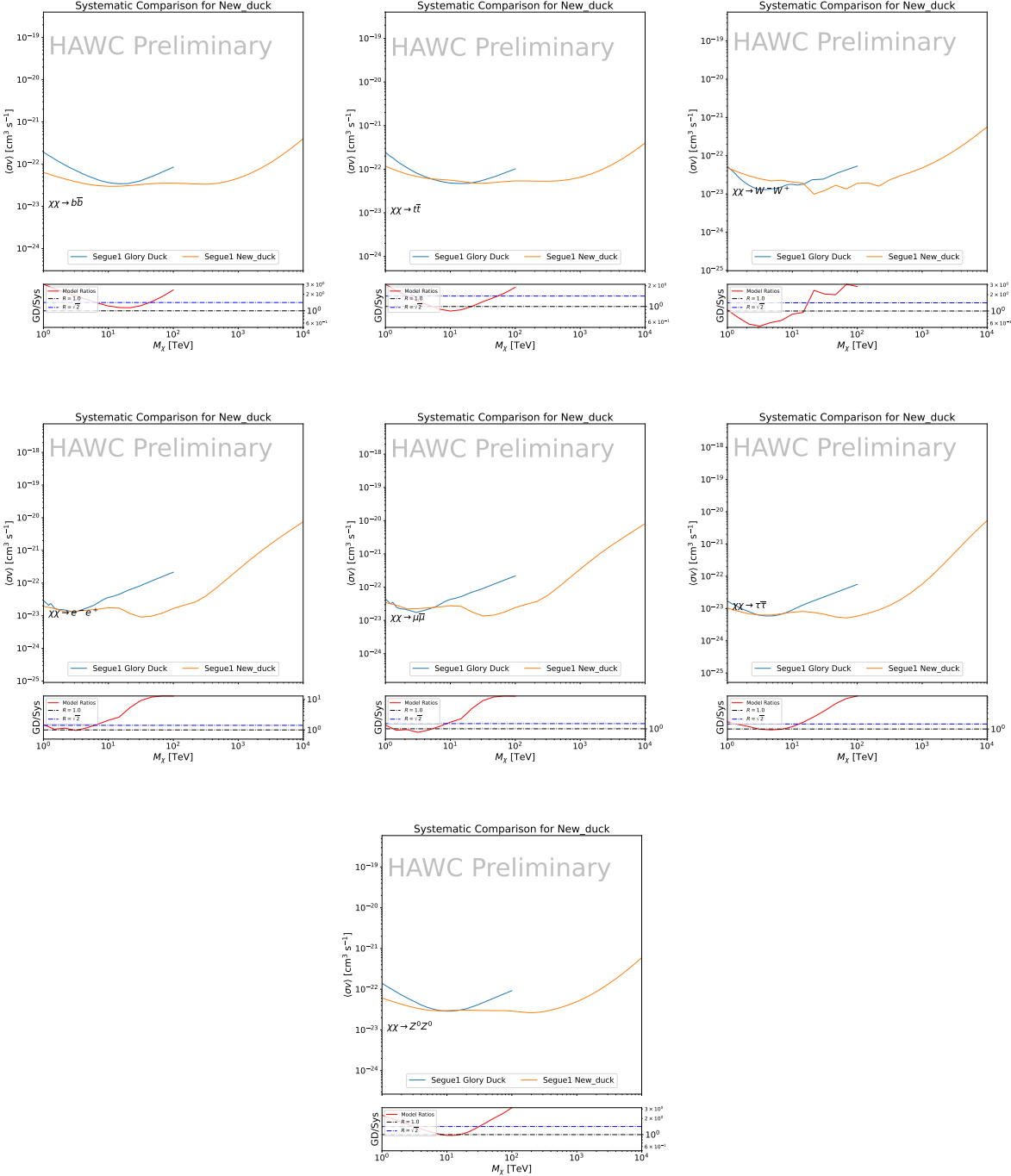


Figure B.3 Same as Fig. B.2 but for Segue 1.

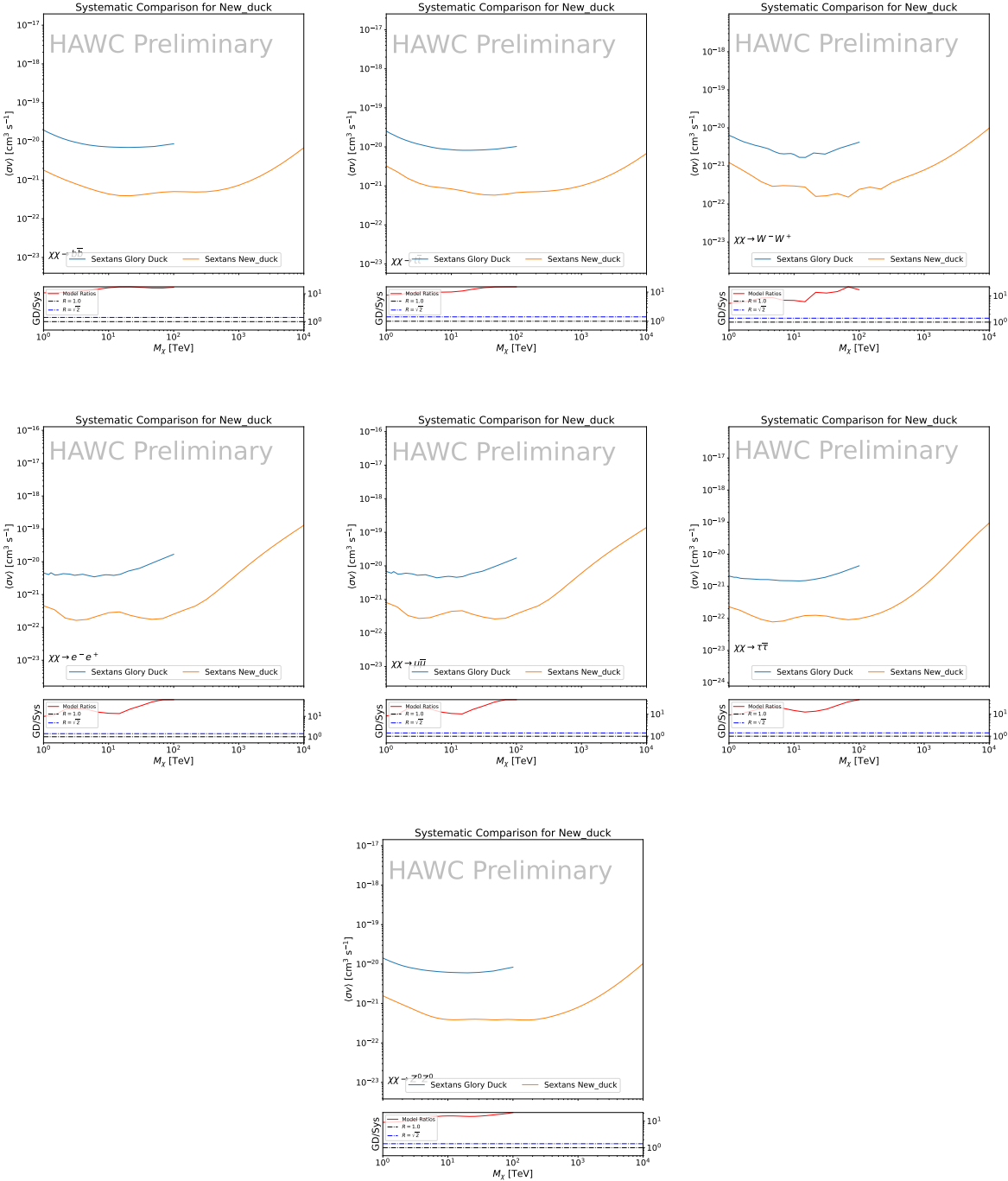


Figure B.4 Same as Fig. B.2 but for Sextans.

APPENDIX C

2233 ICECUBE HEAVY DARK MATTER ANALYSIS SUPPLEMENTARY MATERIAL

2234 C.1 Docker Image for Oscillating Neutrino Spectra

```
2235 1 FROM ubuntu:18.04
2236 2
2237 3 # Execute commands to install software packages
2238 4 RUN apt -y update
2239 5
2240 6     # Install utility programs
2241 7 RUN apt -y install vim wget git cmake
2242 8
2243 9 ARG DEBIAN_FRONTEND=noninteractive
2244 0
2245 1     # Install python
2246 2 RUN apt -y install python python-dev python-pip libjpeg-dev zlib1g-dev
2247 3
2248 4     # We need Python2 for installing Charon.
2249 5 RUN apt -y install python-numpy python-sympy python-matplotlib \
2250 6             python-sympy python-h5py python-astropy python-ipython
2251 7
2252 8     # Install dependencies of Charon : SQuIDS, NuSQuIDS
2253 9 RUN apt -y install libgsl-dev libgslcblas0 libgsl23 gsl-bin pkg-config
2254 0     # Install SQuIDS
2255 1 RUN mkdir /home/SQuIDS /home/SQuIDS_install
2256 2 WORKDIR /home/SQuIDS
2257 3 RUN git clone https://github.com/jsalvado/SQuIDS.git
2258 4 WORKDIR /home/SQuIDS/SQuIDS
2259 5 RUN git checkout 7ad9ba7c6ad06d1f0fa8418f937ebf1a403fef90
2260 6     # Before executing "make install" an environmental variable has to be set.
2261 7 ENV PKG_CONFIG_PATH=/home/SQuIDS/SQuIDS/lib
2262 8 RUN ./configure --prefix=../SQuIDS_install \
```

```

22639     && make
22640 RUN make install
22651
22662 # Set up an environmental variable that is required to install nuSQuIDS..
22673 ENV SQuIDS=/home/SQuIDS/SQuIDS
22684 ENV LD_LIBRARY_PATH=$SQuIDS/lib:$LD_LIBRARY_PATH
22695
22706 # Install NuSQuIDS
22717 RUN mkdir /home/nuSQuIDS
22728 WORKDIR /home/nuSQuIDS
22739 RUN git clone https://github.com/qrliu/nuSQuIDS.git
22740 WORKDIR /home/nuSQuIDS/nuSQuIDS
22751 RUN git checkout 072d8ef740e2fc7330f1fabaea94f0f4540c46f9
22762 RUN apt -y install libhdf5-dev hdf5-tools
22773 RUN apt -y install libboost1.65-all-dev
22784 RUN ./configure --with-squids=$SQuIDS --with-python-bindings --prefix=../
2279     nuSQuIDS_install \
22805     && make \
22816     && make install
22827
22838 # Set up an environmental variable for nuSQuIDS.
22849 ENV nuSQuIDS=/home/nuSQuIDS/nuSQuIDS
22850 ENV LD_LIBRARY_PATH=$nuSQuIDS/lib:$LD_LIBRARY_PATH
22861
22872 # Build the python bindings
22883 WORKDIR /home/nuSQuIDS/nuSQuIDS/resources/python/src
22894 RUN make
22905
22916 # Set up an environmental variable for the python bindings.
22927 ENV PYTHONPATH=$nuSQuIDS/resources/python/bindings/:$PYTHONPATH
22938
22949 # Install Charon in the /home/Charon/charon directory.
22950 RUN mkdir /home/Charon

```

```
22961 WORKDIR /home/Charon
22972 RUN git clone https://github.com/icecube/charon.git \
22983   && apt -y install unzip python-scipy
22994 WORKDIR charon
23005 RUN git checkout c531efe4e01dc364a60d1c83f950f04526ccd771
23016 RUN unzip ./charon/xsec/xsec.zip -d charon/xsec/ \
23027
23038 # Download neutrino spectra tables in the /home/Charon/charon/data directory
2304 .
23059 && mkdir ./charon/data
23060 WORKDIR ./charon/data
23071 RUN wget --no-check-certificate https://icecube.wisc.edu/~qliu/charon/
2308   SpectraEW.hdf5 \
23092 && wget --no-check-certificate https://icecube.wisc.edu/~qliu/charon/
2310   Spectra_PYTHIA.hdf5 \
23113 && wget --no-check-certificate https://icecube.wisc.edu/~qliu/charon/
2312   Spectra_noEW.hdf5
23134
23145 WORKDIR ../..
23156 RUN python setup.py install
23167 WORKDIR /home
```

2317 C.2 Spline Fitting Statuses

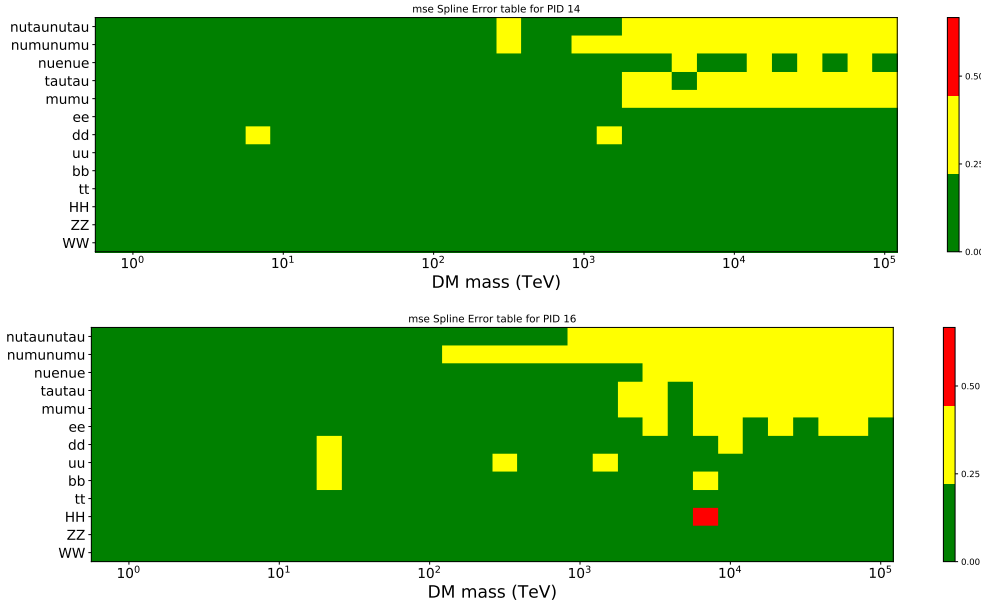


Figure C.1 Current status of spline tables according to constraints defined by Tab. 7.1. Green splines are splines that passed under the GOOD tolerance. Yellow are splines that are OK. Red are splines that FAIL. All yellow splines were inspected individually before running the analysis. Splines were made for the μ (PID 14; top panel) flavor and τ (PID 16; bottom panel) neutrino flavors.

2318 C.3 Neutrino Composite Spectra

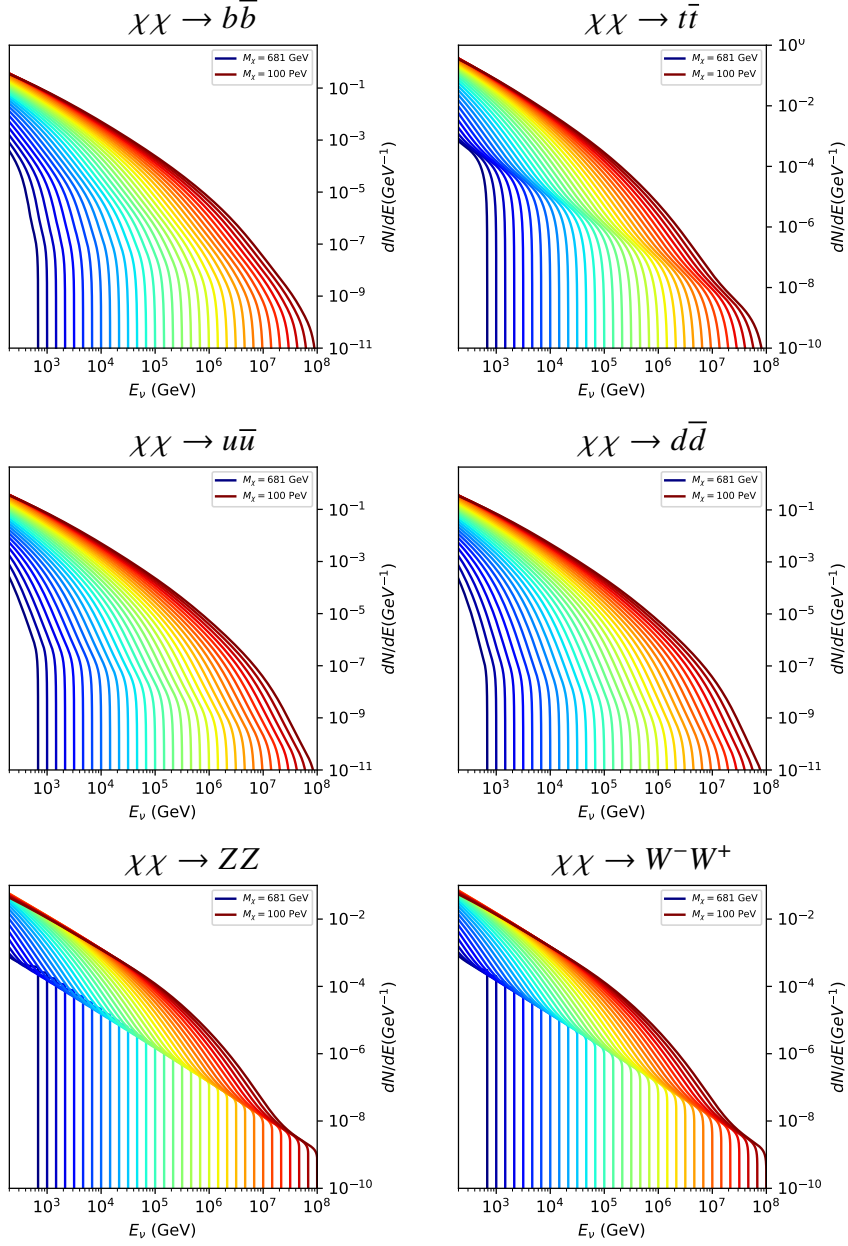


Figure C.2 Sister figure to Fig. 7.5 for annihilation channels that did not require kernel smoothing. These spectra are the composite ($\nu_\mu + \nu_\tau$) of neutrino flavors. Every spectral model used for this analysis is featured as a colored solid line. Bluer lines are for lower DM mass spectral models. DM masses range from 681 GeV to 100 PeV.

2319 C.4 Segue 1 And Ursa Major II Signal Recovery

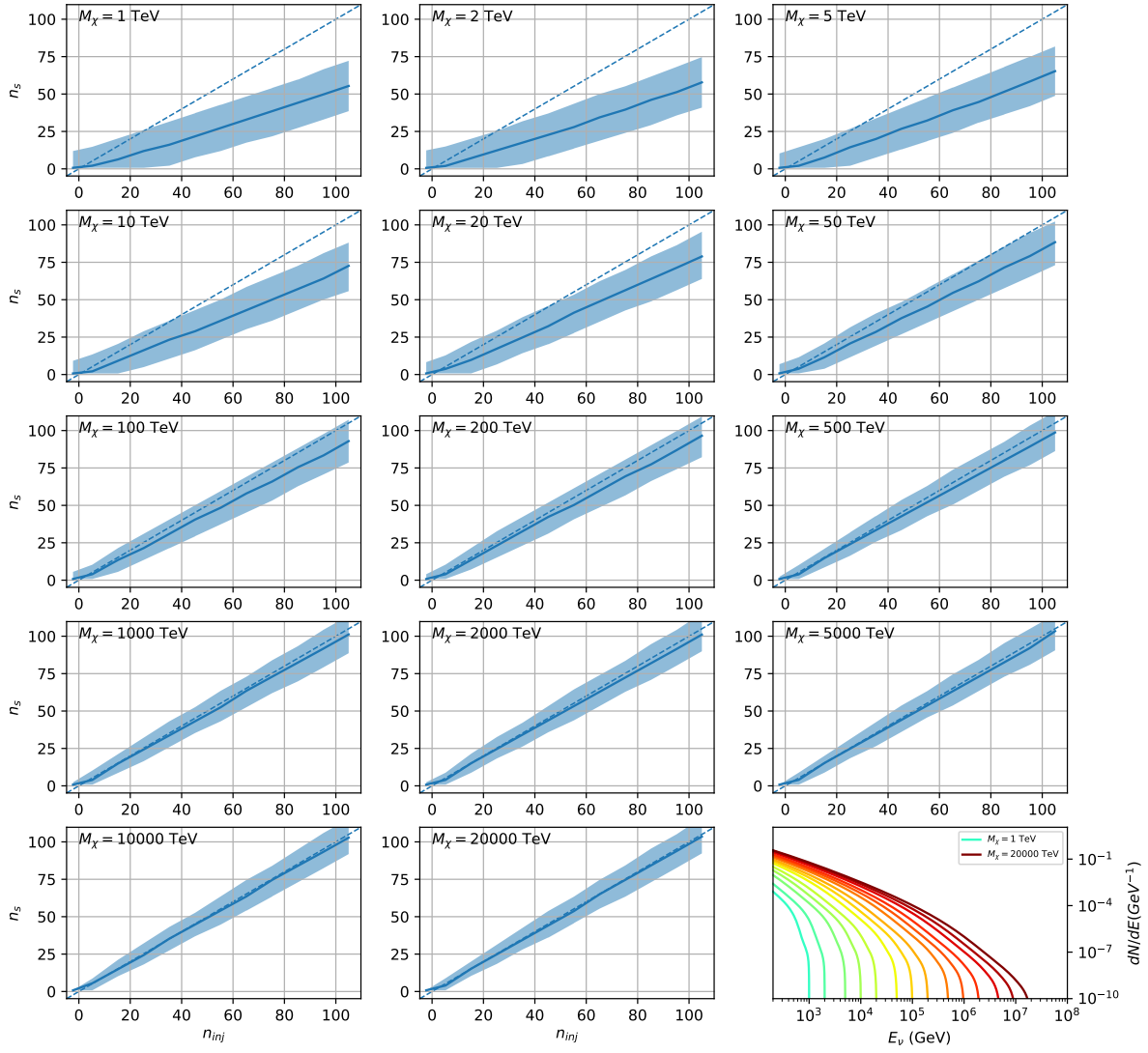


Figure C.3 Same as Fig. 7.23 but for Segue 1 and $\chi\chi \rightarrow b\bar{b}$.

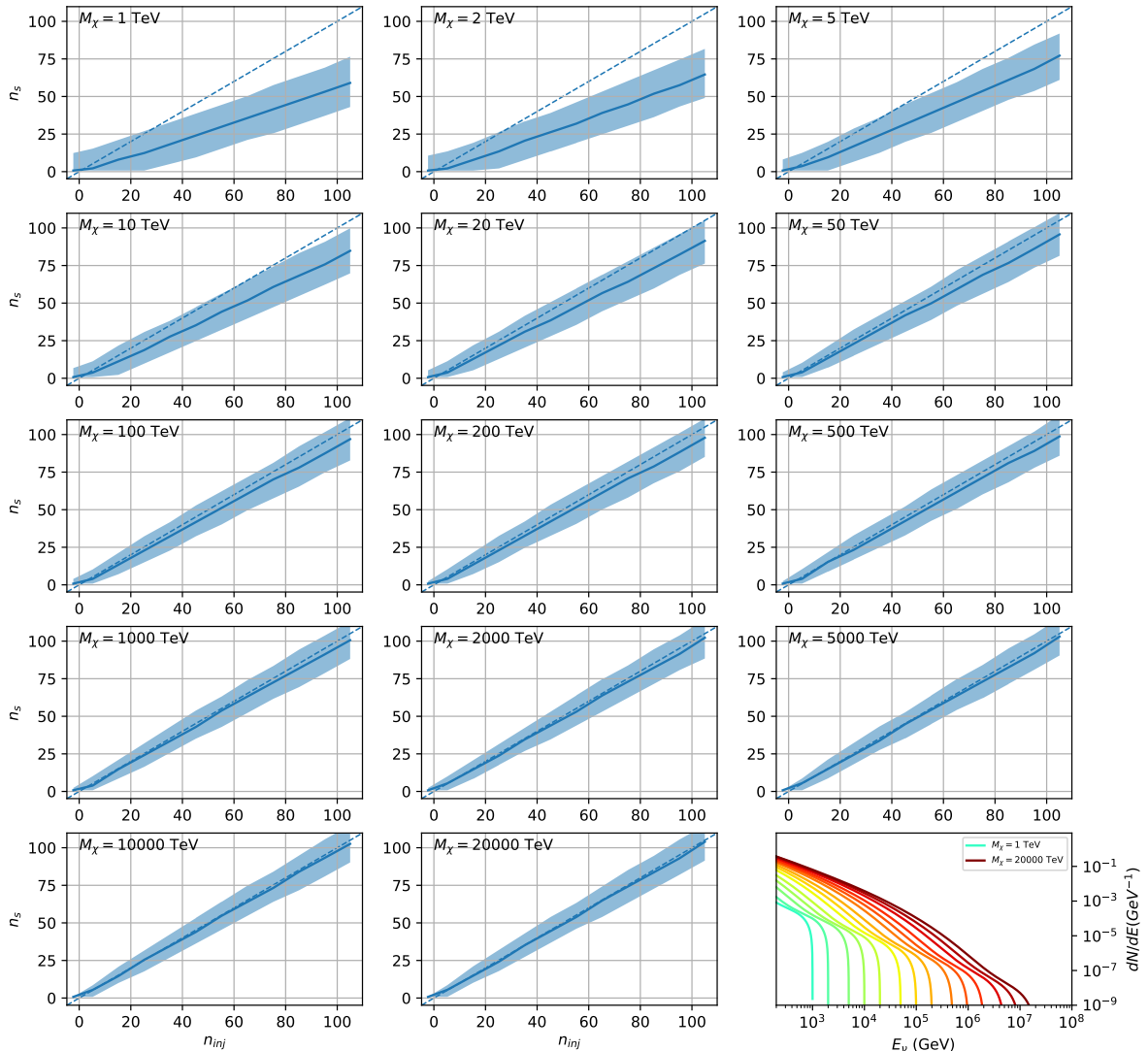


Figure C.4 Same as Fig. 7.23 but for Segue 1 and $\chi\chi \rightarrow t\bar{t}$.

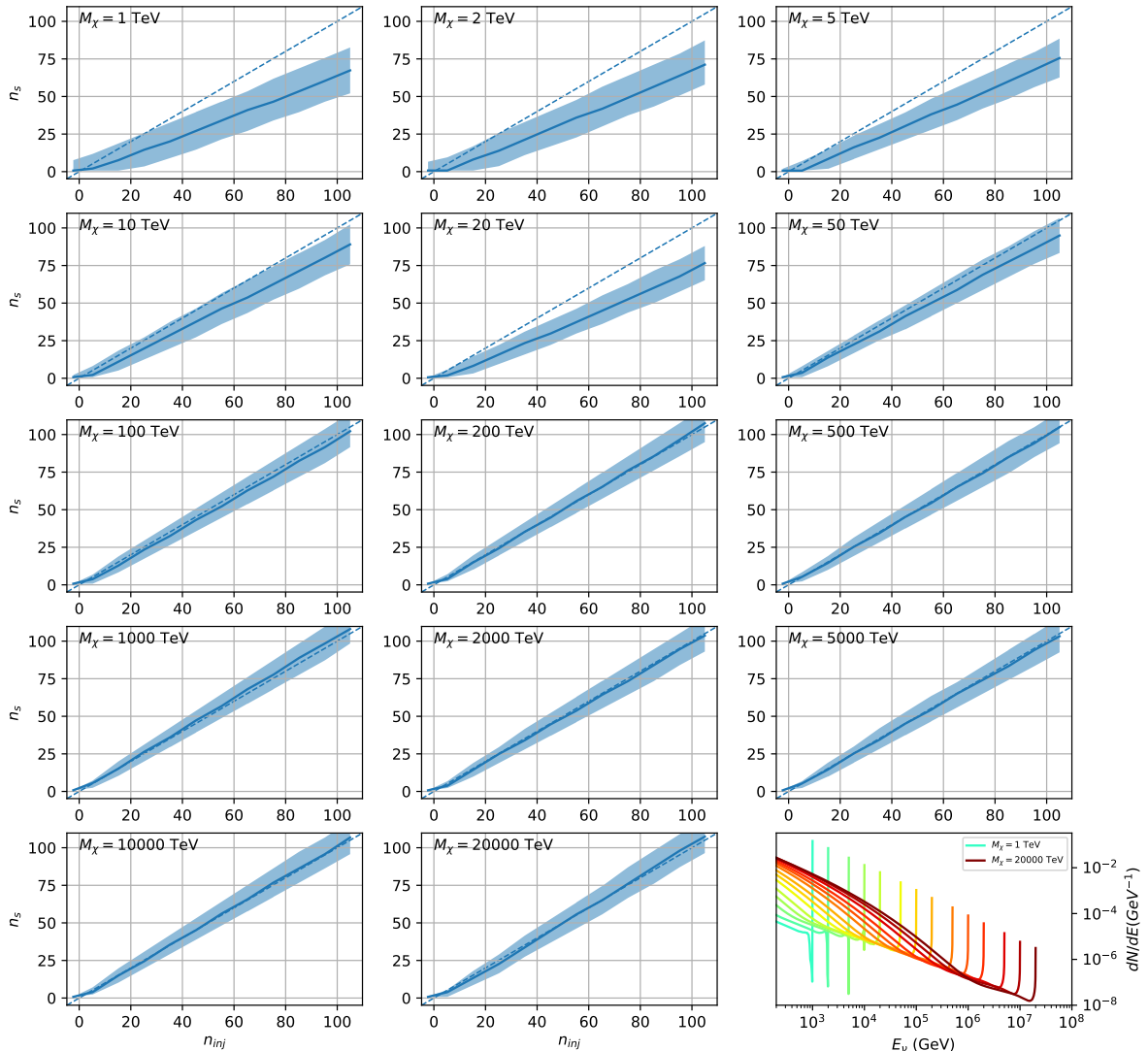


Figure C.5 Same as Fig. 7.23 but for Segue 1 and $\chi\chi \rightarrow \nu_\mu \bar{\nu}_\mu$.

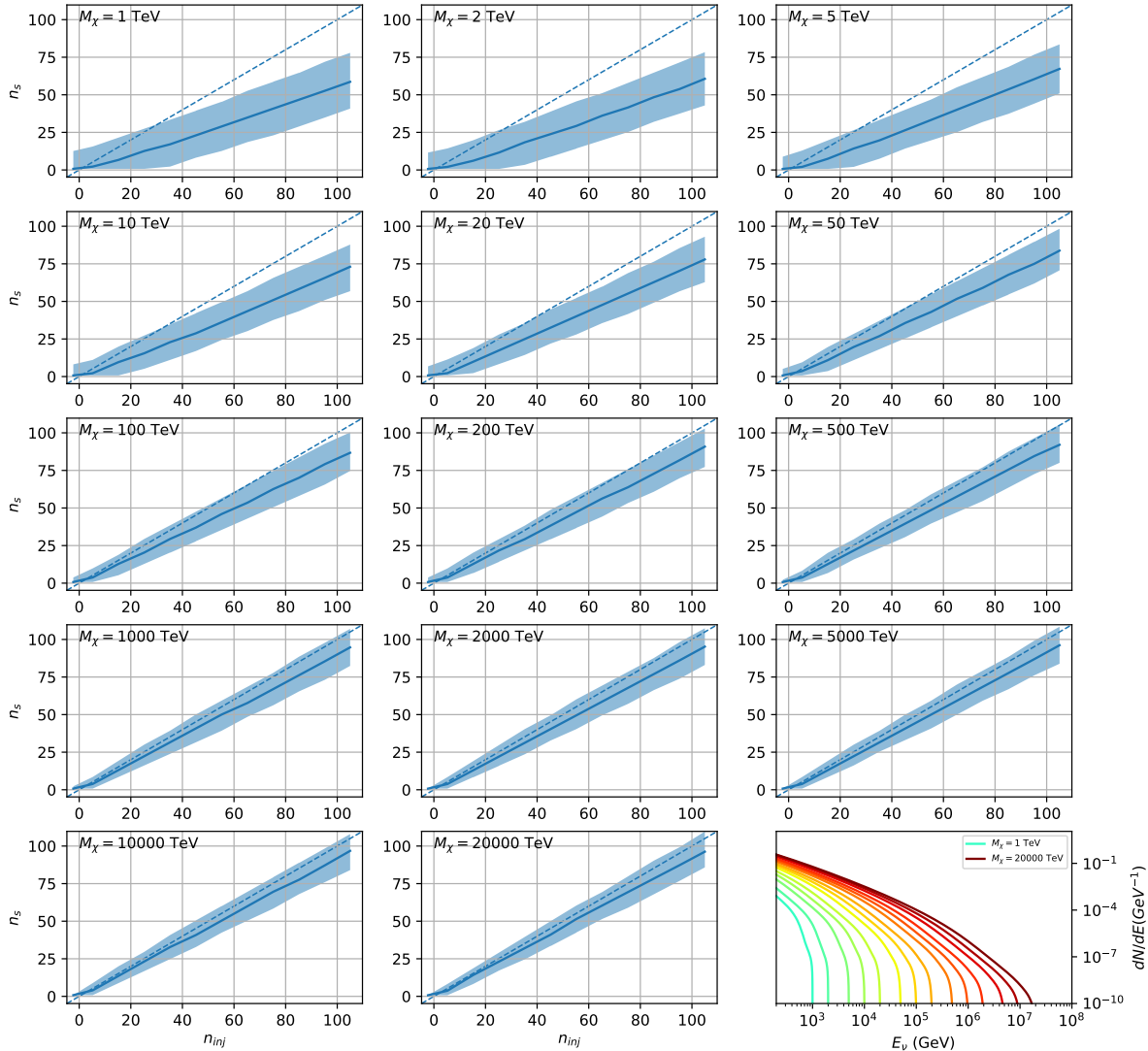


Figure C.6 Same as Fig. 7.23 but for Ursa Major II and $\chi\chi \rightarrow b\bar{b}$.

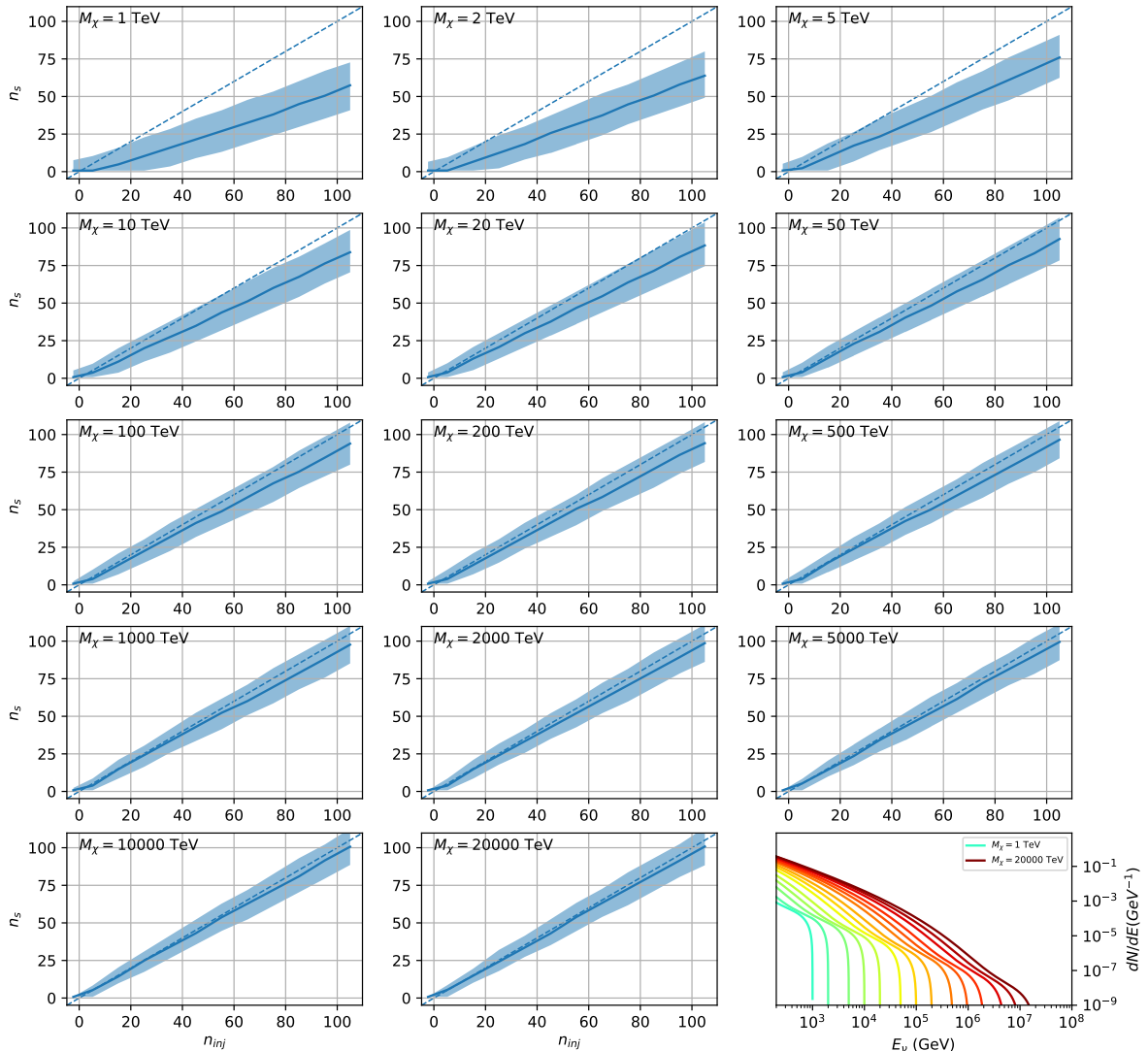


Figure C.7 Same as Fig. 7.23 but for Ursa Major II and $\chi\chi \rightarrow t\bar{t}$.

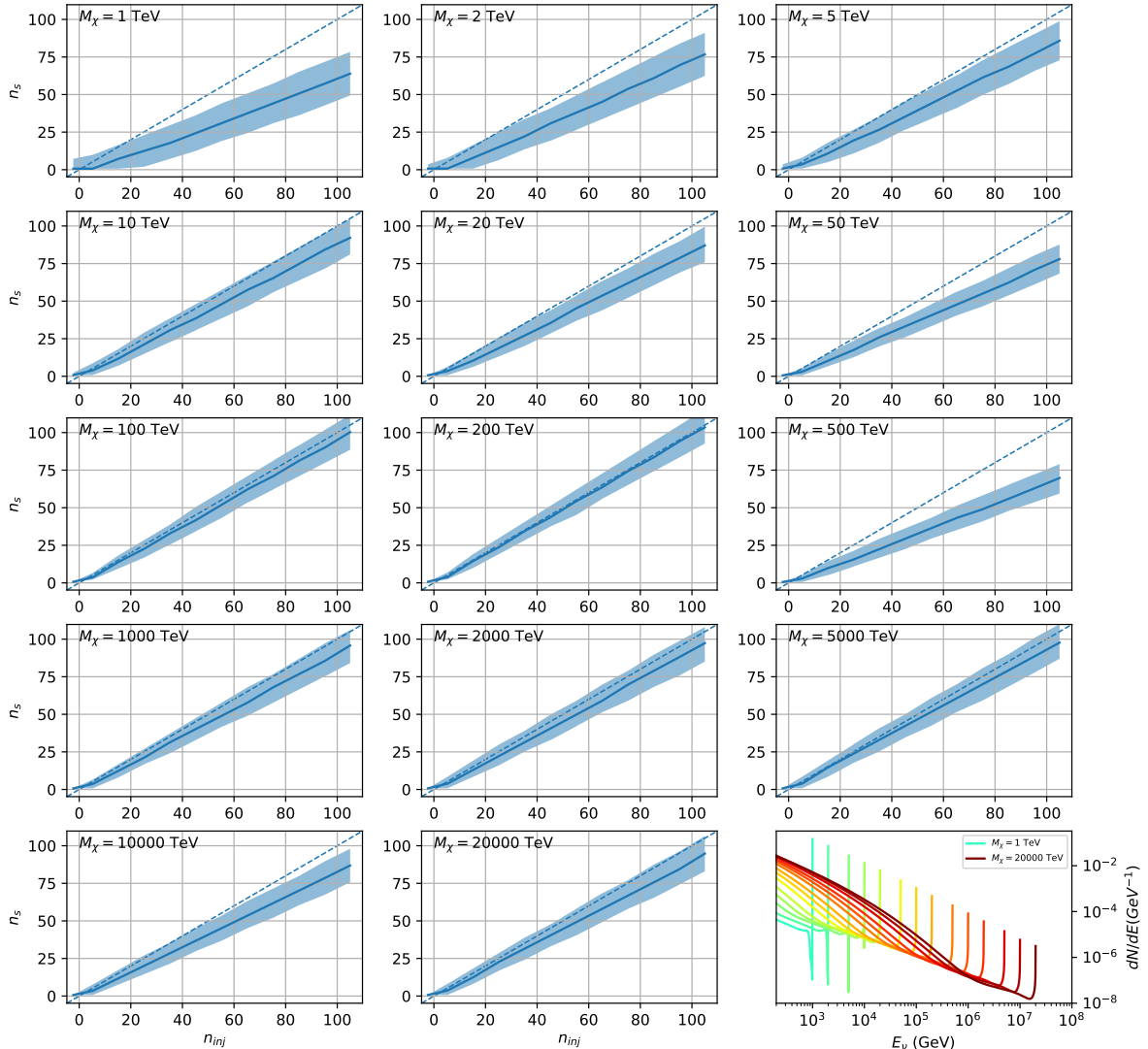


Figure C.8 Same as Fig. 7.23 but for Ursa Major II and $\chi\chi \rightarrow \nu_\mu \bar{\nu}_\mu$.

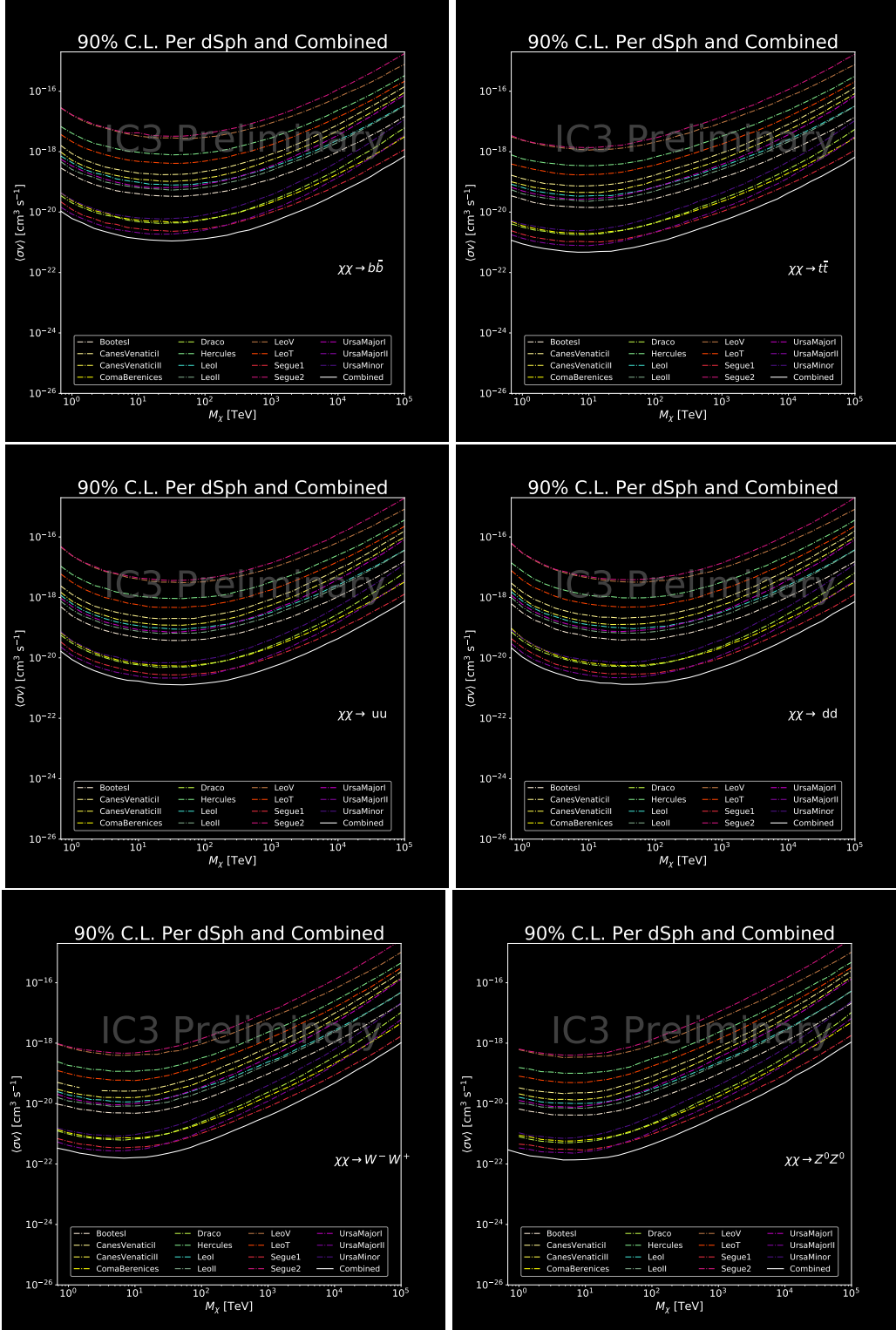


Figure C.9 IceCube North Sky Track Sensitivities for $n_s/\langle N \rangle$. n_s values are the counts fed into Eq. (7.8) to produce Fig. 7.26 and Fig. 7.25.

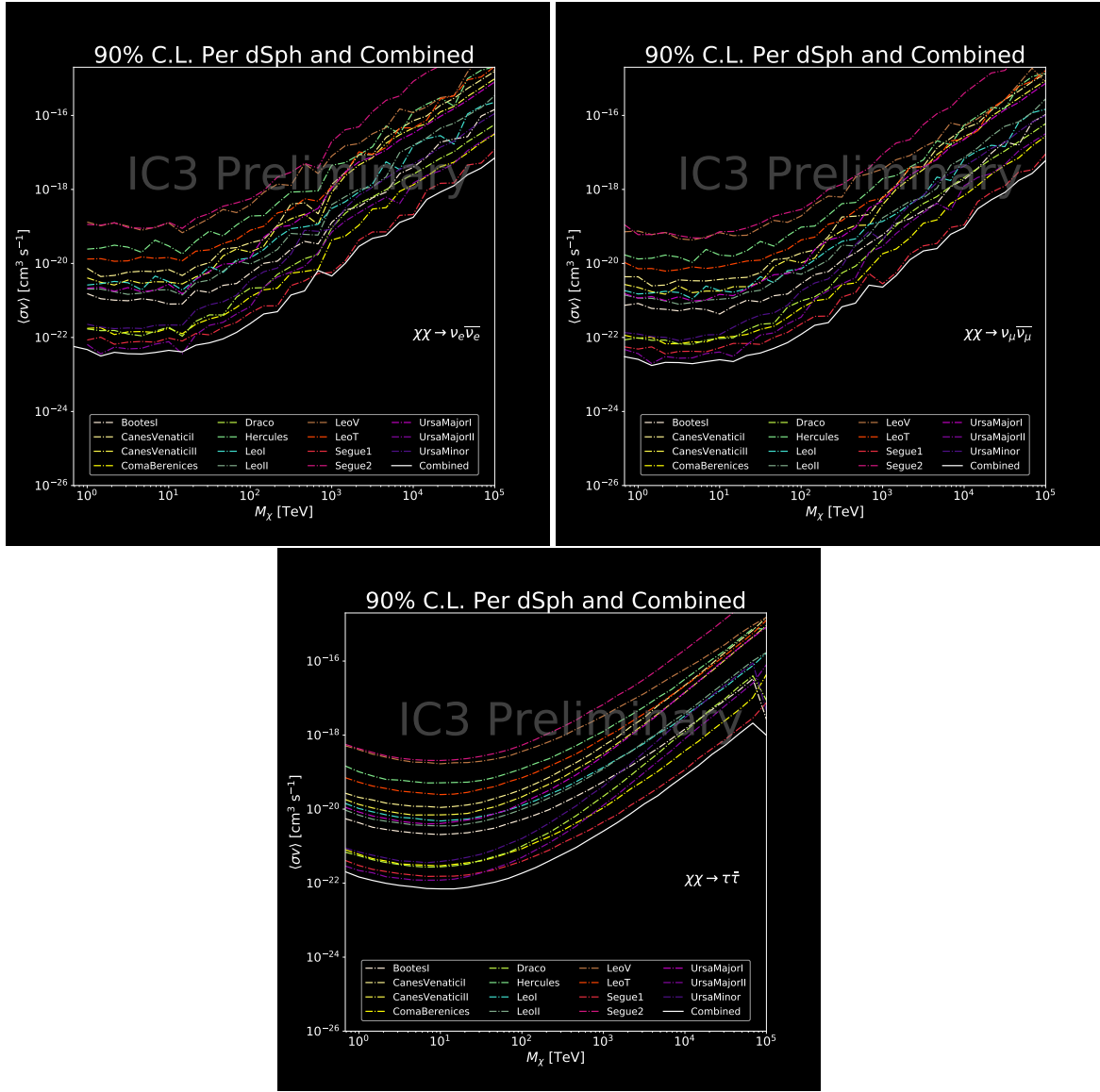


Figure C.10 Same as Fig. C.9 for three additional DM annihilation channels.

BIBLIOGRAPHY

- 2322 [1] Anne M. Green. “Dark matter in astrophysics/cosmology”. In: *SciPost Phys. Lect.*
 2323 *Notes* (2022), p. 37. doi: [10.21468/SciPostPhysLectNotes.37](https://doi.org/10.21468/SciPostPhysLectNotes.37). URL: <https://scipost.org/10.21468/SciPostPhysLectNotes.37>.
- 2325 [2] Bing-Lin Young. “A survey of dark matter and related topics in cosmology”. In: *Frontiers*
 2326 *of Physics* 12 (Oct. 2016). doi: <https://doi.org/10.1007/s11467-016-0583-4>.
 2327 URL: <https://doi.org/10.1007/s11467-016-0583-4>.
- 2328 [3] Gianfranco Bertone, Dan Hooper, and Joseph Silk. “Particle dark matter: evidence,
 2329 candidates and constraints”. In: *Physics Reports* 405.5 (2005), pp. 279–390. ISSN:
 2330 0370-1573. doi: <https://doi.org/10.1016/j.physrep.2004.08.031>. URL:
 2331 <https://www.sciencedirect.com/science/article/pii/S0370157304003515>.
- 2332 [4] Gianfranco Bertone and Dan Hooper. “History of dark matter”. In: *Rev. Mod. Phys.*
 2333 90 (4 Aug. 2018), p. 045002. doi: [10.1103/RevModPhys.90.045002](https://doi.org/10.1103/RevModPhys.90.045002). URL: <https://link.aps.org/doi/10.1103/RevModPhys.90.045002>.
- 2335 [5] Fritz Zwicky. “The Redshift of Extragalactic Nebulae”. In: *Helvetica Physica Acta* 6.
 2336 (1933), pp. 110–127. doi: [10.5169/seals-110267](https://doi.org/10.5169/seals-110267).
- 2337 [6] Vera C. Rubin and Jr. Ford W. Kent. “Rotation of the Andromeda Nebula from a
 2338 Spectroscopic Survey of Emission Regions”. In: *ApJ* 159 (Feb. 1970), p. 379. doi:
 2339 [10.1086/150317](https://doi.org/10.1086/150317).
- 2340 [7] K. G. Begeman, A. H. Broeils, and R. H. Sanders. “Extended rotation curves of spiral galax-
 2341 ies: dark haloes and modified dynamics”. In: *Monthly Notices of the Royal Astronomical So-*
 2342 *ciety* 249.3 (Apr. 1991), pp. 523–537. ISSN: 0035-8711. doi: [10.1093/mnras/249.3.523](https://doi.org/10.1093/mnras/249.3.523).
 2343 eprint: <https://academic.oup.com/mnras/article-pdf/249/3/523/18160929/mnras249-0523.pdf>. URL: <https://doi.org/10.1093/mnras/249.3.523>.
- 2345 [8] *Different types of gravitational lenses*. website. Feb. 2004. URL: <https://esahubble.org/images/heic0404b/>.
- 2347 [9] Douglas Clowe et al. “A Direct Empirical Proof of the Existence of Dark Matter”. In: *apjl*
 2348 648.2 (Sept. 2006), pp. L109–L113. doi: [10.1086/508162](https://doi.org/10.1086/508162). arXiv: [astro-ph/0608407](https://arxiv.org/abs/astro-ph/0608407)
 2349 [[astro-ph](#)].
- 2350 [10] Planck Collaboration and N. et. al. Aghanim. “Planck 2018 results I. Overview and the
 2351 cosmological legacy of Planck”. In: *A&A* 641 (2020). doi: [10.1051/0004-6361/201833880](https://doi.org/10.1051/0004-6361/201833880). URL: <https://doi.org/10.1051/0004-6361/201833880>.
- 2353 [11] Wayne Hu. *Matter Density Animation*. web. 2024. URL: <http://background.uchicago.edu/~whu/animbut/anim2.html>.

- 2355 [12] Wenlong Yuan et al. “A First Look at Cepheids in a Type Ia Supernova Host with JWST”. in:
2356 *The Astrophysical Journal Letters* 940.1 (Nov. 2022). doi: [10.3847/2041-8213/ac9b27](https://doi.org/10.3847/2041-8213/ac9b27).
2357 URL: <https://dx.doi.org/10.3847/2041-8213/ac9b27>.
- 2358 [13] Wendy L. Freedman. “Measurements of the Hubble Constant: Tensions in Perspective”. In:
2359 *The Astrophysical Journal* 919.1 (Sept. 2021), p. 16. doi: [10.3847/1538-4357/ac0e95](https://doi.org/10.3847/1538-4357/ac0e95).
2360 URL: <https://dx.doi.org/10.3847/1538-4357/ac0e95>.
- 2361 [14] Jodi Cooley. “Dark Matter direct detection of classical WIMPs”. In: *SciPost Phys. Lect.
2362 Notes* (2022), p. 55. doi: [10.21468/SciPostPhysLectNotes.55](https://doi.org/10.21468/SciPostPhysLectNotes.55). URL: <https://scipost.org/10.21468/SciPostPhysLectNotes.55>.
- 2364 [15] “Search for new phenomena in events with an energetic jet and missing transverse momentum
2365 in pp collisions at $\sqrt{s} = 13$ TeV with the ATLAS detector”. In: *Phys. Rev. D* 103
2366 (11 July 2021), p. 112006. doi: [10.1103/PhysRevD.103.112006](https://doi.org/10.1103/PhysRevD.103.112006). URL: <https://link.aps.org/doi/10.1103/PhysRevD.103.112006>.
- 2368 [16] *Jetting into the dark side: a precision search for dark matter*. website. July 2020. URL:
2369 <https://atlas.cern/updates/briefing/precision-search-dark-matter>.
- 2370 [17] Celine Armand et. al. “Combined dark matter searches towards dwarf spheroidal galaxies
2371 with Fermi-LAT, HAWC, H.E.S.S., MAGIC, and VERITAS”. in: *Proceedings of Science*.
2372 Vol. 395. Mar. 2022. doi: <https://doi.org/10.22323/1.395.0528>.
- 2373 [18] Tracy R. Slatyer. “Les Houches Lectures on Indirect Detection of Dark Matter”. In: *SciPost
2374 Phys. Lect. Notes* (2022), p. 53. doi: [10.21468/SciPostPhysLectNotes.53](https://doi.org/10.21468/SciPostPhysLectNotes.53). URL:
2375 <https://scipost.org/10.21468/SciPostPhysLectNotes.53>.
- 2376 [19] Christian W Bauer, Nicholas L. Rodd, and Bryan R. Webber. “Dark matter spectra from
2377 the electroweak to the Planck scale”. In: *Journal of High Energy Physics* 2021.1029-8479
2378 (June 2021). doi: [https://doi.org/10.1007/JHEP06\(2021\)121](https://doi.org/10.1007/JHEP06(2021)121).
- 2379 [20] Riccardo Catena and Piero Ullio. “A novel determination of the local dark matter density”.
2380 In: *Journal of Cosmology and Astroparticle Physics* 2010.08 (Aug. 2010), p. 004. doi:
2381 [10.1088/1475-7516/2010/08/004](https://doi.org/10.1088/1475-7516/2010/08/004). URL: <https://dx.doi.org/10.1088/1475-7516/2010/08/004>.
- 2383 [21] B. P. Abbott et al. “Observation of Gravitational Waves from a Binary Black Hole Merger”.
2384 In: *Phys. Rev. Lett.* 116 (6 Feb. 2016), p. 061102. doi: [10.1103/PhysRevLett.116.061102](https://doi.org/10.1103/PhysRevLett.116.061102). URL: <https://link.aps.org/doi/10.1103/PhysRevLett.116.061102>.
- 2386 [22] R. Abbasi et. al. “Observation of high-energy neutrinos from the Galactic plane”. In: *Science*
2387 380.6652 (June 2023), pp. 1338–1343.
- 2388 [23] NASA Goddard Space Flight Center. *Fermi’s 12-year view of the gamma-ray sky*. website.

- 2389 2022. URL: <https://svs.gsfc.nasa.gov/14090>.
- 2390 [24] Marco Cirelli et al. “PPPC 4 DM ID: a poor particle physicist cookbook for dark matter
2391 indirect detection”. In: *Journal of Cosmology and Astroparticle Physics* 2011.03 (Mar.
2392 2011), p. 051. doi: [10.1088/1475-7516/2011/03/051](https://doi.org/10.1088/1475-7516/2011/03/051). URL: <https://dx.doi.org/10.1088/1475-7516/2011/03/051>.
- 2394 [25] The HAWC Collaboration. “The High-Altitude Water Cherenkov (HAWC) observatory in
2395 México: The primary detector”. In: *Nuclear Instruments and Methods in Physics Research*
2396 *Section A: Accelerators, Spectrometers, Detectors and Associated Equipment* 1052 (2023),
2397 p. 168253. ISSN: 0168-9002. doi: <https://doi.org/10.1016/j.nima.2023.168253>.
2398 URL: <https://www.sciencedirect.com/science/article/pii/S0168900223002437>.
- 2400 [26] Alicia Lopez Oramas. “Multi-year Campaign of the Gamma-Ray Binary LS I +61° 303
2401 and Search for VHE Emission from Gamma-Ray Binary Candidates with the MAGIC
2402 Telescopes”. PhD thesis. Instituto de Astrofísica de Canarias, 2014. doi: <http://dx.doi.org/10.13140/RG.2.1.4140.4969>.
- 2404 [27] Hamamatsu Photonics KK. *Large Photocathode Area Photomultiplier Tubes*. 2019. URL:
2405 https://www.hamamatsu.com/content/dam/hamamatsu-photronics/sites/documents/99_SALES_LIBRARY/etd/LARGE_AREA_PMT TPMH1376E.pdf.
- 2407 [28] The Milagro Collaboratio. “Milagrito, a TeV air-shower array”. In: *Nuclear Instruments
2408 and Methods in Physics Research Section A: Accelerators, Spectrometers, Detectors and
2409 Associated Equipment* 449.3 (2000), pp. 478–499. ISSN: 0168-9002. doi: [https://doi.org/10.1016/S0168-9002\(00\)00146-7](https://doi.org/10.1016/S0168-9002(00)00146-7). URL: <https://www.sciencedirect.com/science/article/pii/S0168900200001467>.
- 2412 [29] A.U. Abeysekara et. al. “The High-Altitude Water Cherenkov (HAWC) observatory in México:
2413 The primary detector”. In: *Nuclear Instruments and Methods in Physics Research*
2414 *Section A: Accelerators, Spectrometers, Detectors and Associated Equipment* 1052 (2023),
2415 p. 168253. ISSN: 0168-9002. doi: <https://doi.org/10.1016/j.nima.2023.168253>.
2416 URL: <https://www.sciencedirect.com/science/article/pii/S0168900223002437>.
- 2418 [30] The HAWC Collaboration. “Data acquisition architecture and online processing system
2419 for the HAWC gamma-ray observatory”. In: *Nuclear Instruments and Methods in Physics*
2420 *Research Section A: Accelerators, Spectrometers, Detectors and Associated Equipment* 888
2421 (2018), pp. 138–146. ISSN: 0168-9002. doi: <https://doi.org/10.1016/j.nima.2018.01.051>. URL: <https://www.sciencedirect.com/science/article/pii/S0168900218300688>.
- 2424 [31] Ian Gabriel Wisher. “Real-time Transient Monitoring With the HAWC Detector: Design
2425 and Performance”. PhD thesis. The University of Wisconsin - Madison, 2016.

- 2426 [32] The ZeroMQ authors. “ZeroMQ An open-source universal messaging library”. In: (2021).
2427 URL: <https://zeromq.org>.
- 2428 [33] Zigfried Hampel-Archisman. “Cosmic Ray Observations at the TeV Scale with the HAWC
2429 Observatory”. PhD thesis. University of Wisconsin-Madison, 2017.
- 2430 [34] A. U. Abeysekara et al. “Observation of the Crab Nebula with the HAWC Gamma-Ray
2431 Observatory”. In: *The Astrophysical Journal* 843.1 (June 2017), p. 39. doi: [10.3847/1538-4357/aa7555](https://doi.org/10.3847/1538-4357/aa7555). URL: <https://doi.org/10.3847/1538-4357/aa7555>.
- 2433 [35] Kenneth Greisen. “Cosmic Ray Showers”. In: *ANNUAL REVIEW OF NUCLEAR AND
2434 PARTICLE SCIENCE* 10 (1960), pp. 63–108.
- 2435 [36] Javier Rico. “Gamma-Ray Dark Matter Searches in Milky Way Satellites—A Comparative
2436 Review of Data Analysis Methods and Current Results”. In: *Galaxies* 8.1 (Mar. 2020), p. 25.
2437 doi: [10.3390/galaxies8010025](https://doi.org/10.3390/galaxies8010025). arXiv: [2003.13482 \[astro-ph.HE\]](https://arxiv.org/abs/2003.13482).
- 2438 [37] W. B. Atwood et al. “The Large Area Telescope on the Fermi Gamma-Ray Space Telescope
2439 Mission”. In: *apj* 697.2 (June 2009), pp. 1071–1102. doi: [10.1088/0004-637X/697/2/1071](https://doi.org/10.1088/0004-637X/697/2/1071). arXiv: [0902.1089 \[astro-ph.IM\]](https://arxiv.org/abs/0902.1089).
- 2441 [38] M. Ackermann et al. “Searching for Dark Matter Annihilation from Milky Way Dwarf
2442 Spheroidal Galaxies with Six Years of Fermi Large Area Telescope Data”. In: *prl* 115.23,
2443 231301 (Dec. 2015), p. 231301. doi: [10.1103/PhysRevLett.115.231301](https://doi.org/10.1103/PhysRevLett.115.231301). arXiv:
2444 [1503.02641 \[astro-ph.HE\]](https://arxiv.org/abs/1503.02641).
- 2445 [39] Mattia Di Mauro, Martin Stref, and Francesca Calore. “Investigating the effect of Milky
2446 Way dwarf spheroidal galaxies extension on dark matter searches with Fermi-LAT data”.
2447 In: *Phys. Rev. D* 106 (12 Dec. 2022), p. 123032. doi: [10.1103/PhysRevD.106.123032](https://doi.org/10.1103/PhysRevD.106.123032).
2448 URL: <https://link.aps.org/doi/10.1103/PhysRevD.106.123032>.
- 2449 [40] F. et al. Aharonian. “Observations of the Crab Nebula with H.E.S.S.”. In: *Astron. Astrophys.*
2450 457 (2006), pp. 899–915. doi: [10.1051/0004-6361:20065351](https://doi.org/10.1051/0004-6361:20065351). arXiv: [astro-ph/0607333](https://arxiv.org/abs/astro-ph/0607333).
- 2452 [41] J. Albert et al. “VHE γ -Ray Observation of the Crab Nebula and its Pulsar with the MAGIC
2453 Telescope”. In: *The Astrophysical Journal* 674.2 (Feb. 2008), p. 1037. doi: [10.1086/525270](https://doi.org/10.1086/525270). URL: <https://dx.doi.org/10.1086/525270>.
- 2455 [42] N. Park. “Performance of the VERITAS experiment”. In: *Proceedings, 34th International
2456 Cosmic Ray Conference (ICRC2015): The Hague, The Netherlands, July, 30th July - 6th
2457 August*. Vol. 34. 2015, p. 771. arXiv: [1508.07070 \[astro-ph.IM\]](https://arxiv.org/abs/1508.07070).
- 2458 [43] A. Abramowski et al. “H.E.S.S. constraints on Dark Matter annihilations towards the Sculptor
2459 and Carina Dwarf Galaxies”. In: *Astropart. Phys.* 34 (2011), pp. 608–616. doi: [10.1016/j.astropartphys.2011.02.003](https://doi.org/10.1016/j.astropartphys.2011.02.003).

- 2460 j. astropartphys. 2010.12.006. arXiv: 1012.5602 [astro-ph.HE].
- 2461 [44] A. Abramowski et al. “Search for dark matter annihilation signatures in H.E.S.S. observations
2462 of Dwarf Spheroidal Galaxies”. In: *Phys. Rev. D* 90 (2014), p. 112012. doi: 10.1103/Ph
2463 ysRevD.90.112012. arXiv: 1410.2589 [astro-ph.HE].
- 2464 [45] H. Abdalla et al. “Searches for gamma-ray lines and ‘pure WIMP’ spectra from Dark
2465 Matter annihilations in dwarf galaxies with H.E.S.S”. in: *JCAP* 11 (2018), p. 037. doi:
2466 10.1088/1475-7516/2018/11/037. arXiv: 1810.00995 [astro-ph.HE].
- 2467 [46] J. Aleksić et al. “Optimized dark matter searches in deep observations of Segue 1 with
2468 MAGIC”. in: *JCAP* 1402 (2014), p. 008. doi: 10.1088/1475-7516/2014/02/008.
2469 arXiv: 1312.1535 [hep-ph].
- 2470 [47] V.A. Acciari et al. “Combined searches for dark matter in dwarf spheroidal galaxies observed
2471 with the MAGIC telescopes, including new data from Coma Berenices and Draco”. In: *Physics of the Dark Universe* (2021), p. 100912. issn: 2212-6864. doi: <https://doi.org/10.1016/j.dark.2021.100912>. URL: <https://www.sciencedirect.com/science/article/pii/S2212686421001370>.
- 2475 [48] M. L. Ahnen et al. “Indirect dark matter searches in the dwarf satellite galaxy Ursa Major II
2476 with the MAGIC Telescopes”. In: *JCAP* 1803.03 (2018), p. 009. doi: 10.1088/1475-7
2477 516/2018/03/009. arXiv: 1712.03095 [astro-ph.HE].
- 2478 [49] S. et al. Archambault. “Dark matter constraints from a joint analysis of dwarf Spheroidal
2479 galaxy observations with VERITAS”. in: *prd* 95.8 (Apr. 2017). doi: 10.1103/PhysRevD
2480 .95.082001. arXiv: 1703.04937 [astro-ph.HE].
- 2481 [50] Louise Oakes et al. “Combined Dark Matter searches towards dwarf spheroidal galaxies with
2482 Fermi-LAT, HAWC, HESS, MAGIC and VERITAS”. in: *Proceedings of Science*. 2019.
- 2483 [51] Celine Armand et al. on behalf of the Fermi-LAT, HAWC, HESS, MAGIC, VERITAS.
2484 “Combined Dark Matter searches towards dwarf spheroidal galaxies with Fermi-LAT,
2485 HAWC, HESS, MAGIC and VERITAS”. in: *Proceedings of Science*. 2021.
- 2486 [52] Daniel Kerszberg et al. on behalf of the Fermi-LAT, HAWC, HESS, MAGIC, and VER-
2487 TIAS collaborations. “Search for dark matter annihilation with a combined analysis of
2488 dwarf spheroidal galaxies from Fermi-LAT, HAWC, H.E.S.S., MAGIC and VERITAS”. in:
2489 *Proceedings of Science*. 2023.
- 2490 [53] Giacomo Vianello et al. *The Multi-Mission Maximum Likelihood framework (3ML)*. 2015.
2491 arXiv: 1507.08343 [astro-ph.HE].
- 2492 [54] Marco Cirelli et al. “PPPC 4 DM ID: a poor particle physicist cookbook for dark matter
2493 indirect detection”. In: *Journal of Cosmology and Astroparticle Physics* 2011.03 (Mar.

- 2494 2011). ISSN: 1475-7516. doi: [10.1088/1475-7516/2011/03/051](https://doi.org/10.1088/1475-7516/2011/03/051). URL: <http://dx.doi.org/10.1088/1475-7516/2011/03/051>.
- 2495
- 2496 [55] Alex Geringer-Sameth, Savvas M. Koushiappas, and Matthew Walker. “DWARF GALAXY
2497 ANNIHILATION AND DECAY EMISSION PROFILES FOR DARK MATTER EXPERI-
2498 MENTS”. In: *The Astrophysical Journal* 801.2 (Mar. 2015), p. 74. ISSN: 1538-4357. doi:
2499 [10.1088/0004-637x/801/2/74](https://doi.org/10.1088/0004-637x/801/2/74). URL: <http://dx.doi.org/10.1088/0004-637X/801/2/74>.
- 2500
- 2501 [56] A. Albert et al. “Dark Matter Limits from Dwarf Spheroidal Galaxies with the HAWC
2502 Gamma-Ray Observatory”. In: *The Astrophysical Journal* 853.2 (Feb. 2018), p. 154. ISSN:
2503 1538-4357. doi: [10.3847/1538-4357/aaa6d8](https://doi.org/10.3847/1538-4357/aaa6d8). URL: <http://dx.doi.org/10.3847/1538-4357/aaa6d8>.
- 2504
- 2505 [57] HongSheng Zhao. “Analytical models for galactic nuclei”. In: *Mon. Not. Roy. Astron. Soc.*
2506 278 (1996), pp. 488–496. doi: [10.1093/mnras/278.2.488](https://doi.org/10.1093/mnras/278.2.488). arXiv: [astro-ph/9509122](https://arxiv.org/abs/astro-ph/9509122)
[astro-ph].
- 2507
- 2508 [58] Julio F. Navarro, Carlos S. Frenk, and Simon D. M. White. “The Structure of Cold Dark
2509 Matter Halos”. In: *ApJ* 462 (May 1996), p. 563. doi: [10.1086/177173](https://doi.org/10.1086/177173). eprint:
2510 [astro-ph/9508025](https://arxiv.org/abs/astro-ph/9508025) (astro-ph).
- 2511
- 2512 [59] V. Bonnivard et al. “Spherical Jeans analysis for dark matter indirect detection in dwarf
2513 spheroidal galaxies - Impact of physical parameters and triaxiality”. In: *Mon. Not. Roy.*
2514 *Astron. Soc.* 446 (2015), pp. 3002–3021. doi: [10.1093/mnras/stu2296](https://doi.org/10.1093/mnras/stu2296). arXiv:
[1407.7822](https://arxiv.org/abs/1407.7822) [astro-ph.HE].
- 2515
- 2516 [60] M. Ackermann et al. “Searching for Dark Matter Annihilation from Milky Way Dwarf
2517 Spheroidal Galaxies with Six Years of Fermi Large Area Telescope Data”. In: *prl* 115.23,
2518 231301 (Dec. 2015), p. 231301. doi: [10.1103/PhysRevLett.115.231301](https://doi.org/10.1103/PhysRevLett.115.231301). arXiv:
[1503.02641](https://arxiv.org/abs/1503.02641) [astro-ph.HE].
- 2519
- 2520 [61] M. L. Ahnen et al. “Limits to Dark Matter Annihilation Cross-Section from a Combined
2521 Analysis of MAGIC and Fermi-LAT Observations of Dwarf Satellite Galaxies”. In: *JCAP*
2522 1602.02 (2016), p. 039. doi: [10.1088/1475-7516/2016/02/039](https://doi.org/10.1088/1475-7516/2016/02/039). arXiv: [1601.06590](https://arxiv.org/abs/1601.06590)
[astro-ph.HE].
- 2523
- 2524 [62] Javier Rico et al. *gLike: numerical maximization of heterogeneous joint*
2525 *likelihood functions of a common free parameter plus nuisance parameters.*
2526 <https://doi.org/10.5281/zenodo.4601451>. Version v00.09.03. Mar. 2021. doi: [10.5281/zenodo.4601451](https://doi.org/10.5281/zenodo.4601451). URL: <https://doi.org/10.5281/zenodo.4601451>.
- 2527
- 2528 [63] Tjark Miener and Daniel Nieto. *LklCom: Combining likelihoods from different experiments.*
2529 <https://doi.org/10.5281/zenodo.4597500>. Version v0.5.3. Mar. 2021. doi: [10.5281/zenodo.4597500](https://doi.org/10.5281/zenodo.4597500). URL: <https://doi.org/10.5281/zenodo.4597500>.

- 2530 [64] T. Miener et al. “Open-source Analysis Tools for Multi-instrument Dark Matter Searches”.
 2531 In: *arXiv e-prints*, arXiv:2112.01818 (Dec. 2021), arXiv:2112.01818. arXiv: [2112.01818](#) [[astro-ph.IM](#)].
 2532
- 2533 [65] Alex Geringer-Sameth and Matthew Koushiappas Savvas M. and Walker. “Dwarf galaxy
 2534 annihilation and decay emission profiles for dark matter experiments”. In: *Astrophys.
 2535 J.* 801.2 (2015), p. 74. doi: [10.1088/0004-637X/801/2/74](#). arXiv: [1408.0002](#)
 2536 [[astro-ph.CO](#)].
- 2537 [66] Gianfranco Bertone, Dan Hooper, and Joseph Silk. “Particle dark matter: evidence, can-
 2538 didates and constraints”. In: *Physics Reports* 405.5-6 (Jan. 2005), pp. 279–390. ISSN:
 2539 0370-1573. doi: [10.1016/j.physrep.2004.08.031](#). URL: <http://dx.doi.org/10.1016/j.physrep.2004.08.031>.
 2540
- 2541 [67] V. Bonnivard et al. “Dark matter annihilation and decay in dwarf spheroidal galaxies: The
 2542 classical and ultrafaint dSphs”. In: *Mon. Not. Roy. Astron. Soc.* 453.1 (2015), pp. 849–867.
 2543 doi: [10.1093/mnras/stv1601](#). arXiv: [1504.02048](#) [[astro-ph.HE](#)].
 2544
- 2544 [68] A. et al. Albert. “Searching for Dark Matter Annihilation in Recently Discovered Milky Way
 2545 Satellites with Fermi-LAT”. in: *Astrophys. J.* 834.2 (2017), p. 110. doi: [10.3847/1538-4357/834/2/110](#). arXiv: [1611.03184](#) [[astro-ph.HE](#)].
 2546
- 2547 [69] Mattia Di Mauro and Martin Wolfgang Winkler. “Multimessenger constraints on the dark
 2548 matter interpretation of the Fermi-LAT Galactic Center excess”. In: *prd* 103.12, 123005
 2549 (June 2021), p. 123005. doi: [10.1103/PhysRevD.103.123005](#). arXiv: [2101.11027](#)
 2550 [[astro-ph.HE](#)].
 2551
- 2551 [70] H. C. Plummer. “On the Problem of Distribution in Globular Star Clusters: (Plate 8.)”
 2552 In: *Monthly Notices of the Royal Astronomical Society* 71.5 (Mar. 1911), pp. 460–470.
 2553 ISSN: 0035-8711. doi: [10.1093/mnras/71.5.460](#). eprint: <https://academic.oup.com/mnras/article-pdf/71/5/460/2937497/mnras71-0460.pdf>. URL:
 2554 <https://doi.org/10.1093/mnras/71.5.460>.
 2555
- 2556 [71] Daniel R. Hunter. “Derivation of the anisotropy profile, constraints on the local velocity
 2557 dispersion, and implications for direct detection”. In: *JCAP* 02 (2014), p. 023. doi:
 2558 [10.1088/1475-7516/2014/02/023](#). arXiv: [1311.0256](#) [[astro-ph.CO](#)].
 2559
- 2559 [72] Barun Kumar Dhar and Liliya L. R. Williams. “Surface mass density of the Einasto family
 2560 of dark matter haloes: are they Sersic-like?” In: *Mon. Not. Roy. Astron. Soc.* (2010). doi:
 2561 [10.1111/j.1365-2966.2010.16446.x](#).
 2562
- 2562 [73] M. Baes and E. Van Hese. “Dynamical models with a general anisotropy profile”. In: *Astron. Astrophys.* 471 (2007), p. 419. doi: [10.1051/0004-6361:20077672](#). arXiv:
 2563 [0705.4109](#) [[astro-ph](#)].
 2564

- 2565 [74] Matthew G. Walker, Edward W. Olszewski, and Mario Mateo. “Bayesian analysis of re-
2566 solved stellar spectra: application to MMT/Hectochelle observations of the Draco dwarf
2567 spheroidal”. In: *mnras* 448.3 (Apr. 2015), pp. 2717–2732. doi: [10.1093/mnras/stv099](https://doi.org/10.1093/mnras/stv099).
2568 arXiv: [1503.02589 \[astro-ph.GA\]](https://arxiv.org/abs/1503.02589).
- 2569 [75] Nicholas L. Rodd et al. “Dark matter spectra from the electroweak to the Planck scale”. In:
2570 *J. High Energy Physics* 121.10.1007 (June 2021).
- 2571 [76] Pace, Andrew B and Strigari, Louis E. “Scaling relations for dark matter annihilation and
2572 decay profiles in dwarf spheroidal galaxies”. In: *Monthly Notices of the Royal Astronomical
2573 Society* 482.3 (Oct. 2018), pp. 3480–3496. issn: 0035-8711. doi: [10.1093/mnras/sty2839](https://doi.org/10.1093/mnras/sty2839).
- 2575 [77] Albert, A. et al. “Search for gamma-ray spectral lines from dark matter annihilation in
2576 dwarf galaxies with the High-Altitude Water Cherenkov observatory”. In: *Phys. Rev. D* 101 (10 May 2020), p. 103001. doi: [10.1103/PhysRevD.101.103001](https://doi.org/10.1103/PhysRevD.101.103001). URL:
2577 <https://link.aps.org/doi/10.1103/PhysRevD.101.103001>.
- 2579 [78] Victor Eijkhout and Edmund Show and Robert van de Geijn. *The Science of Computing.
2580 The Art of High Performance Computing*. Vol. 3. Open Copy published under CC-BY 4.0
2581 license, 2023, pp. 63–66.
- 2582 [79] Aartsen, M. et al. “IceCube search for dark matter annihilation in nearby galaxies and galaxy
2583 clusters”. In: *Phys. Rev. D* 88 (12 Dec. 2013), p. 122001. doi: [10.1103/PhysRevD.88.122001](https://doi.org/10.1103/PhysRevD.88.122001). URL: <https://link.aps.org/doi/10.1103/PhysRevD.88.122001>.
- 2585 [80] Pearl Sandick et al. “Sensitivity of the IceCube neutrino detector to dark matter annihilating
2586 in dwarf galaxies”. In: *Phys. Rev. D* 81 (8 Apr. 2010), p. 083506. doi: [10.1103/PhysRevD.81.083506](https://doi.org/10.1103/PhysRevD.81.083506). URL: <https://link.aps.org/doi/10.1103/PhysRevD.81.083506>.
- 2588 [81] Qinrui Liu and Jeffrey Lazar and Carlos A. Argüelles and Ali Kheirandish. “ χ aro: a tool
2589 for neutrino flux generation from WIMPs”. In: *Journal of Cosmology and Astroparticle
2590 Physics* 2020.10 (Oct. 2020), p. 043. doi: [10.1088/1475-7516/2020/10/043](https://doi.org/10.1088/1475-7516/2020/10/043). URL:
2591 <https://dx.doi.org/10.1088/1475-7516/2020/10/043>.
- 2592 [82] Tessa Cerver. “Time Integrated searches for Astrophysical Neutrino Sources using the
2593 IceCube Detector and Gender in Physics studies for the Genera Project”. PhD thesis.
2594 UNIVERSITE DE GEN`EVE, 2019, pp. 57–64.
- 2595 [83] Minjin Jeong on behalf of the IceCube Collaboration. “Search for Dark Matter Decay in
2596 Nearby Galaxy Clusters and Galaxies with IceCube”. In: *Proceedings of Science* 444.38
2597 (2023).
- 2598 [84] IceCube Collaboration. “Evidence for neutrino emission from the nearby active galaxy NGC
2599 1068”. In: *Science* 378.6619 (2022).

- 2600 [85] Nathan Whitehorn and Jakob van Santen. *Photospline*. IceCube: GitHub.
- 2601 [86] Paul H. C. Eilers and Brian D. Marx. “Flexible smoothing with B-splines and penalties”.
2602 In: *Statistical Science* 11.2 (1996), pp. 89–121. doi: [10.1214/ss/1038425655](https://doi.org/10.1214/ss/1038425655). URL:
2603 <https://doi.org/10.1214/ss/1038425655>.
- 2604 [87] The IceCube Collaboration. *Search for neutrino lines from dark matter annihilation and*
2605 *decay with IceCube*. 2023. arXiv: [2303.13663](https://arxiv.org/abs/2303.13663) [[astro-ph.HE](#)].
- 2606 [88] The IceCube Collaboration. “Measurement of the multi-TeV neutrino interaction cross-
2607 section with IceCube using Earth absorption”. In: *Nature* 551 (2017).